# Design of a Viable Homogeneous-Charge Compression-Ignition (HCCI) Engine: A Computational Study with Detailed Chemical Kinetics

by

## Paul E. Yelvington

B.S., North Carolina State University, 1999
M.S.CEP, Massachusetts Institute of Technology, 2001

Submitted to the Department of Chemical Engineering in partial fulfillment of the requirements for the degree of

**DOCTOR OF PHILOSOPHY IN CHEMICAL ENGINEERING**

AT THE
MASSACHUSETTS INSTITUTE OF TECHNOLOGY

SEPTEMBER, 2004

Author.................................................................................................................................
**Paul E. Yelvington**
Department of Chemical Engineering
September 28, 2004

Certified by.........................................................................................................................
**William H. Green, Jr.**
Professor of Chemical Engineering
Thesis Supervisor

Certified by.........................................................................................................................
**Jefferson W. Tester**
Professor of Chemical Engineering
Thesis Supervisor

Accepted by........................................................................................................................
**Daniel Blankschtein**
Professor of Chemical Engineering
Chairman, Committee for Graduate Students

# Abstract

The homogeneous-charge compression-ignition (HCCI) engine is a novel engine technology with the potential to substantially lower emissions from automotive sources. HCCI engines use lean-premixed combustion to achieve good fuel economy and low emissions of nitrogen-oxides and particulate matter. However, experimentally these engines have demonstrated a viable operating range that is too narrow for vehicular applications. Incomplete combustion or misfire can occur under fuel-lean conditions imposing a minimum load at which the engine can operate. At high loads, HCCI engines are often extremely loud and measured cylinder pressures show strong acoustic oscillations resembling those for a knocking spark-ignited engine. The goal of this research was to understand the factors limiting the HCCI range of operability and propose ways of broadening that range.

An engine simulation tool was developed to model the combustion process in the engine and predict HCCI knock and incomplete combustion. Predicting HCCI engine knock is particularly important because knock limits the maximum engine torque, and this limitation is a major obstacle to commercialization. A fundamentally-based criterion was developed and shown to give good predictions of the experimental knock limit. Our engine simulation tool was then used to explore the effect of various engine design parameters and operating conditions on the HCCI viable operating range. Performance maps, which show the response of the engine during a normal driving cycle, were constructed to compare these engine designs. The simulations showed that an acceptably broad operating range can be achieved by using a low compression ratio, low octane fuel, and moderate boost pressure. An explanation of why this choice of parameters gives a broad operating window is discussed.

Our prediction of the HCCI knock limit is based on the autoignition theory of knock, which asserts that local overpressures in the engine are caused by extremely rapid chemical energy release. A competing theory asserts that knock is caused by the formation of detonation waves initiated at autoignition centers ('hot-spots') in the engine. No conclusive experimental evidence exists for the detonation theory, but many numerical simulations in the literature show that detonation formation is possible; however, some of the assumptions made in these simulations warrant re-examination. In particular, the effect of curvature on small (quasi-spherical) hot-spots has often been overlooked. We first examined the well-studied case of gasoline spark-ignited engine knock and observed that the size of the hot-spot needed to initiate a detonation is larger than the end-gas region where knock occurs. Subsequent studies of HCCI engine knock predicted that detonations would not form regardless of the hot-spot size because of the low energy content of fuel-lean mixtures typically used in these engines.

Our predictions of the HCCI viable operating range were shown to be quite sensitive to details of the ignition chemistry. Therefore, an attempt was made to build an improved chemistry model for HCCI combustion using automatic mechanism-generation software developed in our research group. Extensions to the software were made to allow chemistry model construction for engine conditions. Model predictions for *n*-heptane/air combustion were compared to literature data from a jet-stirred reactor and rapid-compression machine. We conclude that automatic mechanism generation gives fair predictions without the tuning of rate parameters or other efforts to improve agreement. However, some tuning of the automatically-generated chemistry models is necessary to give the accurate predictions of HCCI combustion needed for our design calculations.

# Dedication

This work is dedicated to my parents, John and Bonnie Yelvington. I am very grateful for the encouragement and support they have always given me.

# Acknowledgements

# Table of Contents

# Chapter 1:	Introduction

## 1.1 Motivation

Gasoline and diesel automobile engines are large contributors to urban air pollution. Carbon dioxide and unburned hydrocarbon emissions from engines contribute to global warming. Nitrogen oxides and hydrocarbon react in the atmosphere to form photochemical smog. Particulate matter from diesel engines increases rates of asthma and respiratory problems. In an attempt to reduce the air pollution from automobiles, researchers have studied alternative sources of power for transportation such as hybrid gasoline-electric cars and fuel-cell cars. These alternatives have shown potential to be clean sources of power for transportation but involve considerable extra manufacturing costs and fairly untested technologies.

Another alternative technology is the homogeneous-charge compression-ignition (HCCI) engine, which uses largely conventional internal-combustion engine technology. The HCCI engine combines features of both gasoline and diesel engines. The fuel and air are premixed prior to entering the engine cylinder like the gasoline engine. However, the mixture is compression-ignited like a diesel engine rather than a spark-ignited engine. HCCI engines run well on lean fuel/air mixture which leads to lower combustion temperatures favoring low $NO_x$ emissions and good thermal efficiency. Because the fuel/air mixture is premixed, there are no locally fuel-rich regions that are conducive to soot formation.

Although experimental HCCI engines have shown good thermal efficiencies and low emissions of $NO_x$ and soot, several technical hurdles stand in the way of their commercialization. In particular HCCI engines operate stably over a fairly narrow range of operating conditions. For very fuel lean mixtures (used at low power and idle

conditions), the engine can misfire. For near-stoichiometric mixtures (used at high power), significant pressure waves develop in the combustion chamber leading to noisy operation ("knock") and materials damage. The primary goal of this work was to develop a numerical simulation tool that could predict the stable operating range for an HCCI engine and use that simulation tool to design an engine that is stable over a broad range of operating conditions.

The HCCI design research led to two related studies pursued in some depth. The first was a study of the origins of knock in HCCI (and gasoline) engines. Because knock limits the maximum power density of HCCI engines, it was important to get a better understanding of its causes. Two major theories exist in the literature to explain knock. The detonation theory attributes knock to the formation of detonation waves in the engine. The autoignition theory attributes knock to the extremely rapid release of chemical energy which causes local overpressures. Reacting flow calculations were performed to test whether detonation waves can indeed form in an engine cylinder.

Our HCCI design calculations showed that our predictions were sensitive to the detailed chemistry model used in the simulations. This observation led to the second related study, an effort to build an improved chemistry model for HCCI combustion. This study focused on the oxidation of $n$-heptane because our design calculations showed that $n$-heptane is an ideal fuel for HCCI engines because of its low autoignition temperature. The generated models were tested against literature data from rapid-compression machine experiments, which simulate the conditions in an HCCI engine. These modeling efforts lead to conclusions about the predictive capability of current chemical kinetic models.

## 1.2  Thesis Overview by Chapter

### 1.2.1  Chapter Two

This chapter describes the development of an engine-modeling tool capable of predicting the range of operability of an HCCI engine. This tool uses a combination of computational-fluid dynamics (CFD) and chemical kinetics to simulate HCCI combustion. A multi-zone modeling technique from the literature was extended to allow very detailed chemistry models to be efficiently simulated by exploiting the sparsity in the governing equations using automatic differentiation technology.

Also a fundamentally based criterion was developed to predict the onset of engine knock. This criterion arises from a scaling analysis of the relevant competing chemical and physical processes. This knock criterion was combined with the multi-zone engine model to produce a tool capable predicting the viable HCCI operating range. Range predictions are compared with literature data for an HCCI test engine.

### 1.2.2  Chapter Three

This chapter extends the engine-modeling tool used in Chapter 2 to predict HCCI operating ranges on performance maps. These maps show the response of the engine to changes in engine load and speed—the key variables for determining performance of the engine over a typical driving cycle. The engine-modeling tool for this study used a simpler description of the combustion chamber than used previously, but was coupled to a cycle simulation program to model the gas-exchange processes in the engine. Sub-models of wall heat losses and engine friction were used to predict brake properties of the engine such as the useful work delivered to the crankshaft.

The new engine-modeling tool was tested with experimental data from our collaborators at Ford Motor Co. Baseline performance maps were constructed for the

Ford experimental HCCI engine, and then the effects of compression ratio, fuel, and boost pressure on the operating range were tested. Our simulations showed that the correct choice of these operating parameters could lead stable combustion over a range of conditions sufficiently broad for vehicular applications.

### 1.2.3 Chapter Four

This chapter describes a detailed study of engine knock in HCCI and spark-ignited (SI) engines. Because of the importance of engine knock to automotive manufacturers, many studies (mostly of SI engine knock) have been performed. These studies include optical engine experiments, computational fluid dynamics calculations, and theoretical studies. Despite the volume of research that has been done concerning knock, no consensus exists as to the mechanism responsible for the formation of non-uniform pressures in engines. As mentioned, two main theories exist, the autoignition theory and the detonation theory.

To my knowledge there is no direct experimental evidence suggesting the formation of detonations in engines. Many numerical simulations from the literature show detonation formation under engine conditions, but these simulations employ assumptions that have deserve re-examination. The goal of this work was to design and execute a set of reacting flow simulations to determine whether detonations are a likely cause for knock in SI and HCCI engines.

### 1.2.4 Chapter Five

The performance maps for HCCI engines constructed in Chapter 3 proved to be useful for identifying trends and relative effects of various engine parameters on engine performance. However, we observed that errors in the physical model  and the chemistry

model limited the accuracy of our predictions. Therefore we decided to study the chemistry in HCCI combustion in more detail.

This chapter describes work that was done to extend automatic reaction mechanism generation software to engine systems. Although no specific technical hurdle prohibited this extension, it appears that this is the first time that automatically-generated models have been constructed specifically for engine applications. Our goal was to determine the feasibility of automatic chemistry model construction for engines, rather than the build the industry-standard model for HCCI combustion. This next step could certainly be done, but as other researchers have found, requires a certain amount of tuning of model parameters to get acceptable agreement with experiment.

As mentioned, the model-building focused on oxidation of *n*-heptane/air mixtures because our studies in Chapter 3 identified low-octane fuels as ideal for HCCI combustion. Two test cases, a jet-stirred reactor experiment and an rapid-compression machine experiment, are discussed. The influence of both the physical reactor model and the chemistry model are considered in some detail.

# Chapter 2: Development of an HCCI Engine Knock Model and a Fast Multi-zone Engine Model

## 2.1  Introduction

### 2.1.1  Motivation

There is currently a great deal of interest in the homogeneous-charge compression-ignition (HCCI) engine concept since it allows good fuel economy with very low emissions of $NO_x$ and particulate matter [1-3]. However, there is no direct control over the ignition timing in HCCI, and the viable operating range appears to be undesirably small. Incomplete combustion or misfire can occur under very lean conditions imposing a minimum load at which the engine can operate [4-6]. Even if the engine continues to run, a significant fraction of the fuel may be emitted as unburned hydrocarbons. This partial combustion or misfire provides an upper bound on the air/fuel ratio for viable HCCI operation. At low air/fuel ratios (high loads), HCCI engines are often extremely loud and measured in-cylinder pressure traces show strong acoustic oscillations resembling those for a knocking spark-ignited engine.  Although it may be possible to run HCCI engines in this condition without damaging them, the noise would certainly be undesirable in a vehicular application. Here we assume that the onset of HCCI knock provides a lower bound on the air/fuel ratio for normal operation. The region between these two bounds is the viable operating range.

Knowing the viable operating range is critical for engine design and particularly important for the design of control strategies. HCCI engines in vehicles must be able to operate over a range of speed and load conditions.  Knowing the knock limit is especially important because it limits the maximum torque available from the engine. Most experimental HCCI engines have demonstrated maximum torques that are about half of what is required for a vehicle [7]. The knock limit and viable operating range have been

mapped out experimentally for a handful of HCCI engines with particular choices of the engine parameters and fuels [5-8]. As an example, consider the measurements of Oakley et al. [5] reprinted in Figure 2.1. These measurements were made on a single-cylinder Ricardo E6 test engine run at a constant engine speed of 1500 rpm, using a 95 RON primary reference fuel. Various relative air/fuel ratios (lambda) were studied along with various amounts of external exhaust-gas recycle (EGR). The inducted gases were maintained at a constant temperature ($320^{\circ}$C) throughout the experiments. As seen in Figure 2.1, as lambda approaches stoichiometric and EGR is decreased (less dilution by combustion products) knocking is observed.  For large lambda values (very lean) or high EGR rates (very dilute), partial combustion or misfire is observed. In general as the reactivity of the fuel/air mixture increases, the character of the combustion changes from misfire or partial combustion to stable combustion to knocking.

These engine experiments are extremely valuable and doubtless more reliable than any computer model, but of course the experiments are expensive and time-consuming. Hence, the goal of this work is to develop a computational method for rapidly predicting the viable operating range for any specified HCCI engine parameters and fuel chemistry.

**Figure 2.1.** Experimental operating range for a PRF-fueled HCCI engine measured by Oakley et al. [5] (contours are max. rate of pressure rise [bar/CAD]), adapted from SAE 2001-01-3606
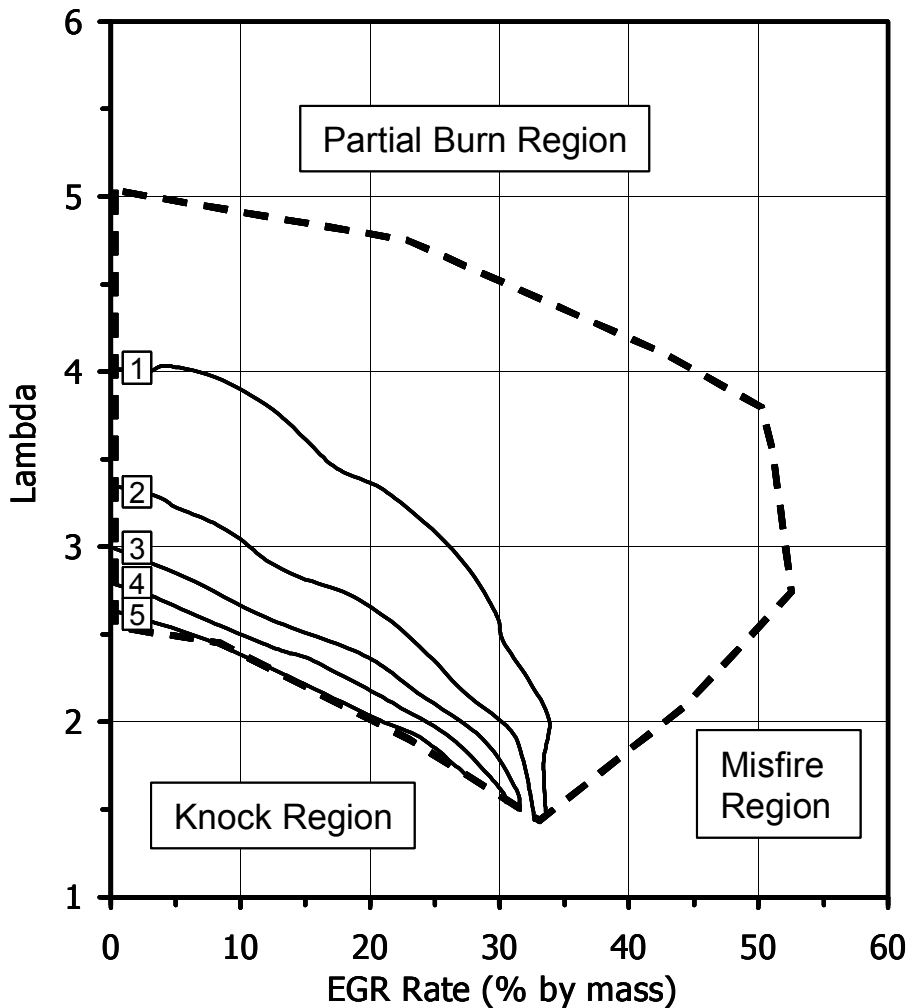


### 2.1.2 Relevant Prior Numerical Simulations of HCCI

Several researchers have presented methods which can be used to estimate the amount of unburned hydrocarbons from HCCI combustion [9-13]. Any of these methods, if applied over a range of conditions, could be used to determine the lean limit for HCCI operability. The key physics is that the cylinder contents are not truly homogeneous with respect to temperature and composition. Most importantly, the charge near the walls is much cooler than in the center of the cylinder. The cooler parcels of

fuel/air mixture never reach combustion temperatures, and their fuel leads to unburned hydrocarbons and CO in the exhaust. There are at least four ways to model this charge inhomogeneity: fully-coupled reacting flow simulations [10], stochastic models [11], quasi-dimensional models [12], and multi-zone models [9, 13]. Popular single-zone models [4, 14] do not capture this inhomogeneity.

Here we focus on the multi-zone approach of Aceves et al. [9], which we consider to be the simplest model that adequately captures the inhomogeneity in the engine cylinder. The multi-zone model uses a sequential approach to couple a computational fluid dynamics (CFD) code and a detailed chemical kinetics solver. A CFD program (KIVA-3V) is used to calculate the temperature field in the cylinder during the compression stroke neglecting chemical heat-release. Using this information, a number of homogeneous zones of different temperatures are defined based on a predetermined zone-partitioning scheme. These zone temperature profiles are used up to a time when chemical heat-release becomes important. At that point the temperature profiles are abandoned, and detailed chemical kinetics are used to determine the state of the zones. Due to the fast time-scale of HCCI combustion, mixing and heat transfer between zones can be ignored during this stage of the calculations. The only interaction between zones is through compression work. This model assumes the pressure is uniform across the engine cylinder. Of course this approximation causes the model to become invalid under knocking conditions.

To our knowledge, no one has previously applied any of the methods that model HCCI inhomogeneity to map out the lean limit for HCCI operation. Most HCCI modeling studies examine only a few sets of engine conditions. This has been done in part because

21

the published simulations are rather computationally intensive if detailed chemistry models are used for the combustion kinetics. Coupled fluid dynamic models with detailed chemistry can take months. Other methods are computationally expensive as well—Aceves et al. [15] report that a conventional ten-zone multi-zone simulation for iso-octane took almost one month on a 450 MHz machine. Even when the model equations were approximated using an approach analogous to operator-splitting, the calculations still required approximately two days [15]. In order to map out the limits of viable HCCI operation, it is necessary to run a large number of simulations (i.e. at many different lambda and EGR values). Consequently, a considerable improvement in computational efficiency is required for these simulations to be useful as a design tool.

Likewise, to our knowledge no one has tried to predict the knock limit (maximum torque and minimum A/F ratio) for HCCI operation. Martinez-Frias et al. [14] used a single-zone model to predict an HCCI speed-load map but did not consider the possibility of knock at high loads. Indeed there has been little speculation on the nature of HCCI knock. In this work it is proposed that knock in HCCI engines is caused by development of local overpressures in the engine cylinder. Local overpressures can occur in HCCI if a given parcel of fuel/air mixture ignites and burns before it has a chance to expand. A scaling analysis is used to derive a simple criterion for judging if knock is likely to occur in an HCCI engine.

In the following sections a procedure for predicting the limits of viable HCCI operation is presented. First we describe the procedure for constructing the zone temperature profiles from KIVA-3V calculations. Next our method for rapidly solving the multi-zone model equations is described. Then criteria for predicting the onset of

knock or partial-burn/misfire are presented. Finally, our predicted operating range is compared to the experimental operating range of Oakley et al. [5].

## 2.2 Development of a Computationally-Efficient Multi-zone Engine Model

### 2.2.1 Overview

The multi-zone modeling procedure used is essentially the same as that proposed by Aceves et al. [9] and will only be briefly described here. The following sections focus on the extensions to the multi-zone model that were made in order to rapidly run a large number of cases. The calculations proceed in several sequential stages. First the non-reacting flow problem is solved using the KIVA-3V [16] CFD code during the compression stage (from intake-valve-closing to top-dead-center) in order to identify the temperature profiles for each zone. Ten zones are defined based on temperature; each is considered to be homogeneous and mixing between the zones is neglected. The same zone mass distribution was used as in Aceves et al. [9] to define the zones. The species conservation equations (including chemical reactions) are solved from 50º BTDC to 30º BTDC using the zone temperature profiles and cylinder pressure computed by KIVA-3V (neglecting any chemical heat release during this pre-ignition phase). The starting and ending points for this stage were based on considerations of both accuracy and computational efficiency. Starting the calculation earlier (i.e. before 50º BTDC) was observed to have very little effect on the simulation results. Finally, the multi-zone model equations are solved from 30º BTDC until 30º ATDC including the effects of chemical heat-release and work interactions between zones. Mass and heat transfer are not considered in this stage (except for a simple model of heat losses to the walls from the

23

boundary layer). The cylinder volume is determined from the slider-crank equation, and pressure is assumed to be uniform across the cylinder.

The numerical method used here for solving the multi-zone equations is significantly different from that used by Aceves et al [9, 15, 17]. Our numerical method takes advantage of sparsity and sparse linear algebra as described in Schwer et al. [18]. Exploiting the sparsity in the multi-zone model equations leads to considerable improvements in computational time. This efficient multi-zone procedure was performed over a range of lambda values (1, 1.5, 2, 2.5, 3, 4, 5, 6, 7) and EGR rates (0, 10%, 20%, 30%, 40%, 50%, 60%). The multi-zone calculation results for each of the 63 cases are post-processed to determine if unacceptably incomplete combustion occurred or a knocking event could be expected.

## 2.2.2  KIVA Computational Fluid Dynamics Calculations

The parameters used in the KIVA simulation are for the single-cylinder, port-fuel-injected Ricardo E6 test engine used at Brunel University. KIVA-3V was used to compute the temperature field in the cylinder from IVC to TDC. The engine parameters used in the simulation are those used by Oakley et al. [5] in their experiments and are summarized in Table 2.1.

**Table 2.1.**  Engine parameters of single-cylinder Ricardo E6 engine used by Oakley et al. and simulated in this paper

| Compression ratio | 11.5 |
|---|---|
| Bore | 76 mm |
| Stroke | 111 mm |
| IVC | 144º BTDC |
| Injection Timing (PFI) | 79º BTDC (compression stroke) |
| Speed | 1500 rpm |
| Inlet Charge Temperature | 320ºC |
| Inlet Pressure (WOT) | taken as 1 bar |

The engine uses port-fuel injection with an injection timing of 79º BTDC during the compression stroke. It was assumed that this injection scheme allows sufficient time for fuel vaporization and mixing to occur in the intake port. Also mixing of the inducted charge with the residual gases was assumed to be fast. Therefore the initial temperature and composition were taken to be uniform in the cylinder at intake-valve closing. The engine cylinder geometry is pancake-shaped, and the walls, piston, and cylinder head were assumed to have a constant temperature of 383 K. A very simple 2-d mesh was used to model the engine. This mesh makes the assumption of axis-symmetry, but allows good resolution of the boundary layer. Information on the crevice geometry was not available so crevices were ignored in the calculation. A large number of mesh points (30,400) were used to adequately resolve the boundary layer. Mesh points were tightly spaced near the wall and more coarsely spaced in the core region. A grid spacing of 60 $\mu$m was employed in the boundary layer (in the direction perpendicular to the walls). Figure 2.2 shows the computational mesh grid and predicted temperature field at the end of compression (top-center). The KIVA calculations were performed in essentially an identical way to those reported previously by Aceves et al. [9], and an identical case was run to confirm agreement.

**Figure 2.2.** Computational grid and KIVA3v2-calculated temperature field for the Ricardo E6 single-cylinder engine at the end of compression (TC)
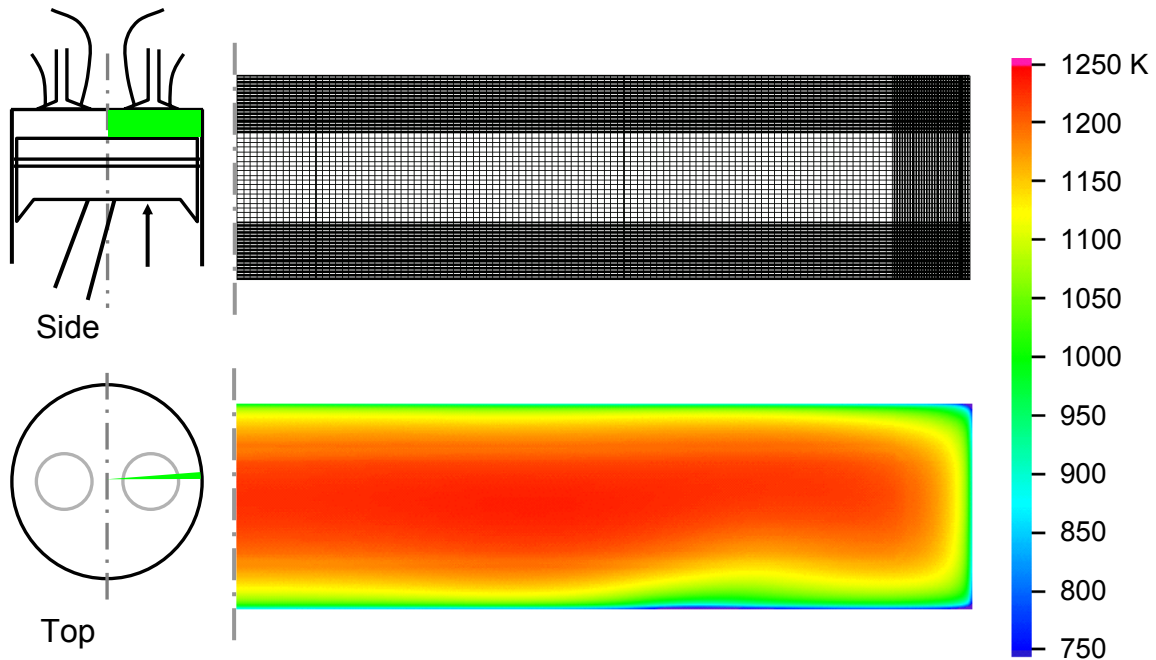


Only one KIVA calculation was performed, assuming the gas in the cylinder was pure air. In reality, some of the residual exhaust gases are always retained in the cylinder (a residual fraction of 5% was used), and considerably more are added using EGR. Of course there is also fuel present in the gas mixture during compression. Hence the heat capacity and mass density of the gas are actually slightly higher than the values assumed in the KIVA simulation. This means that the actual in-cylinder temperatures are somewhat lower than those predicted by KIVA. A simple correction formula was used to correct for differences in heat capacity and density of different fuel/air/EGR mixtures. This procedure avoids repeating the KIVA calculation for each pair of lambda and EGR rates. The correction was computed as,

$$\Delta T_{correction}(\Theta) = T_{FUEL/AIR/EGR}(\Theta) - T_{AIR}(\Theta) \tag{1}$$

$$T_{N}(\Theta) = T_{KIVA,N}(\Theta) + \Delta T_{correction}(\Theta), \tag{2}$$

where $T_{AIR}(\Theta)$ is the temperature of pure air compressed adiabatically from IVC to TDC, and $T_{FUEL/AIR/EGR}(\Theta)$ is the temperature of a fuel/air/EGR mixture compressed adiabatically from IVC to TDC. $T_{AIR}(\Theta)$ and $T_{FUEL/AIR/EGR}(\Theta)$ are computed by doing a simple numerical integration using thermodynamic properties from the NIST Webbook database. At 30º BTDC the resulting corrections, $\Delta T_{correction}$, ranged from -15 to -125 K. The zone temperature profiles ($T_{N}(\Theta)$) used in these calculations were computed by adding the correction to the average zone temperatures computed by KIVA for pure air, as shown in Eq.(2).

The validity of the simple temperature correction was checked by comparing predictions made using the correction formula to results of a KIVA run using a fuel/air/EGR mixture. At a lambda of 3.0 and an EGR rate of 30%, the simple correction was good to within 10 K for the core zones and 50 K for the boundary layer zones. This procedure is of course a very rough approximation to 3-d simulation of a realistic cylinder geometry using the true compositions with detailed models of the intake, exhaust, and fuel/air mixing. However, we believe that the important physics are described by this simple model.

### 2.2.3 Numerical Method for Solving the Multi-zone Model Equations

The majority of the computational time in our prediction of the HCCI operating range comes from solving the multi-zone model equations. As mentioned, the multi-zone model equations are based on the model assumptions described by Aceves et al. [9]. The Woschni correlation [19] was used to predict the heat losses from the cylinder. The core

zones were assumed to be adiabatic, while heat was subtracted from the outer zones and boundary layer (taken together as the coldest 30% of the mass). We acknowledge that this procedure is approximate; however, calculations by Aceves et al. [17] suggest that the simulation is actually quite insensitive to the treatment of heat losses in the second (multi-zone) stage of the calculation.

The chemistry model used for primary reference fuel combustion was taken from Curran et al. [20]. It contains 1,034 species and 4,238 elementary-step reactions.

The multi-zone model equations solved at each set of lambda and EGR rate conditions were written as follows.

$$\frac{dY_{kn}}{dt} = v_n \dot{\omega}_{kn} W_k$$

$$k = 1...Nspecies, n = 1...Nzones$$

$$(3)$$

$$C_{v,n} \frac{dT_n}{dt} + p \frac{dv_n}{dt} = -v_n \sum_{k=1}^{Nspecies} u_{kn} \dot{\omega}_{kn} W_k - \dot{q}_{loss,n}$$

$$n = 1...Nzones$$

$$(4)$$

$$pv_n = \frac{RT_n}{\overline{W}_n}, \quad n = 1...Nzones$$

$$(5)$$

$$p = \frac{R}{V_{cyl}} \sum_{n=1}^{Nzones} \frac{m_n}{\overline{W}_n} T_n$$

$$(6)$$

The species conservation equations, energy equation, and ideal gas law were solved in each zone. Eq.(6) for the cylinder pressure comes from the assumption that the pressure is equal across all zones and that the zone volumes must sum to the cylinder volume. Kinetic and thermodynamic properties were calculated using the CHEMKIN [21] library of subroutines.

The system of multi-zone model equations is very large—using 10 zones and 1034 chemical species leads to over 10,000 differential algebraic equations (DAEs).

These equations were solved efficiently by taking advantage of sparsity in this system of equations. First, the state variables were changed from the conventional $(Y_{kn},T_n,P)$ set used in many CHEMKIN applications to the expanded $(Y_{kn},T_n,P,v_n)$ set. With this reformulation, in which the ideal gas law is added as an algebraic constraint, the Jacobian becomes extremely sparse: only about 0.2% of the over 100 million entries in the Jacobian are non-zero. Special solvers for sparse systems of DAEs require much less memory because only non-zero Jacobian entries are stored. CPU time is also decreased because no CPU cycles are wasted doing operations with Jacobian entries that are identically zero. The number of non-zero Jacobian entries that need to be computed is approximately 260,000. To speed this process these entries are evaluated using analytical derivatives as opposed to finite differences. The solution of detailed kinetic problems with sparse techniques is described in detail by Schwer et al. [18].

The procedure was implemented using the sparse differential-algebraic equation solvers and automatic-differentiation technology included in the DAEPACK software library [22, 23]. DAEPACK was used to identify the sparsity pattern of the equations and construct the analytical derivative expressions. Figure 2.3 shows the sparsity pattern for the Jacobian matrix used in these simulations. The 10 blocks correspond to the 10 zones in the simulations. The solid line at the bottom of the first block comes from the pressure equation, Eq. (6). The other non-zero entries outside of the blocks, which appear as equally-spaced dots at the top of each block, come from the heat-loss term in the energy balance, Eq.(4). The Woschni correlation depends on the cylinder-averaged temperature so the energy balance for each zone depends on the temperature of the other zones.

**Figure 2.3.** Sparsity pattern of the Jacobian matrix for the sparse formulation of the multi-zone governing equations, Eqs.(3)-(6). Model uses 10 zones and the PRF chemistry model of Curran et al. Black areas are non-zero entries; white areas are zeros.
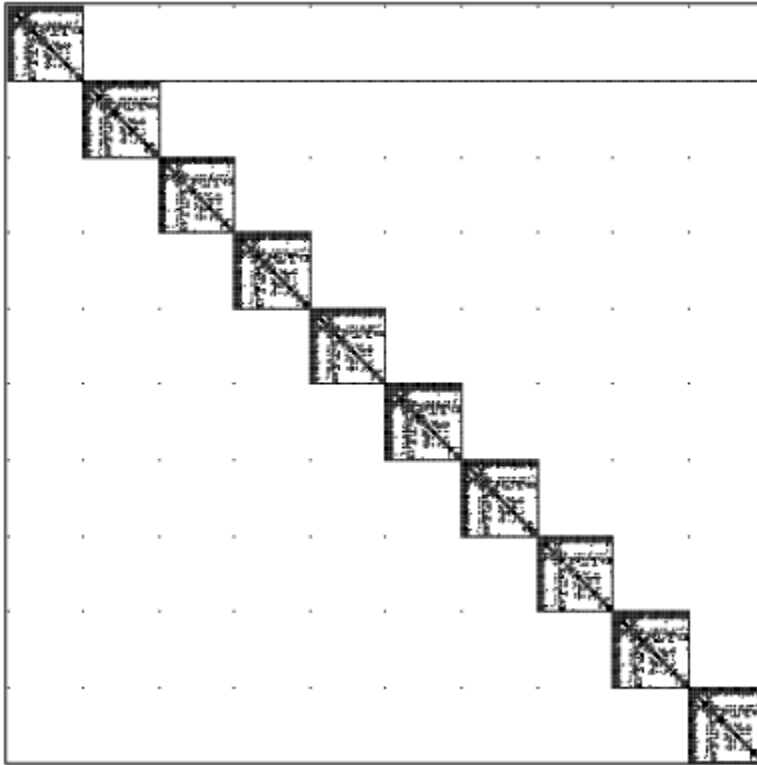


The associated solver, DSL48S, was used to solve the sparse system of DAEs. This problem demonstrates the power of modern DAE software: each multi-zone simulation took only 1 to 4 hours of CPU time on a 733 MHz Pentium 3 running Linux. As a comparison, Aceves et al. [15] report that calculations for a simpler fuel chemistry (iso-octane) can take almost one month using conventional methods. Even when additional approximations were made (which were not made in this work) they report that simulation times were on the order of 2 days for iso-octane on a 450 MHz machine.

Sparsity information and CPU timing for various sized chemistry models from literature is shown in Figure 2.4. Notice that the number of non-zero entries is approximately linear with the number of chemical species in the model, and the percent

sparsity quickly approaches 100%. The increase of CPU time with number of chemical species in more than linear, but better than the $O(N^2)$ dependence expected for dense solution techniques. These plots suggest that even larger chemistry models will still yield reasonable computational times with the sparse-solver strategy.

**Figure 2.4.** Sparsity of the Jacobian matrices (a) and CPU times on a 733 MHz machine for multi-zone model calculations (b) for chemistry models from literature of various sizes. All multi-zone calculations used 10 zones. The chemistry models are, in order of increasing size, for hydrogen, methane, propane, *n*-butane, *n*-heptane, iso-octane, and a primary reference fuel mixture. The PRF model is one used in these simulations.



a) Jacobian Characteristics

b) CPU Time for Multizone Calculation
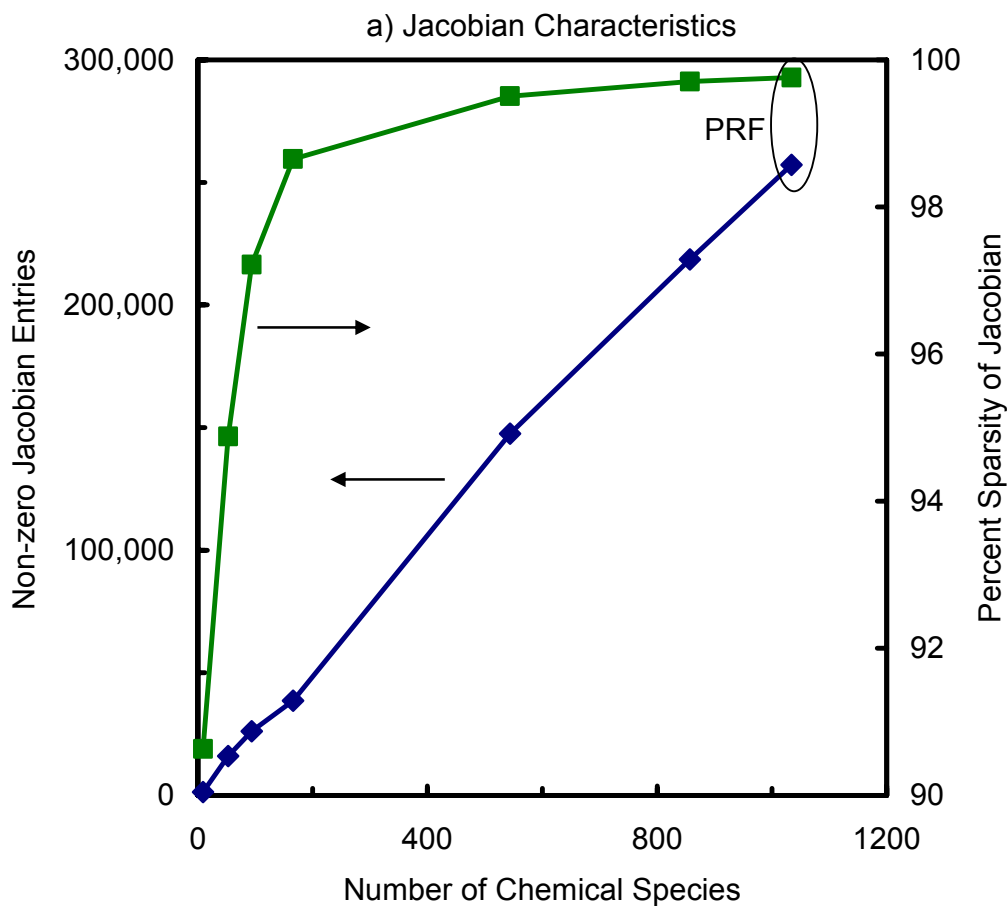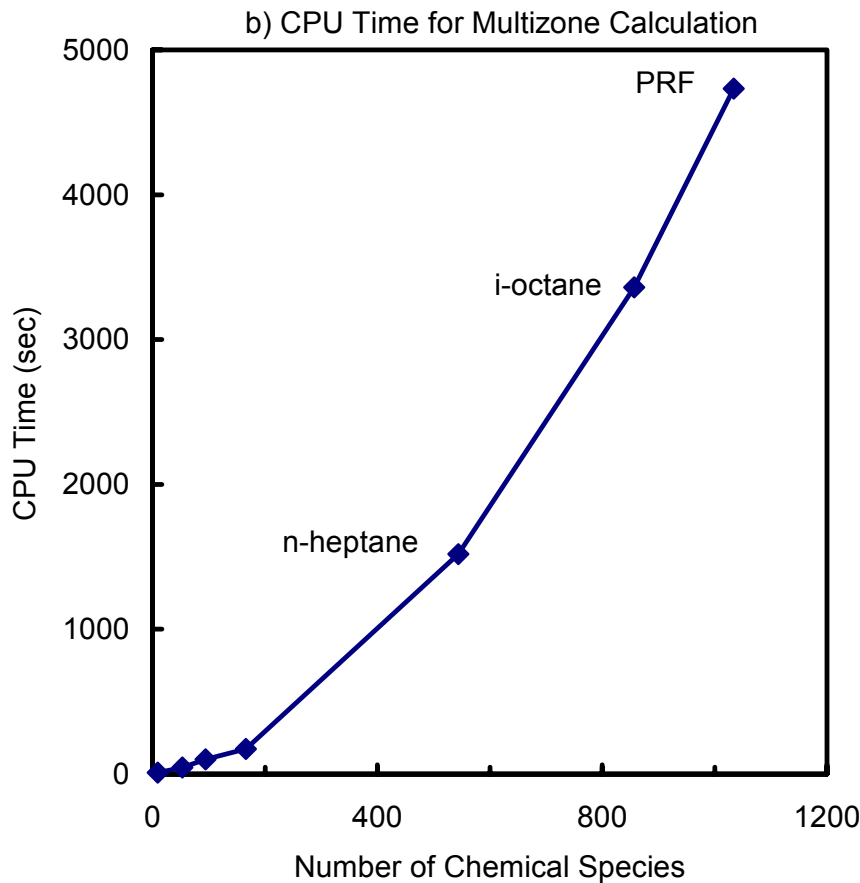
## 2.3  Procedure for Prediction of the Viable Operating Range

After the multi-zone model is solved at each set of conditions (lambda and EGR rate), two tests are applied. A knock criterion is applied to determine if the engine was likely to knock under those conditions. Another criterion is applied to determine if the combustion was unacceptably incomplete. In this way the limits for the viable operating range are constructed.

## 2.3.1  Prediction of the Knock Limit

Although many workers have observed pressure traces from HCCI combustion that exhibit pressure oscillations [2, 24], there is no consensus for the origin or nature of knock in HCCI engines.

At high loads, HCCI engine pressure traces often exhibit large acoustic oscillations with amplitudes as large as several bar. In Figure 2.1, Oakley at al. considered the HCCI engine to be knocking when the amplitude of the acoustic oscillations exceeded 0.5 bar in 10% or more of engine cycles.

It has been shown that the frequency of these acoustic oscillations agrees well with the calculated frequencies for the major acoustic resonant modes for the engine cylinder [24]. It seems clear that these oscillations arise from pressure waves resonating in the cylinder charge. The multi-zone model assumes that the pressure is uniform throughout the cylinder, so this model breaks down under conditions where large amplitude pressure waves are present.

It is proposed here that a locally high pressure can arise in HCCI engine cylinders from very fast combustion in a given parcel of fuel/air mixture, and that these local overpressures then lead to resonant pressure waves. If the combustion rate in a fuel/air parcel is slow enough, the parcel will expand and maintain its pressure nearly equal to that of the rest of the gas in the cylinder. As the combustion rate increases, the rate at which the parcel must expand in order to remain in pressure equilibrium becomes very fast. When the required expansion rate exceeds the speed of sound, a local overpressure will develop.

A study of the competing physical and chemical processes leads to a simple criterion for determining if HCCI knock should be expected. Knock would not be expected and the multi-zone model assumptions are valid if:

$$\beta = \frac{L_c(\gamma - 1)}{\gamma p} \frac{\dot{q}}{u_{sound}} \leq 1 \tag{7}$$

in all of the zones, at all times. $L_c$ is a characteristic length scale (volume/area) of the inhomogeneities in the HCCI cylinder. Also $\dot{q}$ is the chemical heat-release rate (volumetric) defined as the magnitude of the summation term on the right-hand side of Eq.(4). The variable $u_{sound}$ is the speed of sound which is simple to calculate for an ideal gas, and $\gamma$ is the ratio of specific heats. In this work $L_c$ was taken as $1/10^{th}$ the engine bore and $\gamma$ was taken as a constant 1.2. The criterion in Eq.(7) is derived from a scaling analysis of the first law of thermodynamics applied to the given fuel/air parcel. The first law can be written as follows assuming a movable, impermeable, adiabatic control volume around a given fuel/air parcel.

$$\frac{dp}{dt} = -\frac{\gamma p}{V} \frac{dV}{dt} + (\gamma - 1)\dot{q} \tag{8}$$

$$\begin{Bmatrix} \text{rate of} \\ \text{pressure rise} \end{Bmatrix} = \begin{Bmatrix} \text{rate work done by} \\ \text{volume expansion} \end{Bmatrix} + \begin{Bmatrix} \text{rate of chemical} \\ \text{heat release} \end{Bmatrix}$$

The volume expansion term $dV/dt$ has been scaled with $Au_{sound}$, where $A$ is the surface area of the parcel. $Au_{sound}$ is the maximum rate that the fuel/air parcel can expand (note that the sound speed and shock speed are similar under engine conditions). If the chemical heat-release rate is any faster than the maximum rate of expansion, then a local overpressure will occur. In the limit of an infinitely fast chemical heat release, the combustion of the parcel will occur at essentially constant volume and the maximum possible local overpressure will occur. The $\beta$ parameter is dimensionless and characterizes the competition between the rate of chemical heat-release and volume expansion at the speed of sound.

34

Our knock criterion in Eq.(7) is local. However, experimentally knock is highly correlated with the global rate of pressure rise, dP/dΘ, as seen in Figure 2.1. Notice that the contour for 5 bar/CAD nearly overlays the experimental knock limit. The global rate of pressure rise is related to the sum of the local rates of heat release, $\dot{q}$, in all parcels of the fuel/air mixture. Hence in addition to being fundamentally based, our β parameter makes sense in the context of experimental data. Note that basing a knock criterion on the global dP/dΘ is less desirable because this depends strongly on engine specifics such as the degree of charge homogeneity and the fidelity of the model in capturing these slight inhomogeneities.

Some comments about the differences between HCCI knock and SI knock are appropriate. In both cases, it appears (consistent with kinetic calculations) that the heat-release rate from autoignition in a local region can be fast enough to develop a local overpressure. However, there are several important differences between SI knock and HCCI knock. In the familiar SI situation, the mixture is near stoichiometric, so if the end gas autoignites the β parameter in Eq.(7) will almost certainly rise to be greater than one. Hence, if any fuel/air parcel (in the end gas) autoignites, it will almost certainly cause an overpressure (knock). The issue in an SI engine is whether the end gas will autoignite before it is burned by the advancing turbulent flame from the spark plug. Hence in SI engines the competition is between turbulent flame speed and ignition delay.

By contrast, in HCCI engines the bulk of the fuel/air mixture must compression-ignite in order to operate normally. There is little chance that a flame front will come along and burn a parcel before it spontaneously ignites. Thus, flame speed and ignition delay are not the key variables. Instead, the main issue is whether the heat-release rate in

the lean mixture is large enough to cause an overpressure at all. In HCCI engines the competition is between the rate of heat-release and rate at which a fuel/air parcel can expand (and hence equilibrate pressure in the cylinder).

### 2.3.2 Prediction of the Partial-Burn/Misfire Limit

Oakley et al. [6] define the misfire limit as the point at which ignition starts to fail on a small proportion of engine cycles. The partial-burn limit is defined as a point at which a significant proportion of the fuel fails to oxidize leading to high CO and unburned HC emissions.

Since cycle-to-cycle variations are not captured in our model, it is impossible to base our criterion for misfire on something that only occurs in a certain proportion of cycles. It is possible, however, to devise a criterion based on the fraction of the fuel that has been consumed as was done for the experimental partial-burn limit. An earlier study on a gasoline-fueled HCCI engine by Oakley et al. [6] suggest that about 85-90% of the fuel is consumed at the misfire/partial-burn boundary. Since crevices were not included in the model, our predictions for burned fraction are over-estimates. Therefore the criterion of 93% fuel consumption was chosen for our definition of the misfire and partial-burn limit. Obviously, this limit is somewhat hard to capture because the experimental misfire and partial-burn limits lack objective criteria like that used for defining the experimental knock limit.

## 2.4 Knock Limit Predictions for the PRF-fueled Brunel University Test Engine

The computed operating range for an HCCI engine running under Oakley's conditions (Table 2.1) is shown in Figure 2.5. Our predictions can be directly compared with the experimental data from Figure 2.1 (reproduced as a dashed line). Like Oakley et

al., our definition of lambda includes contributions to the in-cylinder oxygen concentration from the fresh charge, recycled exhaust gas, and internal residual gas. The initial charge composition was calculated using the formulas of Heywood [25].

The knock limit on Figure 2.5 (solid line) is drawn where $\beta$ equals unity as calculated by Eq.(7). Below this line, heat-release rates are faster than volume expansion by a pressure wave, and local overpressures can be expected. Above the knock limit, the multi-zone model is expected to give reasonably accurate pressure traces and even emissions speciation, as demonstrated by Aceves et al. [17]. The simple $\beta$ criterion is shown to give good quantitative prediction of the knock limit. The position of the predicted knock limit was determined to be quite insensitive to variations in charge temperature and pressure. It appears the only factors that significantly affect $\beta$ are the mixture composition and fuel type (both of which affect the heat-release rate). Therefore, the most likely source for error in the prediction of the knock limit is an under-prediction of the heat-release rate by the chemistry model. Also note the experimental knock limit is quite conservative—only 10% of cycles showed knock with amplitudes greater than 0.5 bar at this limit.

**Figure 2.5:** Comparison of the predicted and experimental HCCI viable operating range for a PRF-fueled Ricardo E6 test engine
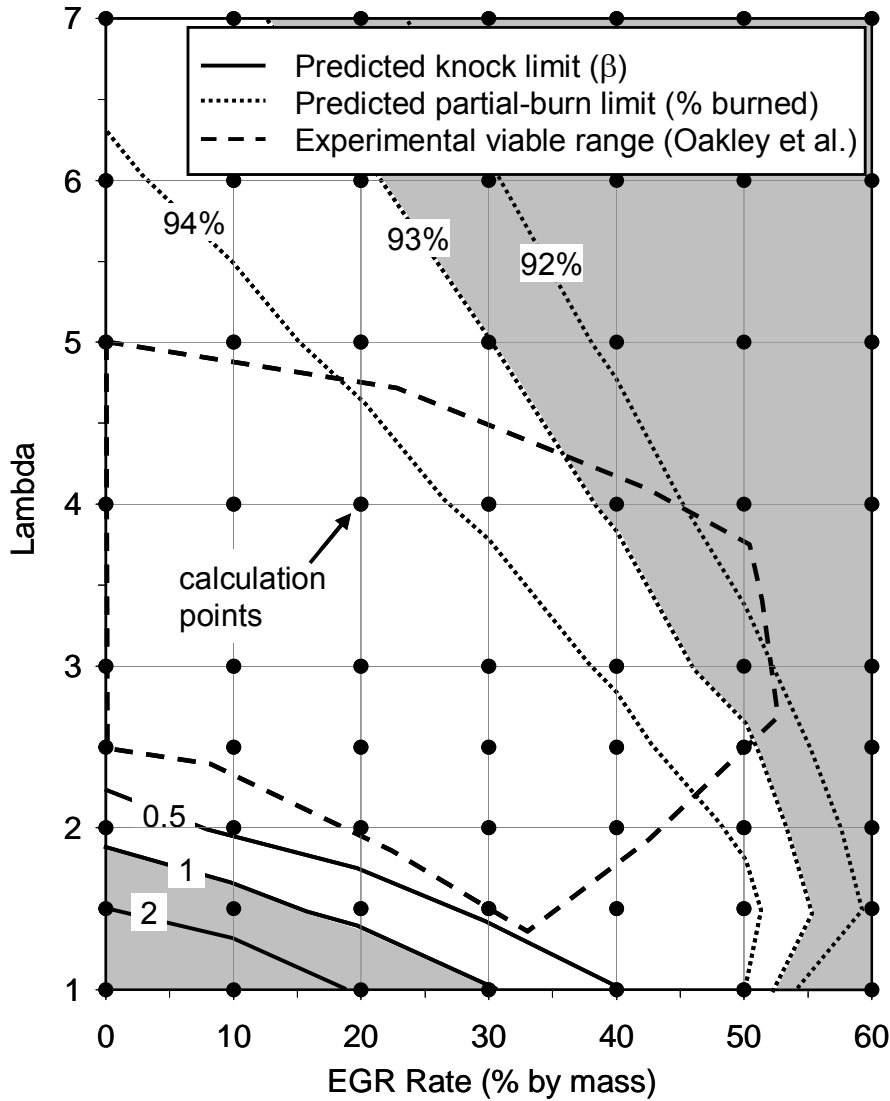


The misfire limit (dotted line) is drawn at a position corresponding to 93% of the fuel being consumed. Above this limit, by our definition the combustion is unacceptably incomplete. As shown, even very lean mixtures burned partially and no true misfire was observed. This was not the case in our previous studies with higher octane number fuels (natural gas and propane). The qualitative shape of the misfire boundary is the same as was observed experimentally. This similarity includes the interesting phenomenon that at high EGR rates (e.g. 50%) as the mixture goes from stoichiometric to lean, the

combustion initially becomes more complete. Oakley et al. [6] suggest that higher oxygen concentrations at higher lambdas cause this phenomenon. Our modeling suggests that a thermal effect (higher charge temperatures at leaner conditions due to a lower mixture heat capacity) is also partially responsible.

Prediction of the misfire/partial-burn boundary is challenging because it is very sensitive to the model assumptions and parameters. Indeed, the true system is also very sensitive if small changes in conditions can lead alternately to stable combustion or complete misfire. The misfire boundary is essentially determined by the ignition delay of the core gas mixture. It is difficult for a chemistry model to accurately predict the ignition delay of a fuel/air mixture over a broad range of temperature, pressure, and composition. It is likely that as kinetic models improve, predictions of this lean limit will also improve.

It is important to remember that the simulated boundaries are purely predictive. No parameters have been tuned to give good agreement with experiment. Indeed the agreement with experiment is acceptable despite the fact that the engine geometry is grossly oversimplified and many other details of this simulation merit re-examination. This agreement suggests that the essential physics have been captured, and that one can use the new simulation technology to fairly accurately predict the bounds on the operating range. Hence this approach could be a powerful tool for testing proposals for expanding the operating range and guiding related experimental investigations.

## 2.5 Conclusions

It has been shown that numerical simulations can be used to predict the viable operating range of HCCI combustion. The predicted operating range is shown to be in good agreement with experimental data of Oakley et al [5]. The multi-zone model of

Aceves et al. [9] has been extended to allow even extremely detailed fuel chemistry (more that 1000 species and 4000 reactions) to be quickly simulated on a standard PC by exploiting sparsity in the model equations. A fundamental criterion for determining the onset of knock was developed based on the idea that HCCI knock originates because of local overpressures due to very fast chemical heat-release. This knock criterion is shown to give accurate predictions of the knock limit and hence maximum torque available from an HCCI engine. This ability to predict the limits of viable HCCI operation should allow engine designs and control strategies to be rapidly screened before experiments are performed.

## 2.6 References

1.  Aoyama, T., et al., *An Experimental Study on Premixed-Charge Compression Ignition Gasoline Engines.* SAE Technical Paper, 1996(960081).
2.  Flowers, D., et al., *HCCI in a CFR Engine: Experiments and Detailed Kinetic Modeling.* SAE Technical Paper, 2000(2000-01-0328).
3.  Kaiser, E.W., et al., *Homogeneous charge compression ignition engine-out emissions--does flame propagation occur in homogeneous charge compression ignition?* International Journal of Engine Research, 2002. **3**(4): p. 185-195.
4.  Dec, J.E., *A Computational Study of the Effects of Low Fuel Loading and EGR on Heat Release Rates and Combustion Limits in HCCI Engines.* SAE Technical Paper, 2002(2002-01-1309).
5.  Oakley, A., H. Zhao, and N. Ladommatos, *Dilution Effects on the Controlled Auto-Ignition (CAI) Combustion of Hydrocarbon and Alcohol Fuels.* SAE Technical Paper, 2001(2001-01-3606).
6.  Oakley, A., H. Zhao, and N. Ladommatos, *Experimental Studies on Controlled Auto-ignition (CAI) Combustion of Gasoline in a 4-Stroke Engine.* SAE Technical Paper, 2001(2001-01-1030).
7.  Yang, J., T. Culp, and T. Kenney, *Development of a Gasoline Engine System Using HCCI Technology--The Concept and the Test Results.* SAE Technical Paper, 2002(2002-01-2832).
8.  Thring, R.H., *Homogeneous-Charge Compression-Ignition (HCCI) Engines.* SAE Technical Paper, 1989(892068).
9.  Aceves, S.M., et al., *A Multi-Zone Model for the Prediction of HCCI Combustion and Emissions.* SAE Technical Paper, 2000(2000-01-0327).
10. Kong, S.-C., et al., *Modeling and Experiments of HCCI Engine Combustion Using Detailed Chemical Kinetics with Multidimensional CFD.* SAE Technical Paper, 2001(2001-01-1026).
11. Kraft, M., et al., *Investigation of Combustion Emissions in a Homogeneous Charge Compression Injection Engine: Measurements and a New Computational Model.* Proceedings of the Combustion Institute, 2000. **28**: p. 1195-1201.
12. Fiveland, S.B. and D.N. Assanis, *Development and Validation of a Quasi-Dimensional Model for HCCI Engine Performance and Emissions Studies Under Turbocharged Conditions.* SAE Technical Paper, 2002(2002-01-1757).
13. Babajimopoulos, A., D.N. Assanis, and S.B. Fiveland, *An Approach for Modeling the Effects of Gas Exchange Processes on HCCI Combustion and its Application in Evaluating Variable Valve Timing Control Strategies.* SAE Technical Paper, 2002(2002-01-2829).
14. Martinez-Frias, J., et al., *Equivalence Ratio-EGR Control of HCCI Engine Operation and the Potential for Transition to Spark-Ignited Operation.* SAE Technical Paper, 2001(2001-01-3613).
15. Aceves, S.M., et al., *A Decoupled Model of Detailed Fluid Mechanics Followed by Detailed Chemical Kinetics for Prediction of Iso-Octane HCCI Combustion.* SAE Technical Paper, 2001(2001-01-3612).

16. Amsden, A., *KIVA-3V: A Block-Structured KIVA Program for Engines with Vertical or Canted Valves*. 1997, Los Alamos National Laboratory: Los Alamos, NM.

17. Aceves, S.M., et al., *A Sequential Fluid-Mechanic Chemical-Kinetic Model of Propane HCCI Combustion.* SAE Technical Paper, 2001(2001-01-1027).

18. Schwer, D.A., et al., *On Upgrading the Numerics in Combustion Chemistry Codes*. Combustion and Flame, 2002. **128**(3): p. 270-291.

19. Woschni, G., *Universally Applicable Equation for the Instantaneous Heat Transfer Coefficient in the Internal Combustion Engine.* SAE Technical Paper, 1967(670931).

20. Pitz, W.J. and H.J. Curran, *personal communication.* May 2002.

21. Kee, R.J., et al., *CHEMKIN III: A FORTRAN Chemical Kinetics Package for the analysis of gas-phase chemical and plasma kinetics*. 1996, Sandia National Laboratories: Livermore, CA.

22. Tolsma, J.E. and P.I. Barton, *DAEPACK: An open modeling environment for legacy codes.* Ind. Eng. Chem. Res., 2000. **39**(6): p. 1826-1839.

23. Barton, P.I., *DAEPACK webpage, http://yoric.mit.edu/daepack/daepack.html*.

24. Tsurushima, T., et al., *The Effect of Knock on Heat Loss in Homogeneous Charge Compression Ignition Engines.* SAE Technical Paper, 2002(2002-01-0108).

25. Heywood, J.B., *Internal Combustion Engine Fundamentals*. 1988, New York: McGraw-Hill, Inc. pp. 100-107.

## 2.7 Supplementary Material

### 2.7.1 KIVA3v2 Mesh Generation File (iprep)

```
K3PREP/100198 6-block / Brunel Ricardo E6 Engine / no crevice
  bore       7.6
  stroke    11.1
  squish     0.46
  thsect     0.5
 nblocks     6
   1 100   1  90   0   2   1   0
   3.4      3.4      0.0      0.0      3.4      3.4      0.0      0.0
   0.0      0.0      0.0      0.0      0.0      0.0      0.0      0.0
   0.3      0.3      0.3      0.3      0.3      0.3      0.3      0.3
   3.0      4.0      5.0      6.0      4.0      4.0
  -1.0     -1.0     -1.0     -1.0     -1.0     -1.0
   2  60   1  90   0   2   1   0
   3.8      3.8      3.4      3.4      3.8      3.8      3.4      3.4
   0.0      0.0      0.0      0.0      0.0      0.0      0.0      0.0
   0.3      0.3      0.3      0.3      0.3      0.3      0.3      0.3
   4.0      2.0      5.0      6.0      4.0      4.0
  -1.0     -1.0     -1.0     -1.0     -1.0     -1.0
   3 100   1  50   0   1   1   0
   3.4      3.4      0.0      0.0      3.4      3.4      0.0      0.0
   0.0      0.0      0.0      0.0      0.0      0.0      0.0      0.0
   0.0      0.0      0.0      0.0      0.3      0.3      0.3      0.3
   3.0      4.0      5.0      6.0      1.0      4.0
  -1.0     -1.0     -1.0     -1.0      0.0     -1.0
   4  60   1  50   0   1   1   0
   3.8      3.8      3.4      3.4      3.8      3.8      3.4      3.4
   0.0      0.0      0.0      0.0      0.0      0.0      0.0      0.0
   0.0      0.0      0.0      0.0      0.3      0.3      0.3      0.3
   4.0      2.0      5.0      6.0      1.0      4.0
  -1.0     -1.0     -1.0     -1.0      0.0     -1.0
   5 100   1  50   0   3   1   0
   3.4      3.4      0.0      0.0      3.4      3.4      0.0      0.0
   0.0      0.0      0.0      0.0      0.0      0.0      0.0      0.0
   0.0      0.0      0.0      0.0      0.3      0.3      0.3      0.3
   3.0      4.0      5.0      6.0      4.0      2.0
  -1.0     -1.0     -1.0     -1.0     -1.0     -1.0
   6  60   1  50   0   3   1   0
   3.8      3.8      3.4      3.4      3.8      3.8      3.4      3.4
   0.0      0.0      0.0      0.0      0.0      0.0      0.0      0.0
   0.0      0.0      0.0      0.0      0.3      0.3      0.3      0.3
   4.0      2.0      5.0      6.0      4.0      2.0
  -1.0     -1.0     -1.0     -1.0     -1.0     -1.0
  ncopy      0
  tiltflag    0
  pentflag    0
 wedgeflag    0
 translate    0
   nlocxy     0
   reshape    0
 npentxy     0
 nvguide     0
 nvalvport   0
 nrunner     0
 nsiamese    0
  nround     0
   npatch    7
   2   1   1   1   1   2
   1   5   3   1   1   1
   2   5   4   1   1   2
   4   1   3   1   1   4
   5   5   1   1   1   5
   6   5   2   1   1   6
   6   1   5   1   1   6
   nrelaxb    0
 nprovtop    0
```

```
   nprovfce      0
 nzcylwall      0
      tilt      0
 ndish          0
 nscallop       0
 xoffset    0.0
 yoffset    0.0
 write17    1.0
plotmesh    1.0
 xband      0.0
 yband      0.0
 zband      0.0
 nxplots       0
 nyplots       1
  0.0
 nzplots       0
  nvhide       0
```

## 2.7.2  KIVA3v2 Input File (itape5)

```
- K122298 6 block / Brunel Ricardo E6 Engine / no crevice
  irest      0
nohydro      0
 lwall       1
 lpr         0
 irez        2
 ncfilm 9999
 nctap8 9999
 nclast 9999
 ncmon      10
ncaspec     7
 -140.0, -120.0, -90.0, -60.0, -30.0, -5.0, 0.0
 gmv        1.0
 cafilm   9.99e+9
 cafin     3.0
 angmom    1.0
 pgssw     1.0
 dti    8.000e-6
 dtmxca    1.0
 dtmax    9.99e+9
 tlimd     1.0
 twfilm   9.99e+9
 twfin    9.99e+9
 fchsp     0.25
 bore      7.6
 stroke   11.1
 squish    0.46
 rpm      1.5e+3
 atdc    -144.0
 datdct    0.0
 revrep    2.0
 conrod   27.0
 swirl     3.0
 swipro    3.11
 thsect    0.5
 sector    1.0
 deact     0.0
 epsy      1.0e-3
 epsv      1.0e-3
 epsp      1.0e-4
 epst      1.0e-3
 epsk      1.0e-3
 epse      1.0e-3
 gx        0.0
 gy        0.0
 gz        0.0
 tcylwl   383.0
 thead    383.0
 tpistn   383.0
```

```
 pardon    0.0
 a0        0.0
 b0        1.0
 artvis    0.0
 ecnsrv    0.0
 adia      0.0
 anu0      0.0
 visrat-.66666667
 tcut     800.0
 tcute   1200.0
 epschm    0.02
 omgchm    1.0
 turbsw    1.0
 sgsl      0.0
trbchem    0.0
 capa     18.0
pmplict    0.0
lospeed    0.0
 airmu1  1.457e-5
 airmu2  110.0
 airla1  252.0
 airla2  200.0
 prl       0.74
 rpr       1.11
 rsc       1.11
 xignit    0.0
 t1ign    -1.0
 tdign    -1.0
 ca1ign  -27.0
 cadign    9.6
 xignl1    0.25
 xignr1    0.75
 yignf1    0.0
 yignd1    0.238
 zignb1   11.75
 zignt1   12.50
 xignl2    0.0
 xignr2    0.0
 yignf2    0.0
 yignd2    0.0
 zignb2    0.0
 zignt2    0.0
 kwikeq    0
 numnoz    0
 numinj    0
 numvel    0
injdist    1
 kolide    0
 tpi     350.0
 turb      1.0
breakup    0.0
 evapp     0.0
 nsp       3
gasoline
      o2    mw2     32.000   htf2     0.0
      n2    mw3     28.016   htf3     0.0
stoifuel   1.0
 stoio2    2.0
 nreg      1
'presi',   1.0000e+6
'tempi',   593.0
'tkei',      0.10
'scli',      0.0
'er',        0.00
'mfracfu',   0.0000
'mfraco2',   0.2300
'mfracn2',   0.7700
 nrk       0
 nre       0
nvalves    0
 isoot     0
```

# Chapter 3: Prediction of Performance Maps for HCCI Engines

## 3.1 Introduction

### 3.1.1 Motivation

The homogeneous-charge compression-ignition (HCCI) engine concept has received a great deal of attention recently due to its high thermal efficiency and low emissions of particulate matter and nitrogen oxides [1-3]. The HCCI engine is also attractive because it requires little untested technology compared with other alternative vehicle concepts such as fuel cells and hybrid-electric vehicles. The HCCI engine is similar to the conventional compression-ignition (i.e. diesel) engine, except that the fuel/air mixture is considerably more well-mixed in an HCCI engine. This minor change in fuel/air mixture preparation allows HCCI to take advantage of the efficiency and emissions benefits of lean, premixed combustion.

Two major technical challenges, however, face HCCI engine development. First, the combustion timing in an HCCI engine is purely controlled by chemical kinetics rather than some mechanical means such as spark timing or injection timing. As a result some control of the mixture properties (e.g. charge temperature) is needed to insure reliable combustion timing for all practical engine speeds and loads. Retention of varying amounts of burned gases from the previous cycle seems like a promising control strategy and is explored in this work. Second, in practice these engines have been limited to a fairly low torque per unit displaced volume. The maximum torque in these engines is limited by the onset of "knock" (non-uniform cylinder pressures) that can lead to engine noise and potential damage to pistons and cylinder liners. Because the power density of dedicated HCCI engines is lower than conventional gasoline engines, larger engines would be needed for many applications.

This work describes a modeling strategy for constructing performance maps for an HCCI engine. A numerical model was developed and used to test several engine designs for potential to overcome these two challenges. While less accurate than experimental tests, this approach can be used to quickly screen various engine designs and guide experimental studies, which are more expensive and time-consuming. Also the constructed performance maps can be used to estimate fuel economy over regulatory drive cycles without doing vehicle tests.

## 3.1.2 Relevant Prior Experimental and Modeling Studies

While many experimental studies of HCCI combustion have been performed, relatively few have done detailed investigations of operating ranges. Thring [4] used a Labeco CLR single-cylinder test engine with intake-air heating to determine the range of air/fuel ratio and exhaust-gas recycle (EGR) rate that would support HCCI combustion at a set engine speed. More recently Oakley et al. [5, 6] also systematically explored the single-speed operating range in a similar fashion for various fuels (e.g. gasoline, n-heptane, methanol) using a single-cylinder Ricardo E6 test engine with intake-air heating. A handful of researchers have experimentally studied a range of both torques and speeds and constructed performance maps for HCCI. Yang et al. [7] describe a high-compression-ratio, gasoline engine which can operate with both HCCI and spark-ignited (SI) combustion. Using intake-air heating, successful HCCI operation was demonstrated from idle up to a load of 5.5 bar net-indicated mean effective pressure and speeds ranging from 750 to 4750 rpm. Zhao et al. [8] constructed performance maps for a four-cylinder Ford Zetec engine run at dilute, stoichiometric conditions using EGR for control.

Recently Hyvönen et al. [9] constructed maps for a 5 cylinder engine with a unique variable-compression-ratio system and exhaust-heat recovery.

In terms of modeling, Martinez-Frias et al. [10] used a perfectly-stirred reactor model and basic thermodynamic model for gas exchange to predict performance maps for a natural-gas HCCI engine. They placed a restriction on maximum pressure to establish the maximum torque rather than some metric for the onset of engine knock. Yelvington and Green [11] presented a method for predicting the knock limit and associated maximum torque and were able to reproduce the single-speed data of Oakley et al. [5] with good accuracy. The current work extends that study to multiple speeds in order to construct performance maps and examine various engine designs.

### 3.1.3  Scope of the Simulation Study

A series of baseline cases was run with an engine configuration similar to the experimental engine described by Yang et al. [7] and hereafter referred to as the "Ford OKP HCCI" engine. This engine was chosen as the baseline because it demonstrated a fairly robust operating range in engine tests. The characteristics of the Ford OKP HCCI engine are summarized in Table 3.1.  The major difference between our simulations and the experimental engine is that variable valve timing was used in the simulations to control the start-of-combustion. In the experimental engine, fixed valve timing was used when the engine was run in HCCI mode.

**Table 3.1.** Baseline engine operating conditions

| Fuel | gasoline (91.4 RON) |
|---|---|
| Compression ratio | 15.51 |
| Bore | 89 mm |
| Stroke | 105.8 mm |
| EVO | 135 cad |
| EVC | 375 cad |
| IVO | 298 cad |
| IVC | 598 cad |
| Inlet air temperature | 121 °C |
| Cylinder liner temperature[†] | 110 °C |
| Piston face temperature[†] | 160 °C |
| Cylinder head temperature[†] | 160 °C |

RON = research octane number, cad = crank angle degrees, EVO = exhaust valve opening, EVC = exhaust valve closing, IVO = intake valve opening, IVC = intake valve closing, [†]estimate based on coolant temperature

A set of performance maps was constructed for four engine configurations using the methodology presented in detail in the next section. The conditions used in these cases are summarized in Table 3.2. The baseline was "Case A" and three other cases (B, C, and D) examined the influence of compression ratio, fuel, and supercharging. The fuel for the baseline case was a 92 RON primary reference fuel, which was used as a surrogate for gasoline. Case B was identical to the baseline case with the exception that the compression ratio was increased. This case investigated the effect of compression ratio on efficiency and maximum torque. Cases C and D vary considerably from the baseline and were an attempt to achieve higher torques from the engine. Cases C and D used normal-heptane (a surrogate for diesel due to its similar cetane number) and were supercharged to a boost pressure of 0.5 bar. Also unlike the baseline case (and the experiment) no external intake-air heating was used in Cases C and D. For these cases, the intake air temperature (73°C) was the temperature that results from compressing ambient air (25°C) to 0.5 bar boost pressure assuming a 75% compressor efficiency. Finally, the valve timing strategy for the supercharged cases (C and D) was different from that used for the naturally-aspirated cases for practical reasons discussed later.

**Table 3.2.** Summary of test cases

| Engine Parameter | A | B | C | D |
|---|---|---|---|---|
| Fuel | PRF 92 | PRF 92 | n-heptane | n-heptane |
| Equivalence ratio | 0.1 to 1 | 0.1 to 1 | 0.1 to 1 | 0.1 to 1 |
| Engine speed (rpm) | 1000 to 4000 | 1000 to 4000 | 1000 to 4000 | 1000 to 4000 |
| Boost pressure (bar) | none | none | 0.5 | 0.5 |
| Inlet air temperature (°C) | 121 | 121 | 73 | 73 |
| Compression ratio | 15.51 | 17.0 | 15.51 | 12.0 |
| Valve timing strategy | late EVC | late EVC | late EVC/IVO | late EVC/IVO |
| EVC (cad) | 375 to 535 | 375 to 535 | 375 to 455 | 375 to 455 |
| IVO (cad) | 298 | 298 | EVC-40 | EVC-40 |

"PRF 92" = 92 octane primary reference fuel (92 vol% 2,2,4 trimethylpentane, 8 vol% n-heptane)

When constructing each performance map, the equivalence ratio and timing for exhaust-valve-closing (EVC) were optimized at each operating point of engine speed and load to minimize fuel consumption. Other objective functions could have been chosen such as pollutant emissions, but fuel consumption was selected because it is practically important and can be reliably predicted with the model. Equivalence ratio affected engine output in the usual way, i.e. burning more fuel produced more work. The EVC timing was used to retain various amounts of residual gases in the cylinder in order to alter the charge temperature and mixture composition and thereby control the ignition timing to achieve stable engine operation over a range of speed/load conditions. Two different valve timing strategies were used. For the naturally aspirated engines, a "late EVC" strategy was used as suggested by the experimental work of Kaahaaina et al. [12]. As shown in Figure 3.1a, the large valve overlap during the intake stroke causes significant amounts of burned gases to be re-inducted into the cylinder. For the supercharged cases, a different valve timing strategy referred to as "late EVC/IVO" was needed to avoid large amounts of fresh charge from bypassing the cylinder and exiting through the exhaust port during the overlap period. Instead of a large valve overlap, the closing of the exhaust valve and opening of the intake valve are done with a short overlap (40 cad) at points

well into the intake stroke (see Figure 3.1b). Essentially, the exhaust valve was open for the beginning of the intake stroke and the intake valve was open at the end of the stroke. Similar burned gas fractions and initial charge temperatures were observed for both strategies; however, pumping losses were considerably higher under some conditions when using the "late EVC/IVO" strategy. Another alternative valve timing strategy described by Duret and Lavy [13], which uses exhaust "trapping" rather than re-induction, might avoid these pumping losses; however, this remains to be tested in future simulations.

**Figure 3.1.** Diagrams of the valve timing strategies
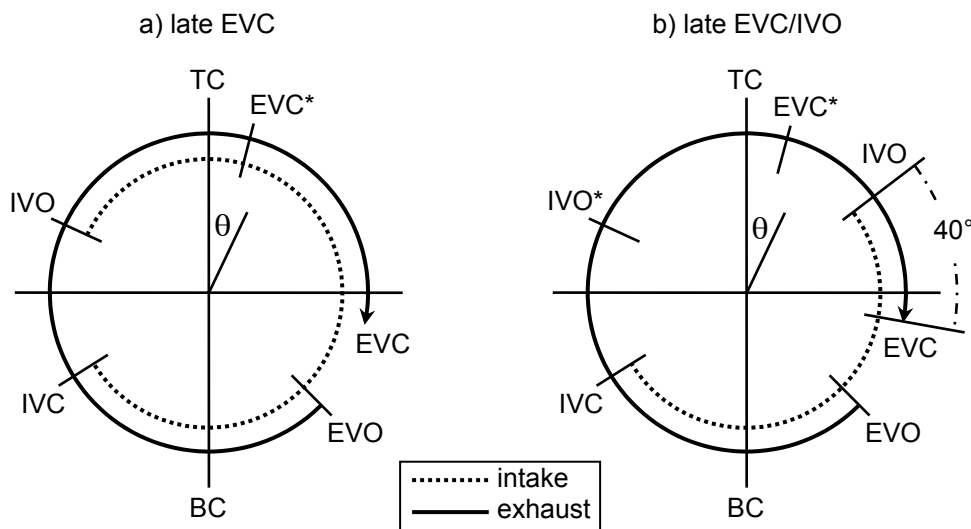


TC = top center, BC = bottom center, θ = crank angle, EVO = exhaust valve opening,
EVC = exhaust valve closing, IVO = intake valve opening, IVC = intake valve closing,
* denotes baseline valve timing

## 3.2  Numerical Procedure

### 3.2.1  Overview

Construction of performance maps for an engine requires a large number of calculations at different operating conditions (similarly a large number of test points are needed to construct these maps experimentally). Therefore it is important to choose a

modeling strategy that is both computationally efficient and accurate. Potential models for the closed portion of the engine cycle (compression/combustion/expansion) range from simple to complex with the most variability in the description of combustion. Examples of combustion models include analytical expressions for the extent of combustion as a function of crank angle (e.g. Wiebe functions), perfectly-stirred reactor models, boundary-layer models [14], multi-zone models [15], and fully coupled reacting flow models [16]. Also for those models that use detailed chemical kinetics, different levels of chemical detail can be used in the kinetic mechanism. In addition, some description of the gas exchange process is needed to have a complete description of the engine cycle. Flowrates of intake and exhaust gases are determined by solving the equations for quasi-steady orifice flow through a restriction (i.e. valve opening) or the one-dimensional unsteady Euler equations (when more detailed multi-cylinder effects are important). Cycle simulations are a combination of one of the compression/combustion/expansion models with a gas exchange model. These simulations start from an initial guess of the mixture state and iterate through several engine cycles to a converged solution. Also sub-models are needed to describe the chemical kinetics, heat losses from the cylinder, and friction losses (in order to calculate brake properties).

The modeling strategy used in this work was a combination of a cycle simulation program with a perfectly-stirred reactor (PSR) model. Rather than use the PSR model at each iteration in the cycle simulation, a simple analytic expression was used to describe combustion. Once a stable solution was found, the conditions at intake-valve-closing

were used to initialize the more accurate PSR calculations. The PSR model was partially

decoupled from the cycle simulations in this way to save computation time.

The computational strategy can be summarized as 3 steps:

1) The cycle simulation program was run to determine the steady-state conditions at intake-valve-closing using the simple analytic combustion model.

2) Using initial conditions obtained in step (1), a perfectly-stirred reactor model was run from intake-valve-closing to exhaust-valve-opening.

3) The results of the perfectly-stirred reactor are post-processed to calculate various performance characteristics of the engine (fuel consumption, efficiency, torque, "tendency to knock").

The validity of partially decoupling the PSR calculations from the cycle

simulations is addressed in the "Construction of Performance Maps" section. The PSR

simulations were compared with experimental data and more accurate multi-zone

calculations to judge the accuracy of the model. Also a sensitivity study was conducted to

determine the sensitivity of the PSR model to uncertainties in several input parameters.

## 3.2.2 Cycle Simulation Calculations

The cycle simulation program used to determine the initial conditions for the PSR

calculations was the General Motors simulation code (GMR) of Meintjes [17]. The

General Motors model takes information about the basic engine geometry, valve

dimensions and timing, and other operating parameters to simulate the intake,

compression, expansion, and exhaust strokes of the engine. The solution converged after

iterating through several engine cycles (e.g. 4). The gas exchange process was modeled

using the quasi-steady equations for orifice flow. The combustion and expansion

processes were modeled by a three-zone (burned, unburned, and boundary layer) model.

The combustion process was specified by the Wiebe function which uses four parameters

to describe the extent of combustion as a function crank angle as given by:

$$\xi_b = 1 - \exp\left[-a\left(\frac{\theta - \theta_0}{\Delta\theta}\right)^{m+1}\right] \qquad (9)$$

The combustion duration ($\Delta\theta$) was taken as 10 cad which is representative of the experimental HCCI engine pressure traces for the Ford OKP HCCI engine. Since our main interest is in performance of optimized HCCI systems, the start-of-combustion was taken as top-center ($\theta_0 = 0$ cad). The exponent $m$ was taken as 2, and $a$ as 3.912 such that $\xi_b = 0.98$ when $\theta = \theta_0 + \Delta\theta$ (i.e. a combustion efficiency of 98%). Throughout the cycle, heat losses were described by a standard correlation developed by Woschni [18].

**Figure 3.2.** Information obtained from cycle simulations and used in later calculations. Charge temperature at IVC, burned gas fraction, and cylinder pressure at IVC provide the initial conditions for the perfectly-stirred reactor simulations. Pumping mean effective pressure (PMEP) is used to calculate brake properties. (Case A, 1500 rpm)



56
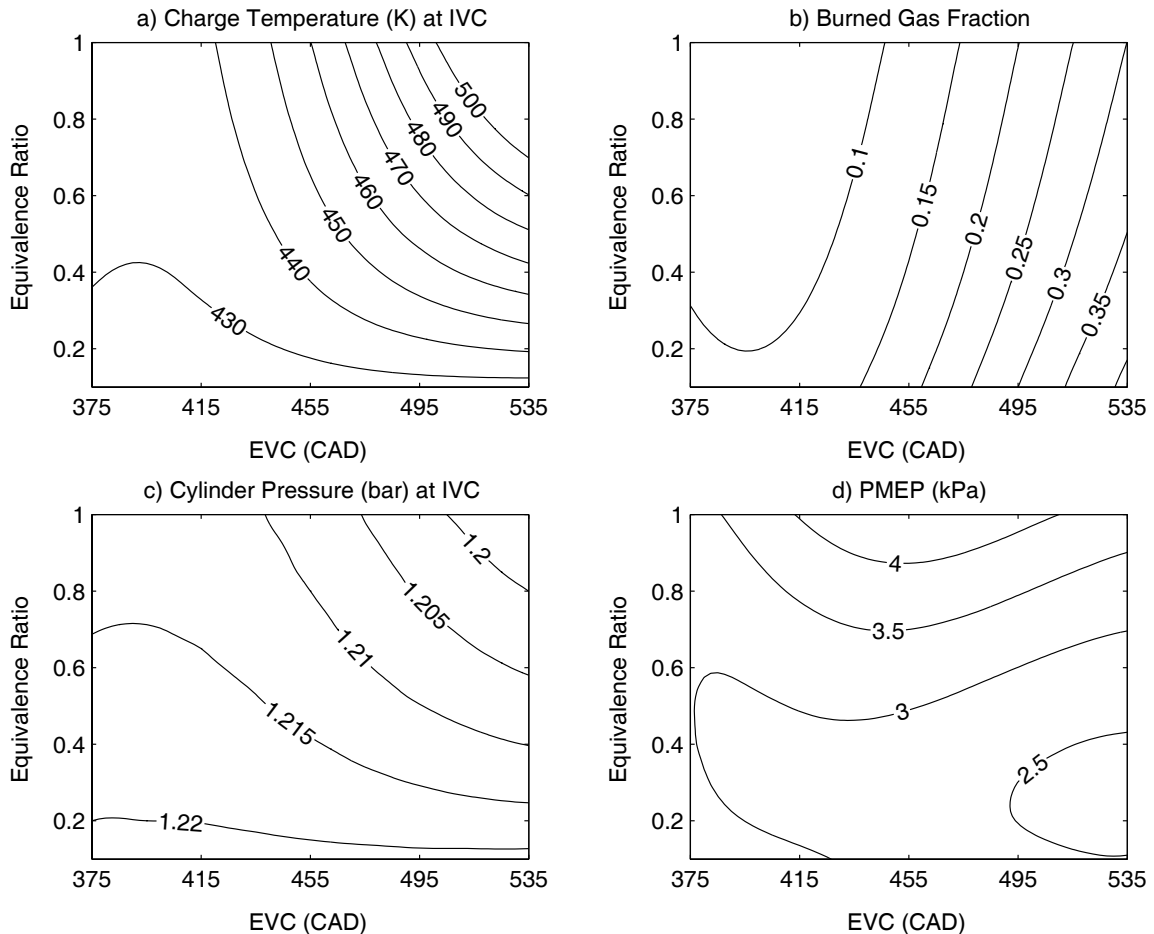
Figure 3.2 shows the results of the cycle simulations for the Case A engine at 1500 rpm—notice that the initial charge temperature can be controlled over a range of approximately 80 K by using variable valve timing. After the cycle simulation reached steady state, the burned fraction, temperature, and pressure at intake-valve-closing (IVC) were recorded. These quantities along with the equivalence ratio completely specify the state of the system at IVC. The equivalence ratio and burned fraction are used to calculate the mass fractions of fuel, oxygen, nitrogen, carbon dioxide, and water (other species are assumed to have negligible concentrations at IVC). Pumping mean effective pressure (pmep) shown in Figure 3.2d is a measure of the work needed to pull fresh charge into the cylinder and push exhaust gases out of the cylinder—pmep was used to calculate brake properties as discussed in a later section.

### 3.2.3 Perfectly-Stirred Reactor (PSR) Simulations

A PSR model was used to calculate the state of the system from intake-valve-closing (IVC) to exhaust-valve-opening (EVO). The PSR model assumes that the mixture is spatially uniform with respect to composition, temperature, and pressure. Of course, in the real engine spatial variations are present which affect the combustion process. In practice, different parcels of gas burn at different times resulting in a longer combustion event. In the PSR model the burning rate is purely controlled by the chemical kinetics—there are no transport limitations for this idealization. As a result, a weakness of the model is that while ignition delays are fairly accurately captured, heat-release rates and peak pressures are overpredicted. The PSR model equations are the following:

$$\frac{dY_k}{dt} = v\dot{\omega}_k W_k \tag{10}$$

$$C_v \frac{dT}{dt} + p\frac{dv}{dt} = -v\sum_{k=1}^{K} u_k \dot{\omega}_k W_k - \dot{q}_{loss} \tag{11}$$

$$pv = \frac{RT}{\overline{W}} \tag{12}$$

where $Y_k, \dot{\omega}_k, W_k$ and $u_k$ are the mass fraction, molar rate of production, molecular weight and specific internal energy of species $k$, respectively. The specific volume, $v$, is calculated as $v = V_{cyl}(t)/m_c$ where $V_{cyl}(t)$ is the cylinder volume given by the slider-crank formula [19], and $m_c$ is the mass of trapped charge. The heat-loss term, $\dot{q}_{loss}$, is calculated using the Woschni [18] heat transfer correlation as shown in Eqs. 5 and 6 below.

$$\dot{q}_{loss} = h_c \left( A_p \left( T - T_p \right) + A_{ch} \left( T - T_{ch} \right) + A_l \left( T - T_l \right) \right) \tag{13}$$

$$h_c [W / m^2 \cdot K] = 3.26 B[m]^{-0.2} p[kPa]^{0.8} T[K]^{-0.55} w[m/s]^{0.8} \tag{14}$$

The average gas velocity, $w$, was estimated using the relation $w = 2.28\overline{S}_p$, where $\overline{S}_p$ is the mean piston speed. Woschni used an additional term in this relation during the combustion and expansion phases in an attempt to capture the additional gas velocity due to combustion. This additional term was not included because the gas velocity caused by HCCI combustion is likely quite different from that caused by diesel combustion (for which the model constants were regressed). Nevertheless, this heat-transfer correlation has been widely applied to HCCI engines (e.g. [10, 20, 21] and is believed to give a reasonable estimate of heat losses. Fiveland and Assanis [14] compared the Woschni model with more detailed heat-transfer models and found that predictions of HCCI

ignition times differed by only a few crank angle degrees—well within the accuracy limits of the chemistry model.

Two chemistry models developed by Curran et al. [22, 23] were used in this study—a PRF model with 1034 chemical species and 4238 reactions and an n-heptane model with 545 chemical species and 2446 reactions. The n-heptane model has been validated with experimental ignition delays from a rapid compression machine [22]. The iso-octane portion of the PRF model has been compared with exhaust speciation data and critical-compression-ratio data from a Co-Operative Fuels Research (CFR) engine [23].

A FORTRAN program was written to solve the system of differential algebraic equations (DAEs) given by Eqs. 2-4. Species formation rates and thermodynamic properties were calculated with the CHEMKIN [24] library of subroutines. Choosing $(T,P,Y_k)^{\mathrm{T}}$ as the solution vector and using slightly modified CHEMKIN subroutines described by Schwer et al. [25] resulted in a sparse Jacobian matrix for this system of equations (95.4% sparsity for n-heptane, 97.8% for PRF). The sparsity pattern of the Jacobian was identified by using the DAEPACK [26, 27] software package developed by Barton and co-workers. DAEPACK was also used to construct a subroutine (using automatic differentiation technology) that evaluates analytical expressions for derivatives and returns the non-zero elements in the Jacobian matrix. Subsequently the associated sparse solver, DSL48S [28], was used to solve the system of DAEs using sparse matrix storage and sparse linear algebra. This numerical approach requires only a fraction of the CPU time used by standard solvers (e.g. DASSL, VODE). As a demonstration, the CPU time was calculated for ten typical runs (all of which ignited) using PRF (Case A) and n-heptane (Case D) at 1000 rpm using a 733 MHz Linux machine. Using DSL48S and the

sparse analytical Jacobian generated by DAEPACK, the average CPU times were 3.77 min (n-heptane) and 6.98 min (PRF). Using DASSL with a finite-difference Jacobian and conventional (dense) linear algebra, the CPU times were 28.04 min (n-heptane) and 98.48 min (PRF). Considering that many of these calculations (17x19x13 = 4199) are needed to construct each performance map, this study would not have been feasible without the use of DAEPACK and the DSL48S solver.

Figure 3.3 shows a comparison of computed and experimental pressure traces for the Ford OKP HCCI engine at two equivalence ratios. For the purposes of this comparison, the inlet air temperature was adjusted such that ignition occurred in the simulations at approximately the same crank angle as in the experiments. The inlet air temperatures used in the simulations were 146°C (A/F = 39.79) and 153°C (A/F = 39.21) compared with the experimental value of 121°C. The magnitude of the inlet air temperature adjustment (approx. 30°C) needed to match the experiments gives a measure of the limitations of the chemistry model and/or physical model. No tuning of intake temperature or other parameters was done when constructing the performance maps—the values of intake temperatures used to construct the maps are listed in Table 3.1. Notice that the PSR model overpredicts the peak pressure (12% difference, A/F = 39.79; 6% difference, A/F = 39.21) and heat-release rate. The PSR model does, however, accurately predict the net work per cycle from the engine (<1% difference, A/F = 39.79; 1% difference, A/F = 39.21). The accuracy of our prediction for the knock limit was verified by a more rigorous set of multi-zone model calculations discussed later. Sensitivity of the PSR calculations to errors in the model parameters is also discussed at the end of this

section. Certainly the PSR model is sufficiently accurate to predict trends and the relative

importance of various engine parameters for performance.

**Figure 3.3**. Comparison of cylinder pressure from the Ford OKP HCCI engine and perfectly-stirred reactor (PSR) model at two air/fuel (A/F) ratios and conditions from Table 1.1 (1500 rpm)
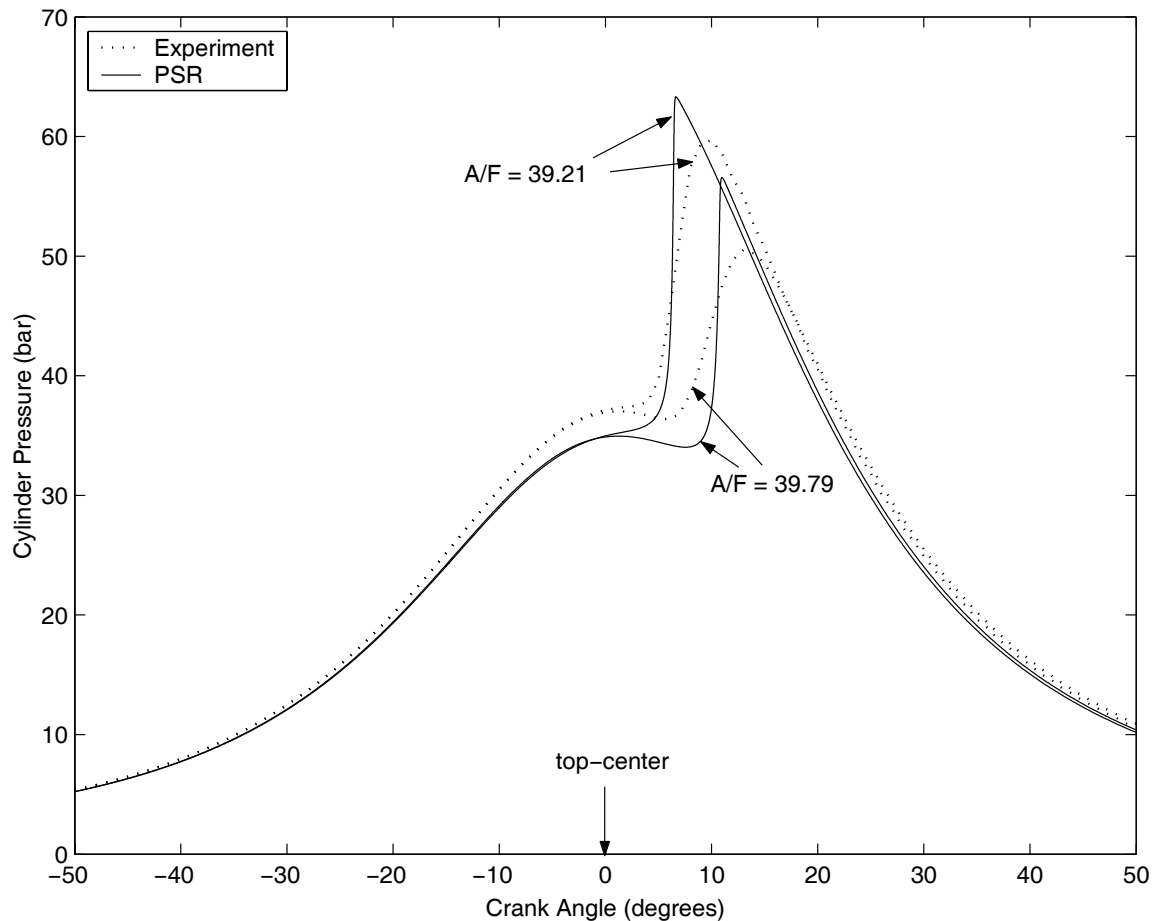


## 3.2.4  Post-Processing of Results

### 3.2.4.1 Calculation of Brake Properties

The outputs of the PSR calculation are profiles of temperature, pressure, and

mixture composition as a function of time (or crank angle) from IVC to EVO. The

standard engine performance characteristics were calculated from these profiles and

information from the cycle simulations. Net indicated work was calculated by integrating

the cylinder pressure with the change in volume over the four engine strokes. The PSR was used to calculate work for the closed portion of the cycle from IVC to EVO (compression/combustion/expansion), and the GMR cycle simulation was used to calculate work for the gas exchange portion of the cycle (Eq. 7). It is convenient to express engine work as a mean effective pressure, defined as work per cycle per unit displaced volume, to allow engines of different sizes to be compared fairly (Eq. 8).

$$W_{c,in} = W_c(\text{PSR, comp./comb./expn.}) + W_c(\text{GMR, gas exchange}) \qquad (15)$$

$$\text{imep}_n = \frac{W_{c,in}}{V_d} \qquad (16)$$

Finally, brake work (i.e. usable work delivered by the crankshaft) or brake mean effective pressure was calculated for its practical importance to engine design. To calculate brake properties, engine friction was subtracted from the net indicated work:

$$\text{bmep} = \frac{W_{c,b}}{V_d} = \text{imep}_n - \text{amep} - \text{rfmep} \qquad (17)$$

Friction losses were grouped in two categories: auxiliary friction (oil pump, water pump, alternator) and rubbing friction (valvetrain, crankshaft, piston, etc.). The correlation of Sandoval and Heywood [29] was used to estimate the auxiliary friction mean effective pressure (amep) and the rubbing friction mean effective pressure (rfmep). This correlation is a recent update of the widely-used correlation of Patton et al. [30] and accounts for recent engine developments that have decreased friction losses. For the supercharged cases, the work needed to compress the intake air was calculated using Eq. 10, where $W_{sc}$(isentropic) is the work required for an adiabatic, reversible compression.

$$W_{sc} = \frac{W_{sc}(\text{isentropic})}{\eta_{sc}} = \frac{n_{intake}}{\eta_{sc}} \frac{\gamma R T_1}{\gamma - 1} \left[ \left( \frac{P_2}{P_1} \right)^{(\gamma-1)/\gamma} - 1 \right] \qquad (18)$$

A compressor efficiency, $\eta_{sc} = 0.75$, was used to calculate the actual work that needs to be supplied to the supercharger. The ratio $W_{sc}/V_d$ (approximately 60 kPa) represents another component of the auxiliary friction mean effective pressure that needs to be accounted for in the supercharged cases.

## 3.2.4.2 Determination of Knock Limit and Maximum Torque

As mentioned, low maximum torque is a serious limitation of dedicated HCCI engines. Hence a good criterion for determining the maximum available torque is a key to computing useful performance maps. In practice, excessive engine noise due to an extremely rapid heat-release process or development of pressure waves in the cylinder (marked by oscillations in the measured pressure trace) are observed at higher torques. The onset of this rough "knocking" operation limits the maximum torque from the engine. Experimentally the knock limit can be defined in various ways; Oakley at al. [5] considered the HCCI engine to be knocking when the amplitude of the pressure oscillations exceeded 0.5 bar in 10% or more of engine cycles.

Although many workers have observed pressure traces from HCCI combustion that exhibit pressure oscillations, there is no consensus for the origin or nature of knock in HCCI engines. Earlier studies have verified that the frequency of these pressure oscillations agrees well with the calculated frequencies for the major acoustic resonant modes for the engine cylinder. Clearly, these oscillations arise from pressure waves resonating in the cylinder charge. It is proposed here that a locally high pressure can arise in HCCI engine cylinders from very fast combustion in a given parcel of fuel/air mixture,

and that these local overpressures then lead to resonant pressure waves. If the combustion rate in a fuel/air parcel is slow enough, the parcel will expand and maintain its pressure nearly equal to that of the rest of the gas in the cylinder. As the combustion rate increases, the rate at which the parcel must expand in order to remain in pressure equilibrium becomes very fast. When the required expansion rate exceeds the speed of sound, a local overpressure will develop.

A study of the competing physical and chemical processes leads to a simple criterion for determining if HCCI knock should be expected. Knock would not be expected when:

$$\beta = \frac{L_c(\gamma - 1)}{\gamma p} \frac{\dot{q}}{u_{sound}} \leq 1 \qquad (19)$$

throughout the cylinder, at all times. $L_c$ is a characteristic length scale (volume/area) of the inhomogeneities in the HCCI cylinder (taken as 0.1·bore). Of course since no inhomogeneities are present in the PSR model, it is assumed that the mixture average properties are representative of the local properties in the cylinder. This assumption, which should be acceptable if knocking usually occurs in the nearly-uniform core gas region, is verified by the multi-zone calculations described in the next section. The quantity $\dot{q}$ is the chemical heat-release rate (volumetric), defined as the magnitude of the summation term on the right-hand side of Eq. 3. The variable $u_{sound}$ is the speed of sound, which is simple to calculate for an ideal gas, and $\gamma$ is the ratio of specific heats $C_p$ /$C_v$, which is calculated from the mixture heat capacity. The criterion in Eq. 11 is derived from a scaling analysis of the first law of thermodynamics applied to a given fuel/air parcel. The first law can be written as follows assuming a movable, impermeable,

adiabatic control volume around a given fuel/air parcel and assuming the change in average molecular weight upon combustion is small.

$$\frac{dp}{dt} = -\frac{\gamma p}{V}\frac{dV}{dt} + (\gamma - 1)\dot{q}$$

(20)

$$\left\{\begin{array}{l}\text{rate of}\\\text{pressure rise}\end{array}\right\} = \left\{\begin{array}{l}\text{rate work done by}\\\text{volume expansion}\end{array}\right\} + \left\{\begin{array}{l}\text{rate of chemical}\\\text{heat release}\end{array}\right\}$$

The volume expansion term $dV/dt$ has been scaled with $A{\cdot}u_{sound}$, where $A$ is the surface area of the parcel. $A{\cdot}u_{sound}$ is the maximum rate that the fuel/air parcel can expand (note that the sound speed and shock speed are similar under engine conditions). If the chemical heat-release rate is any faster than the maximum rate at which expansion work can be done, then a local overpressure will occur. In the limit of an infinitely fast chemical heat release, the combustion of the parcel will occur at essentially constant volume and the maximum possible local overpressure will occur. The $\beta$ parameter is dimensionless and characterizes the competition between the rate of chemical heat-release and volume expansion at the speed of sound.

Our approach used to determine the knock limit or maximum torque differs from that taken by Martinez-Frias et al. [10] who used a restriction on the maximum pressure. The results section for Case A discusses whether knocking (i.e. engine noise and potentially damaging pressure waves) or peak pressure (mechanical strength limitations) is the appropriate criterion for determining maximum torque. Researchers [31] have also observed high $NO_x$ emissions under high loads. Although this study focused on fuel economy and operability rather than emissions, the possibility that $NO_x$ could limit the maximum available torque is briefly discussed in the Results section under Case D.

### 3.2.5 Construction of Performance Maps

Construction of the performance maps was a two-step process. First, a matrix of simulations was run for each case over a range of fuel/air equivalence ratios ($\phi$) and exhaust-valve-closing (EVC) timings. The range of $\phi$ was 0.1 to 1 at intervals of 0.05 (19 levels). The range of EVC timing was 375 to 535 cad for the naturally-aspirated cases at intervals of 10 cad and 375 to 455 cad for the supercharged cases at intervals of 5 cad (17 levels). Hence a total of 323 (17x19) runs were performed for each engine speed. In the second step, the data from each speed was examined to find the conditions (equivalence ratio and EVC timing) that minimize fuel consumption for a given load (bmep). This optimum point was found for a series of desired loads from idle up to the maximum load, and the locus of these optima form a "best trajectory". Finally, this procedure was repeated for a range of engine speeds from 1000 to 4000 rpm at increments of 250 rpm (13 levels), and this data was used to construct the performance maps (each best trajectory supplied the information for one vertical slice on the performance maps). Figure 3.4d shows the results from a matrix of runs for Case A at 1500 rpm. Because calculations were done for discrete values of $\phi$ and EVC timing, the optimum operating points (solid dots) do not lie along a perfectly smooth curve; therefore, the "best trajectory" (heavy solid line) was taken as an approximation to those points. Notice that points along this line minimize the fueling rate (dashed contours), for a given brake mean effective pressure (solid contours).

**Figure 3.4.** Plots a, b, and c show pressure traces computed with the perfectly-stirred reactor (PSR) and cycle simulation (GMR) at three values of brake mean effective pressure (bmep). Plot d shows a single-speed operating map for Case A at 1500 rpm with conditions corresponding to plots a, b, and c indicated. Shown on plot d are the "best trajectory" (heavy solid line), contours of bmep (solid lines), and contours of fueling rate, fr, (dashed lines).
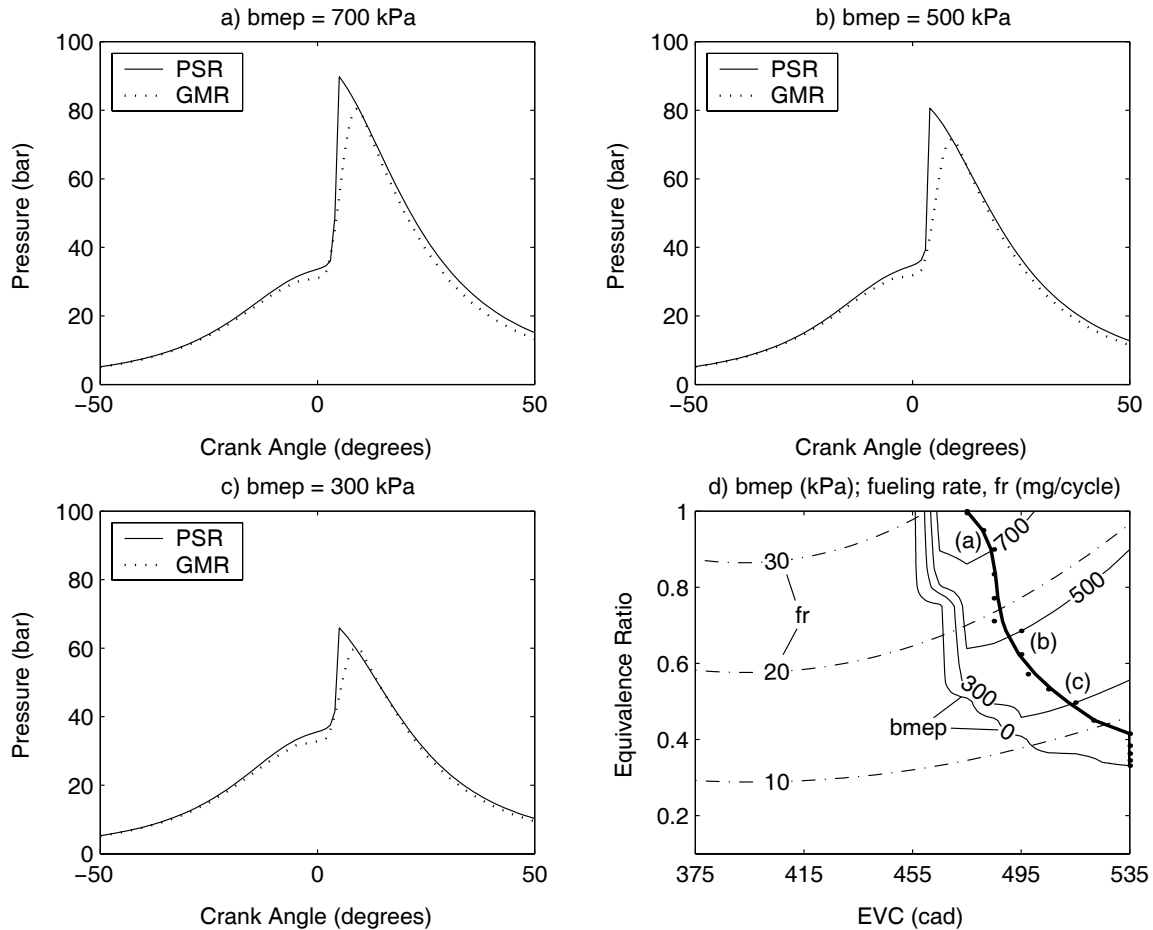


The validity of our assumption that the PSR calculation can be partially decoupled from the cycle simulations needs to be evaluated in more depth. Recall this decoupling allowed us to use the simple analytic combustion model in the cycle simulations to reduce computational time. The cycle simulations take only seconds with the simple combustion model compared to several minutes for the PSR model. If the analytical combustion model agrees with the PSR (and hopefully the real engine) this decoupling is justified. Figures 3.4a-c show computed pressure traces from the PSR model and the

67

GMR cycle simulation with the simple combustion model for various points along the best trajectory. The timing for the start-of-combustion (SOC) was quite similar for the two models (recall that SOC is set to top center in GMR and controlled by the kinetics in the PSR model). The agreement was always acceptable along the best trajectory because our objective function (fuel consumption) was minimized when the SOC was near top center. Of course the agreement was worse at points that do not lie along the best trajectory, but those points were not used to construct the performance maps. As mentioned previously, the rate of combustion was also a consideration because the PSR model is well-known to overpredict rates of combustion. The combustion duration was fixed in the cycle simulations to a realistic value in accord with the available experimental data from Figure 3.3. So with regard to combustion duration, the simple Wiebe-function combustion model was actually more realistic than the more-detailed PSR model. Apparently, using a simple combustion model in the cycle simulations is valid for the purposes of constructing HCCI performance maps with this procedure, as long as the engine is operating near-optimally.

### 3.2.6 Multi-zone Calculations

In order to test the validity of our assumption that the HCCI engine can be adequately modeled as a PSR, several multi-zone calculations were performed. The multi-zone model developed by Aceves et al. [15] more accurately describes the engine because spatial variations in charge temperature are included. Additionally, Yelvington and Green [11] have shown that the multi-zone model accurately predicts the onset of HCCI engine knock based on a detailed comparison with the experimental data of Oakley et al.[6].The main objective of these calculations was to check that the knock limit

predicted by the PSR model agreed with the more realistic multi-zone model. Our implementation of the multi-zone model has been described previously [11] so the details of the model will be only briefly summarized here. The multi-zone model first uses the KIVA3v2 computational fluid dynamics package developed by Amsden [32] to estimate the temperature field inside the engine during compression without any chemical heat release. A simple disc-shaped engine cylinder geometry was used for these calculations— the engine was assumed to have a flat cylinder head and no piston crevices. The temperature field data are averaged into ten homogeneous zones based on a predetermined mass distribution. In the first stage of the calculation, the species conservation equations are integrated (with chemical reactions) using the zone temperature profiles and cylinder pressure from KIVA from intake-valve-closing to some point where chemical heat release becomes important. At that point, the KIVA zone temperature profiles are abandoned and the multi-zone model equations are solved for the remainder of the combustion and expansion processes. In this second stage, each zone is considered a variable-volume perfectly-stirred reactor, and pressure is assumed spatially uniform throughout the cylinder. The zones interact through compression work (e.g. hotter zones burn and expand which compresses the colder unburned zones). Other interactions between zones such heat and mass transfer are considered negligible. Heat losses during the second stage were calculated identically to the PSR model except that heat was subtracted only from the outer zones near the wall (defined as the coldest 30% of the mass). The DAEPACK package was again used to solve the multi-zone model equations using sparse linear algebra, and the gain in computational efficiency was even greater than was observed for the PSR model [11]. With this fast kinetics solver, the slow

step in the computation is the non-reacting KIVA simulation of the temperature distribution during the compression stroke.

Figure 3.5 shows a comparison of pressure traces from Case A at an engine speed of 2500 rpm, equivalence ratio of 0.65, and EVC timing of 505 cad.

**Figure 3.5.** Comparison of predicted cylinder pressure from the multi-zone model and the perfectly-stirred reactor model (PSR) for Case A (2500 rpm , equivalence ratio = 0.65, EVC timing = 505 cad)
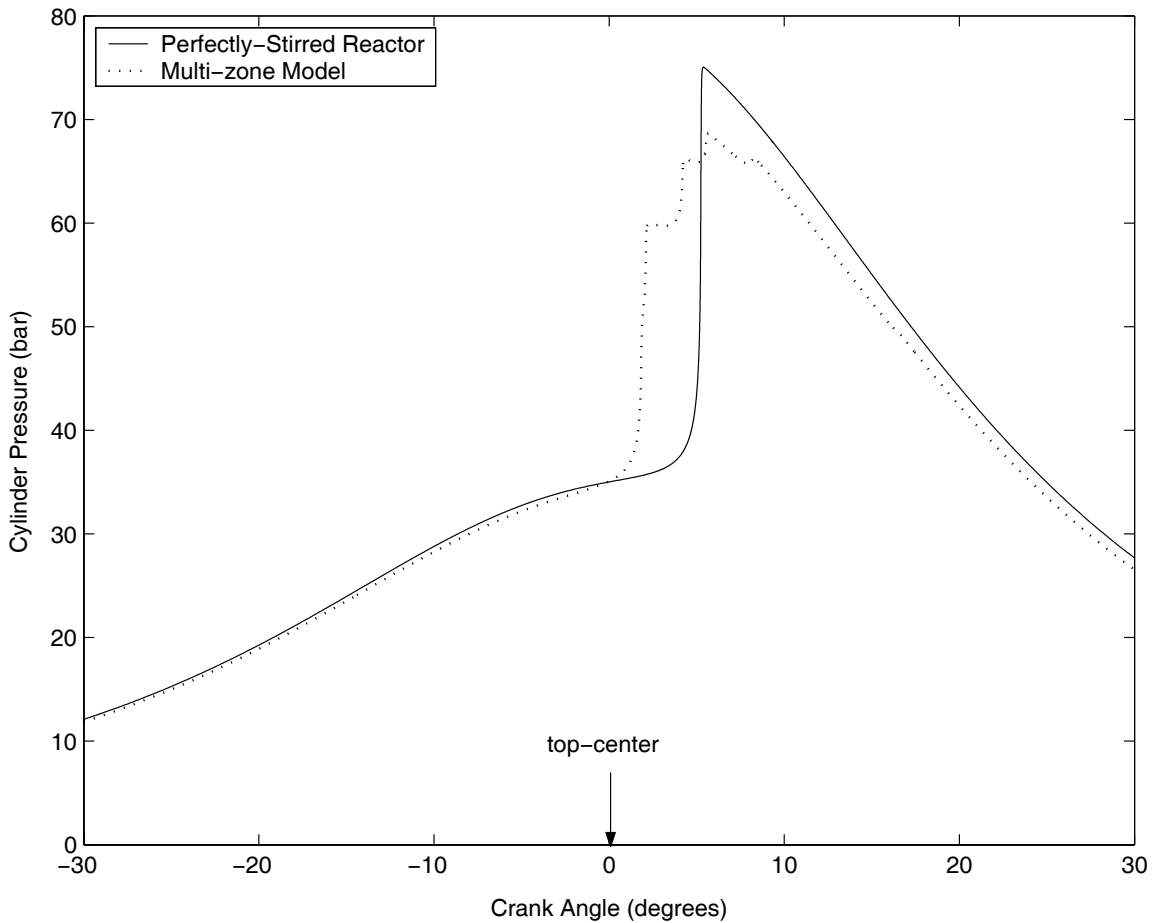


The knocking parameter, $\beta$, was 0.956 for the PSR and 0.932 for the multi-zone model. This good agreement suggested that the PSR model could be used to predict the HCCI knock limit accurately. The calculated work expressed as a net indicated mean effective pressure ($imep_n$) was 556 kPa for the PSR and 514 kPa for the multi-zone

model. The peak pressure was 75.0 bar for the PSR and 68.8 bar for the multi-zone model. Comparisons for the n-heptane cases (C and D) yielded a similar level of agreement. The multi-zone model ignites slightly earlier because the core gas is assumed to be adiabatic (all heat loss is from the boundary layer) which results in a core gas temperature that is higher than the bulk PSR temperature during compression. The multi-zone pressure trace is somewhat jagged because the time-scale for heat-release from each zone is short compared to the difference in ignition times among zones (which is symptomatic of high $\beta$). Overall, the PSR model seems sufficiently accurate for the purposes of constructing performance maps.

### 3.2.7  Sensitivity of PSR Calculations

Several calculations were conducted to judge the sensitivity of our PSR model predictions to uncertainties in the input parameters. The heat-transfer coefficient ($h_c$) for the PSR calculations was doubled to determine the sensitivity of the model predictions to the physical model, and the reaction rate coefficients were doubled to measure sensitivity to the chemistry model. These calculations were performed for the Case A engine configuration at an engine speed of 1500 rpm (initial conditions shown in Figure 3.2).

As shown in Figure 3.6b, when the heat-transfer coefficient was doubled, the contours of bmep and the best trajectory were shifted to a later EVC timing by approximately 40 cad. In order for ignition to occur with the higher heat losses, more heating by residual gas is necessary. The system appears quite sensitive to heat-transfer, but recall that fairly large changes in EVC timing result in fairly small changes in the charge temperature at IVC. With the original $h_c$, the mixture ignited when $T_{IVC}$ was greater than about 460 K (see Figure 3.2a), while a $T_{IVC}$ of 490 K was necessary when $h_c$

71

was doubled—only a 30K difference in initial temperature. Nevertheless, under these conditions the PSR calculations do appear quite sensitive to the physical model. In order to obtain quantitative accuracy from simulations, it is important to have good experimental measurements of HCCI engine heat transfer.

The effect of doubling the reaction rate constants is shown in Figure 3.6c. The forward and reverse rate constants of all the reactions were doubled to maintain the same equilibrium state. With this increase in reaction rates, the mixture ignited over the full range of conditions, and the best trajectory was shifted to earlier EVC timing by approximately 70 cad. Less heating by residual exhaust was needed because the mixture ignited more easily with the increased reaction rates. Again the PSR predictions were quite sensitive to details of the chemical kinetics for ignition. Indeed the system as a whole seems quite sensitive as demonstrated by sensitivity of the experimental engine— Figure 3.3 shows that experimentally the ignition timing and peak pressure changed dramatically for a minor change in air/fuel ratio. Carefully constructed chemical kinetic models appear necessary to obtain quantitative accuracy from the simulations. The current simulations should, however, accurately predict trends in performance with changes in engine parameters and the relative importance of various design considerations (e.g. fuel, boost pressure, compression ratio).

**Figure 3.6.** Sensitivity of perfectly-stirred reactor (PSR) calculations. Plot a shows the base case for comparison. Plot b shows the results of doubling the heat-transfer coefficient, and plot c shows the results of doubling the reaction rate constants. (Case A, 1500 rpm)
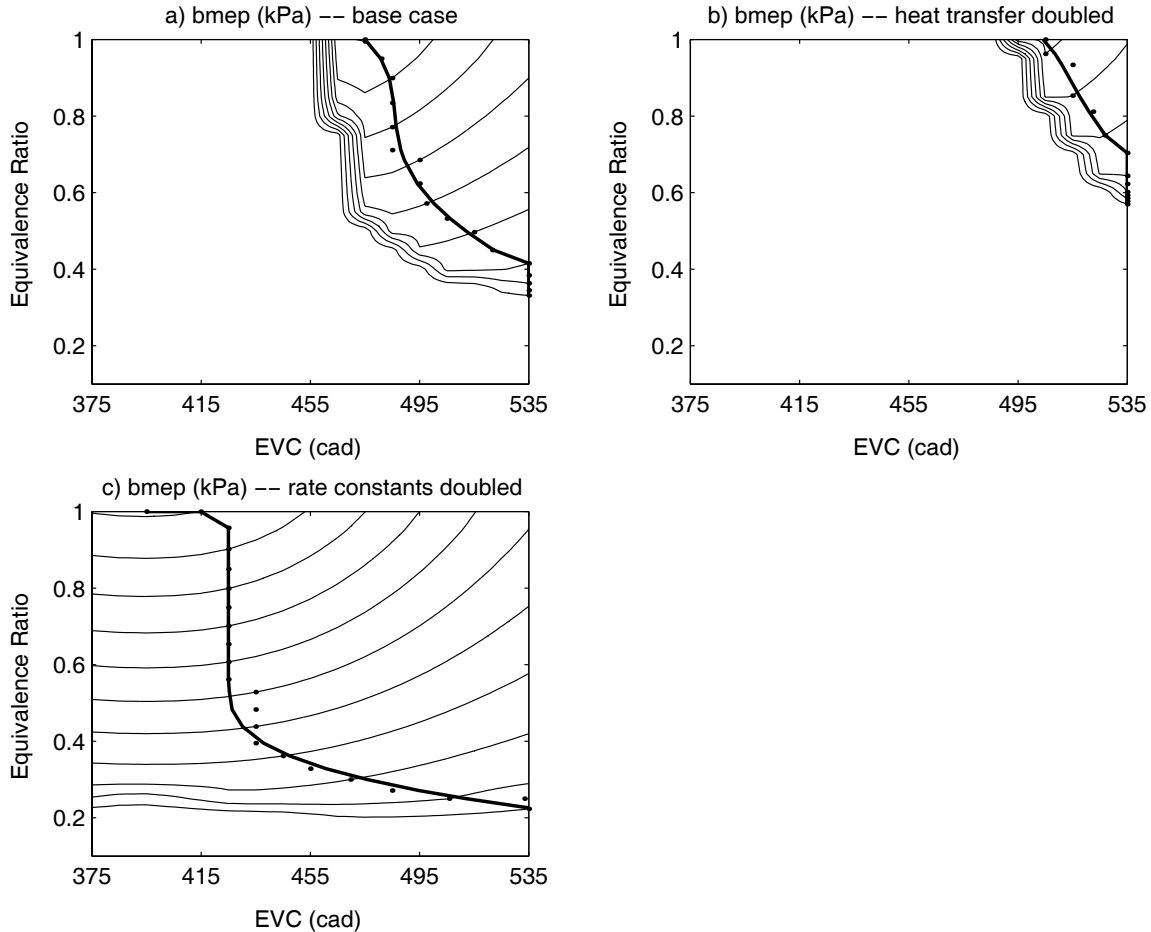


## 3.3  Results for Various HCCI Engine Designs

### 3.3.1  Test Case A (Baseline)

Figure 3.7 and Figure 3.8 show the results for Case A, the baseline case which most nearly approximates the experimental engine described by Yang et al. [7]. Figure 3.7 shows the optimum operating conditions collected from the best trajectories at each speed from 1000 rpm to 4000 rpm at 250 rpm increments. The optimum fuel/air equivalence ratio ($\phi$) and optimum EVC timing (Figure 3.7a,b) give the conditions under which the engine should be operated to minimize fuel consumption for a given load

73

(bmep) and engine speed (rpm). Figure 3.7c and Figure 3.7d show the burned gas fraction, $x_b$, (the fraction of the trapped cylinder charge which is exhaust gas) and the gas temperature at intake-valve-closing ($T_{IVC}$ in K). Figure 3.8 shows the performance characteristics (fuel conversion efficiency, crank angle for 80% fuel burned, the knocking parameter ($\beta$), and peak cylinder pressure) of an engine operated at the conditions given in Figure 3.7.

The key to high efficiency over a broad range of speed and load is to maintain nearly ideal combustion timing (i.e. close to top center). Other factors such as heat losses and mixture heat capacity contribute to efficiency, but to a lesser extent. The mottled contours in Figure 3.8b show that the combustion event occurred within 3 to 6 cad after-top-center with no observable trends with speed or load. The variable-valve-timing control strategy was successful at maintaining the correct combustion timing over the full range of speed and load. It is helpful to look at the effects of speed and load independently. Recall that the start-of-combustion in an HCCI engine is purely controlled by the ignition kinetics of the fuel/air mixture. The ignition process is exponentially dependent on charge temperature and more weakly dependent (linearly or squared) on species concentration. At a speed of 2000 rpm in Figures 3.7 and 3.8, as you move down from the heavy stoichiometric ($\phi = 1$) line, the mixture becomes increasingly fuel lean ($\phi = 1...0.4$) resulting in lower exhaust gas temperatures. As a result, more exhaust gas needs to be recycled ($x_b = 0.15...0.35$) in order to maintain roughly the same charge temperature at the start-of-compression (at IVC). At this speed, $T_{IVC}$ was maintained at approximately 480 K over the range of $\phi$ from 0.4 to 1.0, and this was sufficient to control the ignition time. As $\phi$ is decreased below about 0.4, the EVC timing reaches its

maximum; since no more exhaust can be retained, the charge temperature decreases and ignition timing becomes later.

At a constant load (bmep) of for instance 400 kPa, the equivalence ratio increases slightly at higher speeds ($\phi$ = 0.55…0.7). Friction losses increase with speed (fmep increased from 110 kPa to 180 kPa in the range 1000 to 4000 rpm) and more fuel must be burned to maintain the same amount of useful work delivered by the crankshaft. Again nearly ideal timing is observed (Figure 3.8b) over this range of speeds, which means the ignition delay must have decreased by a factor of 4 between 1000 and 4000 rpm. This decrease in ignition delay is achieved by later EVC timing (EVC = 490…515). Note that the burned gas fraction actually remains nearly constant, but the exhaust temperatures increase due to lower heat losses (shorter time per cycle for heat transfer). The result is an increase of initial charge temperature ($T_{IVC}$ = 460…510 K) from 1000 to 4000 rpm.

Figure 3.8a shows the brake fuel conversion efficiency. The maximum efficiency occurs at a bmep of 700 kPa and speed of 1000 rpm. At bmep values below this (lower torque, leaner mixture) fuel conversion efficiency decreases as friction and heat losses become more important relative to useful work. Eventually $\eta_{f,b}$ must go to zero when the work produced is just enough to overcome friction (bmep = 0). As mentioned, Figure 3.8b shows little change in ignition delay within this range due to EVC control. Figure 3.8c is quite important because it shows the maximum load (bmep) that is attainable without causing engine knock ($\beta$ < 1). Recall that this is the real limit of operability rather than the stoichiometric line ($\phi$ = 1). The maximum attainable bmep is about 500 kPa at low speed and 400 kPa at high speed. Note that the peak pressure is about 70 to 80 bar along this contour, just inside the mechanical strength limit of a gasoline SI engine

which is approximately 70-80 bar [7]. For higher peak pressures, more robust diesel-like engine would be required. Recall, however, that the comparison of our PFR calculations with experiment and the multi-zone simulations showed that the calculated peak pressures from the PSR model are approximately 10% higher than the actual values. Therefore it is likely that the engine will knock (noisy combustion probably accompanied by resonant pressure waves in the charge) before the peak pressure became prohibitively high. So in this case, engine noise and vibration are likely to limit the maximum torque rather than materials constraints due to high peak pressures.

Notice that the contours for $\beta$ closely follow the contours of equivalence ratio. This correspondence between $\beta$ and $\phi$ can be explained by the analysis of the $\beta$ expression (Eq. 11). $\beta$ is essentially a scaled, local chemical heat-release rate. The major dependences should be temperature and composition (affect $\dot{q}$) and cylinder pressure (affects $\dot{q}$ and appears in denominator). Keep in mind that $\beta$ changes during the PSR simulations—the reported values are maximums generally occurring during the fastest part of the combustion event. Temperature has by far the strongest influence on $\beta$ because of the exponential dependence of heat-release rate on temperature. Peak combustion temperature increases with increasing $\phi$ leading to faster chemistry and hence higher $\beta$ value. For Case A, peak combustion temperature increased from about 1600 to 3000 K as $\phi$ goes from 0.4 to 0.9. Other factors that affect combustion temperature are minor by comparison; for example, $T_{IVC}$ changed only 60 K over the whole map. Because contours of combustion temperature correspond closely with $\phi$ and other effects are minor, $\beta$ corresponds closely with $\phi$ also. For these simulations, the knock limit ($\beta$=1) corresponded to a critical $\phi$ of approximately 0.65.

**Figure 3.7.** Optimum operating conditions (Case A): Naturally-aspirated, PRF-fueled engine with baseline compression ratio ($r_c = 15.51$)
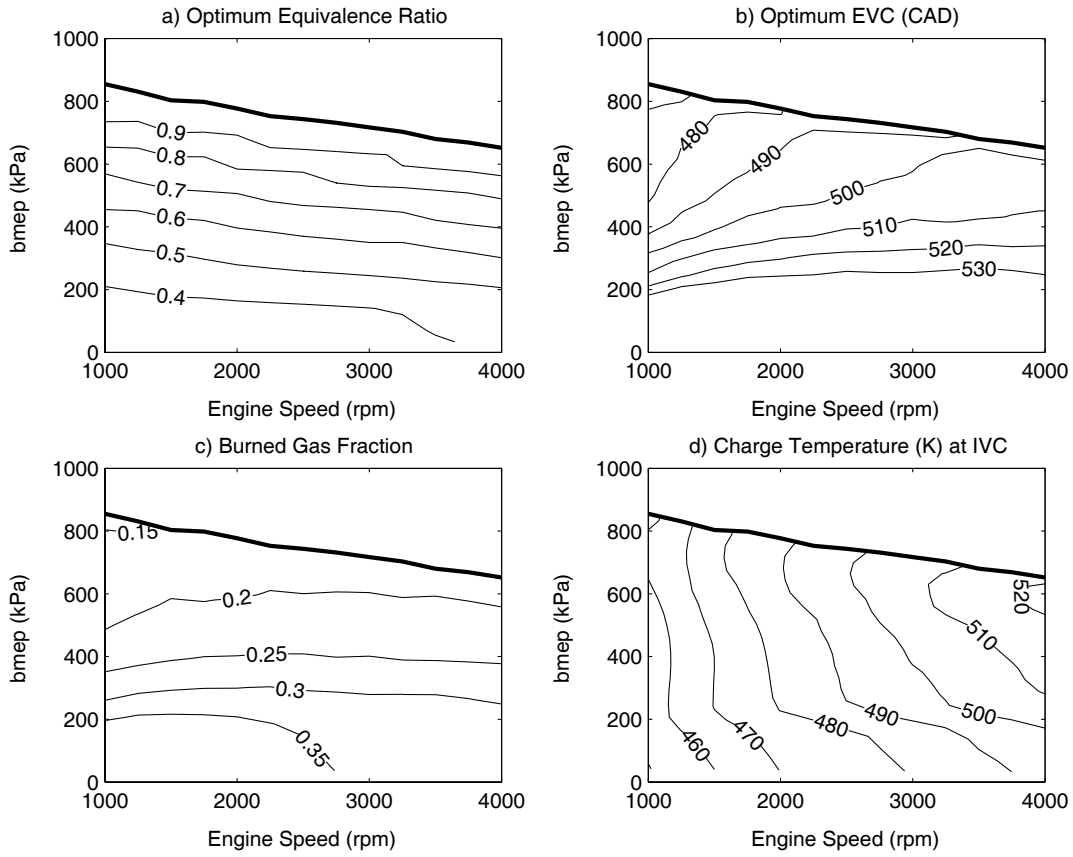
**Figure 3.8.** Performance characteristics (Case A): Naturally-aspirated, PRF-fueled engine with baseline compression ratio ($r_c$ = 15.51). The knock limit ($\beta$=1) is shown as a dashed line.
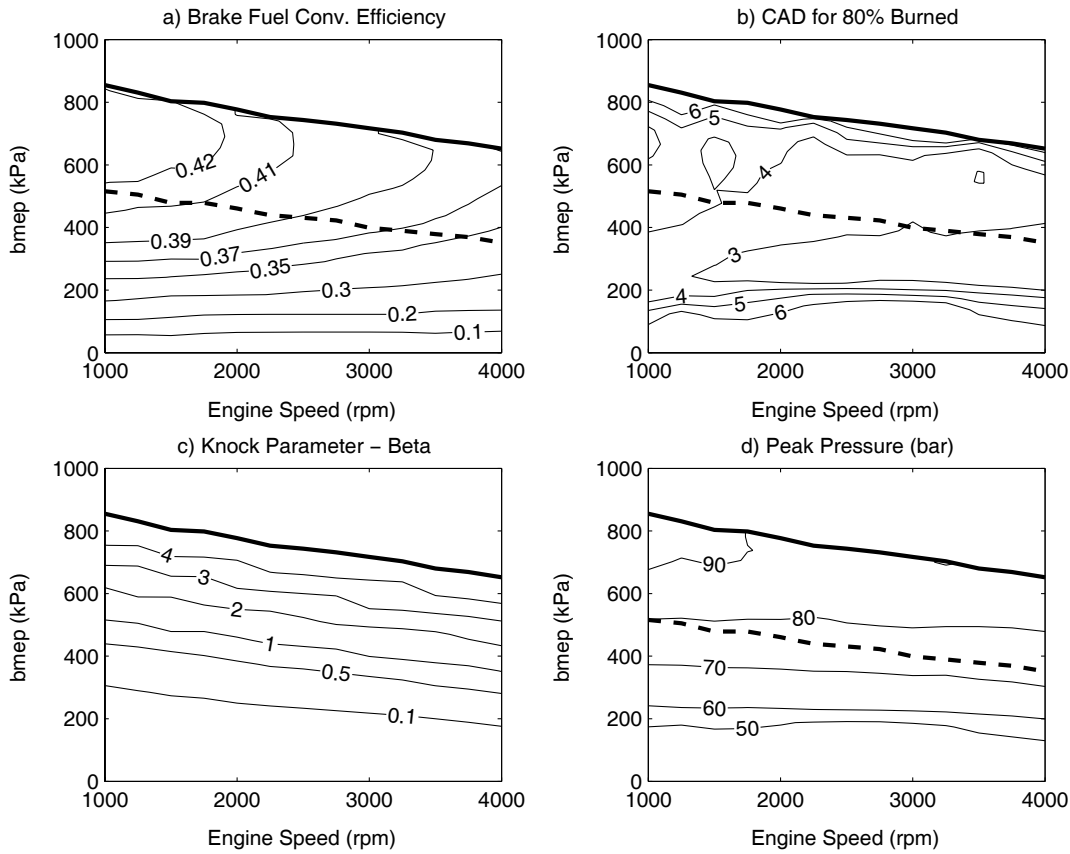


### 3.3.2 Test Case B

Case B was identical to the baseline (Case A) except that the compression ratio was higher ($r_c$ = 17.0). Increasing the compression ratio was expected to yield higher efficiency, but the influence on the knock limit was more difficult to predict. Figure 3.9 shows that a 5% lower burned gas fraction and hence lower initial charge temperature was needed compared to the lower compression ratio case (Case A). Less heating by residual gases was needed to achieve the same end-of-compression temperature in Case B. A lower burned gas fraction means lower dilution by inert species; therefore, a higher mass of fuel (and hence torque) is present for the same equivalence ratio. This higher

torque can be seen in the fact that the bold stoichiometric ($\phi$ = 1) line was shifted up approximately 1 bar compared to Case A.

Figure 3.10a shows that the brake fuel conversion efficiency was higher than Case A by approximately 2%. This result is in accord with a basic thermodynamic cycle analysis which shows that higher compression ratios yield higher efficiencies. Again the crank angle for 80% fuel burned was mottled, showing that the control strategy was effective at maintaining the correct combustion timing.

Comparison of the knock limit ($\beta$ = 1) in Figure 3.10c with that in Figure 3.8c for case A is interesting. First observe that the knock limit has shifted up only slightly (~0.3 bar) compared to a 1 bar shift in the stoichiometric line. This can be explained by examination of the $\beta$ expression (Eq. 11). The characteristic dimension, $L_c$, is constant and $\gamma$ and $u_{sound}$ are weak functions of temperature and composition only. The strongest dependence comes from $\dot{q}$ and $p$. The end-of-compression temperatures must be similar between Cases A and B (because the combustion timing remained the same) so that leaves pressure ($p$) and dilution as the main factors. Case B peak pressures were about 10 bar higher and the burned gas fraction decreased by about 5%. The lower dilution and higher pressure both resulted in faster chemistry and higher $\beta$. (Note that although pressure also appears in the denominator, the dependence is stronger in the numerator— usually squared assuming the rate-limiting reactions are bi-molecular). Hence the knock limit occurred at a lower equivalence ratio in this case ($\beta$=1 corresponded to $\phi\approx0.6$ for Case B and $\phi\approx0.65$ for Case A). Therefore although the brake torque for a given $\phi$ was higher in Case B (due to higher fuel concentration), the critical $\phi$ for the onset of knock had decreased. The net effect was that the knock-limited torque output was shifted up

only slightly. Figure 3.10 also shows the peak pressures were about 85-90 bar at the knock limit. Therefore, Case B is less attractive than Case A because for this configuration mechanical strength of the engine would be a concern, and the gain in additional torque is minimal.

**Figure 3.9.** Optimum operating conditions (Case B): Naturally-aspirated, PRF-fueled engine with increased compression ratio ($r_c = 17.0$)
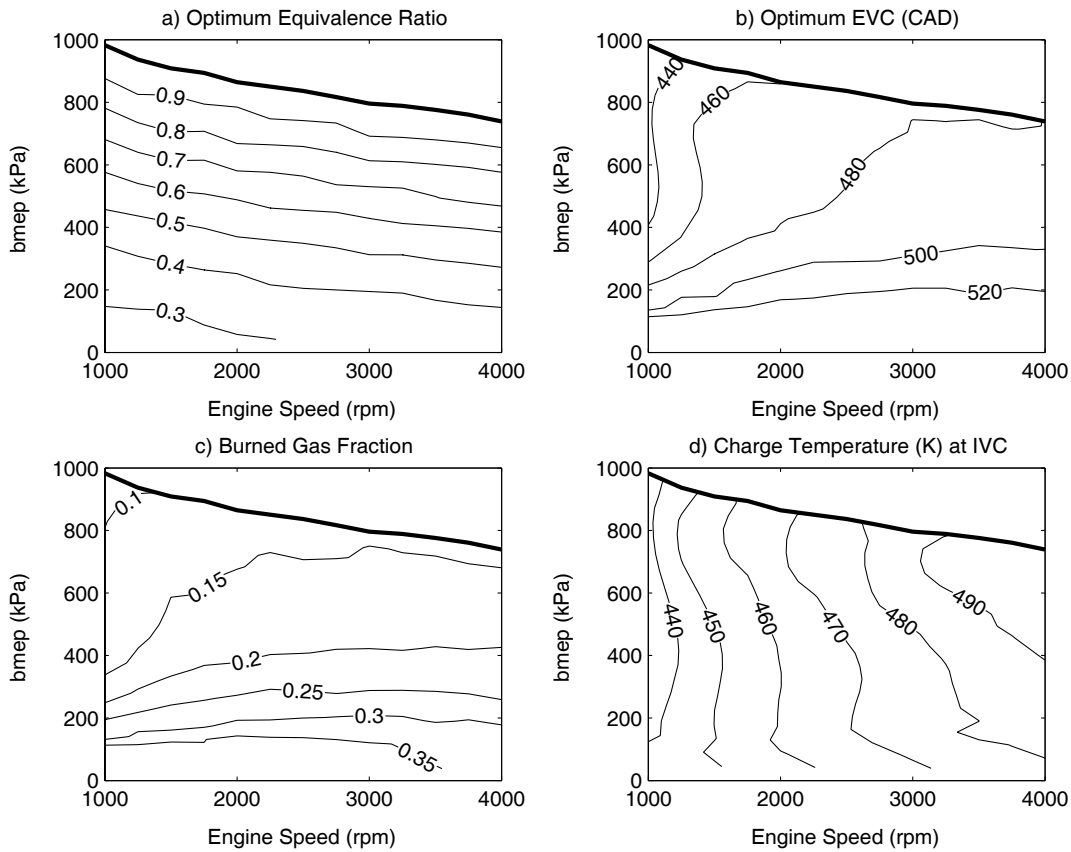
**Figure 3.10.** Performance characteristics (Case B): Naturally-aspirated, PRF-fueled engine with increased compression ratio ($r_c$ = 17.0). The knock limit ($\beta$=1) is shown as a dashed line.
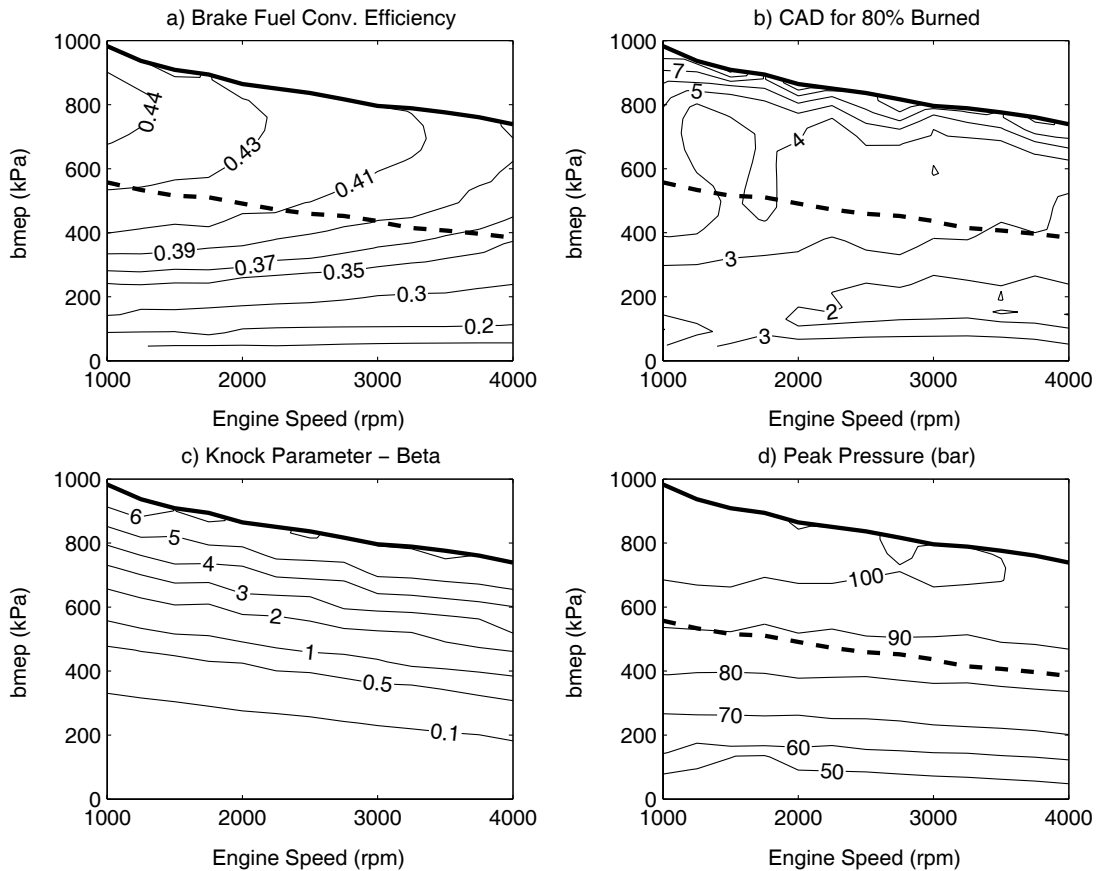


### 3.3.3 Test Case C

Case C, which differed considerably from Cases A and B, examined the use of boost pressure to achieve higher engine torque. The benefits of boost pressure have been demonstrated by the experimental success of boosted HCCI engines [31]. Also a more reactive fuel (n-heptane) was used in an attempt to avoid the need for supplemental intake air heating. The inlet temperature to the cylinder for Case C (73°C) was calculated from the compression of ambient air to 0.5 bar boost pressure assuming a compressor efficiency of 75%. Supercharging and the colder intake temperature resulted in a denser

cylinder charge, hence more fuel per cycle for a given equivalence ratio than previous cases. A drawback of boosting was that a different valve timing strategy was necessary which resulted in significantly higher pumping losses (approximately 50 kPa reduction in bmep at low loads where late exhaust-valve-closing was needed). This penalty in pumping work might be avoided by using a "trapping" valve timing strategy as mentioned, or by fading out the boost pressure at low load and using the original "late IVC" strategy.

The contours in Figure 3.11 (Case C) look quite different from the previous cases. Most notably, the optimum EVC was a constant 375 cad (the lower bound of our search space) over much of the range. Because n-heptane is much more reactive than the PRF 92, no heating by residual exhaust gas was necessary at this compression ratio (even with no intake air heating). Effectively, n-heptane was overly successful in reducing the necessary inlet charge temperature and, as Figure 3.12b shows, the result is an early ignition time (-22 to -10 cad atc)[1]. At low values of bmep (below 300 kPa), there was an abrupt switch to late EVC and high levels of residual gas and a correspondingly high charge temperature at IVC. This switch occurred as ignition abruptly began to fail as equivalence ratio was decreased. This abrupt quenching of the combustion reactions at low equivalence ratios was also observed computationally by Dec [33] for $\phi<0.15$ and experimentally by Kaiser et al. [3] for $\phi<0.19$. The induction of more hot residual gas attempted to maintain a high combustion efficiency at the low load conditions. The change in EVC timing is more abrupt in this case than previous cases because the

---

[1] Note that the partial decoupling of the cycle simulations and PSR model discussed previously is still valid in this case even though ignition does not occur near top center—the residual fraction is very low (2-4%) over much of the map, so there is little communication between cycles and details of the combustion process have little effect on the charge conditions at IVC.

residual heating was not used to fine-tune the combustion timing (timing was too early even with minimum residuals) but instead to insure high combustion efficiency at extremely low equivalence ratios.

Even with the sub-optimal ignition timing, the results shown in Figure 3.12 are promising. The efficiency was quite high over a substantial operating range. Also the bmep for a given equivalence ratio was much higher (e.g. the stoichiometric line has shifted up considerably) because there was more fuel per cycle due to the denser charge and lower burned gas fraction. Most importantly the knock-limited bmep was approximately 10 bar, almost twice that of previous cases.

Again an analysis of the $\beta$ expression (Eq. 11) is useful for comparison with Case A. This case differed from that one by fuel type, intake temperature and pressure, and necessary residual fraction. Residual fraction was lower and pressure was higher, both of which should increase $\beta$. The intake temperature was lowered by 48°C (121 to 73 °C), which resulted in an end-of-compression temperature that was approximately 125°C lower. All of these factors, however, were overwhelmed by the effect of supercharging on $\phi$ and the combustion temperature for a given load. For example, at a bmep of 500 kPa and speed of 1500 rpm, the combustion temperature was 1800 K for Case C versus 2400 K for Case A. The 600 K decrease in combustion temperature dramatically reduced the heat-release rate and hence the tendency to knock was greatly reduced. The trapped charge was denser for Case C, which meant the peak combustion temperatures were lower because the same torque could be achieved with a leaner mixture ($\phi$ = 0.3 versus 0.6). The additional excess air for the leaner mixture added thermal mass to the system which resulted in lower combustion temperatures. The engine in Case C did not knock

until ϕ increased to the point where combustion temperatures were similar to those in Case A. The result was that similar equivalence ratios (ϕ = 0.6) were attainable in this case as in previous cases, but for this case the torque for a given ϕ was almost twice that in Case A.

One drawback of the Case C engine configuration is that the peak pressures were substantially higher (+50 bar) than Cases A. A stronger diesel-like engine would be necessary to accommodate these high pressures.

**Figure 3.11.** Optimum operating conditions (Case C): Supercharged (0.5 bar boost), n-heptane-fueled engine with baseline compression ratio ($r_c$ = 15.51)
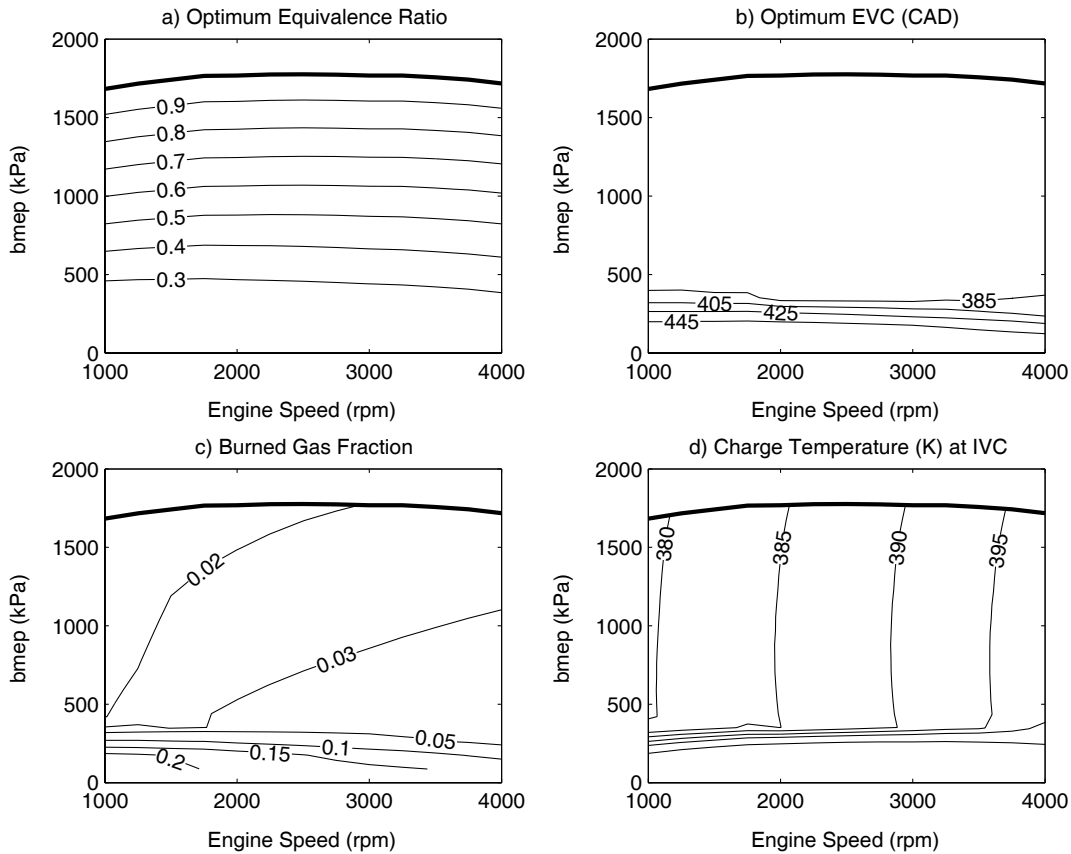
**Figure 3.12.** Performance Characteristics (Case C): Supercharged (0.5 bar boost), n-heptane-fueled engine with baseline compression ratio ($r_c$ = 15.51). The knock limit (β=1) is shown as a dashed line.
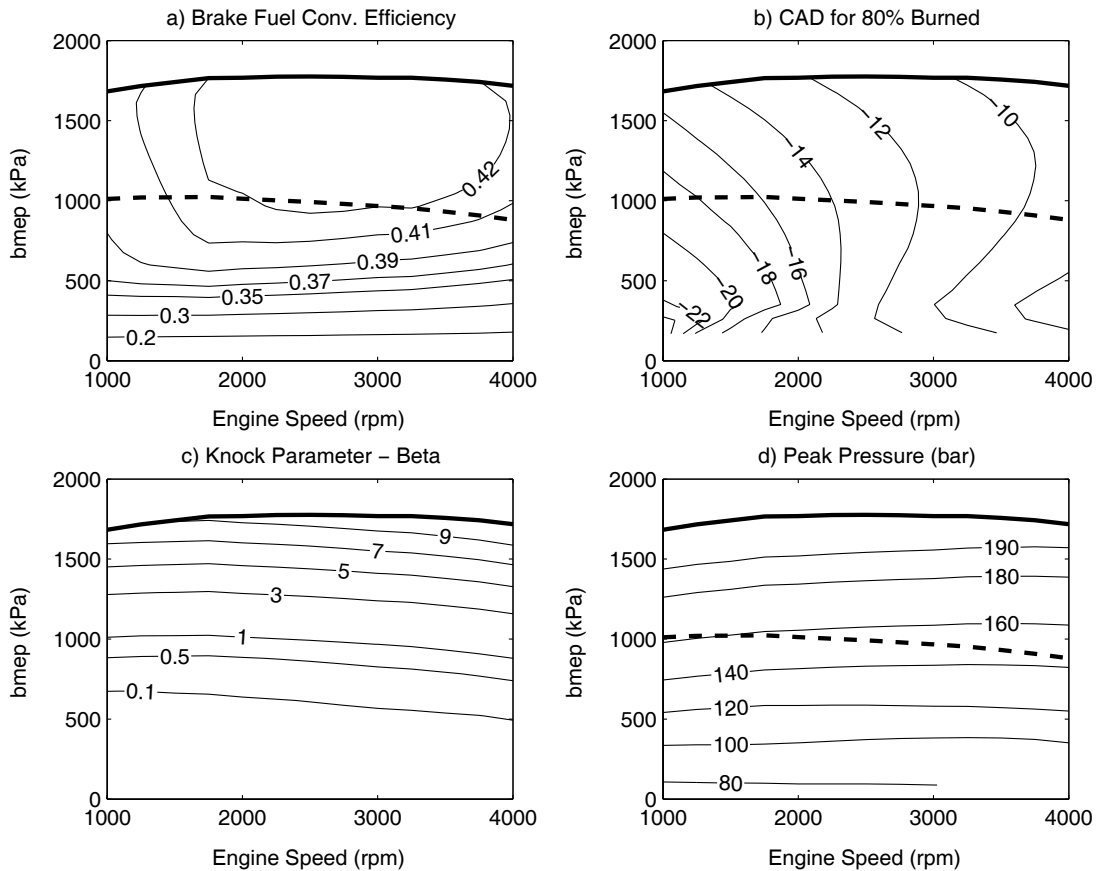


### 3.3.4 Test Case D

Finally, Case D was identical to Case C except that the compression ratio was lowered ($r_c$ = 12) in an attempt to achieve more ideal combustion timing. Figure 3.13 shows that the minimum residual heating was used over a smaller range and that the switch to later exhaust timing was more gradual than Case C. The knock-limited maximum torque was approximately 1 bar higher due to better combustion timing and lower cylinder pressure which decreases β as mentioned in the discussion of Case B. Combustion timing (Figure 3.14b) was improved by approximately 5 cad. Efficiency at lower speeds was increased due to improved timing despite the negative effects of lower

compression ratio on efficiency from a thermodynamic standpoint. Efficiency at higher speeds was decreased slightly.

By far the most noticeable effect was on the peak pressure, which decreased by about 40 bar from Case C. The lower peak pressure occurred despite the better timing because of a lower end-of-compression pressure. These lower pressures would require a lower mechanical strength for the engine and correspondingly lower engine weight (which is good for total vehicle efficiency). Also recall that the peak pressure was overestimated by about 10%. The calculated peak pressure at the knock limit was about 120 bar; thus 108 bar is a reasonable estimate for the real engine peak pressure. This peak pressure approaches that which can be withstood by a conventional gasoline (rather than diesel) engine.

**Figure 3.13.** Optimum operating conditions (Case D): Supercharged (0.5 bar boost), n-heptane-fueled engine with lowered compression ratio ($r_c = 12.0$)
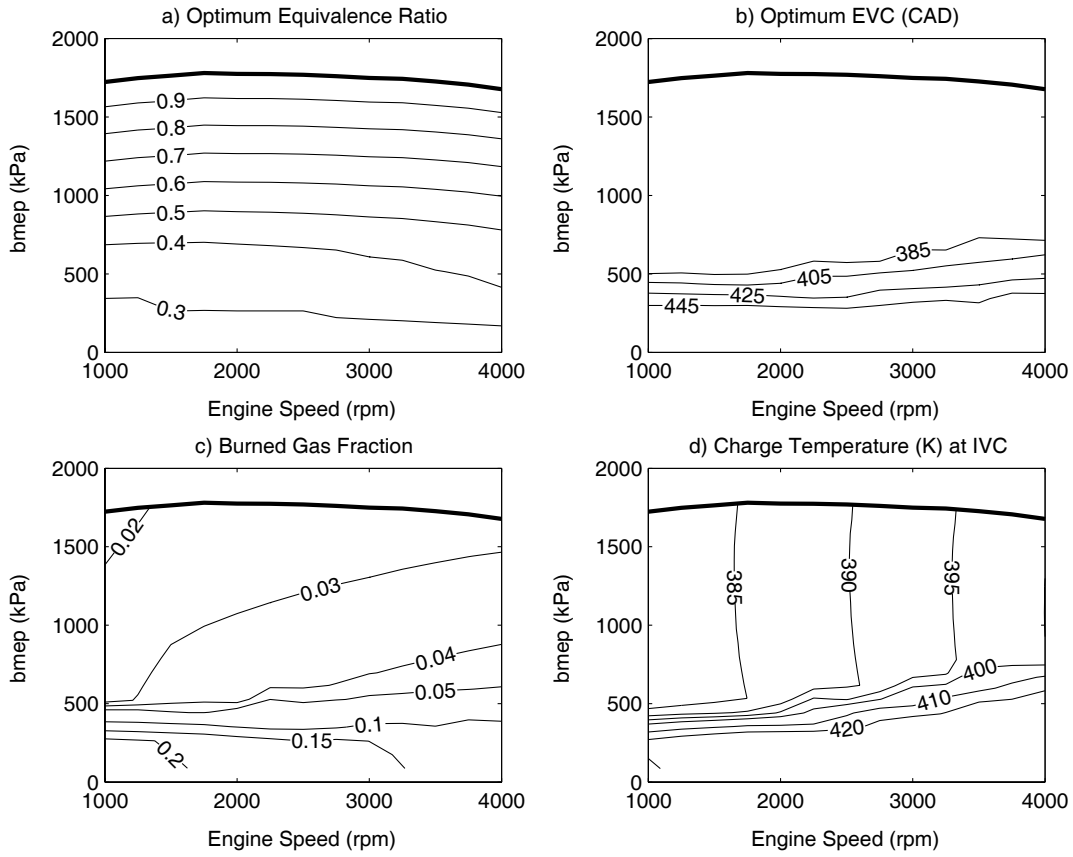
**Figure 3.14.** Performance characteristics (Case D): Supercharged (0.5 bar boost), n-heptane-fueled engine with lowered compression ratio ($r_c$ = 12.0). The knock limit ($\beta$=1) is shown as a dashed line.
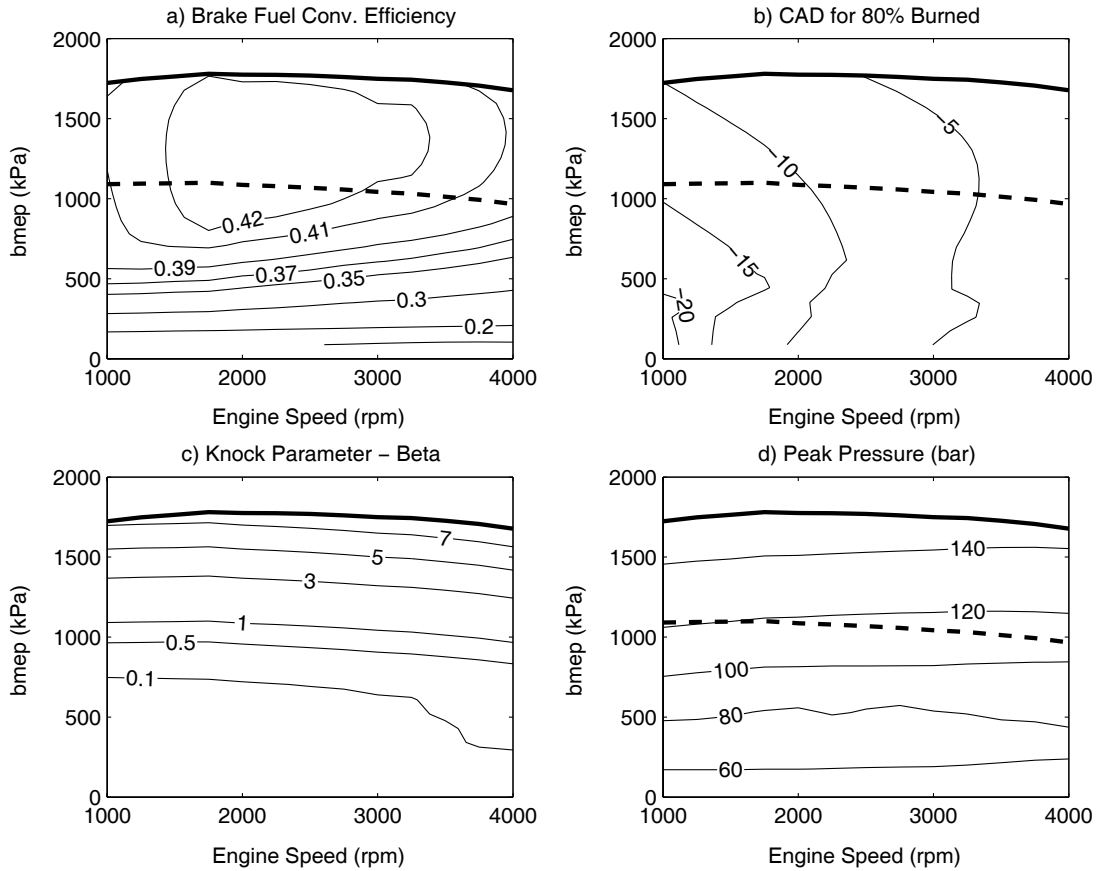


*Emissions of Oxides of Nitrogen ($NO_x$)*: The focus of this work has been to identify the region where HCCI combustion is viable (i.e. not knocking or misfiring) with no regard to emissions within the viable region. It is worth mentioning, however, whether emissions are prohibitively high anywhere in the viable operating region. A series of calculations was performed for Case D (the highest torque case) at 1500 rpm and $\phi$ ranging from 0.35 to 0.6 (knock limit). At the knock limit, the $NO_x$ emissions (taken as the sum of NO and $NO_2$) were 5300 ppmv. The $NO_x$ concentration quickly dropped off as equivalence ratio was decreased ($\phi$=0.45, 70 ppmv; $\phi$=0.35, <1 ppmv). The chemistry model used for these calculations was a combination of the n-heptane model of Curran et

al. [22] and the Leeds University $NO_x$ model [34]. Other $NO_x$ models were also tested, and all predictions agreed to within a factor of about two. As a comparison, the engine-out emissions from a spark-ignited engine are approximately 1000 ppmv [19]. Additionally, the current Tier 1 $NO_x$ standard in the U.S. is 0.6 g/mi averaged over a predetermined driving cycle. This standard corresponds to an average $NO_x$ concentration of 135 ppmv in the tailpipe assuming a fuel economy of 20 mi/gallon. Lean-burn engines have the disadvantage that three-way catalysts cannot be used to remove $NO_x$ from the exhaust. In order to meet this standard, the purely HCCI-powered vehicle could operate in the high-torque region for only a small fraction of the driving cycle. This standard provides a "soft" limit for maximum torque because some amount of time in the high-emissions, high-torque region of the performance map is acceptable. In contrast, the knock limit is a "hard" limit because knocking operation would probably never be tolerated in a production engine. Obviously both $NO_x$ and knock are important design considerations—we have focused here on operability and reserve more detailed emissions studies for future calculations.

## 3.4  Discussion

Table 3.3 summarizes the performance characteristics of the four engine configurations studied. Indicated are the important differences between engine cases: the maximum efficiency, the maximum attainable torque without knocking ($\beta < 1$), and the engine speed and peak pressure at that maximum torque. The large increase in attainable torque with Cases C and D compared with Cases A and B is striking. Supercharging is clearly an effective strategy for achieving higher torques from an HCCI engine; however, the engine must withstand higher peak pressures.

The maximum efficiency was similar among the four cases. Case B was more efficient than Case A because higher compression ratios are favorable thermodynamically; however, higher peak pressure makes Case B the less attractive option. The efficiency of Case C was similar to D because the improvement of combustion timing in Case D was offset by the negative impact of lowering the compression ratio. Peak pressure for Case D was considerably lower than Case C due to lower end-of-compression pressure (lower $r_c$). Normal-heptane, an easily-ignitable fuel, lent itself naturally to HCCI because supplemental intake air heating was unnecessary, and lower compression ratios could be used which resulted in lower peak pressures.

Supercharged engines showed less tendency to knock because the equivalence ratio needed to achieve a given load was lower. Lower equivalence ratios resulted in lower combustion temperatures because there was more excess air in the cylinder (additional thermal mass). Because reaction rates are exponentially dependent on temperature, lower combustion temperatures produce dramatically lower heat-release rates. The $\beta$ knock model shows that lower heat-release rates make local overpressures (and associated "knocking") less likely to occur. For the cases studied, the knock limit corresponded to a critical $\phi \approx 0.6$. Any design changes which will lower combustion temperatures will be beneficial for avoiding HCCI engine knock (as well as reducing $NO_x$ emissions). Note that supercharging often makes SI engines more prone to knock because SI engine knock is controlled by ignition delay in the end-gas; whereas, HCCI knock is controlled by the heat-release rate of the combustible mixture.

With modest boost pressures, the observed maximum mean effective pressure was comparable to the best values reported experimentally by Olsson et al. [31] and

Christensen et al. [35]. The maximum torque demonstrated in these calculations is acceptably high for an automotive application over the range of engine speed studied. Only a moderate effort has been made to optimize the engine, and further optimization is certainly possible. As a final caveat, both the simulations and the limited available experimental data show that HCCI ignition timing is quite sensitive to heat transfer and fuel chemistry—the latter with much poorer mechanistic understanding. For these reasons, it is unlikely that the current simulations are quantitatively as accurate as precise experimental measurements. However, the good agreement between the simulations and the experimental data suggests that the simulation predictions are accurate enough to guide experimental research in this area.

**Table 3.3.** Summary of performance characteristics for Cases A, B, C, and D

| | | | | | | Maximum torque (knock-limited) | | |
|------|-----------|-----------|---------------------------|---------------------|--------------------|---------------|----------------|----------------------------|
| Case | Fuel | $r_c$ | Boost Pressure, bar | Inlet air temp., °C | Max. $\eta_{f,b}$ | bmep, kPa | Speed, rpm | Peak pressure, bar |
| A | PRF 92 | 15.51 | none | 121 | 0.428 | 520 | 1000 | 80 |
| B | PRF 92 | 17.0 | none | 121 | 0.443 | 560 | 1000 | 91 |
| C | n-heptane | 15.51 | 0.5 | 73 | 0.428 | 1020 | 1750 | 158 |
| D | n-heptane | 12.0 | 0.5 | 73 | 0.426 | 1100 | 1750 | 119 |

$\eta_{f,b}$ = brake fuel conversion efficiency, $r_c$ = compression ratio, PRF = primary reference fuel

## 3.5 Conclusions and Design Recommendations

- Cycle simulations and perfectly-stirred reactor models can be used to construct performance maps for HCCI engine designs and evaluate performance over the range of operating conditions seen in regulatory drive cycles.

- A dimensionless knock parameter and PSR model can be used to predict the onset of HCCI knock and hence the maximum attainable torque. The predictions of the knock parameter, β, from the perfectly-stirred reactor model are in good

91

agreement with the multi-zone model, which has been shown previously to accurately predict knock in experimental engines.

- For detailed chemistry models, computational time can be reduced by a factor of 10 or more by exploiting sparsity in the model equations for a perfectly-stirred reactor.

- Numerical simulations of HCCI engines are quite sensitive to the heat-transfer model and chemistry model. Accurate heat-transfer measurements and good chemical kinetics are necessary to achieve quantitative accuracy from the simulations.

- Variable-valve timing is an effective control strategy for controlling combustion timing over the range of engine speed and engine load necessary for automotive applications.

- Due to its low ignition temperature, n-heptane is an attractive fuel for HCCI because supplemental intake air heating would not be necessary even for modest compression ratios. Use of lower compression ratios leads to dramatically lower peak pressures.

- Supercharging can be used to achieve higher torques from an HCCI engine because the $\phi$ and combustion temperature are lower than a naturally-aspirated engine at the same load. Lower combustion temperatures result in lower heat-release rates and hence a decrease in the tendency of the engine to "knock".

## 3.6 Nomenclature

| | | | |
|---|---|---|---|
| $\beta$ | dimensionless knock parameter | $m_c$ | mass of trapped charge |
| $\gamma$ | ratio of specific heats | $n_{intake}$ | moles of intake air |
| $\eta_{f,b}$ | brake fuel conversion efficiency | $p$ | pressure |
| $\eta_{sc}$ | supercharger efficiency | $\dot{q}$ | chemical heat-release rate |
| $\theta$ | crank angle | $\dot{q}_{loss}$ | rate of heat loss from cylinder |
| $\xi_b$ | extent of combustion | $r_c$ | compression ratio |
| $\phi$ | fuel/air equivalence ratio | $R$ | universal gas constant |
| $\dot{\omega}_k$ | molar rate of production of species $k$ | $\overline{S}_p$ | mean piston speed |
| EVO | exhaust valve opening | $t$ | time |
| EVC | exhaust valve closing | $T$ | temperature |
| IVO | intake valve opening | $u_k$ | internal energy of species $k$ |
| IVC | intake valve closing | $u_{sound}$ | speed of sound |
| PRF | primary reference fuel | $v$ | specific volume |
| atc | after top center | $V_{cyl}$ | cylinder volume |
| cad | crank angle (degrees) | $V_d$ | displaced volume |
| mep | mean effective pressure (work per cycle per unit displaced volume) | $w$ | average gas velocity |
| $imep_n$ | net indicated mep | $W_k$ | molecular weight of species $k$ |
| bmep | brake mep | $\overline{W}$ | average molecular weight |
| amep | auxiliary friction mep | $W_{c,in}$ | net indicated work per cycle |
| rfmep | rubbing friction mep | $W_{c,b}$ | brake work per cycle |
| $a, m$ | Parameters for Wiebe function | $W_{sc}$ | supercharger work |
| $A$ | area | $x_b$ | burned gas fraction |
| $B$ | bore (diameter of cylinder) | $Y_k$ | mass fraction of species $k$ |
| $C_v$ | constant volume heat capacity | subscripts | |
| $h_c$ | heat transfer coefficient | $ch$ | cylinder head |
| $L_c$ | characteristic length | $l$ | cylinder liner |
| | | $p$ | piston |

## 3.7 References

1.      Aoyama, T., et al., *An Experimental Study on Premixed-Charge Compression Ignition Gasoline Engines.* SAE Technical Paper, 1996(960081).
2.      Flowers, D., et al., *HCCI in a CFR Engine: Experiments and Detailed Kinetic Modeling.* SAE Technical Paper, 2000(2000-01-0328).
3.      Kaiser, E.W., et al., *Homogeneous charge compression ignition engine-out emissions--does flame propagation occur in homogeneous charge compression ignition?* International Journal of Engine Research, 2002. **3**(4): p. 185-195.
4.      Thring, R.H., *Homogeneous-Charge Compression-Ignition (HCCI) Engines.* SAE Technical Paper, 1989(892068).
5.      Oakley, A., H. Zhao, and N. Ladommatos, *Experimental Studies on Controlled Auto-ignition (CAI) Combustion of Gasoline in a 4-Stroke Engine.* SAE Technical Paper, 2001(2001-01-1030).
6.      Oakley, A., H. Zhao, and N. Ladommatos, *Dilution Effects on the Controlled Auto-Ignition (CAI) Combustion of Hydrocarbon and Alcohol Fuels.* SAE Technical Paper, 2001(2001-01-3606).
7.      Yang, J., T. Culp, and T. Kenney, *Development of a Gasoline Engine System Using HCCI Technology--The Concept and the Test Results.* SAE Technical Paper, 2002(2002-01-2832).
8.      Zhao, H., et al., *Performance and Analysis of a 4-Stroke Multi-Cylinder Gasoline Engine with CAI Combustion.* SAE Technical Paper, 2002(2002-01-0420).
9.      Hyvönen, J., G. Haraldsson, and B. Johansson, *Operating range in a Multi Cylinder HCCI engine using Variable Compression Ratio.* SAE Technical Paper, 2003(2003-01-1829).
10.     Martinez-Frias, J., et al., *Equivalence Ratio-EGR Control of HCCI Engine Operation and the Potential for Transition to Spark-Ignited Operation.* SAE Technical Paper, 2001(2001-01-3613).
11.     Yelvington, P.E. and W.H. Green, *Prediction of the Knock Limit and Viable Operating Range for a Homogeneous-Charge Compression-Ignition (HCCI) Engine.* SAE Technical Paper, 2003(2003-01-1092).
12.     Kaahaaina, N., et al., *Use of Dynamic Valving to Achieve Residual-Affected Combustion.* SAE Technical Paper, 2001(2001-01-0549).
13.     Duret, P. and J. Lavy, *Process for controlling self-ignition in a 4-stroke engine, US Patent 6,082,342.* 2000.
14.     Fiveland, S.B. and D.N. Assanis, *Development of a Two-Zone HCCI Combustion Model Accounting for Boundary Layer Effects.* SAE Technical Paper, 2001(2001-01-1028).
15.     Aceves, S.M., et al., *A Multi-Zone Model for the Prediction of HCCI Combustion and Emissions.* SAE Technical Paper, 2000(2000-01-0327).
16.     Kong, S.-C., et al., *Modeling and Experiments of HCCI Engine Combustion Using Detailed Chemical Kinetics with Multidimensional CFD.* SAE Technical Paper, 2001(2001-01-1026).
17.     Meintjes, K., *A User's Guide for the GM Engine-Simulation Program.* 1987, General Motors Research Laboratories: Warren, MI.

18.     Woschni, G., *Universally Applicable Equation for the Instantaneous Heat Transfer Coefficient in the Internal Combustion Engine.* SAE Technical Paper, 1967(670931).

19.     Heywood, J.B., *Internal Combustion Engine Fundamentals.* 1988, New York: McGraw-Hill, Inc. pp. 100-107.

20.     Erlandsson, O., et al., *Simulation of HCCI--Addressing Compression Ratio and Turbo Charging.* SAE Technical Paper, 2002(2002-01-2862).

21.     Aceves, S.M., et al., *A Sequential Fluid-Mechanic Chemical-Kinetic Model of Propane HCCI Combustion.* SAE Technical Paper, 2001(2001-01-1027).

22.     Curran, H.J., et al., *A Comprehensive Modeling Study of n-Heptane Oxidation.* Combustion and Flame, 1998. **114**: p. 149-177.

23.     Curran, H.J., et al., *A Comprehensive Modeling Study of iso-Octane Oxidation.* Combustion and Flame, 2002. **129**: p. 253-280.

24.     Kee, R.J., et al., *CHEMKIN III: A FORTRAN Chemical Kinetics Package for the analysis of gas-phase chemical and plasma kinetics.* 1996, Sandia National Laboratories: Livermore, CA.

25.     Schwer, D.A., et al., *On Upgrading the Numerics in Combustion Chemistry Codes.* Combustion and Flame, 2002. **128**(3): p. 270-291.

26.     Tolsma, J.E. and P.I. Barton, *DAEPACK: An open modeling environment for legacy codes.* Ind. Eng. Chem. Res., 2000. **39**(6): p. 1826-1839.

27.     Barton, P.I., *DAEPACK webpage, http://yoric.mit.edu/daepack/daepack.html.*

28.     Barton, P.I., R.J. Allgor, and W.F. Feehery, *DSL48S: A Large-Scale Differential-Algebraic and Parametric Sensitivity Solver.* 1997, Massachusetts Institute of Technology, Department of Chemical Engineering: Cambridge, MA.

29.     Sandoval, D. and J.B. Heywood, *An Improved Friction Model for Spark-Ignition Engines.* SAE Technical Paper, 2003(2003-01-0725).

30.     Patton, K.J., R.G. Nitschke, and J.B. Heywood, *Development and Evaluation of a Friction Model for Spark-Ignition Engines.* SAE Technical Paper, 1989(890836).

31.     Olsson, J.-O., et al., *The Effect of Cooled EGR on Emissions and Performance of a Turbocharged HCCI Engine.* SAE Technical Paper, 2003(2003-01-0743).

32.     Amsden, A., *KIVA-3V: A Block-Structured KIVA Program for Engines with Vertical or Canted Valves.* 1997, Los Alamos National Laboratory: Los Alamos, NM.

33.     Dec, J.E., *A Computational Study of the Effects of Low Fuel Loading and EGR on Heat Release Rates and Combustion Limits in HCCI Engines.* SAE Technical Paper, 2002(2002-01-1309).

34.     Hughes, K., et al., *An Investigation of Important Gas Phase Reactions of Nitrogen Species from the Simulation of Bulk Experimental Data in Combustion Systems.* Combustion and Flame, 2001. **124**: p. 573-589.

35.     Christensen, M., et al., *Supercharged Homogeneous Charge Compression Ignition.* SAE Technical Paper, 1998(980787).

# Chapter 4: The Relationship of Knock to Gaseous Detonations in HCCI and SI Engines

## 4.1 Introduction

Engine knock poses a serious limitation to both homogeneous-charge compression-ignition (HCCI) and spark-ignited (SI) engines. As shown in previous chapters, the maximum energy density of an HCCI engine is limited by the onset of knock. In SI engines, knock limits the maximum compression ratio that can be used, which in turn limits the maximum efficiency of the engine. Knock is defined here as the development of non-uniform cylinder pressures. Knock can be observed as an oscillation in the measured pressure trace with a frequency approximately equal to the resonant acoustic frequency of the combustion chamber. Also, knock can often be audibly detected as a pinging noise coming from the engine. In addition to the aesthetic concerns about noisy engine operating, knock can cause pitting and other structural damage to pistons and cylinder liners [1].

Because of the importance of engine knock to automotive manufacturers, many studies (mostly of SI engine knock) have been performed. These studies include optical engine experiments, computational fluid dynamics calculations, and theoretical studies. In addition, engine knock has been the motivation for much kinetic model building, shock tube experiments, rapid-compression machine studies, and theoretical and computational studies of gaseous detonations. Despite the volume of research that has been done concerning knock, no consensus exists as to the mechanism responsible for the formation of non-uniform pressures in engines. Two main theories exist, the autoignition theory and the detonation theory. The autoignition theory claims that non-uniform cylinder pressures arise in engines because when certain parcels of fuel/air mixture burn, those parcels convert their chemical energy to thermal energy at a rate faster than the rate

at which mechanical equilibrium can be maintained (which is proportional to the sound speed). When the heat-release process is extremely rapid, local overpressures form.Autoignition theory provides the basis for the β parameter used to predict knock in previous chapters.

The detonation theory claims that locally high cylinder pressures arise due to the formation of gaseous detonations in the engine initiated at hot-spots in the end-gas. A recent paper [2] has also suggested that formation of detonation waves at hot-spots is also responsible for knock in HCCI engines. To my knowledge no conclusive experimental evidence suggesting the presence of detonation waves in engines has ever been observed. However many numerical simulations have been performed which show detonation formation under engine conditions. Unfortunately, many of the calculations showing the formation of detonations in relation to engines employ some assumptions that have questionable validity. These assumptions are described in more detail in the next section. The goal of this work is to design and execute a set of reacting flow simulations to determine whether detonations are really a likely cause for knock in SI and HCCI engines.

Due to the somewhat confusing terminology associated with knock in engines, a few common terms are defined below.

*hot-spot* (also called an *autoignition center* or an *exothermic center*) – a region of locally-high reactivity due to local high temperatures. Hot-spots can occur in engines due to imperfect mixing of residual exhaust gas with the fresh cylinder charge. Figure 4.1 shows diagrammatically how hot-spots form in HCCI and SI engines.

*end*-gas – the region of unburned gas ahead of the turbulent flame front in spark-ignited engine. High-speed photographic data have shown that this is where knock originates in SI engines.

*excitation time* – the timescale for the heat-release event following autoignition of a premixed combustible mixture. The excitation time is usually much shorter O(1 μs) than the ignition time O(1 ms) that comes beforehand.

*deflagration* – heat and radicals diffuse into unburned gases inducing ignition. This ordinary type of flame propagates at subsonic speed, O(1-10 m/s), at engine conditions. Because the burned gases have a much lower density than the unburned gases, the burned gas compresses the unburned mixture. So the interface between the burned gases and unburned gases is usually moving at an apparent speed higher than that due solely to flame propagation, O(100 m/s).

*detonation* – strong shock wave compressively heats the unburned mixture so strongly that it ignites in phase with and so contributes to the shock. These shock waves travel at supersonic speeds, typically several times the speed of sound, O(1000 m/s). Note that the presence of a shock wave *does not* imply that a detonation is taking place. As discussed below and in Chapter 2, shock waves can be produced by spontaneous ignition. Only in the case that the shock wave is amplified by and in phase with the chemistry is it a detonation. Because of this amplification/coherence, the shock waves in detonations can achieve extremely high peak pressures (several hundred bar) that would cause serious mechanical damage to an engine.

*thermal explosion* (also called an *induction wave*) – different parcels of gas ignite spontaneously, without being induced by the heat/radicals/shock wave in an adjacent

parcel. If there is a continuous gradient (e.g. of temperature) in the mixture, then the spontaneous ignition times of each parcel will be slightly different, and as they each ignite at different times the combustion will appear to propagate across the system (even though each parcel has no significant effect on its neighbors). This mode of combustion depends on the gradient of ignition delay, and can propagate at an arbitrarily fast apparent speed.

**Figure 4.1:** Schematic of the combustion process in a) an HCCI engine and b) SI engine. The HCCI schematics are based on the direct imaging of the HCCI combustion process conducted in a *n*-heptane-fueled test engine at 600 rpm [3]. The SI schematics are based on high-speed schlieren photographs of an PRF80-fueled engine at 1100 rpm experiencing weak knock [4]. (white areas, burned gas; black areas, unburned gas; x, spark plug location; arrow, direction of swirl)
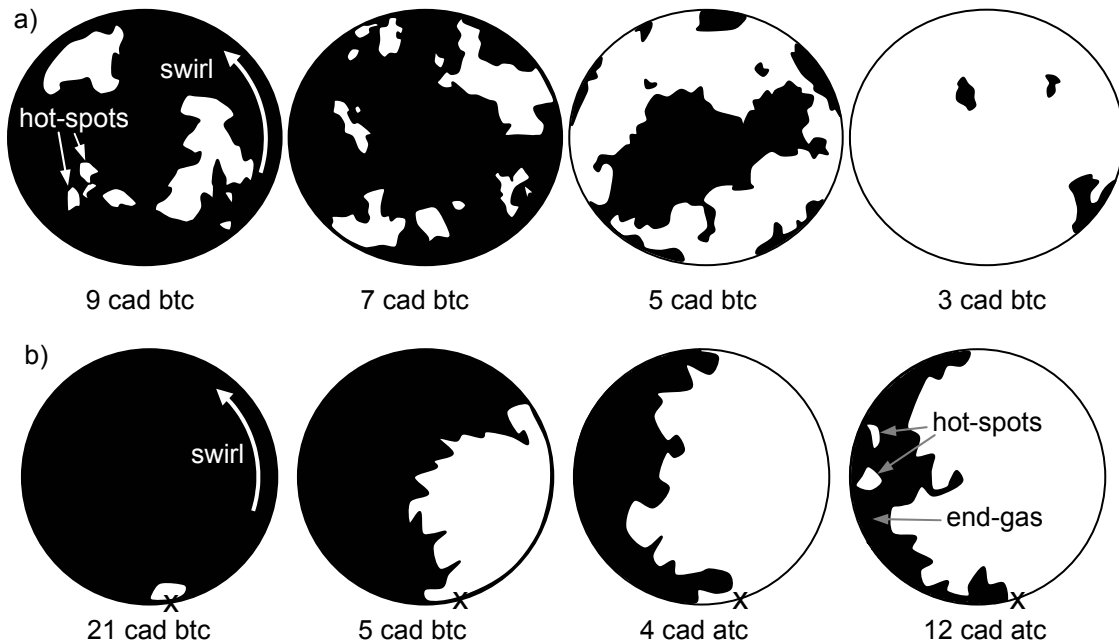


## 4.2  Previous Studies of Knock and Detonation

### 4.2.1  Experimental Investigations of Knock

Knock in spark-ignited engines has been the study of many experimental investigations. Since use of high-speed cameras became prevalent in the 1930s and 40s,

many of these studies have included high-speed natural light or schlieren cinematography in optically-accessible engines. The schlieren technique records regions in the engine where large gradients in density are present and so clearly shows the passage of flames and even shock waves if the framing rate is sufficiently fast. One of the first high-speed photographic studies of SI engine knock (and to this day probably the most extensive) was made by Miller in the early 1940s [5]. Miller used a single-cylinder test engine run at 500 rpm and fueled by a mixture of M-1 and S-2 reference fuels. Most of his schlieren pictures were taken at 40,000 frames per second (fps) except for one series which was taken at 200,000 fps.

Miller argues, based on a review of literature data and his own photographic studies, that knock is caused by regions of the end-gas that autoignite and subsequently initiate detonation waves. (Miller points out that "Though many writers refer to knock as "detonation," they do not mean to imply that they believe knock is caused by a detonation wave.") Miller concludes that detonation waves are responsible for the strong overpressures characteristic of knock based on several arguments. His first argument is that simple end-gas autoignition is not fast enough relative to the acoustic velocity to cause the formation of local overpressures. Miller reports that a literature review indicates that the excitation time (i.e. the timescale for combustion) is an order of magnitude longer than the time for the "explosive knock reaction" he observed by high-speed photography (which he estimates to be 50 $\mu$s). However, recent rapid-compression machine data from Tanaka et al.[6] suggest that excitation times (defined as the time between 20% and 80% of the energy release as manifested by the pressure rise in the vessel) are, for example, 90 $\mu$s (iso-octane, $\phi = 0.5$) and 49 $\mu$s (*n*-heptane, $\phi = 0.5$).

Excitation times are expected to be even shorter for stoichiometric fuel/air mixtures, and this is supported by the detailed chemistry calculations of Lutz et al. [7]. This argument by Miller seems somewhat questionable in light of more recent excitation time data.

Miller's second argument was that autoignition is too slow to produce local overpressures and the associated "gas vibrations" [pressure oscillations] observed during knocking, but this argument is essentially the same as the first. Calculations by many researchers (e.g. Lutz et al. [7], Pan et al. [8], Weber, Mack and Roth [9]) have shown, using numerical simulations of hot-spot ignition, that autoignition is sufficiently fast to cause local overpressures.

Miller's final argument, based on his own photographic studies of engine knock, was that during knock a combustion wave traverses the end-gas at a speed of up to 6500 ft/s (2000 m/s), which agrees with experimentally measured detonation velocities in long tubes. However, many authors (e.g. [10]) have shown that induction waves (i.e. an apparent wave caused by the autoignition of neighboring parcels of gas at nearly the same instant) can travel at an arbitrarily fast apparent wave speed. Therefore is seems that there is at least the possibility of another explanation for the very high combustion wave speeds observed in the photographs. Furthermore there is a considerable amount of subjectivity that goes into determining the wave speeds from the photographs. These wave speeds are estimated to be accurate to only within a factor of two, in accord with the findings of Male [11].

In 1949, soon after Miller's study, Male [11] photographed a two-stroke, *n*-heptane-fueled engine operated at 600 rpm. Male took images both high-speed (40,000 fps) and ultra-high-speed (500,000 fps). While filming at 500,000 fps, he writes

that he observed three waves (which he refers to as detonation waves) originating in the end-gas and traversing the engine cylinder. Male determined that the three waves traveled at approximately 4200, 4900 and 5500 feet/sec with an estimated error of 50%. We believe however that it is unclear whether the observed waves were detonation waves or strong shock waves originating from an extremely rapid heat release event following autoignition of the end gas. We have performed cycle simulations of Male's engine based on the engine parameters and operating conditions presented in his paper [11] and our own estimation of the enflamed volume fraction (~70%) at the point of end-gas autoignition. These calculations predict an end-gas temperature and pressure of roughly 900 K and 30 bar, respectively, at the point where knock begins. Assuming that 1) end-gas autoignition leads to a heat-release event that is sufficiently fast that is occurs at essentially constant-volume and 2) the burned gas is sufficiently hot that the combustion products are in chemical equilibrium, we estimate the maximum possible local pressure (in the absence of detonation) to be 100 bar in the end-gas. The propagation speed of a shock with this strength ($P_2/P_1$ = 3.3) would be $M_{shock}$ = 1.8 based on the ideal normal shock relations with $\gamma$ = 1.2. Assuming the gas ahead of the shock is nearly stationary, the observed shock velocity in the burned gas ($c_{sound}$ = 980 m/s) would be 1700 m/s (5600 ft/s). Thus waves propagating at the speeds observed by Male could be explained by phenomena other than the formation of a gaseous detonation.

Over 35 years after Male's experiments, Hayashi et al. [12] from Toyota Central Research photographed knock in a rapid compression/expansion machine at an equivalent engine speed of 1200 rpm using stoichiometric *n*-butane/air mixtures. They also observed the formation of a strong shock wave originating in the end-gas at a framing rate of

100,000 frames per second. Hayashi and his coworkers determine the speed of the propagating wave (which they refer to as a shock wave, not a detonation wave) to be between 1320 and 1700 m/s depending on the method that was used to determine wave speed and the particular frames that are examined. As shown in the above analysis of Male's data, a constant-volume end-gas explosion can cause a shock wave that propagates sufficiently fast to explain observed wave speeds in this range.

During the 1990s a series of papers [4, 8, 13, 14] describing optical engine studies of SI knock was published by a group of researchers from Daimler-Benz AG and the University of Leeds. The works of Konig et al. [13] and Konig and Bradley [4] used schlieren and natural light photography to study knock in a two-stroke Yamaha motorcycle engine modified for optical access running at 1400 rpm and using a PRF80 fuel. Those researchers observed many knocking cycles of various severities; however, their framing rate (10,000 fps) was inadequate to observe supersonic waves arising from shocks or detonations. Instead they cited the earlier works of Miller [5], Male [11], and Hayashi et al. [12] as evidence that developing detonations are responsible for the most severe knock observed in engines. Interestingly Konig and Sheppard [4] show that a plot of knock intensity versus end-gas temperature is nearly linear on a log scale. This suggests that knock intensity, which is a metric of the magnitude of pressure oscillations, has an exponential dependence on temperature. One would expect an exponential temperature dependence based on the autoignition theory (overpressures depend on the Arrhenius kinetics of the heat-release) but not from the detonation theory (overpressures depend solely on the thermodynamic state of the unburned mixture).

Studies by Pan and Sheppard [14] and Pan et al. [8] in the late 1990s studied knock in a two-stroke, modified JLO test engine running 1500 rpm and fueled by a 90 RON PRF. High-speed cinematography was also used in this study with a framing rate of 8,000 frames per second (again too slow to visualize supersonic waves). In some experiments, finely ground black pepper was injected into the cylinder to allow estimation of fluid velocities by particle tracking in the natural light images. Additionally pressure was recorded from four equally-spaced pressure transducers arranged around the cylinder circumference. Measurements from a severely knocking cycle showed that pressure oscillations reaching as high as 150 bar compared to the average pressure of 50 bar (pressure ratio ~3). Again, as shown in the analysis of Male's data pressure ratios in this range occur with constant volume explosions. Particle tracking shows fluid velocities in the burned gas of up to 520 m/s, which is subsonic (again the acoustic velocity in the burned gas is ca. 900-1000 m/s). Again both observations are explainable by the autoignition theory as well as the detonation theory. The researchers from Daimler-Benz and Leeds University have been major proponents of the detonation theory of knock, but their evidence for the presence of developing detonations during severely knocking cycles comes from numerical simulations rather than experimental observation.

In 1984, Green and Smith [15] and Smith et al. [16] studied engine knock in a low compression ratio engine run at 600 rpm with $n$-butane and iso-butane used as the fuels. Their test engine used four spark plugs arranged around the perimeter of the cylinder to produce an end-gas region that is located in the center of the engine. Green and Smith reported that their schlieren photography system had demonstrated sufficient sensitivity to discern shock waves. However, neither shock waves nor detonation fronts were

observed during knocking cycles in their experiments, leading them to concluded that detonations were not a necessary condition for knock.

## 4.2.2  Numerical Simulations of Engine Knock

Numerical simulation of knock in spark-ignited engines have been carried out by a number of authors [8-10, 13, 14, 17-20]. The first detailed simulation was by Zel'dovich et al. [10], who numerically solved the reactive Euler equations for a premixed fuel/air mixture exposed to linear gradient in temperature. Zel'dovich and coworkers noticed that after ignition of the hotter gas a combustion wave propagated into the colder mixture by one of three mechanisms; 1) deflagration, 2) detonation, and 3) thermal explosion. They also noticed that the deflagration mode occurred for large temperature gradients, the detonation mode for moderate temperature gradients, and the thermal explosion mode for small temperature gradients.

Based on his pioneering calculations, Zel'dovich made a strong claim that gaseous detonation waves were responsible for engine knock. These calculations, however, used a planar geometry, one-step chemistry model, and unrealistic end-gas conditions—all assumptions which need to be evaluated as to their appropriateness. Similar one-dimensional calculations were performed by Goyal and coworkers [18, 19] using detailed chemistry for hydrogen/oxygen and methane/air mixtures. Gu, Emerson and Bradley [20] studied ignition and propagation of spherical hot-spots with detailed chemistry for $H_2$/air and $H_2$/CO/air mixtures; however, the effects of curvature were only mentioned in a few words. The Gu et al. study observed detonation formation from hot-spots even for fairly small hot-spots (6 mm diameter) where curvature should be very important. This observation could be caused by the high reactivity of the $H_2$/CO/air

mixtures and high temperatures (1000 K in gas surrounding hot-spot) used in their simulations. Konig et al. [13] performed one-dimensional calculations using one-step chemistry and planar coordinates. Their calculations were slightly different in that a portion of the domain was assumed to be already burned to simulate the presence of burned gas adjacent to the unburned end-gas in the engine.

Konig et al. [13], Pan and Sheppard [14] and Pan et al. [8] also performed two-dimensional simulations of engine knock. The earlier works were largely supplanted by the work of Pan et al. [8] which used a more accurate adaptive grid and triangular mesh. To give an idea of the importance of the numerical technique, the most recent work by Pan and coworkers repeated some of the calculations done with the program used in previous papers—the result was that the case resulting in detonation with the older code no longer resulted in detonation with the newer code [8]. These two-dimensional calculations assumed that fluid motion was limited in the $z$-direction by the cylinder head and piston. This assumption may be accurate for the engine used in their experiments and simulations, which had an unusually narrow squish, but in general three-dimensional gas motion is important. The calculations used a one-step chemistry model and neglected viscous terms. These calculations were able to show the three modes of combustion wave propagation described above, however, the observation of detonation waves could have been an artifact of the calculations. Some notable possible sources of error are neglect of viscous terms, use of one-step chemistry, the use of unrealistic initial conditions and the two-dimensional assumption. The initial hot-spot shape used was a linear "tent" shape with a peak temperature of 1000 K and a surrounding temperature of 600 K. That difference in temperature between the hot-spot and surrounding end-gas is about an

order-of-magnitude larger than the temperature fluctuations measured experimentally [21, 22].

Although most of the numerical simulations focus on SI engines, a recent paper by Sheppard, Tolegano, and Woolley [2] has applied the same methodology to HCCI engines. Their work applies the same planar, one-dimensional, one-step chemistry code used by Konig et al. [13] to study lean mixtures used in HCCI engines. Sheppard and coworkers found that in their simulations some lean mixtures initiated a detonation, but for very lean mixtures ($\phi < 0.3$) the energy content of the fuel/air mixture was too low to support detonations. Similarly Bradley [17] observed that when the energy content of the fuel/air mixture dropped below about $10^{13}$ W/m$^3$ detonation was not observed regardless of the ignition kinetics used.

In summary, although many one- and two-dimensional reacting flow calculations have been performed which show that detonations can form in mixtures containing a hot-spot, these calculations usually contain one or more questionable assumptions that deserve re-examination. This work revisits those assumptions by performing one-dimensional calculations with curvature effects, detailed chemistry, viscous effects, and realistic initial conditions to show whether detonations are likely formed under real engine operating conditions.

### 4.2.3 Relevant Theoretical Studies of Detonation

A few authors have performed theoretical studies to determine critical conditions for detonation formation from hot-spots. A series of papers by He and coworker [23-29] which culminates in the work of He and Law [24] propose a theoretical framework for determining the critical size of a hot-spot needed to form a spherical detonation wave.

They observed that for their parameters, which are not necessarily applicable to an engine, the critical size for a hot spot was about 300 times the thickness of a Chapman-Jouguet (CJ) detonation. He and Law's theory has been used to predict critical hot-spot sizes for SI and HCCI engines, and the results are presented in this work.

Bradley [17] also studied the critical size for a hot-spot but from a different vantage point. He determined the critical hot-spot size needed for autoignition to occur before the local high temperature is dissipated. A parametric study was performed to determine this critical size as a function of energy content of the mixture and global ignition kinetics. Because the critical size determined by He and Law [24] is always larger than that of Bradley (because ignition is a necessary precursor to detonation formation) we focus our attention on the former theoretical work.

### 4.2.4 Summary

Previous researchers, who attempted to attribute knocking to detonation waves, have based there conclusions on numerical simulations of the reactive Navier-Stokes equations. These simulations have usually suffered from one of several questionable assumptions, namely, 1) use of a planar geometry which is much more conducive to detonation formation because of the lack of divergence effects, 2) use of initial conditions which are dissimilar to the actual engine, 2) simplified one-step chemistry models which do not predict ignition delays important in detonation initiation, 3) formulation of the governing equations in a non-conservative fashion which is unsuitable for high-speed flows present for detonations. In this chapter, the development of a numerical simulation is described which addresses these issues.

The basic approach was to run some simulations of hot-spot ignition and propagation of combustion waves under typical SI and HCCI engine conditions, and observe whether the simulations predicted the formation of detonation waves, deflagrations, or induction waves. We hypothesized that our planar one-dimensional calculations would lead to detonation formation as seen by many researchers [2, 10, 13, 17]. However, we believed that small spherical hot-spots would produce deflagrations because of dissipation due to curvature. Consequently, a range of hot-spot sizes were simulated to determine the critical radius below which detonations cannot form. This critical radius was then compared to the relevant lengthscales in an engine (e.g. size of the end-gas) to judge whether a hot-spot of that size is feasible.

These simulations were conducted on the assumption that gas motion from the hot-spot is one-dimensional and spherically symmetric. However, as noted by Zel'dovich [10], steady-state one-dimensional detonations are unsteady with respect to two-dimensional disturbances. Therefore, the numerical calculations presented in this paper should be viewed as evidence that a critical hot-spot size exists and can be determined approximately, rather than a detailed account of the three-dimensional structure of the detonation wave.

Additionally theoretical calculations were performed to help verify our numerical predictions. These calculations use a theoretical framework described by He and Law [24] to determine the critical size of a hot-spot needed to initiate a spherical detonation. This critical radius was calculated for engine conditions and again compared to the typical SI end-gas lengthscale.

## 4.2.5 Numerical 1-D Unsteady Reacting Flow Calculations

## 4.2.5.1 Governing Equations and Assumptions

The conservation equations for a reactive fluid mixture are the following.

$$\frac{\partial \rho}{\partial t} + \nabla \cdot \rho \upsilon = 0 \quad \text{(mass conservation)} \tag{1.1}$$

$$\frac{\partial \rho \upsilon}{\partial t} + \nabla \cdot \rho \upsilon \upsilon = -\nabla p + \nabla \cdot \tau \quad \text{(momentum conservation)} \tag{1.2}$$

$$\frac{\partial E}{\partial t} + \nabla \cdot E \upsilon = -\nabla \cdot p \upsilon - \nabla \cdot q + \nabla \cdot [\tau \cdot \upsilon] \quad \text{(energy conservation)} \tag{1.3}$$

$$\frac{\partial \rho Y_k}{\partial t} + \nabla \cdot \rho Y_k \upsilon = -\nabla \cdot \rho Y_k V_k + \dot{\omega}_k W_k \quad \text{(species conservation)} \tag{1.4}$$

In the above equations, $\rho, \upsilon, E, p, \tau, Y_k, V_k, \dot{\omega}_k$ and $W_k$ are respectively mass density, mass-averaged velocity, total energy density, pressure, stress, mass fraction, diffusion velocity, molar rate of production, and molecular weight of species $k$. These conservation equations along with an equation of state, constitutive equations, and appropriate initial and boundary conditions completely specify the dynamics of the system. With appropriate assumptions regarding symmetry, these equations can be written for one (radial) spatial dimension as follows,

$$\frac{\partial \rho}{\partial t} + \frac{1}{r^\alpha} \frac{\partial}{\partial r} \left( r^\alpha \rho \upsilon_r \right) = 0 \tag{1.5}$$

$$\frac{\partial \rho \upsilon_r}{\partial t} + \frac{1}{r^\alpha} \frac{\partial}{\partial r} \left( r^\alpha \rho \upsilon_r \upsilon_r \right) = -\frac{\partial p}{\partial r} + \left( \frac{1}{r^\alpha} \frac{\partial}{\partial r} \left( r^\alpha \tau_{rr} \right) - \frac{\alpha \tau_{\theta\theta}}{r} \right) \tag{1.6}$$

$$\frac{\partial E}{\partial t} + \frac{1}{r^\alpha} \frac{\partial}{\partial r} \left( r^\alpha E \upsilon_r \right) = -\frac{1}{r^\alpha} \frac{\partial}{\partial r} \left( r^\alpha p \upsilon_r \right) - \frac{1}{r^\alpha} \frac{\partial}{\partial r} \left( r^\alpha q_r \right) + \frac{1}{r^\alpha} \frac{\partial}{\partial r} \left( r^\alpha \tau_{rr} \upsilon_r \right) \tag{1.7}$$

$$\frac{\partial \rho Y_k}{\partial t} + \frac{1}{r^\alpha} \frac{\partial}{\partial r} \left( r^\alpha \rho Y \upsilon_r \right) = -\frac{1}{r^\alpha} \frac{\partial}{\partial r} \left( r^\alpha \rho Y V_{k,r} \right) + \dot{\omega}_k W_k \tag{1.8}$$

where $\alpha$ equals 0, 1 and 2 for planar, cylindrical and spherical coordinates, respectively. Assuming the fluid is a Newtonian ideal-gas mixture, the following definitions and constitutive equations are applied to the above conservation equations, Eqs. (1.1)-(1.8).

$$E = \rho e + \frac{1}{2} \rho v_r^2 \tag{1.9}$$

$$e = \sum_{k=1}^{K} Y_k e_k \tag{1.10}$$

$$e_k = \int_{T_\circ}^{T} C_{v,k} dT + \left(\Delta e_f\right)_k^\circ \tag{1.11}$$

$$q_r = -\frac{1}{r^\alpha} \frac{\partial}{\partial r}\left(r^\alpha \lambda \frac{\partial T}{\partial r}\right) + \frac{1}{r^\alpha} \frac{\partial}{\partial r}\left(r^\alpha \sum_{k=1}^{K} \rho Y_k V_{k,r} h_k\right) \tag{1.12}$$

$$V_{k,r} = -\frac{D_k}{Y_k} \frac{\partial Y_k}{\partial r} \tag{1.13}$$

$$\tau_{rr} = \mu\left[2\frac{\partial v_r}{\partial r} - \frac{2}{3}\left(\frac{1}{r^\alpha} \frac{\partial}{\partial r}\left(r^\alpha v_r\right)\right)\right] \tag{1.14}$$

$$\tau_{\theta\theta} = \tau_{\phi\phi} = \mu\left[2\frac{v_r}{r} - \frac{2}{3}\left(\frac{1}{r^\alpha} \frac{\partial}{\partial r}\left(r^\alpha v_r\right)\right)\right] \tag{1.15}$$

In the above equations, $v_r, e, q_r, \lambda, \tau_{\theta\theta}, \tau_{\phi\phi}, \mu, e_k, (\Delta e_f)_k^\circ, C_{v,k}, h_k$ and $D_k$ are respectively the radial velocity, specific internal energy, radial heat flux, thermal conductivity, normal stress in the $\theta$-direction, normal stress in the $\phi$-direction, viscosity, specific internal energy of species $k$, internal energy of formation of species $k$ at standard state conditions, constant-volume heat capacity of species $k$, specific enthalpy of species $k$ and diffusivity of species $k$.

Eqs. (1.5) to (1.8) are written in the conservative form, so called because the quantities in the time-derivatives are conserved quantities (mass density, momentum

density, total energy density, and species mass density). This form of the equations is valid for high-speed flows with shocks because the Rankine-Hugoniot conditions are automatically enforced across shock waves. This approach is called the shock-capturing approach in computational fluid mechanics. Writing the equations in terms of the primitive variables $(T, p, \upsilon, Y_k)$ is not valid for flows with shock waves and leads to incorrect wave speeds. Several assumptions were made when deriving these governing equations: 1) thermal diffusion (Soret effect) and radiation are negligible; 2) the gas mixture behaves as an ideal gas; 3) no body forces are acting on the system. Additionally, turbulent effects were not considered in these simulations.

The temperature initial condition used a spherically-symmetric hot-spot which has a higher temperature than the surrounding gas. The shape of the hot-spot was assumed to be a constant-temperature core region surrounded by a Gaussian curve (Figure 4.2).

$$T(r) = \begin{cases} T_{base} + \Delta T, r \leq L_{hot} \\ T_{base} + \Delta T \exp\left[ -\left( \dfrac{r - L_{hot}}{L_{mix}} \right)^2 \right], r > L_{hot} \end{cases} \qquad (1.16)$$

This shape was chosen so that the size of the hot-spot and the slope of the mixing region between the hot-spot and surrounding gas could easily be varied independently. Different size hot-spots were studied by changing the size of the core high-temperature region ($L_{hot}$) of the hot-spot. The length of the mixing region ($L_{mix}$) was fixed at 1 cm throughout these series of calculations. All other fluid variables were initially uniform across the computational domain. The boundary conditions were axis or solid wall boundaries depending on whether spherical, cylindrical, or planar coordinates were used.

**Figure 4.2:** Example of initial conditions for the hot-spot used in the reacting flow calculations
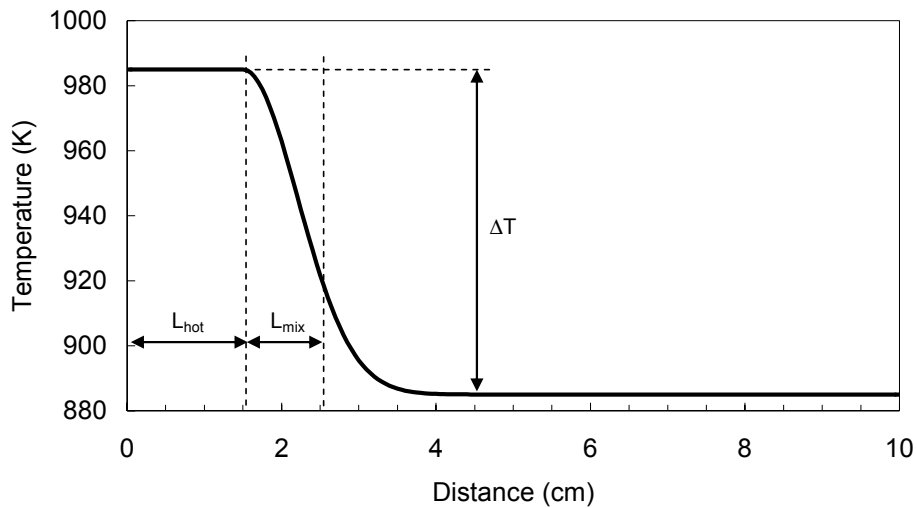


## 4.2.5.2 Chemistry Model

The chemistry model used in these simulations was the reduced model (32 species, 55 reactions) for primary reference fuel combustion developed by Tanaka et al. [30]. This model has been thoroughly tested with experimental ignition-delay data from a rapid-compression machine operated under lean conditions common to HCCI engines. The mechanism is based on the earlier model of Hu and Keck [31], which was developed to study autoignition and knock in an SI engine at stoichiometric conditions. The model uses hydrogen/oxygen chemistry from the detailed $H_2$ mechanism of Marinov et al. [32] and CO oxidation chemistry from GRIMech3.0 [32]. The large-molecule reaction steps use lumped species based on the accepted mechanistic understanding for low-temperature oxidation of alkanes. The CHEMKIN input file received from S. Tanaka was slightly modified to make it work with the standard CHEMKIN library by using the FORD keyword (see [33]) to make the six global reactions zero-order in oxygen concentration.

Tanaka and Keck accomplished the same result by making chemistry-model-specific changes to the CHEMKIN subroutine that calculates reaction rates.

Transport properties for H/O species were taken from the $H_2$ chemistry model of Marinov et al. [34], and CO and $CO_2$ transport properties come from GRI-Mech3.0 [32]. Transport properties for larger species were estimated from the transport files for the detailed *n*-heptane and iso-octane chemistry models of Curran et al. [35, 36]. For species where an exact match was not available, transport properties for a species with similar molecular size and structure were used. The chemistry and transport files used in these calculations are given as a supplement at the end of this chapter.

### 4.2.5.3 Numerical Solution Strategy

Equations (1.5) through (1.8) were solved using the finite-volume technique. The spatial discretization and time integration were done using the LCPFCT program [37]. LCPFCT is an implementation of the flux-corrected transport algorithm of Boris [38], which solves the generalized 1-D continuity equation:

$$\frac{\partial \rho}{\partial t} + \frac{1}{r^\alpha}\frac{\partial}{\partial r}\left(r^\alpha \rho \upsilon\right) = -\frac{1}{r^\alpha}\frac{\partial}{\partial r}\left(r^\alpha D_1\right) + C_2 \frac{\partial D_2}{\partial r} + D_3 \qquad (1.17)$$

Flux-corrected transport (FCT) is a high-order, monotone, conservative, positivity preserving algorithm [37]. The FCT method has the stability of an upwind differencing method, but with much less numerical diffusion. As evident from Eq. (1.17), LCPFCT was written to handle one-dimensional problems in planar, cylindrical, and spherical coordinates. The program also handles several types of diffusion and source terms, which are present in our system of governing equations. Moving grids are also handled in a natural way by only considering the velocity relative to the cell interfaces when

calculating the numerical fluxes. These qualities of LCPFCT make it ideal for solving reacting flow problems where good spatial resolution is important.

A FORTRAN program called RFLOW1D was written to solve the system of governing equations for ignition of a hot-spot and subsequent propagation of a combustion wave into the unburned mixture. The RFLOW1D program sets up the initial conditions for the conserved variables, defines the governing equations and boundary conditions, calculates the necessary chemistry source terms, thermodynamic properties, and transport properties and calls LCPFCT repeatedly to advance the solution in time. The chemistry source terms, thermodynamic properties, and transport properties were evaluated using the CHEMKIN library of subroutines and associated TRANSPORT library. The boundary conditions used at both ends of the domain were those for a solid wall or axis. This was accomplished in the program by setting the gradients of mass density, species mass density, and total energy density to zero at the cell interfaces with the boundaries. Momentum density was set to zero at the boundaries.

Because the device scale (i.e. the size of the engine cylinder) is large compared to the scale of phenomena we wish to capture (e.g. flame thickness), it is advantageous to use an adaptive spatial grid to improve the spatial resolution. RFLOW1D uses a *sliding rezone* as described by Oran and Boris [38], which uses a fixed number of cells but repositions the interfaces of those cells during the calculation. The algorithm for determining the positions of the cell interfaces is due to Dorfi and Drury [39]. This technique is based on the principle of equidistribution, which moves the grid to make the product of the cell width and some monitor function (which is proportional to gradients in the solution) equal for all cells. Equidistribution results in small cell widths at places

117

where there are steep gradients in the solution. The Dorfi and Drury [39] algorithm also insures that the ratio of adjacent cell widths is within some tolerance and that the grid does not move too quickly, which can hinder accuracy of the spatial differencing. The grid motion algorithm results in the solution of an implicit set of ordinary differential equations for the interface locations. This integration is performed using DASSL and is subcycled at a timestep (chosen by DASSL based on user-specified tolerances) that is smaller than the transport timestep.

Because the chemical kinetics are generally stiff and the timestep necessary to accurately solve for the evolution of chemical species is small, the chemistry calculation is split from the transport calculation and subcycled at a smaller timestep. This timestep splitting technique improves the computational speed by allowing the transport calculation to use a larger timestep than that required by the chemistry. During the chemistry calculation, only the terms in the species conservation equations resulting from chemical reactions are solved. It is assumed that each cell is at constant pressure during the transport timestep, and the resulting equations are those for a well-mixed, constant-pressure, closed, batch reactor

$$\frac{dY_k}{dt} = \frac{\dot{\omega}_k W_k}{\rho}.$$

(1.18)

During the chemistry calculation, the temperature is calculated from the energy equation, which reduces to $dh = 0$ for a closed, constant-pressure system, and the temperature can be calculated by integrating

$$c_p \frac{dT}{dt} + v \sum_{k=1}^{K} h_k \dot{\omega}_k W_k = 0$$

(1.19)

Because the transport time integration is explicit, some care needs to be taken with choosing an appropriate timestep. The transport timestep is reduced if the chemical heat release is too large in any computational cell. This check is implemented by halving the timestep, if $\Delta T_{chem,i} > 10 \text{ K}$, where $\Delta T_{chem,i}$ is the temperature rise associated with chemical heat release in the $i$-th cell. The transport timestep is also limited by the Courant-Friedrichs-Lewy (CFL) stability criterion,

$$\text{CFL} = \frac{\Delta t}{\Delta x_i} \max\left(|v_i + c_i|, |v_i - c_i|\right) \leq 0.1, \tag{1.20}$$

where the index $i$ runs over all cells in the computational domain. This criterion really only requires that the CFL number be less than unity, so that information cannot travel more than one computational cell during a timestep. In practice however, a smaller CFL number (0.1) was used to insure that the simulation remains stable. This explicit time integration technique is appropriate for high-speed flows like detonations because the phenomena of interest move at approximately the acoustic velocity. Explicit time integration is inefficient, however, for studying low speed phenomena like flames. Nevertheless, acceptable computational efficiencies (CPU times of about 4 hours) were observed using the explicit approach for our calculations.

In order to improve the accuracy of the time integration, a half-step integration technique was used. This technique resembles the predictor-corrector approach in that the source terms in Eqs. (1.5) to (1.8) are calculated using the values of $T$, $P$ and $v$ estimated by first explicitly integrating the equations one-half timestep. The half-step integration approach, timestep splitting of the chemistry terms, and movement of the cell interface positions are combined into the following integration procedure for one timestep:

1. Integrate the equations for a half timestep, $\Delta t/2$, to find first-order accurate estimates of the fluid variables in the middle of the whole timestep.

   a. Calculate $v^0$, $p^0$, and $T^0$ using the values of $\rho^0$, $\rho^0 v^0$, $E^0$, and $\rho^0 Y_k^0$.

   b. Calculate new cell interface locations based on the gradients of $p^0$ and $T^0$.

   c. Integrate the chemistry equations Eq. (1.18) using DASSL a whole timestep from $t^0$ to $t^0 + \Delta t$ using $T^0$, $p^0$, and $Y_k^0$. Calculate $\langle \dot{\omega} \rangle_k W_k$, the chemistry source term averaged over the full timestep.

   d. Evaluate $-\nabla p^0$ and $-\nabla \cdot (p^0 v^0)$ terms for the momentum and energy equations, respectively.

   e. Evaluate the viscous terms, $\nabla \cdot \tau^0$, $\nabla \cdot q^0$, $\nabla \cdot [\tau^0 \cdot v^0]$, and $\nabla \cdot \rho^0 Y_k^0 V_k^0$ terms for the momentum, energy and species equations.

   f. Convect $\rho^0$, $\rho^0 v^0$, $E^0$, and $\rho^0 Y_k^0$ for a half timestep to $\rho^{\frac{1}{2}}$, $\rho^{\frac{1}{2}} v^{\frac{1}{2}}$, $E^{\frac{1}{2}}$, and $\rho^{\frac{1}{2}} Y_k^{\frac{1}{2}}$ using $-\nabla p^0$, $-\nabla \cdot (p^0 v^0)$, $\nabla \cdot \tau^0$, $\nabla \cdot q^0$, $\nabla \cdot [\tau^0 \cdot v^0]$, $\nabla \cdot \rho^0 Y_k^0 V_k^0$, and $\langle \dot{\omega} \rangle_k W_k$.

2. Integrate the equations for a whole timestep, $\Delta t$, using the "time-centered" source terms calculated by the half-step integration. The results are second-order accurate at the end of the whole-step.

   a. Calculate $v^{\frac{1}{2}}$, $p^{\frac{1}{2}}$, and $T^{\frac{1}{2}}$ using the half-step values of $\rho^{\frac{1}{2}}$, $\rho^{\frac{1}{2}} v^{\frac{1}{2}}$, $E^{\frac{1}{2}}$, and $\rho^{\frac{1}{2}} Y_k^{\frac{1}{2}}$.

   b. Evaluate the $-\nabla p^{\frac{1}{2}}$ and $-\nabla \cdot (p^{\frac{1}{2}} v^{\frac{1}{2}})$ terms for the momentum and energy equations, respectively.

   c. Evaluate the viscous terms, $\nabla \cdot \tau^{\frac{1}{2}}$, $\nabla \cdot q^{\frac{1}{2}}$, $\nabla \cdot [\tau^{\frac{1}{2}} \cdot v^{\frac{1}{2}}]$, and $\nabla \cdot \rho^{\frac{1}{2}} Y_k^{\frac{1}{2}} V_k^{\frac{1}{2}}$ terms for the momentum, energy and species equations.

   g. Convect $\rho^0$, $\rho^0 v^0$, $E^0$, and $\rho^0 Y_k^0$ for a full timestep to $\rho^1$, $\rho^1 v^1$, $E^1$, and $\rho^1 Y_k^1$ using $-\nabla p^{\frac{1}{2}}$, $-\nabla \cdot (p^{\frac{1}{2}} v^{\frac{1}{2}})$, $\nabla \cdot \tau^{\frac{1}{2}}$, $\nabla \cdot q^{\frac{1}{2}}$, $\nabla \cdot [\tau^{\frac{1}{2}} \cdot v^{\frac{1}{2}}]$, $\nabla \cdot \rho^{\frac{1}{2}} Y_k^{\frac{1}{2}} V_k^{\frac{1}{2}}$, and $\langle \dot{\omega} \rangle_k W_k$.

3. Repeat the two steps given above to advance the solution again from $t^1$ to $t^2$.

## 4.2.5.4 Determination of Initial Conditions

In order to make the simulations resemble the real engine as much as possible, an effort was made to estimate realistic HCCI and SI engine conditions. In order to accomplish this, cycle simulations and batch homogeneous (also referred to previously as perfectly-stirred) reactor simulations were performed. The engine design parameters and operating conditions for the HCCI and SI engine cases are given in Table 4.1. The HCCI engine design mimics the single-cylinder Ford OKP HCCI engine described in Chapter 3. The operating conditions for the HCCI case produced slight knocking when used in the Ford OKP engine. The SI case uses typical engine-design parameters and operating conditions with two exceptions: 1) The compression ratio (12) is higher than a typical SI engine; 2) An early spark-timing (30 cad btc) was used. This choice of compression ratio and spark-advance, would almost certainly mean that this engine would experience engine knock under these conditions. This assertion is confirmed in our calculations by checking that the end-gas would autoignite before the arrival of the turbulent flame front. Also, another case was run that used a more typical compression ratio and spark advance. This variation of the SI case is discussed in the section entitled "Sensitivity to Initial Conditions".

**Table 4.1:** Test case engine-design parameters and operating conditions

|  | HCCI Case | SI Case |
|---|---|---|
| Fuel | PRF 92 | PRF 92 |
| Equivalence ratio | 0.385 | 1.0 |
| Engine speed | 1500 rpm | 1500 rpm |
| Start of combustion | top-center[a] | 30 cad btc[b] |
| Combustion duration | 12 cad | 50 cad |
| Compression ratio | 15.51 | 12.0 |
| Bore | 89 mm | 89 mm |
| Stroke | 105.8 mm | 105.8 mm |
| Intake temperature | 113°C[c] | 25°C |
| Intake pressure | 97.6 kPa | 101.1 kPa (WOT) |
| Exhaust pressure | 99.9 kPa | 101.1 kPa |
| Cylinder liner temperature | 110°C | 110°C |
| Piston face temperature | 160°C | 160°C |
| Cylinder head temperature | 160°C | 160°C |
| Exhaust valve opening | 135 cad | 130 cad |
| Exhaust valve closing | 375 cad | 370 cad |
| Intake valve opening | 298 cad | 345 cad |
| Intake valve closing | 598 cad | 590 cad |

[a] Combustion is assumed to start at top-center in the cycle simulations. However, in the PSR calculations start-of-combustion is controlled by the ignition kinetics.
[b] This is the spark-timing for the SI case.
[c] The intake temperature used experimentally was 123°C. This temperature was adjusted in the calculations to match the experimental ignition timing.
WOT = wide-open throttle, cad = crank-angle degrees

The initial conditions for the HCCI engine case were estimated using the combined cycle-simulation/perfectly-stirred-reactor approach described in Chapter 3. The General Motors Research (GMR) cycle simulation program was run using the inputs shown in Table 4.1 with a simple analytical combustion model. The temperature, pressure and residual fraction at intake-valve closing from GMR were used to initialize the perfectly-stirred-reactor (PSR) model. The PSR model was run from intake-valve closing through exhaust-valve opening. Note that the intake temperature was adjusted slightly to match the experimental ignition timing as discussed in the footnotes to Table 4.1. The conditions at 5 cad btc (about 1 ms before ignition) were chosen as the initial conditions for the mixture surrounding the hot-spot in the reacting flow calculations.

Figure 4.3 compares the profiles of temperature and pressure resulting from these calculations with experimental data from the Ford OKP HCCI engine.

**Figure 4.3:** Profiles of temperature and pressure used to initialize the reacting flow calculations for the HCCI engine case. The lines are calculations from a perfectly-stirred reactor calculation using the chemistry model of Tanaka et al. [30]. The open symbols are cycle-averaged pressure data from the Ford OKP engine [40]. Simulated intake temperature modified to match experimental ignition timing.
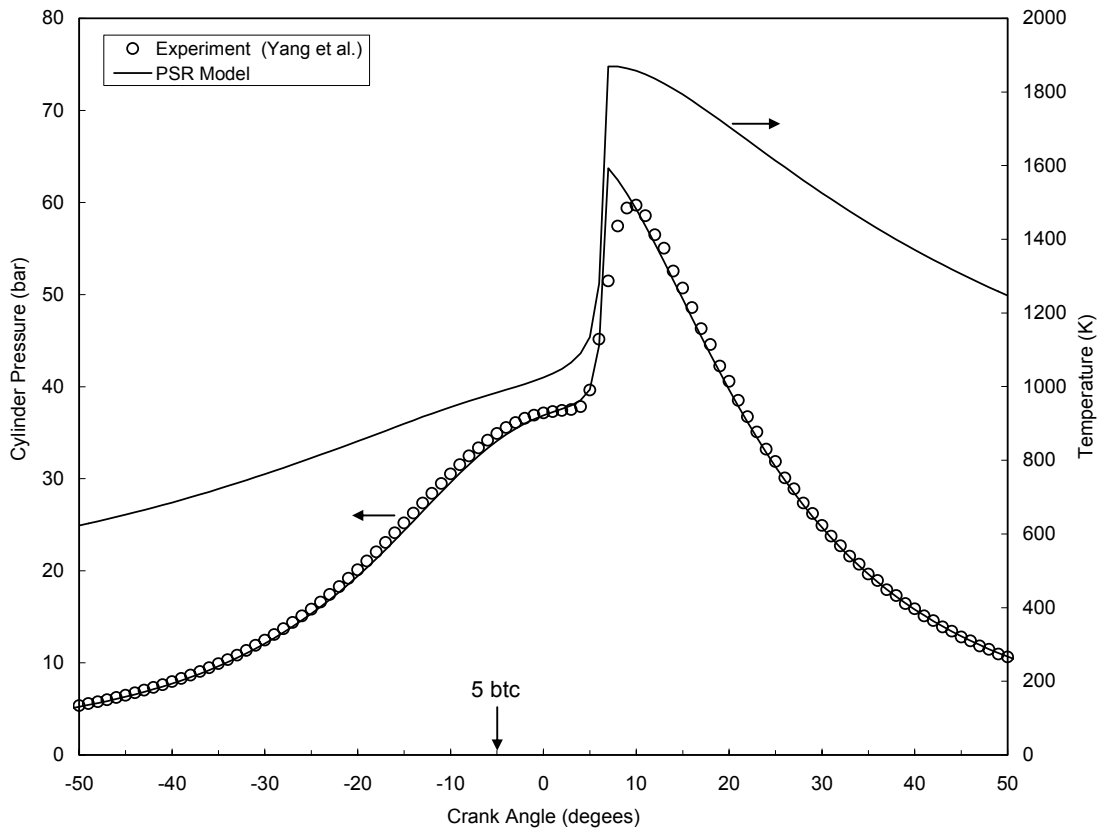


Similar simulations were performed to estimate the initial conditions for the SI engine case. However in the SI case, the cycle simulation program was used to estimate the unburned end-gas temperature. The end-gas temperature was estimated in GMR using the Wiebe function to specify the burning rate, with a three-zone (burned, unburned, boundary layer) physical model of the engine cylinder. Heat losses to the cylinder walls were calculated using the Woschni [41] correlation to estimate the heat-transfer

coefficient. Profiles of cylinder pressure, unburned gas temperature, and burned fraction calculated using GMR are shown in Figure 4.4. Next, the species conservation equations were integrated under conditions of variable temperature and pressure according to these profiles starting from intake-valve closing. The conditions at 5 cad atc were used to initialize the reacting flow simulations in the SI engine case. This choice of crank angle corresponds to a 75% burned fraction and the approximate peak of cylinder pressure and unburned gas temperature.

**Figure 4.4:** Calculated profiles of unburned (end-gas) temperature, cylinder pressure, and burned fraction used to initialize the reacting flow simulations for the SI engine case. These profiles were calculated by the General Motors Research (GMR) cycle simulation program using the inputs given in Table 4.1. Note that the peak unburned temperature occurs slightly before the peak pressure due to heat losses from the cylinder as confirmed by adiabatic calculations.
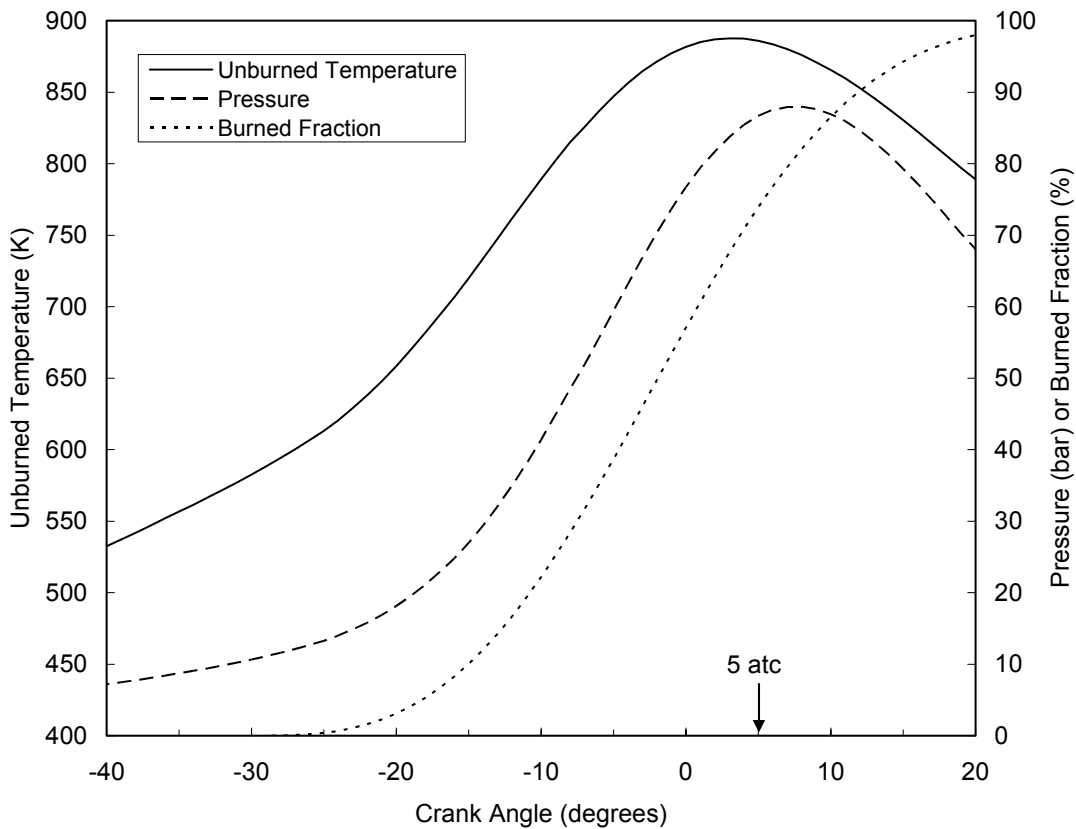
The conditions of temperature, pressure and composition used as initial conditions for the reacting flow calculations are given in Table 4.2. Only species with mass fractions greater than 0.0001 are shown; however, all species concentrations were initialized in this way. Rather severe (high temperature and pressure) initial conditions were purposefully chosen to make the formation of detonations more likely. As a result our estimates of the critical radius for detonation formation are likely to be conservative underestimates. To our knowledge, previous calculations of detonation formation in engines have not considered the effects of the chemistry in the unburned gases before ignition, which significantly affects the pool of radicals and peroxides.

The size and intensity of the hot-spots were more difficult to estimate. Smith [22] made measurements of end-gas temperatures in an SI engine by a pulsed Raman scattering technique. After subtracting out the statistical uncertainty of his signal, Smith found that the fluctuations in the end-gas temperature averaged about 50-70 K. A more recent study by Schiesl and Maas [21], used two-dimensional laser-induced fluorescence of formaldehyde to indirectly estimate spatial variation of end-gas temperature. Those authors found the fluctuations to be on the order 20 K or larger. Based on these measurements, the temperature difference between the hot-spots and surrounding gas was taken as 100 K, which appears to be the correct order of magnitude from the available experimental data.

**Table 4.2:** Initial Conditions used for the reacting flow calculations to determine the critical radius for the formation of spherical detonation in spark-ignited (SI) and homogeneous-charge compression-ignition (HCCI) engines.

| | HCCI Case | SI Case |
|---|---|---|
| Hot-spot temperature | 1084 K | 985 K |
| Surrounding temperature | 984 K | 885 K |
| Pressure | 33.6 atm | 85.5 atm |
| Fluid velocity | 0 m/s | 0 m/s |
| Mass fractions:[a] | | |
| i-$C_8H_{18}$ | 1.95E-02 | 4.86E-02 |
| n-$C_7H_{16}$ | 1.53E-03 | 2.14E-03 |
| $O_2$ | 2.14E-01 | 1.87E-01 |
| $N_2$ | 7.49E-01 | 7.20E-01 |
| $H_2O$ | 5.23E-03 | 1.46E-02 |
| $H_2O_2$ | 1.25E-04 | 1.93E-03 |
| $HO_2$ | 3.58E-04 | 5.36E-04 |
| CO | 1.97E-03 | 1.67E-02 |
| $CO_2$ | 8.54E-03 | 7.75E-03 |

[a] Only species with mass fractions greater than 1E-4 shown

## 4.2.6 Theoretical Calculations

He and Law [24] developed a theoretical framework that allows the estimation of the critical radius of a hot-spot needed for the formation of a spherical detonation. This theoretical framework was used with slight modifications to verify the critical radii calculated numerical in our reacting flow simulations. The results of the theoretical calculations are not expected to be as accurate as the numerical simulations due to addition approximations that He and Law made in developing the theory. However, order of magnitude agreement between the two approaches does suggest the predicted critical radii are accurate.

The derivation presented by He and Law [24] begins with the unsteady, one-dimensional, reactive Navier-Stokes equations presented earlier in Eqs. (1.5)-(1.8). By assuming the detonation wave is quasi-steady in a reference frame that is attached to the detonation front, they are able to discard the unsteady terms in those equations. He and Law then assume a square-wave model, which approximates the detonation structure as a

shock wave followed by an induction zone and then a reaction zone (see Figure 4.5). The reaction zone and shock wave are assumed to have negligible thickness compared to the induction zone, which is the only characteristic length-scale in this system.

**Figure 4.5:** Structure of a detonation wave assumed by the square-wave approximation
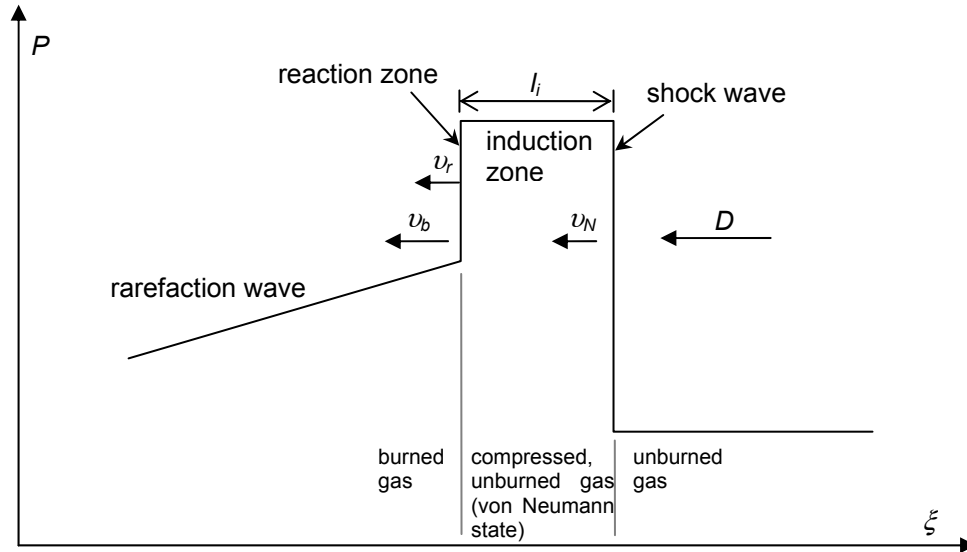


Next by assuming the gas is thermally and calorically perfect, they are able to integrate the continuity, momentum and energy equations across the induction zone. Curvature of the induction zone is accounted for in the expressions for the fluxes into and out of the induction zone. Similarly the continuity, momentum and energy equations are written with a control volume that includes the reaction zone. This set of balances allowed He and Law to account for movement of the reaction zone away from the shock wave because the induction time increases as the detonation moves off from the hot-spot. Combining these two sets of algebraic equations and using the sonic condition at the end of the reaction zone ($v_b = c_b$), the authors were able to derive the following

transcendental equation which can be solved for the detonation velocity (D) for a given radial position[2].

$$\frac{\gamma^2}{2(\gamma^2-1)} \frac{\left\{p_i/(\rho_i D^2) + \left[1 - (\upsilon_N/D)(\Gamma_1 + 2\Gamma_2)\right]\right\}^2}{\left[\gamma/(\gamma-1)\right]p_i/(\rho_i D^2) + \frac{1}{2} + Q/D^2 - (\upsilon_N^2/D^2)\Gamma_2}$$

$$= (1 - \Gamma_1 - \Gamma_2)^2 \tag{1.21}$$

In the above equation, $p_i$ and $\rho_i$ are the pressure and density ahead of the shock wave, $\upsilon_N$ is the velocity at the von Neumann state, and $\gamma = C_p/C_v$ in the ideal gas state. $\Gamma_1$ is a term representing the curvature effect (i.e. divergence due to the spherical geometry), and $\Gamma_2$ is a term that represents the temperature effect (i.e. lengthening of the induction zone as the unburned temperature decreases). After some manipulation, Eq. (1.21) can be written in terms of $M$, the Mach number of the detonation wave in the unburned mixture, only. Four dimensionless parameters are required to define the system; 1) the ratio of specific heats, 2) the energy content of the fuel/air mixture, 3) the global activation energy for the combustion process, 4) the ratio of the hot-spot temperature to the surrounding temperature. The parameter values used by He and Law were appropriate for a stoichiometric fuel/oxygen mixture with a very hot spot surrounded by cold unburned gas.

$$\gamma = 1.2, \quad \frac{Q}{RT_0} = 50, \quad \frac{E_a}{RT_0} = 26, \quad T_{i0}/T_0 = 3.5. \tag{1.22}$$

$T_{i0}$ and $T_0$ are the hot-spot temperature and the temperature of the surrounding gas, respectively. Parameter values representing the HCCI and SI engine case are

---

[2] Note that there is a typographical error in the original reference 24.   He, L. and C.K. Law, *Geometrical effect on detonation initiation by a nonuniform hot pocket of reactive gas.* Phys. Fluids, 1996. **8**: p. 248-256. for Eq. (1.21)

$$\gamma = 1.2, \quad \frac{Q}{RT_0} = 10.4, \quad \frac{E_a}{RT_0} = 16.9, \quad T_{i0}/T_0 = 1.11 \text{ (SI)}, \tag{1.23}$$

$$\gamma = 1.2, \quad \frac{Q}{RT_0} = 3.5, \quad \frac{E_a}{RT_0} = 15.2, \quad T_{i0}/T_0 = 1.10 \text{ (HCCI)}. \tag{1.24}$$

The mixture energy content, $Q/RT_0$, was estimated based on the lower-heating value of a mixture of *n*-heptane and iso-octane at the equivalence ratios given in Table 4.1. The normalized activation energy, $E_a/RT_0$, was calculated using an Arrhenius temperature of 15,000K, typical of global kinetic models for hydrocarbon oxidation [42].

Calculation of the critical hot-spot radius for formation of a spherical detonation involves two steps. The first step is to solve Eq. (1.21) for different radial positions ranging from zero to several hundred times the thickness of the induction zone, $l_i$. This equation typically yields *C*-shaped curved when $M$ (or the pressure in the von Neumann sate, $P_N/P_0$) is plotted versus radial position. The minimum radial position where Eq. (1.21) has a solution, called $R_c$, will depend on the size of the hot-spot. Second, the radial position where the Zel'dovich criterion for detonation initiation is calculated from

$$c(r) = \left( \frac{d\tau_i}{dr} \right)^{-1} \tag{1.25}$$

where $c$ is the sound speed and $\tau_i$ is the ignition delay. The radial position where Eq. (1.25) is satisfied, called $R_z$, is also dependent on the size of the hot-spot. For small hot-spots $R_z$ will be less than $R_c$, which means that a detonation would be initiated at $R_z$ but could not propagate stably because of the dissipation caused by the curvature of the detonation front. Therefore, the criterion used to determine the critical hot-spot size is

$$R_z \geq R_c \tag{1.26}$$

A few minor modifications to the original theoretical framework of He and Law were made before applying this methodology to our engine test cases. First, the expression for $\Gamma_2$ uses the normal shock relations to calculate the jump conditions for temperature across the shock wave. He and Law were interested in very strong detonations (e.g. those in stoichiometric fuel/oxygen mixtures) and so justifiably used a strong-shock approximation to the jump conditions. Since we are interested in weaker detonations, the full expression for the jump condition was used. Similarly the Mach number for a Chapman-Jouguet detonation, $M_{CJ}$, needed to compute $\Gamma_2$ was calculated using the full expression rather than the strong-shock approximation. Third, He and Law assumed an exponential shape for the hot-spot temperature profile, but our calculations use the Gaussian profile shown in Figure 4.2. The results of applying this methodology to our HCCI and SI test cases and the results are discussed in Sections 4.3.1.2 and 4.3.2.2.

## 4.3 Results

### 4.3.1 SI Engine Calculations

This section describes the results of numerical simulations and theoretical calculations of hot-spot ignition and subsequent combustion wave propagation for the spark-ignited test case ("SI Case" in Tables 4.1 and 4.2).

### 4.3.1.1 Numerical Simulations

The following series of plots show the response of a reactive mixture of PRF 92 and air at the initial conditions given in Table 4.2 for hot-spots in the size range $L_{hot} = $ 0-2 cm. Both spherical and planar geometry results are shown.

Figure 4.6 shows the ignition of a spherical hot-spot with $L_{hot} = 0$ cm. In this case, the mixture ignites after a delay time of 250 μs and very soon after the fuel is completely

consumed[3] in the hot-spot and the temperature reaches approximately 2700 K. After ignition the combustion wave propagates into the colder mixture at a speed of approximately 43 m/s, which is typical of a deflagration wave. Notice that the ignition causes small oscillations in the pressure, but overall the pressure in the vessel remains nearly uniform.

Figure 4.7 and Figure 4.8 contrast the mode of propagation for spherical and planar hot-spots ($L_{hot}$ = 0). In the spherical case (Figure 4.7), the hot-spot pressure remains nearly uniform throughout the vessel and the combustion propagates as a deflagration. However, in the planar case (Figure 4.8) the combustion wave quickly transitions to a fully developed detonation wave. The wave speed is 1480 m/s which is approaching the Chapman-Jouguet (CJ) detonation velocity of 1800 m/s calculated from chemical equilibrium for a fully developed detonation. The observed pressure ratio, $P_{max}/P_0$, is approximately 7, which also is approaching the pressure ratio calculated for the von Neumann state of the CJ detonation, $P_N/P_0 = 11$. The peak pressure caused by the detonation wave is extremely high (~600 bar), which would certainly cause damaging thermal and mechanical stresses to the engine cylinder. The spherical hot-spot did not develop into a detonation wave because the divergence caused by the curvature of the hot-spot at small radii quickly dissipates any pressure wave resulting from the exothermicity of the reaction. This comparison illustrates the importance of including the effects of curvature in one-dimensional calculations of hot-spot ignition.

---

[3] Note that the mixture ignites well before the turbulent flame front would have arrived to consume the end-gas. Based on this ignition delay and the engine speed (1500 rpm), end-gas autoignition occurs at 7 cad atc, which is well before the turbulent flame would have consumed the end-gas (20 cad atc), see Figure 4.4.

Figure 4.8 through Figure 4.16 show the effect of increasing the size of the spherical hot-spot in increments of 2.5 mm. As the size of the hot-spot increases, the effects of curvature on the development of pressure waves decreases. At some critical hot-spot size, the divergence effect will have diminished to the extent that a detonation wave can be formed. In the series of plots between Figure 4.9 and Figure 4.12 ($L_{hot}$ = 2.5-10 mm), we see increasingly high pressures during the ignition event. This is caused by the increasing amount of high-temperature gas contained in the hot-spot and the decreasing effect of curvature at the boundary of the hot-spot. In Figure 4.12 ($L_{hot}$ = 10 mm), we start to see the formation of a pressure wave that resembles a developing detonation, however, this pressure wave is eventually quenched as it detaches from the reaction front and runs ahead. This quenching is also seen (with higher peak pressures) in Figure 4.13 for $L_{hot}$ = 12.5 mm. Finally in Figure 4.14 ($L_{hot}$ = 15 mm), we see the formation of a stable detonation wave. And the wave speed (1370 m/s) is approaching the CJ detonation velocity (1800 m/s) and agrees with the wave speed for the planar detonation (1480 m/s). Hence based on these simulations, the critical value of $L_{hot}$ is somewhere between 12.5-15 mm. If we consider the critical hot-spot size ($L_{crit}$) to be $L_{hot}$ + $L_{mix}$ and use the smaller of the two bracketing values for $L_{hot}$ to give a conservative underestimate, we find $L_{crit}$ = 2.25 cm. By defining $L_{crit}$ = $L_{hot}$ + $L_{mix}$, we have defined that the hot-spot size to be the point were the temperature is within 37% of the surrounding temperature based on our Gaussian shape. For reference a hot-spot of this size is slightly larger than a standard golf ball ($r$ = 2.13 cm). The remaining plots (Figure 4.15 and Figure 4.16) show the behavior of larger hot-spots ($L_{hot}$ = 17.5-20 mm). For both cases formation of a stable detonation wave is also observed. Figure 4.16, which shows the

simulation for the largest spherical hot-spot ($L_{hot}$ = 20 mm), closely resembles the planar

calculation for the same size hot-spot. This comparison shows that the importance of

curvature is no longer significant for hot-spots larger than approximately 20 mm.

**Figure 4.6:** Representative contours of temperature, pressure, velocity, and fuel mass fraction for a deflagration initiated at a hot-spot (SI case, $L_{hot}$ = 0 mm). The apparent flame speed is approximately 43 m/s, typical of this mode of combustion. Contours correspond to instants in time between 0 μs and 500 μs at increments of 50 μs.
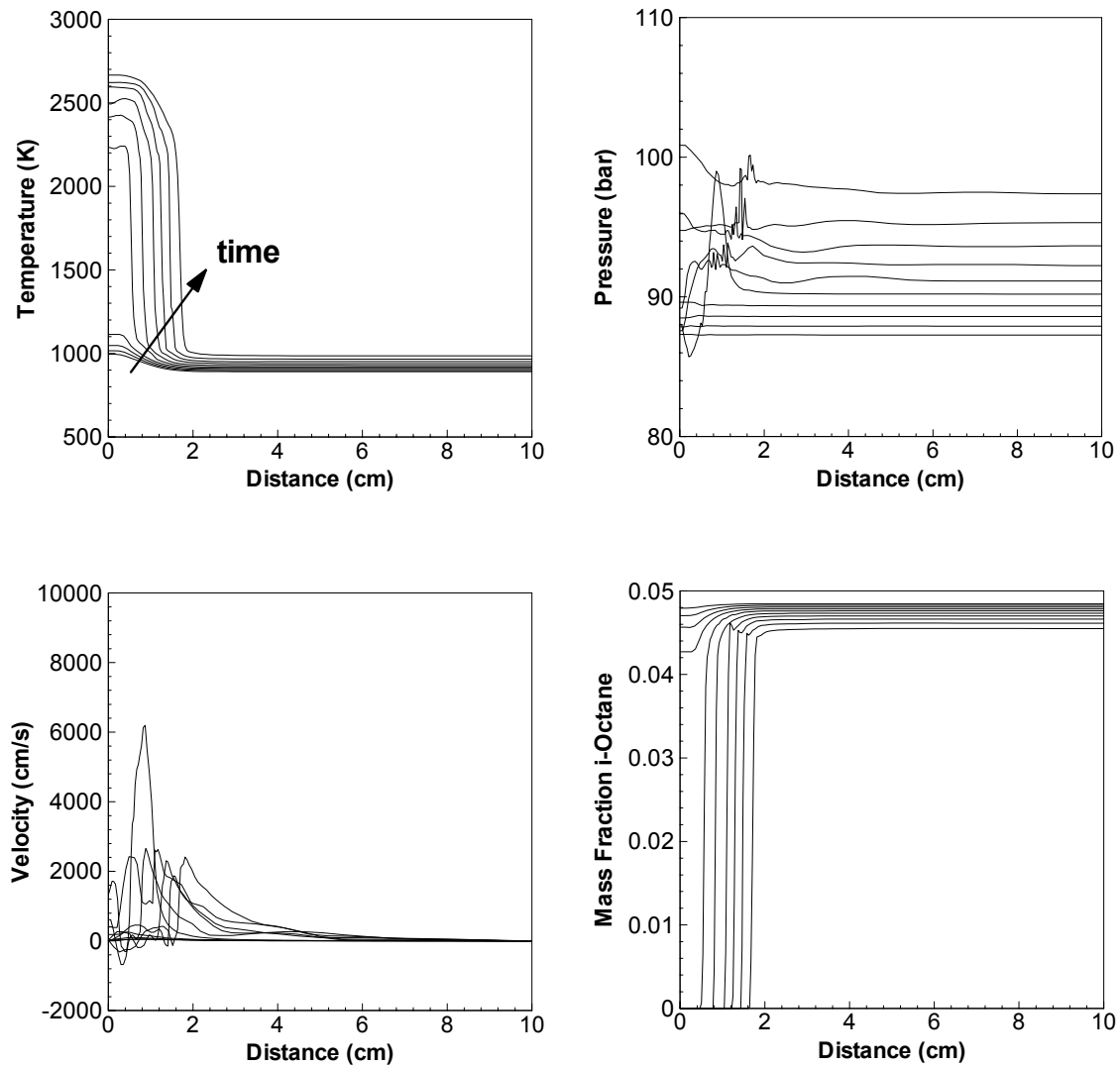
**Figure 4.7:** Ignition of a spherical hot-spot with and propagation of the resulting combustion wave (SI case, $L_{hot}$ = 0 mm). This case resulted in a (subsonic) deflagration wave. Contours correspond to instants in time between 0 μs and 500 μs at increments of 20 μs.
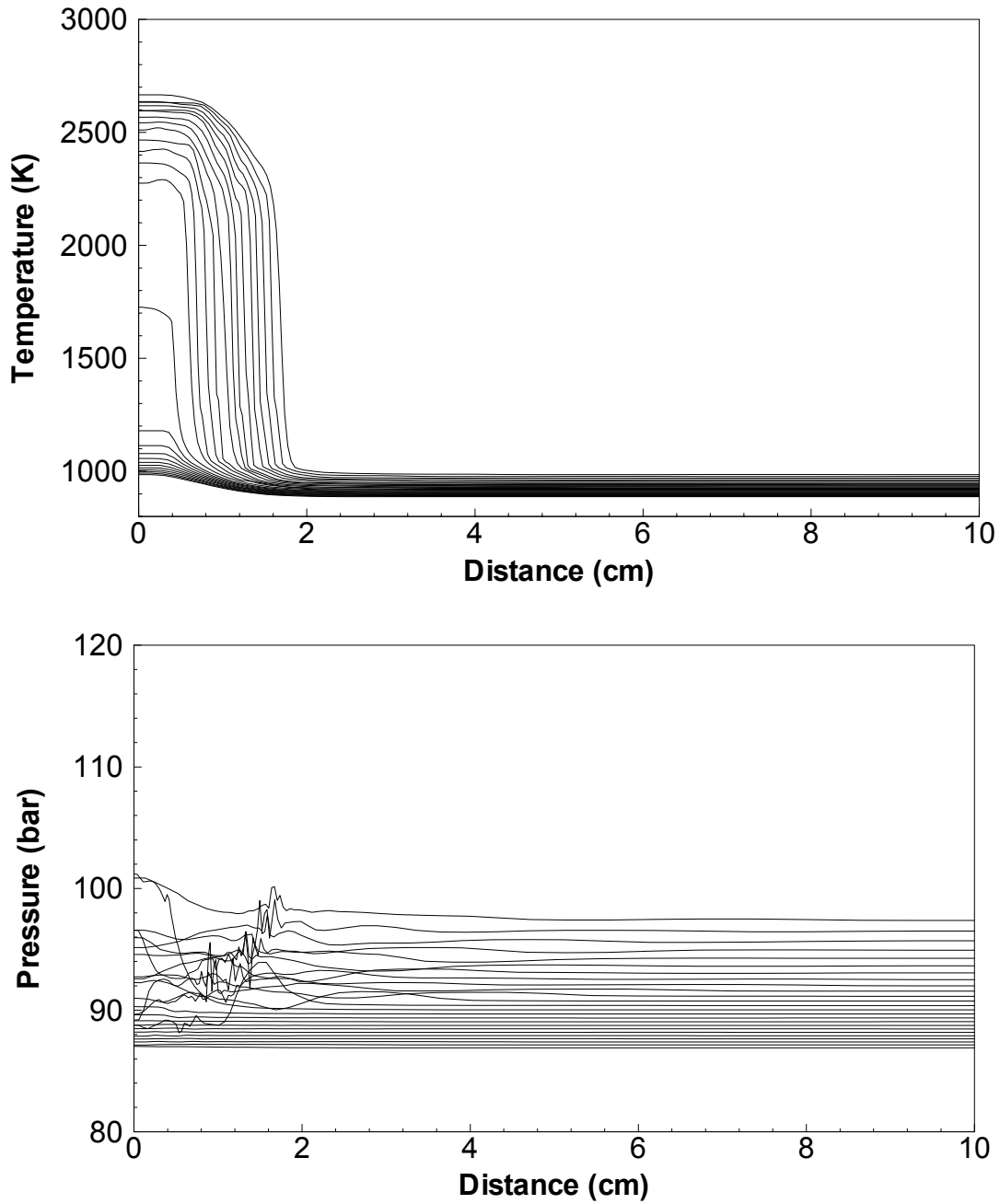
**Figure 4.8:** Ignition of a planar hot-spot with and propagation of the resulting combustion wave (SI case, $L_{hot}$ = 0 mm). The planar case resulted in a detonation wave in contrast to the spherical case shown in Figure 4.7. Contours correspond to instants in time between 0 µs and 280 µs at increments of 10 µs.
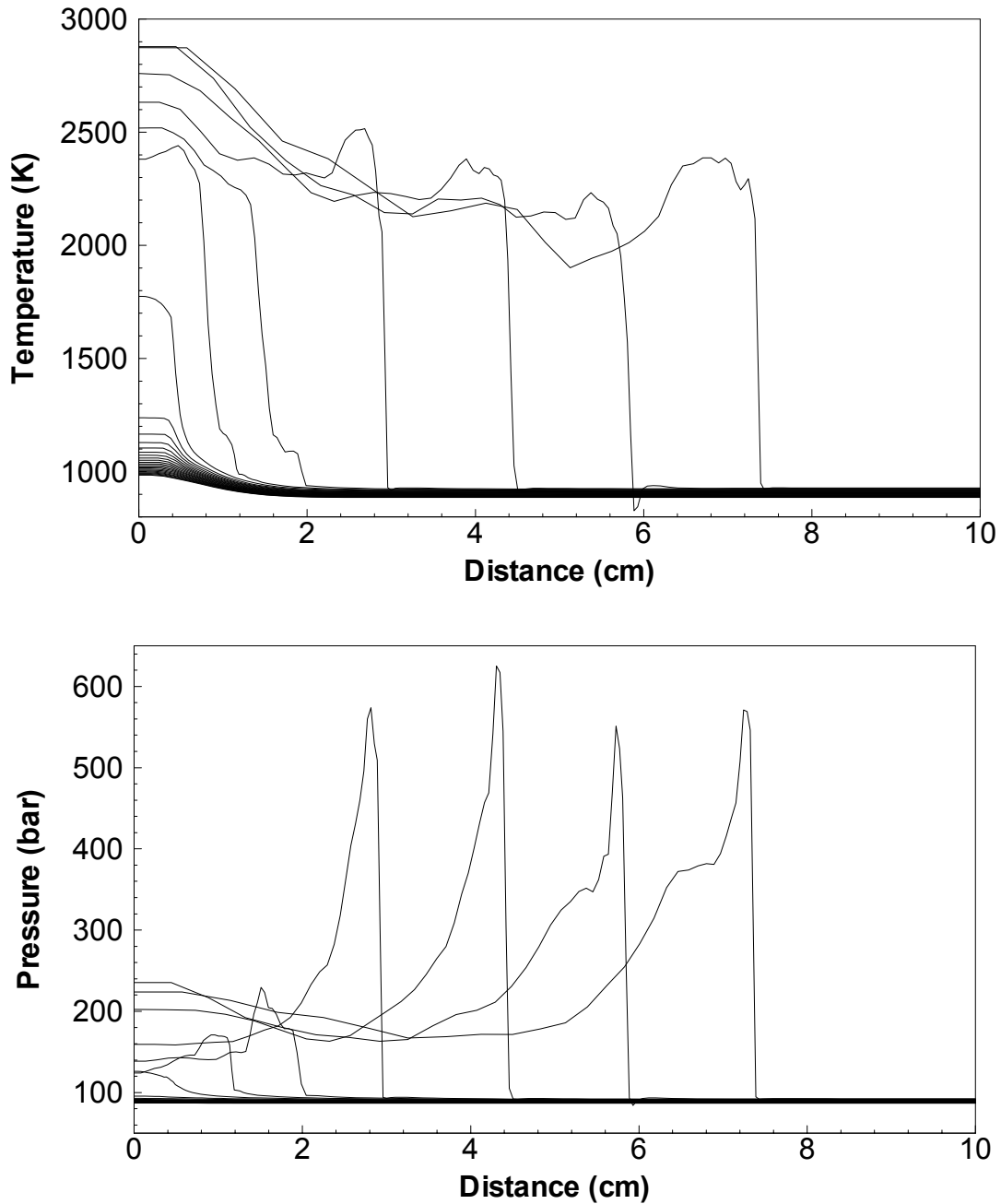
**Figure 4.9:** Ignition of a spherical hot-spot with and propagation of the resulting combustion wave (SI case, $L_{hot}$ = 2.5 mm). This case resulted in a (subsonic) deflagration wave. Contours correspond to instants in time between 0 μs and 440 μs at increments of 20 μs.
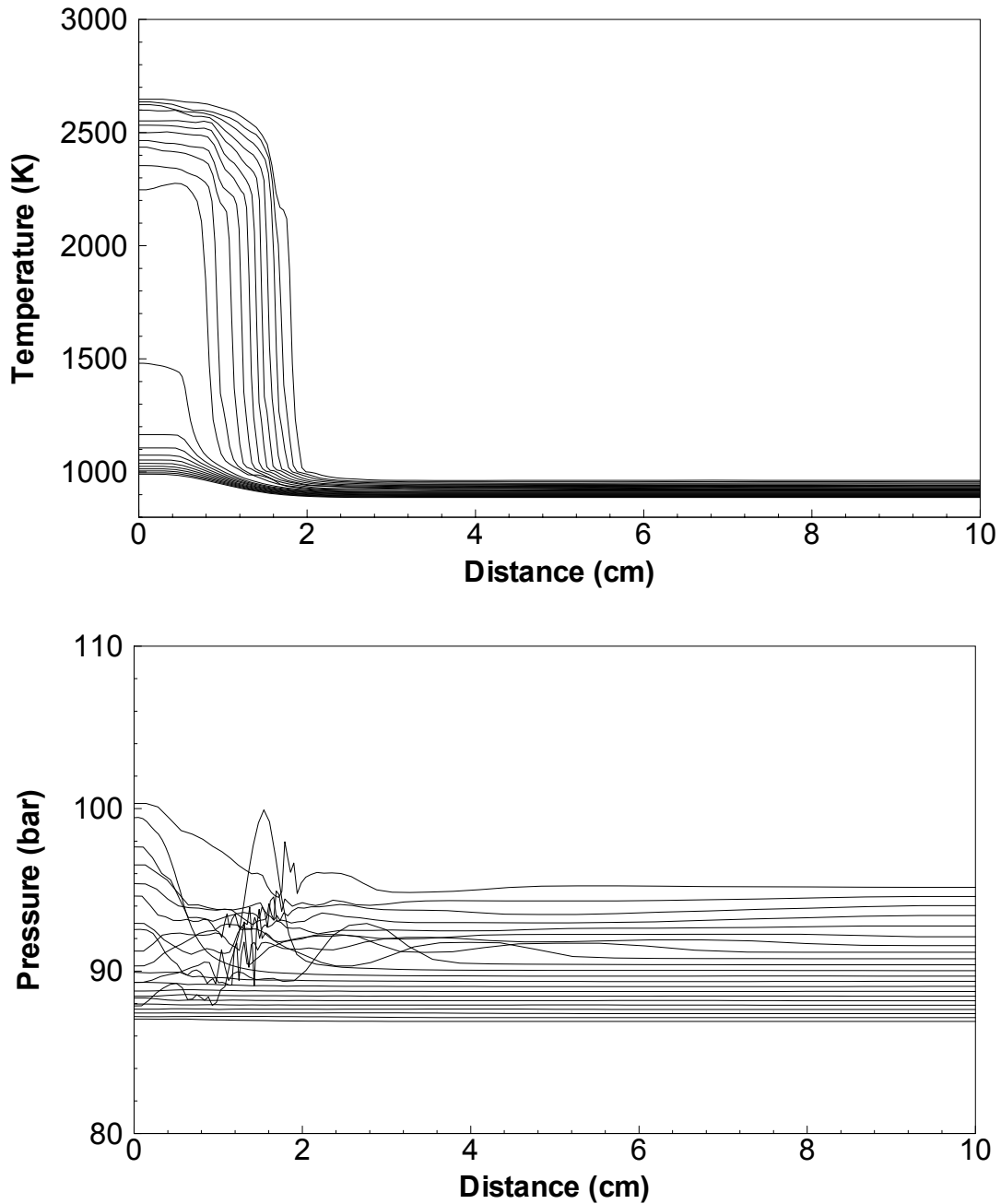
**Figure 4.10:** Ignition of a spherical hot-spot with and propagation of the resulting combustion wave (SI case, $L_{hot}$ = 5 mm). This case resulted in a (subsonic) deflagration wave. Contours correspond to instants in time between 0 μs and 360 μs at increments of 20 μs.
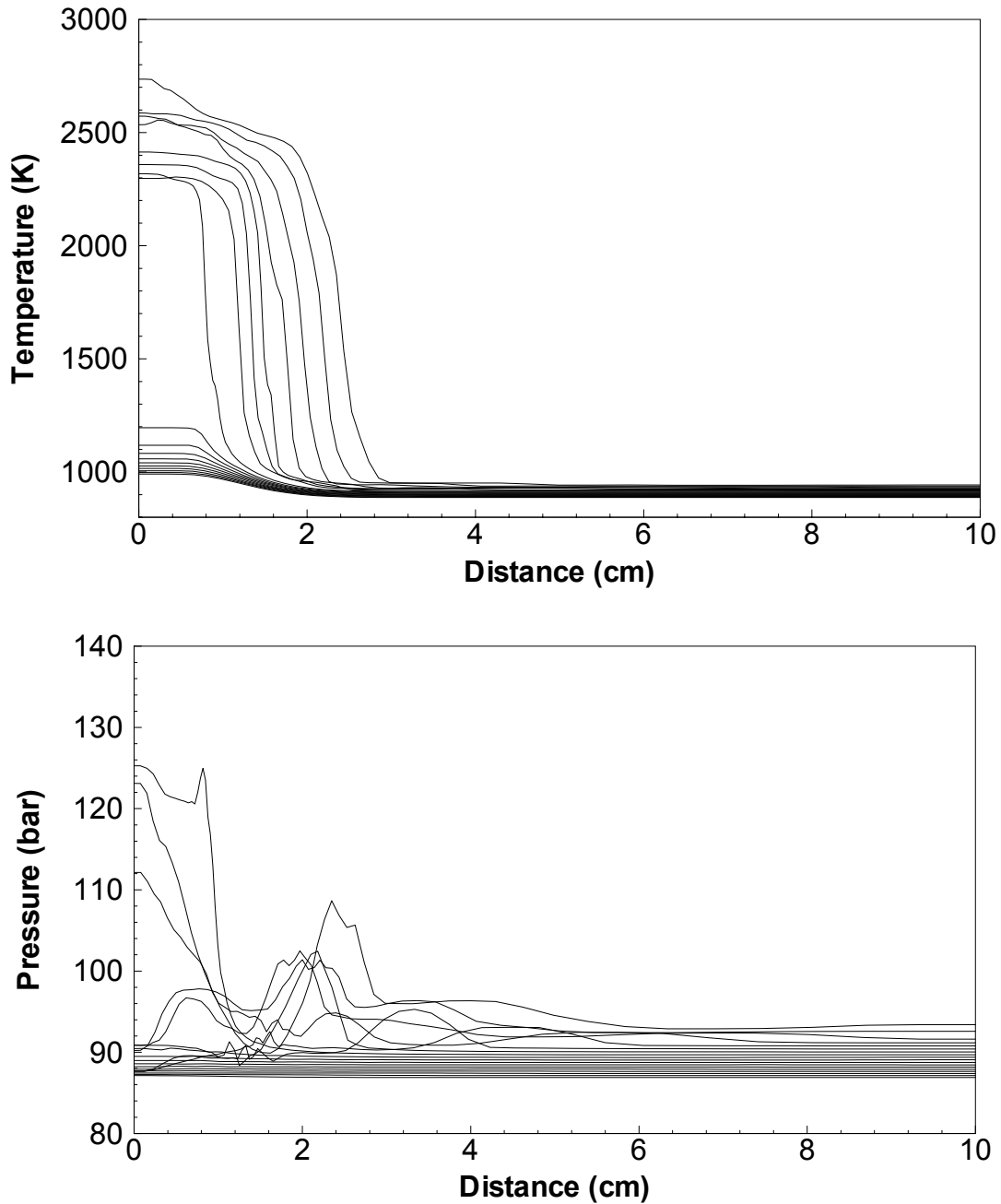
**Figure 4.11:** Ignition of a spherical hot-spot with and propagation of the resulting combustion wave (SI case, $L_{hot}$ = 7.5 mm). This case resulted in a (subsonic) deflagration wave. Contours correspond to instants in time between 0 µs and 540 µs at increments of 20 µs.
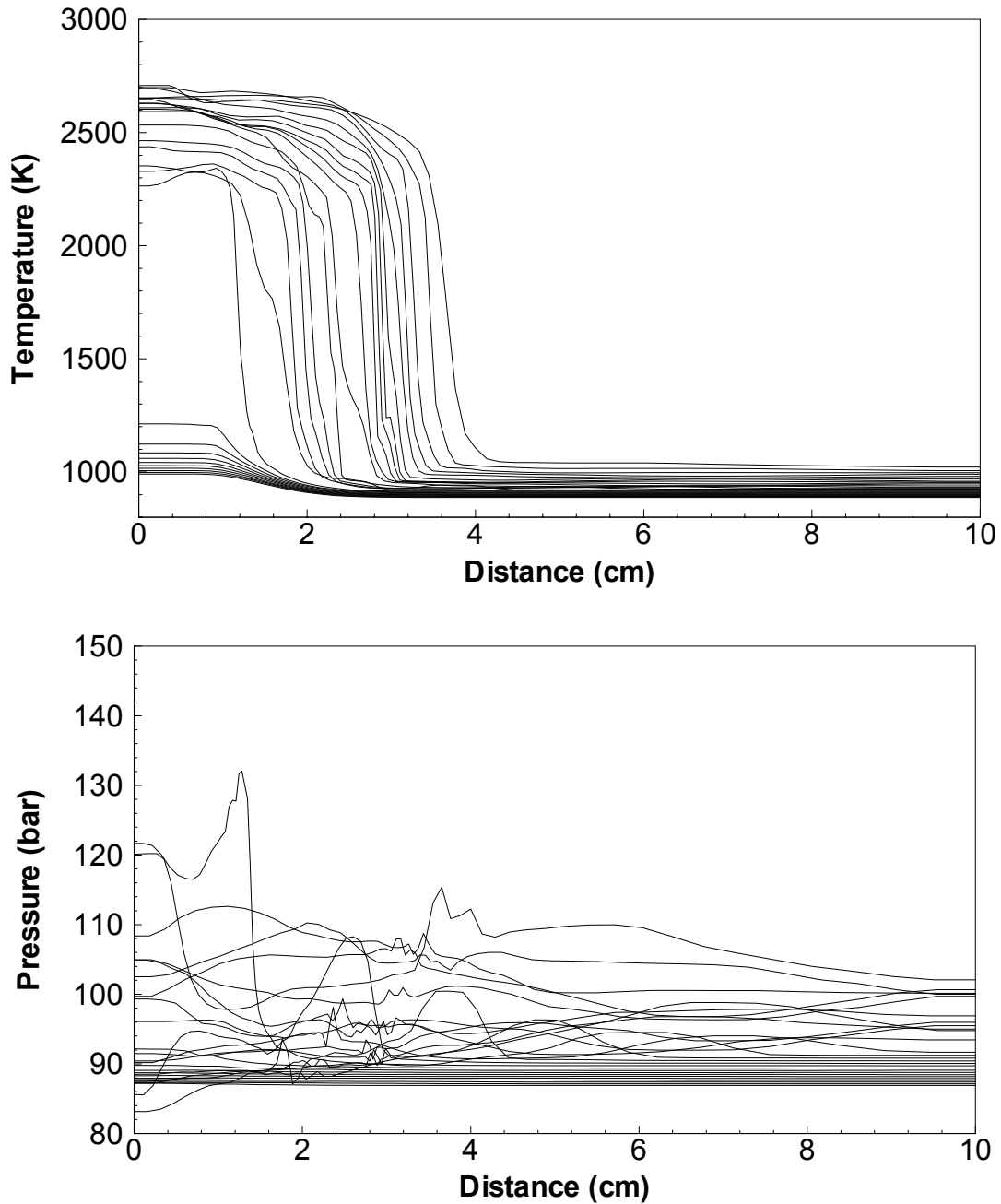
**Figure 4.12:** Ignition of a spherical hot-spot with and propagation of the resulting combustion wave (SI case, $L_{hot}$ = 10 mm). This case initially resulted in high local pressures, but eventually formed a deflagration as the shock wave outran the flame. Contours correspond to instants in time between 0 μs and 250 μs at increments of 10 μs.
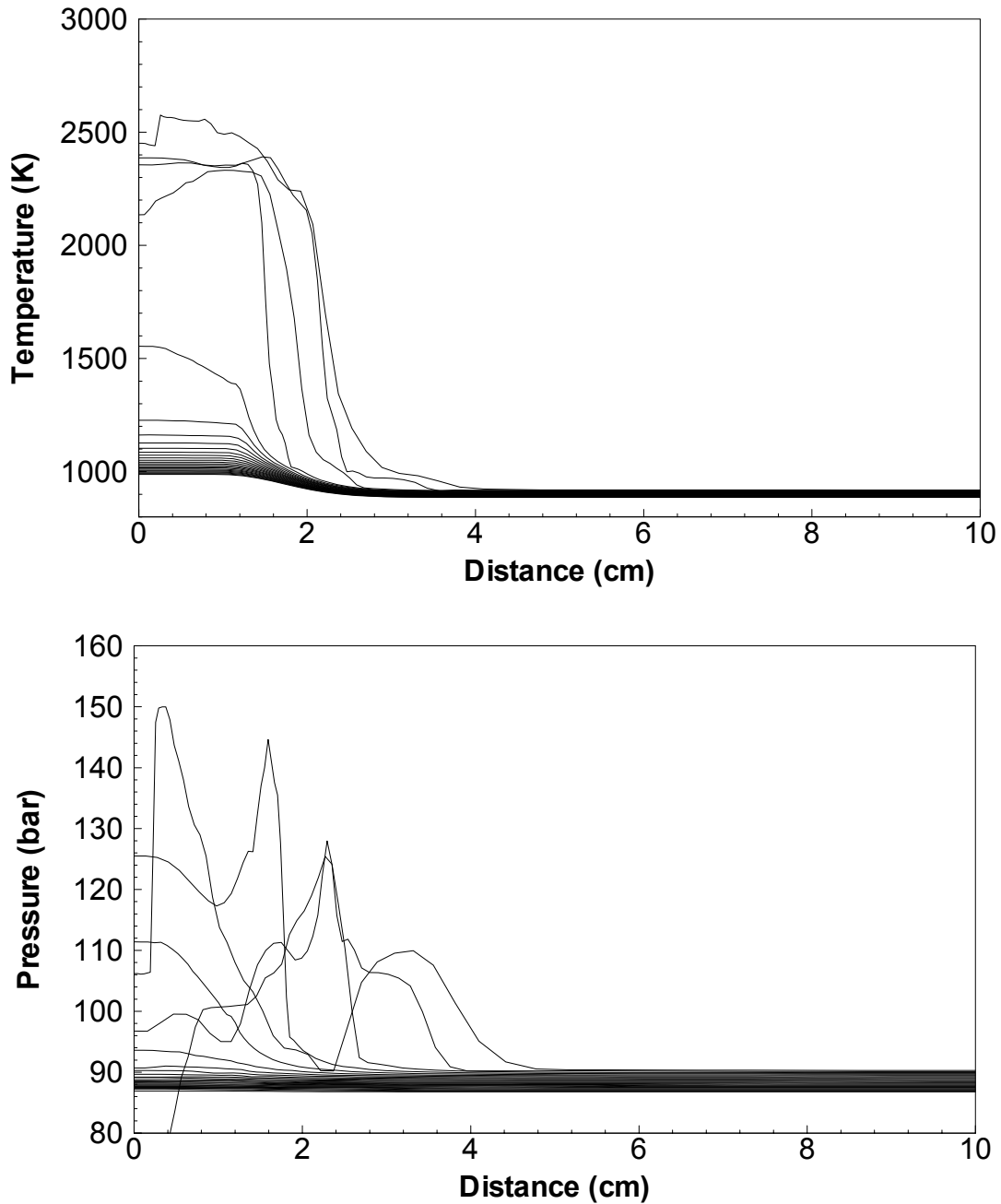
**Figure 4.13:** Ignition of a spherical hot-spot with and propagation of the resulting combustion wave (SI case, $L_{hot}$ = 12.5 mm). This case initially resulted in high local pressures, but eventually formed a deflagration as the shock wave outran the flame. Contours correspond to instants in time between 0 μs and 280 μs at increments of 10 μs.
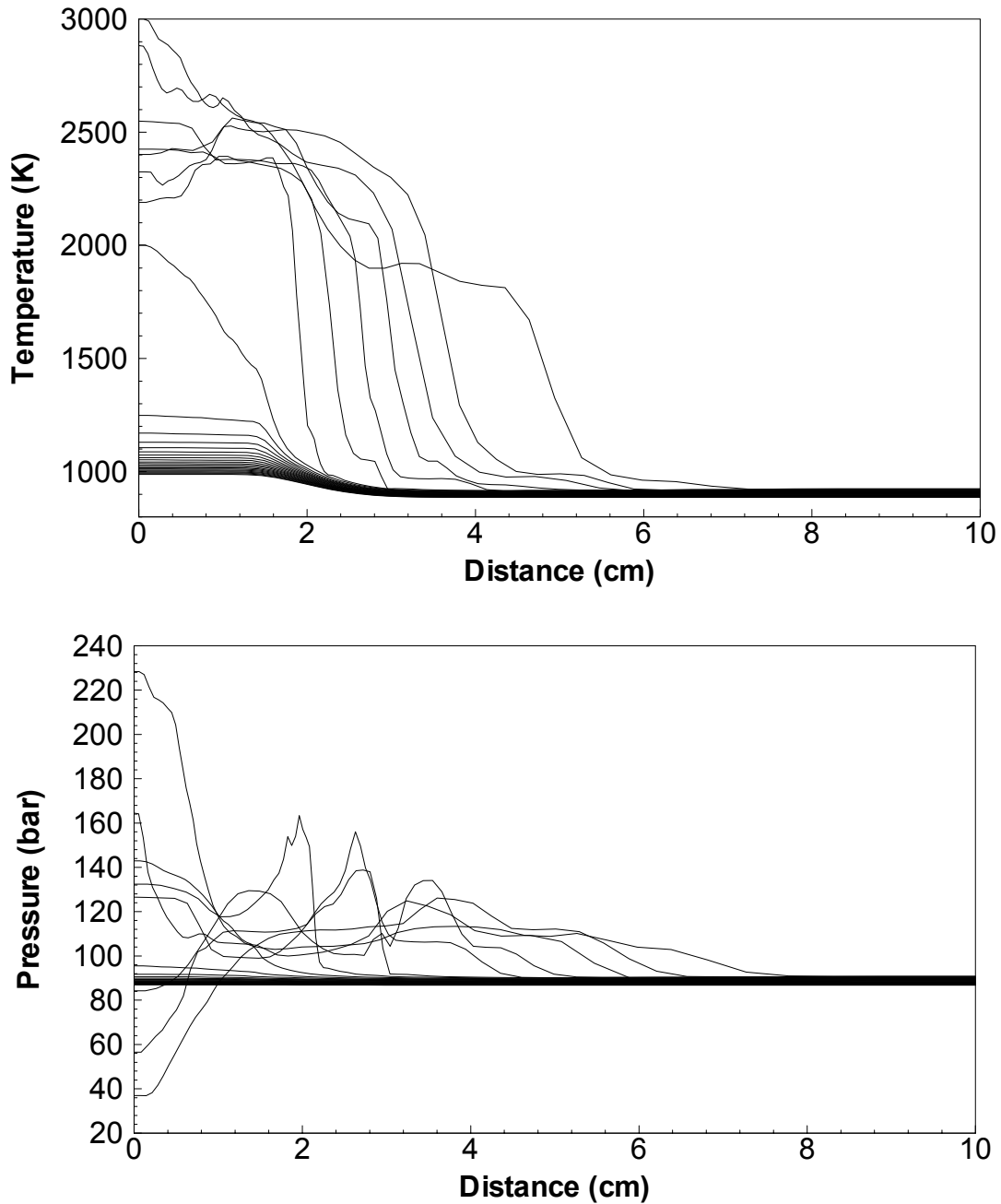
**Figure 4.14:** Ignition of a spherical hot-spot with and propagation of the resulting combustion wave (SI case, $L_{hot}$ = 15 mm). This case resulted in the formation of a spherical detonation wave. Contours correspond to instants in time between 0 μs and 270 μs at increments of 10 μs.
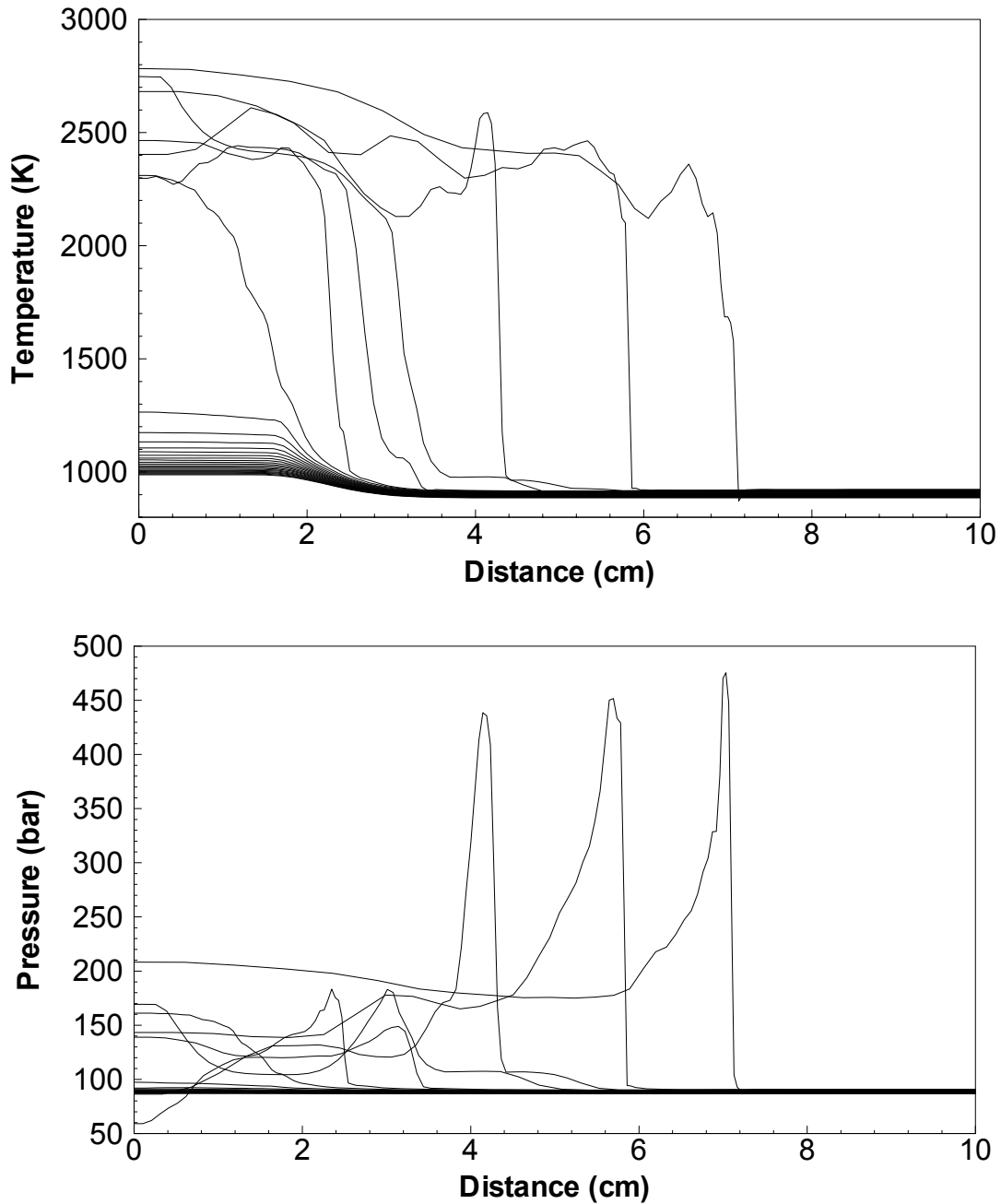
**Figure 4.15:** Ignition of a spherical hot-spot with and propagation of the resulting combustion wave (SI case, $L_{hot}$ = 17.5 mm). This case resulted in the formation of a spherical detonation wave. Contours correspond to instants in time between 0 μs and 270 μs at increments of 10 μs.
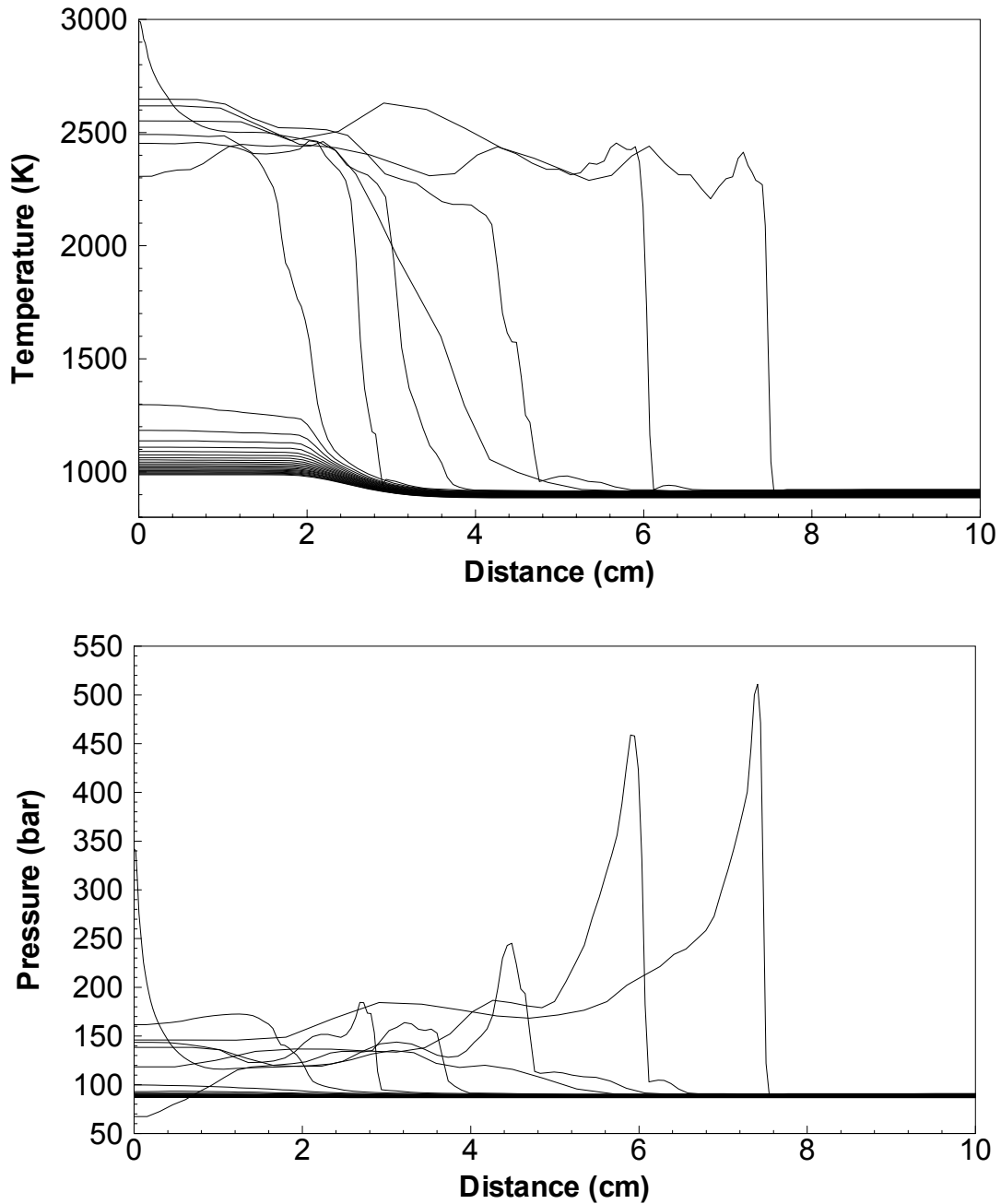
**Figure 4.16:** Ignition of a spherical hot-spot with and propagation of the resulting combustion wave (SI case, $L_{hot}$ = 20 mm). This case resulted in the formation of a spherical detonation wave. Contours correspond to instants in time between 0 μs and 280 μs at increments of 10 μs.
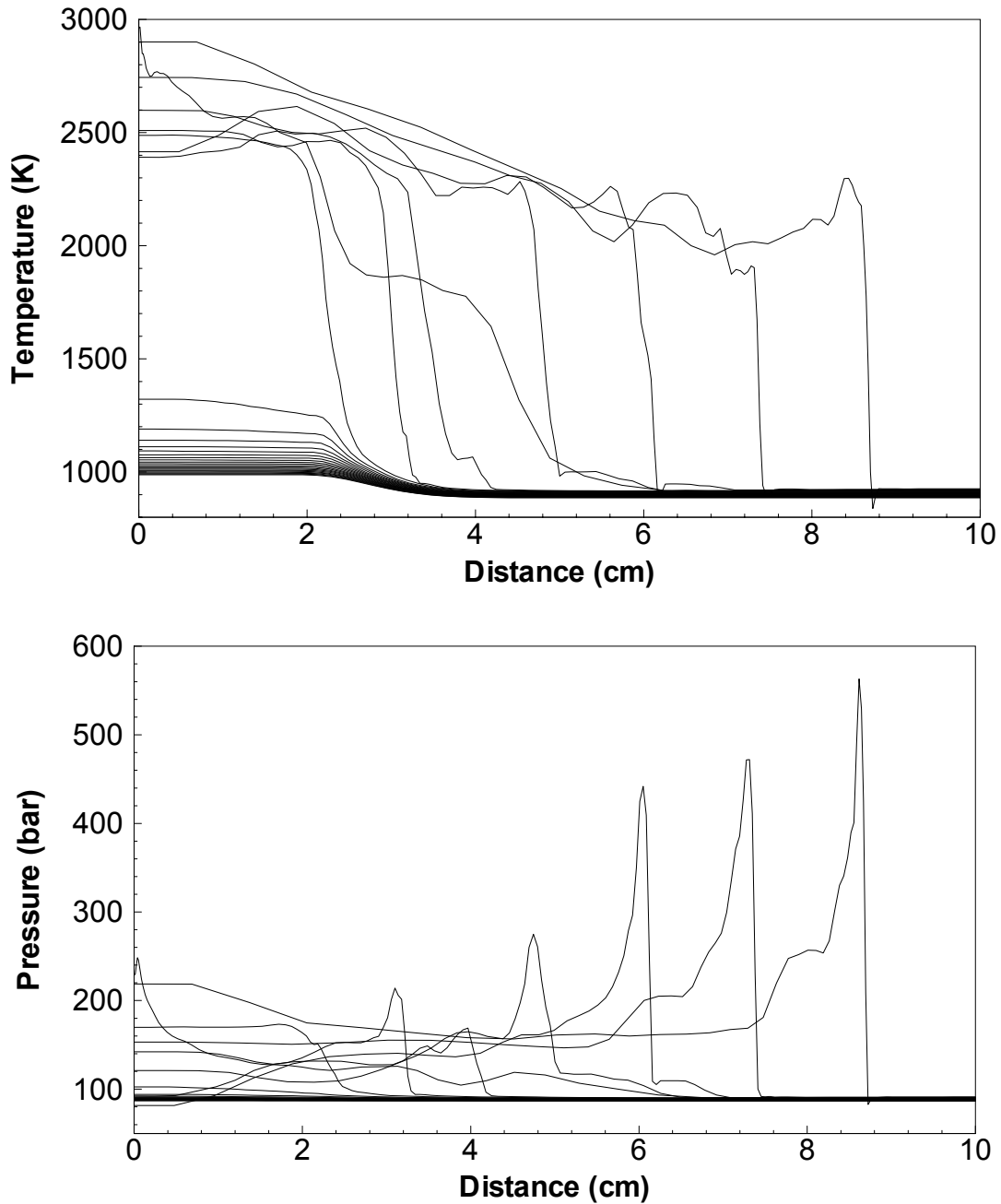
## 4.3.1.2 Sensitivity to Initial Conditions for Numerical Simulations

*Estimation of $L_{mix}$ and $\Delta T$*

The largest uncertainty in the parameters used in these calculations comes from the hot-spot intensity ($\Delta T$) and the size of the hot-spot mixing region ($L_{mix}$). Consequently a series of calculations was performed to determine the sensitivity of our predicted critical hot-spot radius to these parameters. When $\Delta T$ was decreased from 100 K to 50 K, we observed that the predicted critical radius decreased from 2.25 cm to 1.75 cm. When $L_{mix}$ was decreased from 1 cm to 0.25 cm, the critical radius increased to greater than 3 cm (i.e. no spherical detonations were observed even for the largest hot-spot considered). Planar calculations for both of these cases all lead to detonation regardless of hot-spot size.

*Cylindrical Hot-Spot geometry*

Because the squish (i.e. the distance between piston and cylinder head) is typically about 1 cm, large hot-spots would not be able to expand in the axial direction. In this case, the propagation of the hot-spot would be nearly cylindrical and the effect of curvature would be decreased. To estimate the effect of geometry on our prediction of critical hot-spot radius, a series of cylindrical calculations were performed for the SI case. These simulations predicted that the critical radius for a cylindrically-expanding hot-spot is 1.75 cm. As expected, this radius is slightly smaller than the 2.25 cm radius predicted for the spherical case.

*Typical compression ratio and spark-advance*

We asserted that our predictions for the critical radius for the SI case were conservative underestimates because of our choice of somewhat severe engine parameters (high compression ratio, $r_c = 12$; early spark timing, 30 cad btc). In order to test this

144

assertion, a modified SI case was run with more typical engine parameters (compression ratio = 10, spark advance = 20 cad). This modified SI case predicted a critical spherical hot-spot radius of greater than 3cm, which was the largest hot-spot considered. Therefore, the actual critical radius for a more-typical SI engine is larger than that predicted by our calculations.

### 4.3.1.3 Theoretical Calculations

This section describes a series of theoretical calculations performed using the methodology presented in Section 4.2.6 and using the parameters given in Eq. (1.23) for an SI engine. The goal of the theoretical calculations is to confirm the critical radius predicted by the numerical simulations. Based on the numerous additional assumptions, the agreement is not expected to be better than order-of-magnitude.

Figure 4.17 shows that for small hot-spots ($L_{hot}/l_{cjo}$ = 0) the Zel'dovich criterion, Eq. (1.25), is satisfied at two points (marked $R_z$). Additionally, both points are smaller than the critical radius for detonation propagation given by Eq. (1.21) and denoted by $R_c$. This result means that although a detonation could initiate at $R_{z,a}$ or $R_{z,b}$, there is no mechanism by which it can stably propagate in the region between $R_z$ and $R_c$. Consequently a stable detonation wave could not form for a hot-spot of size $L_{hot}/l_{cjo}$ = 0. Here, the critical size is made dimensionless by the thickness of a CJ detonation wave. At the end of this section, this thickness will be estimated to allow comparison of the theoretical predictions with the numerical simulations.

Figure 4.18 shows that for a hot-spot of size $L_{hot}/l_{cjo}$ = 25, $R_{z,b}$ is only slightly less than $R_c$. In Figure 4.19 ($L_{hot}/l_{cjo}$ = 50), $R_{z,b}$ is now larger than $R_c$, which means that a detonation formed at the low-temperature Zel'dovich point ($R_{z,b}$) would be stable. Based

on our criterion that $R_z > R_c$, we conclude that the critical hot-spot dimension is in the range $L_{hot}/l_{cjo}$ = 25-50. In these calculations the mixing length was taken as $L_{mix} = 100 l_{cjo}$. Again defining the critical hot-spot size as $L_{crit} = L_{hot} + L_{mix}$, gives a theoretical estimate of $L_{crit} = 125 l_{cjo}$.

As $L_{hot}/l_{cjo}$ is further increase, Eq. (1.21) demonstrates incredibly rich behavior. Figures 4.17-4.19 are all fairly similar and the only difference is that the Zel'dovich points continue to translate to the right as the hot-spot becomes larger. In Figure 4.20 ($L_{hot}/l_{cjo}$ = 125), however, we observed something quite interesting. A second *O*-shaped region demonstrating a solution to Eq. (1.21) appears around the high-temperature Zel'dovich point ($R_{z,a}$). This shows that a detonation that initiated at $R_{z,a}$ could stably propagate for a short time, but would eventually be quenched because of instability caused by the temperature gradient, which causes the reaction front to move away from the shock wave as discussed in Section 4.2.6. As in previous plots the condition $R_{z,b} > R_c$ is also met.

As the hot-spot becomes larger still, as shown in Figures 4.21-22 ($L_{hot}/l_{cjo}$ = 150-200), the size of the *O*-shaped region increases and eventually connects to the *C*-shaped curve (Figure 4.22, $L_{hot}/l_{cjo}$ = 175). Hence when $L_{hot}/l_{cjo} > 175$ both detonations initiated at both the high-temperature and low-temperature Zel'dovich points can form stable detonation waves because $R_{z,a} > R_c$ and $R_{z,b} > R_c$. This brings about the question as to whether $R_{z,a} > R_c$ or $R_{z,b} > R_c$ is the appropriate criterion to determine the critical hot-spot size. It seems likely $R_{z,a} > R_c$ is the more appropriate criterion because $R_{z,a}$ is the point that ignites first; if a detonation begins at $R_{z,a}$ it will likely induce combustion at $R_{z,b}$ before $R_{z,b}$ could spontaneously ignite. Even the weaker shock wave caused by the

146

spontaneous combustion of the hot core might be enough to induce a significant change in $d\tau_i/dr$ at $R_{z,b}$. Thus taking $L_{crit}$ = (150 + 100)$l_{cjo}$ also seems reasonable. Since we expect the theoretical calculations to be no more than an order-of-magnitude estimate of the critical hot-spot size we simply conclude that the theoretical estimate of the critical hot-spot size, $L_{crit}$, is in the range of 125 to 250 times the thickness of a planar CJ detonation wave.

In order to dimensionalize this estimate of $L_{crit}$, the thickness of a planar CJ detonation under these conditions, $l_{cjo}$, needs to be estimated. The first step was to estimate the Mach number for a CJ detonation, $M_{cjo}$, using the classical formula (see Thompson [43] for a derivation).

$$M_{cjo} = \sqrt{h_0 + 1} + \sqrt{h_0}, \qquad h_0 = \frac{\gamma^2 - 1}{2\gamma} \frac{Q}{RT_0}. \tag{1.27}$$

Then velocity, pressure, and temperature in the von Neumann state were calculated from the normal shock relations giving $T_{NCJO}$ = 1700 K, $p_{NCJO}$ = 900 bar, and $\upsilon_{NCJO}$ = 317 m/s. Note that $\upsilon_{NCJO}$ is the velocity relative to the leading shock wave. The ignition delay in the von Neumann state, $\tau_i = \tau_i(T_{NCJO}, p_{NCJO})$, is estimated using shock tube data from Vermeer, Meyer, and Oppenheim [44] for stoichiometric iso-octane/air mixtures with 70% argon dilution. This estimated ignition delay is only a rough estimate because $p_{NCJO}$ is outside of the range of pressures measured by Vermeer and coworkers. Consequently, the data had to be extrapolated to higher pressures, but fortunately the ignition delay is a rather weak function of pressure as shown by Vermeer's measurements in the range 2-22 atm. This lack of data for the ignition delay, which we estimate as $\tau_i \approx 0.3\mu s$, still undoubtedly limits the accuracy of our calculations.

Once the ignition delay is known, the length of the planar CJ detonation can be estimated as

$$l_{cjo} = \tau_i \upsilon_{NCJO}. \tag{1.28}$$

Under SI engine conditions, we estimate the thickness of a CJ detonation to be $l_{cjo} \approx 0.1\,\text{mm}$. Hence the critical hot-spot size, which we calculated to be 125 to 250 times $l_{cjo}$, corresponds to $L_{crit} \approx 1.25 - 2.5\,\text{cm}$. This estimate agrees remarkably well with the estimate determined by the numerical simulations in the previous section ($L_{crit,numerical}$ = 2.25 cm); however, we consider this agreement to be somewhat fortuitous because of the degree of uncertainty in determining $l_{cjo}$. The order-of-magnitude agreement does, however, give us confidence that the critical hot-spot sizes that we calculate are legitimate and not merely an artifact of our numerical technique.

**Figure 4.17:** Theoretical calculations of spherical detonation wave initiation and propagation ($L_{hot}/l_{cjo} = 0$, where $l_{cjo}$ is the thickness of a CJ detonation). The *C*-shaped curve is the solution to Eq. (1.21). $R_c$ is the minimum radius for which a detonation wave can stably propagate. $R_{z,a}$ and $R_{z,b}$ are the two points where the Zel'dovich criterion for detonation initiation, Eq. (1.25), is satisfied. A stable detonation could not form in this case because $R_{z,a} < R_c$ and $R_{z,b} < R_c$.
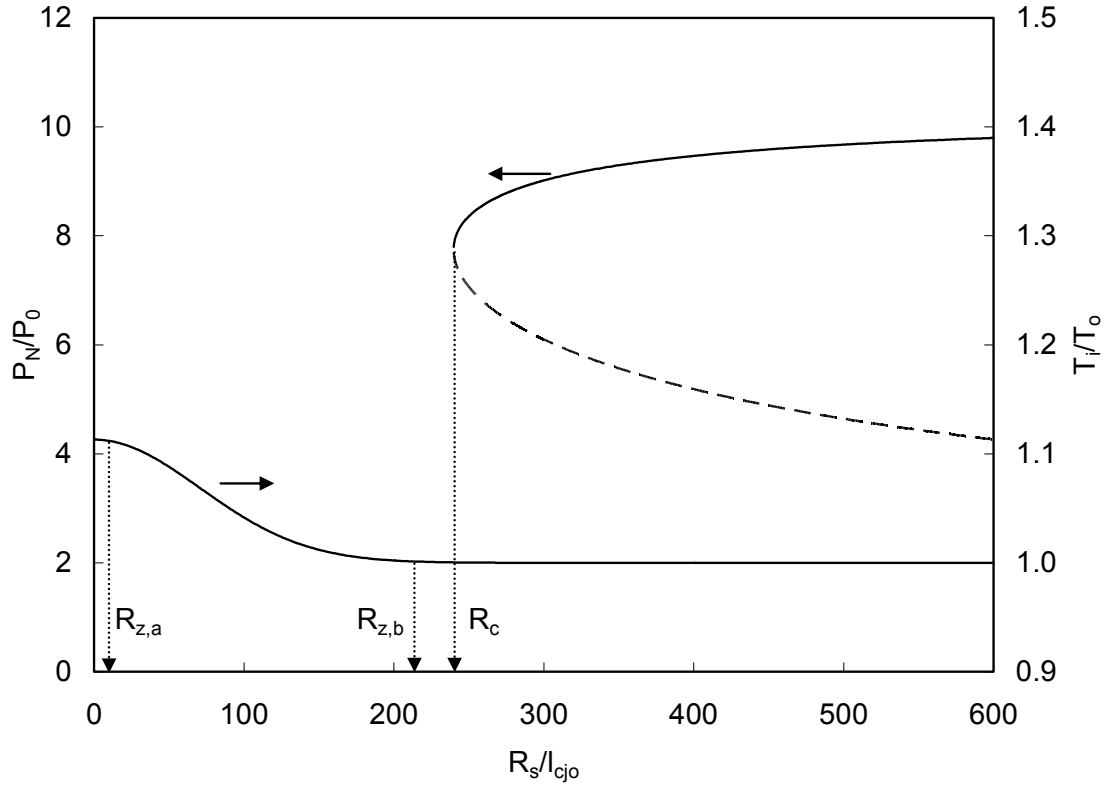
**Figure 4.18:** Theoretical calculations of spherical detonation wave initiation and propagation ($L_{hot}/l_{cjo} = 25$, where $l_{cjo}$ is the thickness of a CJ detonation). The *C*-shaped curve is the solution to Eq. (1.21). $R_c$ is the minimum radius for which a detonation wave can stably propagate. $R_{z,a}$ and $R_{z,b}$ are the two points where the Zel'dovich criterion for detonation initiation, Eq. (1.25), is satisfied. A stable detonation could not form in this case because $R_{z,a} < R_c$ and $R_{z,b} < R_c$; however, $R_{z,b}$ is very close to $R_c$.
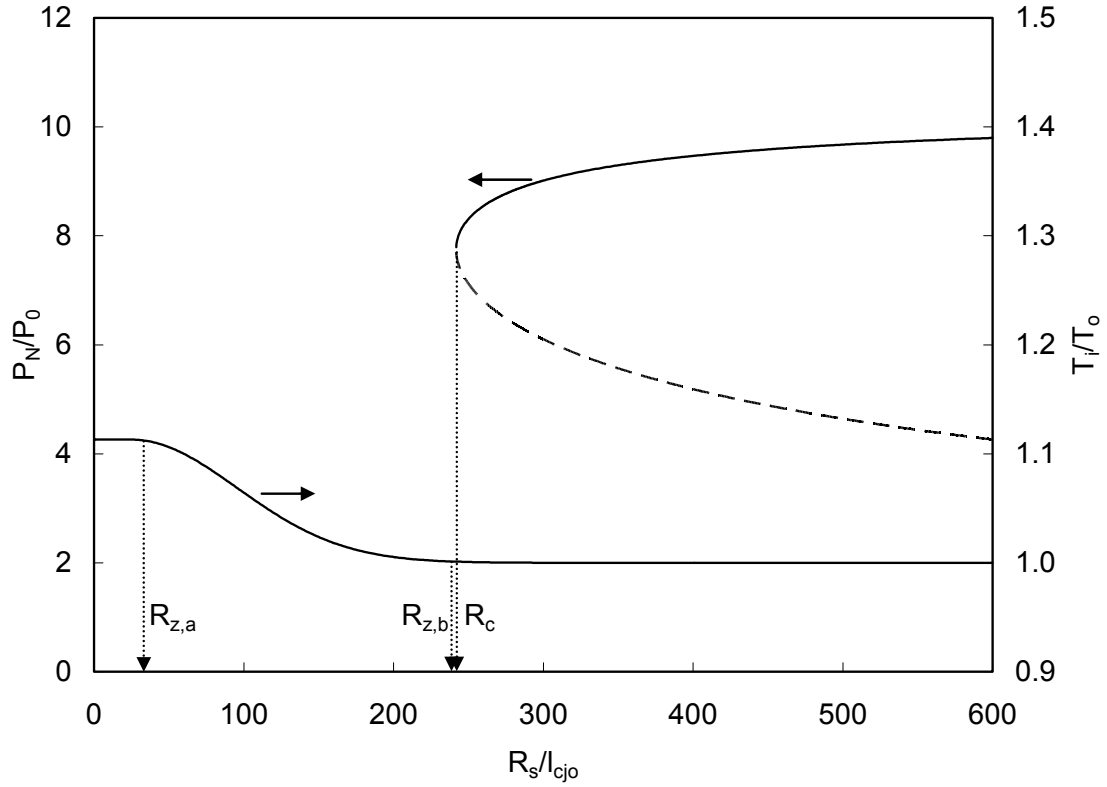
**Figure 4.19:** Theoretical calculations of spherical detonation wave initiation and propagation ($L_{hot}/l_{cjo} = 50$, where $l_{cjo}$ is the thickness of a CJ detonation). The *C*-shaped curve is the solution to Eq. (1.21). $R_c$ is the minimum radius for which a detonation wave can stably propagate. $R_{z,a}$ and $R_{z,b}$ are the two points where the Zel'dovich criterion for detonation initiation, Eq. (1.25), is satisfied. For this size hot-spot, $R_{z,b} > R_c$ so a detonation initiated at $R_{z,b}$ could develop into a stable detonation.
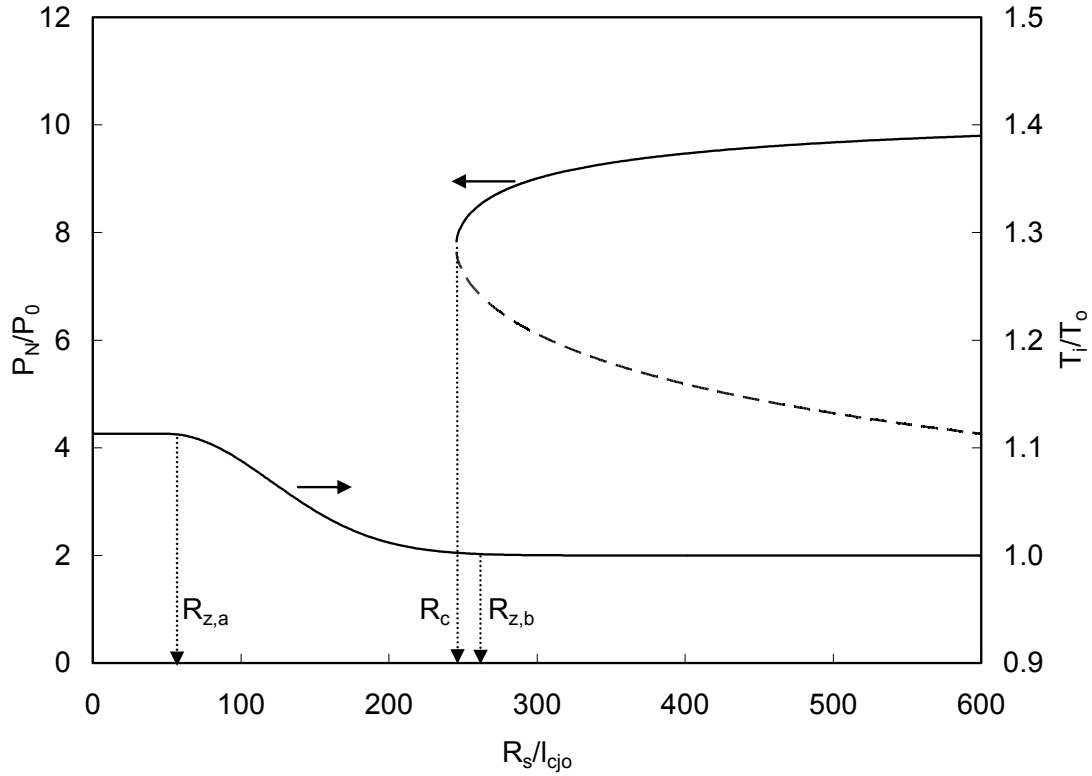
**Figure 4.20:** Theoretical calculations of spherical detonation wave initiation and propagation ($L_{hot}/l_{cjo} = 125$, where $l_{cjo}$ is the thickness of a CJ detonation). The *C*-shaped curve is the solution to Eq. (1.21). $R_c$ is the minimum radius for which a detonation wave can stably propagate. $R_{z,a}$ and $R_{z,b}$ are the two points where the Zel'dovich criterion for detonation initiation, Eq. (1.25), is satisfied. For this size hot-spot, $R_{z,b} > R_{c,b}$ so a detonation initiated at $R_{z,b}$ could develop into a stable detonation. A detonation initiated at $R_{z,a}$ is predicted to propagate stably for short time and then be quenched.
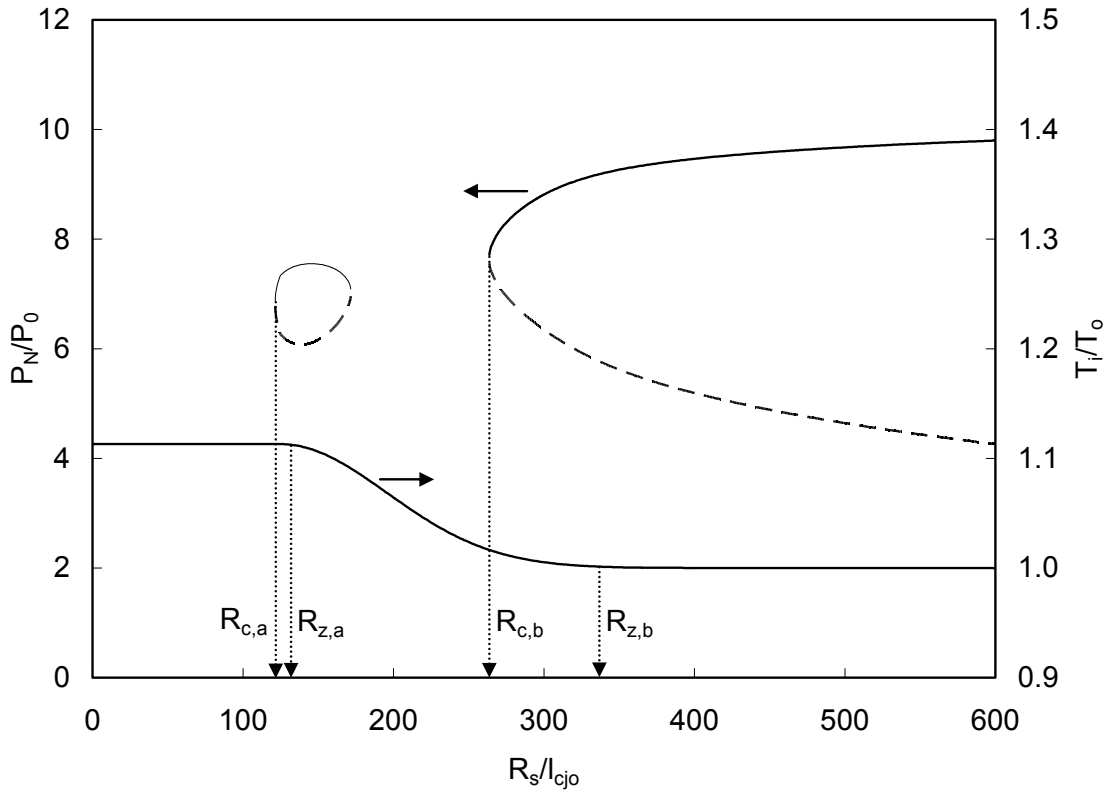
**Figure 4.21:** Theoretical calculations of spherical detonation wave initiation and propagation ($L_{hot}/l_{cjo}$ = 150, where $l_{cjo}$ is the thickness of a CJ detonation). The *C*-shaped curve is the solution to Eq. (1.21). $R_c$ is the minimum radius for which a detonation wave can stably propagate. $R_{z,a}$ and $R_{z,b}$ are the two points where the Zel'dovich criterion for detonation initiation, Eq. (1.25), is satisfied. For this size hot-spot, the interpretation is the same as Figure 4.20, except that the *O*-shaped region has enlarged.
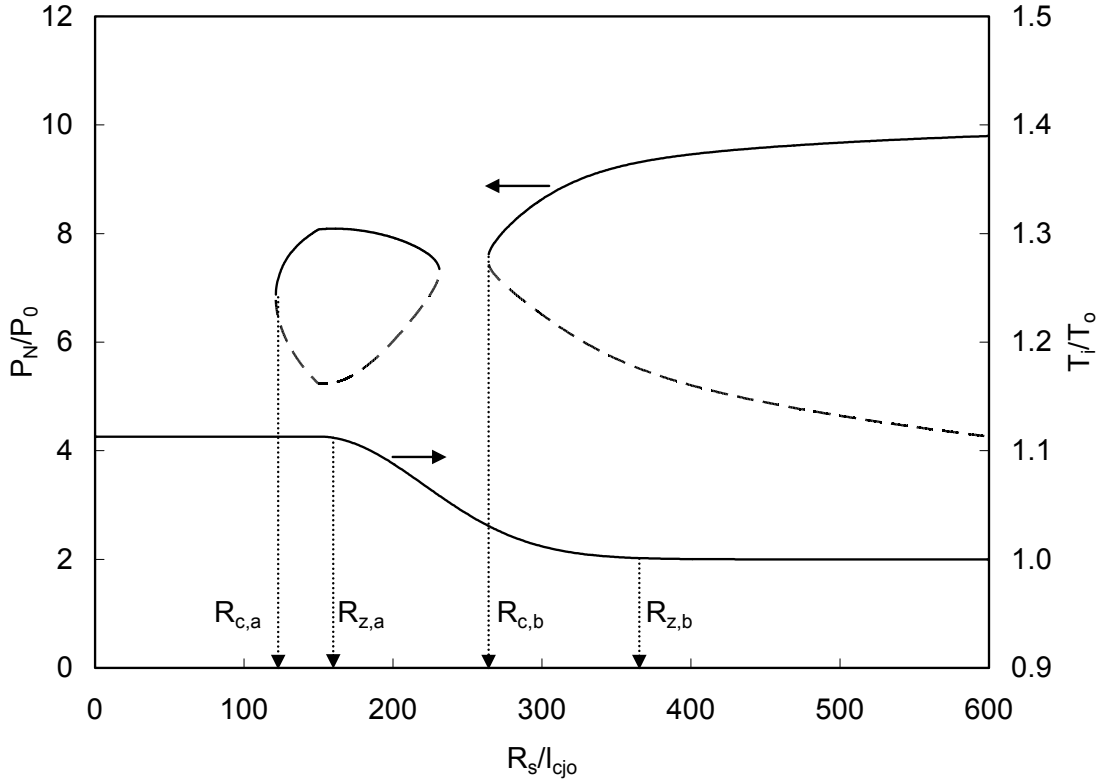
**Figure 4.22:** Theoretical calculations of spherical detonation wave initiation and propagation ($L_{hot}/l_{cjo}$ = 175, where $l_{cjo}$ is the thickness of a CJ detonation). The *C*-shaped curve is the solution to Eq. (1.21). $R_c$ is the minimum radius for which a detonation wave can stably propagate. $R_{z,a}$ and $R_{z,b}$ are the two points where the Zel'dovich criterion for detonation initiation, Eq. (1.25), is satisfied. A stable detonation can only form when $L_{hot}/l_{cjo}$ is large enough such that $R_z > R_c$. For this size hot-spot and larger, the *O*-shaped region and *C*-shaped region have merged. Because $R_{z,b} > R_c$ and $R_{z,b} > R_c$, a detonation initiated at either Zel'dovich point is predicted to form a stable detonation.
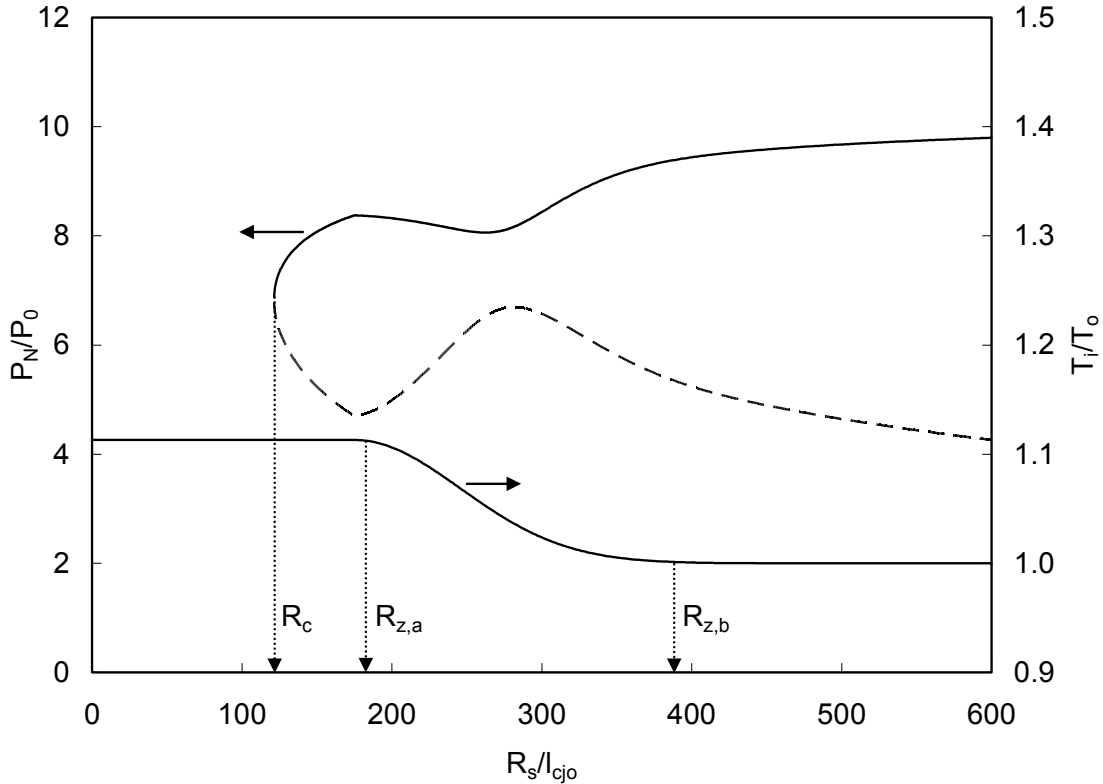


## 4.3.2 HCCI Engine Calculations

This section describes the results of numerical simulations and theoretical calculations of hot-spot ignition and subsequent combustion wave propagation for the homogeneous-charge compression-ignition test case ("HCCI Case" in Tables 4.1 and 4.2).

154

### 4.3.2.1 Numerical Simulations

Numerical simulations were performed in an identical fashion to the SI case using the parameters determined in Section 4.2.5.4 for the HCCI engine of Yang et al. [40] under lightly knocking conditions. No detonation waves were observed in these calculations for both the spherical and planar cases for hot-spots in the range $L_{hot}$ = 0-20 mm. We believe this occurs because the energy-content of the mixture is too low and the ignition kinetics are too slow under lean HCCI conditions ($\phi$ = 0.385). Notice that the temperature is 100 K higher in the HCCI case than the SI case, which is *more* conducive to detonation formation; however, the additional thermal mass from the excess air and residuals still makes the ignition kinetics too slow under HCCI conditions.

To verify that low equivalence ratios could account for the lack of detonation formation in the HCCI case, a series of planar calculations was done at equivalence ratios, $\phi$ = 0.385, 0.5, 0.6, 0.7, 0.8, 0.9, and 1.0. The initial temperature and pressure were the same as those shown in Table 4.2. Detonations were only observed in these calculations for $\phi$ > 0.9. It would be difficult to achieve equivalence ratios this high in HCCI engines without very heavy exhaust gas recirculation because our calculations in Chapter 3 show that knock occurs according to the autoignition theory at significantly lower equivalence ratios ($\phi$ > 0.6).

The only propagation mode observed under HCCI conditions was the deflagration; however, significant local overpressures were still observed for large hot-spots due to the fast autoignition of the end-gas. The pressures ranged from ca. 0.5 bar for $L_{hot}$ = 0 mm to ca. 2.5 bar for $L_{hot}$ = 20 mm. Hence it appears from these calculations that the autoignition theory is sufficient to explain the pressure oscillations observed for these HCCI operating conditions which where reported to cause light knocking.

### 4.3.2.2 Theoretical Calculations

The theoretical calculations for the HCCI case also supported the conclusion that lean mixtures used in HCCI engines cannot support detonation waves. Eq. (1.21) still had a solution with an $R_c \approx 100 l_{cjo}$, but the Zel'dovich criterion, Eq. (1.25), was not satisfied at any radial position. $L_{mix}$ was varied to change the gradient of temperature, but still no solution was found. This observation leads to the conclusion that the ignition kinetics of the mixture are nowhere sufficient to initiate a detonation, in agreement with our numerical simulations.

## 4.4 Discussion

The numerical simulations and theoretical calculations suggest that the critical hot-spot size necessary to form a detonation wave is approximately 4 cm in diameter under SI engine conditions. A recent optical engine study by Schiesl and Maas [21] used laser-induced fluorescence to visualize hot-spots in the end-gas of an SI engine. Those authors observed hot-spots in the size range of 1-10 mm. Bradley [17] reports that "The integral length scale for turbulence in a conventional gasoline engine is ca. 1 mm and the length scale for temperature fluctuations is about half of the integral length scale." Therefore, based on our calculations the critical hot-spot diameter necessary to form a gaseous detonation wave in a spark-ignited engine is approximately an order-of-magnitude larger than those hot-spots observed in engines.

High-speed photography of engine knock from various researchers [4, 5, 8, 11, 12, 15, 16, 21, 45] suggests that the average dimension of the end-gas at the point of knock is approximately 1-2 cm in the direction perpendicular to the advancing flame front. Thus, the critical hot-spot diameter is not only large with respect to observed hot-

spots in the end-gas, but it is also large with respect to the entire end-gas region. Based on this observation it seems unlikely that a detonation wave could form in a spark-ignited engine. This conclusion is also supported by our review of the available experimental data presented in Section 4.2.1.

We believe that a more likely explanation for the local overpressures associated with spark-ignited engine knock is given by the autoignition theory. Our findings do not suggest that there is no interplay between chemical heat-release and development of a pressure wave, but it seems unlikely that interaction ever leads to a substantially developed detonation wave.

In contrast to the spark-ignited engine, the HCCI engine simulations showed no signs of detonation waves under the conditions of our test. Detonation waves were only observed in our calculations at $\phi > 0.9$, which is above the normal HCCI operating limits found by many researchers (e.g. [40, 46, 47]).

## 4.5  Conclusions

- An analysis of high-speed photographic records and pressure traces from knocking cycles in spark-ignition engines suggest that high apparent combustion wave speeds during end-gas autoignition and large pressure oscillations can be explained by thermal explosion of the end-gas rather than formation of detonation waves.

- Numerical reacting flow simulations and theoretical calculations for a quasi-steady detonation wave show that only hot-spots larger than some critical size can initiate detonation waves. This critical size is estimated to 4 cm in diameter for a typical spark-ignited engine under knocking conditions.

- The fuel/air mixtures typically used in homogeneous-charge compression-ignition (HCCI) engines are too lean to support the formation of detonations regardless of hot-spot size. For our initial conditions, an equivalence ratio of $\phi > 0.9$ was necessary to initiate detonation waves.

## 4.6 References

1. Heywood, J.B., *Internal Combustion Engine Fundamentals*. 1988, New York: McGraw-Hill, Inc. pp. 100-107.
2. Sheppard, C.G.W., S. Tolegano, and R. Woolley, *On the Nature of Autoignition Leading to Knock in HCCI Engines*. SAE Technical Paper Series, 2002(2002-01-2831).
3. Peng, Z., H. Zhao, and N. Ladommatos, *Visualization of the homogeneous charge compression ignition/controlled autoignition combustion process using two-dimensional planar laser-induced fluoresncence imaging of formaldehyde*. Proc. Instn Mech. Engrs, Part D: J. Automobile Engineering, 2003. **217**: p. 1125-1134.
4. Konig, G. and C.G.W. Sheppard, *End Gas Autoignition and Knock in a Spark Ignition Engine*. SAE Technical Paper Series, 1990(902135).
5. Miller, C.D., *Knock as Shown by Photographs Taken at 40,000 and 200,00 Frames per Second*. SAE Quarterly Transactions, 1947. **1**(1): p. 99-143.
6. Tanaka, S., et al., *Two-stage ignition in HCCI combustion and HCCI control by fuels and additives*. Combustion and Flame, 2003. **132**: p. 219-239.
7. Lutz, A.E., et al. *Dynamic Effects of Autoignition Centers for Hydrogen and $C_{1,2}$-Hydrocarbon Fuels*. in *Proceedings of the Combustion Institute*. 1998: The Combustion Institute.
8. Pan, J., et al., *End Gas Inhomogeneity, Autoignition and Knock*. SAE Technical Paper Series, 1998(982616).
9. Weber, H.-J., A. Mack, and P. Roth, *Combustion and Pressure Wave Interactions in Enclosed Mixtures Initiated by Temperature Nonuniformities*. Combustion and Flame, 1994. **97**: p. 281-295.
10. Zel'dovich, Y.B., et al., *On the Development of Detonation in a Non-Uniformly Preheated Gas*. Astronautica Acta, 1970. **15**: p. 313-321.
11. Male, T., *Photographs at 500,000 Frames per Second of Combustion and Detonation in a Reciprocating Engine*. Proceedings of the Combustion Institute, 1949. **3**: p. 721-726.
12. Hayashi, T., et al., *Photographic Observation of Knock with a Rapid Compression Expansion Machine*. SAE Technical Paper Series, 1984(841136).
13. Konig, G., et al., *Role of Exothermic Centres on Knock Initiation and Knock Damage*. SAE Technical Paper Series, 1990(902136).
14. Pan, J. and C.G.W. Sheppard, *A Theoretical and Experimental Study of the Modes of End Gas Autoignition Leading to Knock in S.I. Engines*. SAE Technical Paper Series, 1994(942060).
15. Green, R., *An Experimental Study of Engine Knock (Technical Report WSS/CI-84-46)*. 1984, Sandia National Laboratories: Livermore, CA.
16. Smith, J.R., et al. *An Experimental and Modeling Study of Engine Knock*. in *Proceedings of the Combustion Institute*. 1984: The Combustion Institute.
17. Bradley, D., *'Hot spots' and gasoline engine knock*. J. Chem. Soc., Faraday Trans., 1996. **92**(16): p. 2959-2964.

18.     Goyal, G., J. Warnatz, and U. Maas. *Numerical Studies of Hot Spot Ignition in H₂-O₂ and CH₄-Air Mixtures*. in *Proceedings of the Combustion Institute*. 1990: The Combustion Institute.

19.     Goyal, G., U. Maas, and J. Warnatz, *Simulation of the Transition from Deflagration to Detonation.* Society of Automotive Engineers Technical Papers, 1990.

20.     Gu, X.J., D.R. Emerson, and D. Bradley, *Modes of reaction front propagation from hot spots.* Combustion and Flame, 2003. **133**: p. 63-74.

21.     Schiesl, R. and U. Maas, *Analysis of endgas temperature fluctuations in an SI engine by laser-induced fluorescence.* Combustion and Flame, 2003. **133**: p. 19-27.

22.     Smith, J.R., *Temperature and Density Measurements in an Engine by Pulsed Raman Spectroscopy.* SAE Technical Paper Series, 1980(800137).

23.     He, L. and P. Calvin, *Critical Conditions for Detonation Initiation in Cold Gaseous Mixtures by Nonuniform Hot Pockets of Reactive Gases.* Proceedings of the Combustion Institute, 1992. **24**: p. 1861-1867.

24.     He, L. and C.K. Law, *Geometrical effect on detonation initiation by a nonuniform hot pocket of reactive gas.* Phys. Fluids, 1996. **8**: p. 248-256.

25.     He, L., *Theoretical Determination of the Critical Conditions for the Direct Initiation of Detonations in Hydrogen-Oxygen Mixtures.* Combustion and Flame, 1996. **104**: p. 401-418.

26.     He, L., *The dynamical limit of one-dimensional detonations.* Phys. Fluids, 1995. **7**(5): p. 1151-1158.

27.     He, L., *Stability Analysis of One-Dimensional Gaseous Detonations.* Europhysics Letters, 1995. **32**(4): p. 325-330.

28.     He, L. and C.K. Law, *Geometrical effect on detonation initiation by a nonuniform hot pocket of reactive gas.* Phys. Fluids, 1995. **8**(1): p. 248-257.

29.     He, L. and P. Clavin, *On the direct initiaion of gaseous detonations by an energy source.* J. Fluid Mech., 1994. **277**: p. 227-248.

30.     Tanaka, S., F. Ayala, and J.C. Keck, *A reduced chemical kinetic model for HCCI combustion of primary reference fuels in a rapid compression machine.* Combustion and Flame, 2003. **133**: p. 467-481.

31.     Hu, H. and J.C. Keck, *Autoignition of Adiabatically Compressed Combustible Gas Mixtures.* SAE Technical Paper Series, 1987(872110).

32.     Smith, G.P., et al., *GRI-Mech 3.0, http://www.me.berkeley.edu/gri_mech/.*

33.     Kee, R.J., et al., *CHEMKIN III: A FORTRAN Chemical Kinetics Package for the analysis of gas-phase chemical and plasma kinetics*. 1996, Sandia National Laboratories: Livermore, CA.

34.     Marinov, N., C.K. Westbrook, and W.J. Pitz, eds. *Detailed and Global Chemical Kinetics Model of Hydrogen*. Transport Phenomena in Combustion, ed. S.H. Chan. Vol. 1. 1996: Washington, DC.

35.     Curran, H.J., et al., *A Comprehensive Modeling Study of n-Heptane Oxidation.* Combustion and Flame, 1998. **114**: p. 149-177.

36.     Curran, H.J., et al., *A Comprehensive Modeling Study of iso-Octane Oxidation.* Combustion and Flame, 2002. **129**: p. 253-280.

37. Boris, J.P., et al., *LCPFCT--Flux-Corrected Transport Algorithm for Solving Generalized Continuity Equations*. 1993, Naval Research Laboratory: Washington, DC.

38. Oran, E.S. and J.P. Boris, *Numerical Simulation of Reactive Flow*. 1987, New York: Elsevier.

39. Dorfi, E.A. and L.O.C. Drury, *Simple Adaptive Grids for 1-D Initial Value Problems*. Journal of Computational Physics, 1987. **69**: p. 175-195.

40. Yang, J., T. Culp, and T. Kenney, *Development of a Gasoline Engine System Using HCCI Technology--The Concept and the Test Results*. SAE Technical Paper, 2002(2002-01-2832).

41. Woschni, G., *Universally Applicable Equation for the Instantaneous Heat Transfer Coefficient in the Internal Combustion Engine*. SAE Technical Paper, 1967(670931).

42. Westbrook, C.K. and F.L. Dryer, *Simplified Reaction Mechanisms for the Oxidation of Hydrocarbon Fuels in Flames*. Combustion Science and Technology, 1981. **27**: p. 31-43.

43. Thompson, P., *Compressible-Fluid Dynamics*. 1988: RPI Press.

44. Vermeer, D.J., J.W. Meyer, and A.K. Oppenheim, *Auto-Ignition of Hydrocarbos Behind Reflected Shock Waves*. Combustion and Flame, 1972. **18**: p. 327-336.

45. Bauerle, B., et al., *Detection of Hot Spots in the End Gas of an Internal Combustion Engine Using Two-Dimensional LIF of Formaldehyde*. Proceedings of the Combustion Institute, 1994. **25**: p. 135-141.

46. Oakley, A., H. Zhao, and N. Ladommatos, *Dilution Effects on the Controlled Auto-Ignition (CAI) Combustion of Hydrocarbon and Alcohol Fuels*. SAE Technical Paper, 2001(2001-01-3606).

47. Thring, R.H., *Homogeneous-Charge Compression-Ignition (HCCI) Engines*. SAE Technical Paper, 1989(892068).

## 4.7 Supplementary Material

## 4.7.1 CHEMKIN chemistry input file

```
! Reaction set for HCCI combustion of n-heptane and iso-octane mixtures--------
! Developed by Tanaka and Keck, June 2002------------------------------------
!
! Modified the rxn order of O2 in the 6 global rxns. The order was made to zero
! so that the rate is calculated as r = k*[hydrocarbon][HO2]. This was done by
! Tanaka by making specialized modifications to the CHEMKIN libraries (cklib.f).
! This modified version of the chem.inp file works for the standard CHEMKIN
! library. <pey 6-aug-04>
!!!!!!!!!!!!!!!!!!!!!!!!!!!!!!!!!!!!!!!!!!!!!!!!!!!!!!!!!!!!!!!!!!!!!!!!!!!!!!!!!!
! C8H18&C7H16:             iso-octane and n-heptane
! C8H17&C7H15:             alkyl radical
! C8H16&C7H14:             Olefin
! C8H17OO&C7H15OO:         ROO radical
! C8H16OOH&C7H14OOH:       ROOH radical
! OOC8H16OOH&OOC7H14OOH:   OOROOH radical
! OC8H15OOH&OC7H13OOH:     OROOH
! OC8H15O&OC7H13O:         ORO radical
! OC8H14O&OC7H12O:         alkane-dione
! OC8H12O&OC7H10O:         alkene-dione
!!!!!!!!!!!!!!!!!!!!!!!!!!!!!!!!!!!!!!!!!!!!!!!!!!!!!!!!!!!!!!!!!!!!!!!!!!!!!!!!!!


ELEMENTS
H O N AR C
END


SPECIES
H2 H O2 O OH HO2 H2O2 H2O N2 CO CO2 AR
C7H16 C7H15 C7H14 C7H15OO C7H14OOH OOC7H14OOH OC7H13OOH OC7H13O OC7H12O OC7H10O
C8H18 C8H17 C8H16 C8H17OO C8H16OOH OOC8H16OOH OC8H15OOH OC8H15O OC8H14O OC8H12O
END


THERMO ALL
   300.000  1000.000  5000.000
C7H16                   C   7H  16O   0    G  0300.00   5000.00  1000.00      1
 4.58480121E+01 0.00000000E+00 0.00000000E+00 0.00000000E+00 0.00000000E+00    2
-3.60582788E+04-2.09838141E+02 4.58480121E+01 0.00000000E+00 0.00000000E+00    3
 0.00000000E+00 0.00000000E+00-3.60582788E+04-2.09838141E+02                   4
C7H15                   C   7H  15O   0    G  0300.00   5000.00  1000.00      1
 4.58480121E+01 0.00000000E+00 0.00000000E+00 0.00000000E+00 0.00000000E+00    2
-1.32600906E+04-2.09144993E+02 4.58480121E+01 0.00000000E+00 0.00000000E+00    3
 0.00000000E+00 0.00000000E+00-1.32600906E+04-2.09144993E+02                   4
C7H14                   C   7H  14O   0    G  0300.00   5000.00  1000.00      1
 4.21238047E+01 0.00000000E+00 0.00000000E+00 0.00000000E+00 0.00000000E+00    2
-2.13098138E+04-1.89828834E+02 4.21380471E+01 0.00000000E+00 0.00000000E+00    3
 0.00000000E+00 0.00000000E+00-2.13098138E+04-1.89828834E+02                   4
C7H15OO                 C   7H  15O   2    G  0300.00   5000.00  1000.00      1
 5.09310518E+01 0.00000000E+00 0.00000000E+00 0.00000000E+00 0.00000000E+00    2
-3.12821339E+04-2.28905115E+02 5.09310518E+01 0.00000000E+00 0.00000000E+00    3
 0.00000000E+00 0.00000000E+00-3.12821339E+04-2.28905115E+02                   4
C7H14OOH                C   7H  15O   2    G  0300.00   5000.00  1000.00      1
 5.09310518E+01 0.00000000E+00 0.00000000E+00 0.00000000E+00 0.00000000E+00    2
-2.64004026E+04-2.28211967E+02 5.09310518E+01 0.00000000E+00 0.00000000E+00    3
 0.00000000E+00 0.00000000E+00-2.64004026E+04-2.28211967E+02                   4
OOC7H14OOH              C   7H  15O   4    G  0300.00   5000.00  1000.00      1
 5.60140916E+01 0.00000000E+00 0.00000000E+00 0.00000000E+00 0.00000000E+00    2
-4.44224459E+04-2.48665236E+02 5.60140916E+01 0.00000000E+00 0.00000000E+00    3
 0.00000000E+00 0.00000000E+00-4.44224459E+04-2.48665236E+02                   4
OC7H13OOH               C   7H  14O   3    G  0300.00   5000.00  1000.00      1
 4.95218923E+01 0.00000000E+00 0.00000000E+00 0.00000000E+00 0.00000000E+00    2
-6.22663312E+04-2.17958028E+02 4.95218923E+01 0.00000000E+00 0.00000000E+00    3
 0.00000000E+00 0.00000000E+00-6.22663312E+04-2.17958028E+02                   4
OC7H13O                 C   7H  13O   2    G  0300.00   5000.00  1000.00      1
 4.68042275E+01 0.00000000E+00 0.00000000E+00 0.00000000E+00 0.00000000E+00    2
```

```
-4.48988425E+04-2.06602061E+02 4.68042275E+01 0.00000000E+00 0.00000000E+00    3
 0.00000000E+00 0.00000000E+00-4.48988425E+04-2.06602061E+02                   4
OC7H12O           C   7H  12O   2     G  0300.00   5000.00  1000.00            1
 4.34323100E+01 0.00000000E+00 0.00000000E+00 0.00000000E+00 0.00000000E+00    2
-6.35215903E+04-1.89343258E+02 4.34323100E+01 0.00000000E+00 0.00000000E+00    3
 0.00000000E+00 0.00000000E+00-6.35215903E+04-1.89343258E+02                   4
OC7H10O           C   7H  10O   2     G  0300.00   5000.00  1000.00            1
 4.06139909E+01 0.00000000E+00 0.00000000E+00 0.00000000E+00 0.00000000E+00    2
-5.10561651E+04-1.74796844E+02 4.06139909E+01 0.00000000E+00 0.00000000E+00    3
 0.00000000E+00 0.00000000E+00-5.10561651E+04-1.74796844E+02                   4

C8H18             C   8H  18O   0     G  0300.00   5000.00  1000.00            1
 5.28938098E+01 0.00000000E+00 0.00000000E+00 0.00000000E+00 0.00000000E+00    2
-4.40965274E+04-2.50459075E+02 5.28938098E+01 0.00000000E+00 0.00000000E+00    3
 0.00000000E+00 0.00000000E+00-4.40965274E+04-2.50459075E+02                   4
C8H17             C   8H  17O   0     G  0300.00   5000.00  1000.00            1
 5.28938098E+01 0.00000000E+00 0.00000000E+00 0.00000000E+00 0.00000000E+00    2
-2.06440866E+04-2.49360462E+02 5.28938098E+01 0.00000000E+00 0.00000000E+00    3
 0.00000000E+00 0.00000000E+00-2.06440866E+04-2.49360462E+02                   4
C8H16             C   8H  16O   0     G  0300.00   5000.00  1000.00            1
 5.04781077E+01 0.00000000E+00 0.00000000E+00 0.00000000E+00 0.00000000E+00    2
-2.98386512E+04-2.27383228E+02 5.04781077E+01 0.00000000E+00 0.00000000E+00    3
 0.00000000E+00 0.00000000E+00-2.98386512E+04-2.27383228E+02                   4
C8H17OO           C   8H  17O   2     G  0300.00   5000.00  1000.00            1
 5.76748868E+01 0.00000000E+00 0.00000000E+00 0.00000000E+00 0.00000000E+00    2
-3.71166583E+04-2.66807780E+02 5.76748868E+01 0.00000000E+00 0.00000000E+00    3
 0.00000000E+00 0.00000000E+00-3.71166583E+04-2.66807780E+02                   4
C8H16OOH          C   8H  17O   2     G  0300.00   5000.00  1000.00            1
 5.76748868E+01 0.00000000E+00 0.00000000E+00 0.00000000E+00 0.00000000E+00    2
-3.15806744E+04-2.66402315E+02 5.76748868E+01 0.00000000E+00 0.00000000E+00    3
 0.00000000E+00 0.00000000E+00-3.15806744E+04-2.66402315E+02                   4
OOC8H16OOH        C   8H  17O   4     G  0300.00   5000.00  1000.00            1
 6.24559638E+01 0.00000000E+00 0.00000000E+00 0.00000000E+00 0.00000000E+00    2
-4.80532461E+04-2.84542781E+02 6.24559638E+01 0.00000000E+00 0.00000000E+00    3
 0.00000000E+00 0.00000000E+00-4.80532461E+04-2.84542781E+02                   4
OC8H15OOH         C   8H  16O   3     G  0300.00   5000.00  1000.00            1
 5.57624560E+01 0.00000000E+00 0.00000000E+00 0.00000000E+00 0.00000000E+00    2
-6.39750377E+04-2.53191970E+02 5.57624560E+01 0.00000000E+00 0.00000000E+00    3
 0.00000000E+00 0.00000000E+00-6.39750377E+04-2.53191970E+02                   4
OC8H15O           C   8H  15O   2     G  0300.00   5000.00  1000.00            1
 5.30447911E+01 0.00000000E+00 0.00000000E+00 0.00000000E+00 0.00000000E+00    2
-4.66075491E+04-2.41836004E+02 5.30447911E+01 0.00000000E+00 0.00000000E+00    3
 0.00000000E+00 0.00000000E+00-4.66075491E+04-2.41836004E+02                   4
OC8H14O           C   8H  14O   2     G  0300.00   5000.00  1000.00            1
 4.88173125E+01 0.00000000E+00 0.00000000E+00 0.00000000E+00 0.00000000E+00    2
-6.32138903E+04-2.10887157E+02 4.88173125E+01 0.00000000E+00 0.00000000E+00    3
 0.00000000E+00 0.00000000E+00-6.32138903E+04-2.10887157E+02                   4
OC8H12O           C   8H  12O   2     G  0300.00   5000.00  1000.00            1
 4.71565174E+01 0.00000000E+00 0.00000000E+00 0.00000000E+00 0.00000000E+00    2
-5.30058379E+04-1.88600619E+02 4.71565174E+01 0.00000000E+00 0.00000000E+00    3
 0.00000000E+00 0.00000000E+00-5.30058379E+04-1.88600619E+02                   4
! H2/O2 thermo from LLNL (Marinov)-----------------------------------------------
AR                120186AR  1          G  0300.00   5000.00  1000.00            1
 0.02500000e+02 0.00000000e+00 0.00000000e+00 0.00000000e+00 0.00000000e+00    2
-0.07453750e+04 0.04366001e+02 0.02500000e+02 0.00000000e+00 0.00000000e+00    3
 0.00000000e+00 0.00000000e+00-0.07453750e+04 0.04366001e+02                   4
H                 120186H   1          G  0300.00   5000.00  1000.00            1
 0.02500000e+02 0.00000000e+00 0.00000000e+00 0.00000000e+00 0.00000000e+00    2
 0.02547163e+06-0.04601176e+01 0.02500000e+02 0.00000000e+00 0.00000000e+00    3
 0.00000000e+00 0.00000000e+00 0.02547163e+06-0.04601176e+01                   4
H2                121286H   2          G  0300.00   5000.00  1000.00            1
 0.02991423e+02 0.07000644e-02-0.05633829e-06-0.09231578e-10 0.01582752e-13    2
-0.08350340e+04-0.01355110e+02 0.03298124e+02 0.08249442e-02-0.08143015e-05    3
-0.09475434e-09 0.04134872e-11-0.01012521e+05-0.03294094e+02                   4
H2O               20387H   2O  1       G  0300.00   5000.00  1000.00            1
 0.02672146e+02 0.03056293e-01-0.08730260e-05 0.01200996e-08-0.06391618e-13    2
-0.02989921e+06 0.06862817e+02 0.03386842e+02 0.03474982e-01-0.06354696e-04    3
 0.06968581e-07-0.02506588e-10-0.03020811e+06 0.02590233e+02                   4
H2O2              120186H   2O  2       G  0300.00   5000.00  1000.00            1
 0.04573167e+02 0.04336136e-01-0.01474689e-04 0.02348904e-08-0.01431654e-12    2
-0.01800696e+06 0.05011370e+01 0.03388754e+02 0.06569226e-01-0.01485013e-05    3
```

163

```
-0.04625806e-07 0.02471515e-10-0.01766315e+06 0.06785363e+02             4
HO2               20387H   1O   2          G  0300.00   5000.00  1000.00       1
 0.04072191e+02 0.02131296e-01-0.05308145e-05 0.06112269e-09-0.02841165e-13    2
-0.01579727e+04 0.03476029e+02 0.02979963e+02 0.04996697e-01-0.03790997e-04    3
 0.02354192e-07-0.08089024e-11 0.01762274e+04 0.09222724e+02                   4
O                 120186O   1             G  0300.00   5000.00  1000.00       1
 0.02542060e+02-0.02755062e-03-0.03102803e-07 0.04551067e-10-0.04368052e-14    2
 0.02923080e+06 0.04920308e+02 0.02946429e+02-0.01638166e-01 0.02421032e-04    3
-0.01602843e-07 0.03890696e-11 0.02914764e+06 0.02963995e+02                   4
O2                121386O   2             G  0300.00   5000.00  1000.00       1
 0.03697578e+02 0.06135197e-02-0.01258842e-05 0.01775281e-09-0.01136435e-13    2
-0.01233930e+05 0.03189166e+02 0.03212936e+02 0.01127486e-01-0.05756150e-05    3
 0.01313877e-07-0.08768554e-11-0.01005249e+05 0.06034738e+02                   4
OH                121286O   1H   1        G  0300.00   5000.00  1000.00       1
 0.02882730e+02 0.01013974e-01-0.02276877e-05 0.02174684e-09-0.05126305e-14    2
 0.03886888e+05 0.05595712e+01 0.03637266e+02 0.01850910e-02-0.01676165e-04    3
 0.02387203e-07-0.08431442e-11 0.03606782e+05 0.01358860e+02                   4
N2                121286N   2             G  0300.00   5000.00  1000.00       1
 0.02926640e+02 0.01487977e-01-0.05684761e-05 0.01009704e-08-0.06753351e-13    2
-0.09227977e+04 0.05980528e+02 0.03298677e+02 0.01408240e-01-0.03963222e-04    3
 0.05641515e-07-0.02444855e-10-0.01020900e+05 0.03950372e+02                   4
! CO and CO2 thermo from GRIMech 3.0---------------------------------------
CO                TPIS79C   1O   1        G  200.000   3500.000 1000.000      1
 2.71518561E+00 2.06252743E-03-9.98825771E-07 2.30053008E-10-2.03647716E-14    2
-1.41518724E+04 7.81868772E+00 3.57953347E+00-6.10353680E-04 1.01681433E-06    3
 9.07005884E-10-9.04424499E-13-1.43440860E+04 3.50840928E+00                   4
CO2               L 7/88C   1O   2        G  200.000   3500.000 1000.000      1
 3.85746029E+00 4.41437026E-03-2.21481404E-06 5.23490188E-10-4.72084164E-14    2
-4.87591660E+04 2.27163806E+00 2.35677352E+00 8.98459677E-03-7.12356269E-06    3
 2.45919022E-09-1.43699548E-13-4.83719697E+04 9.90105222E+00                   4
END


! Units are cm3, mole, cal; k = A T**n exp(-E/RT)-----------------------------
REACTIONS
!---------------HEPTANE REACTIONS --------------------------------------------
C7H16+O2<=>C7H15+HO2                       1.000E+16   0.00     46000
 REV          / 1.000E+12   0.00   0.0 /
C7H15+O2<=>C7H15OO                         1.000E+12   0.00     00.0
 REV          / 2.512E+13   0.00  27400 /
C7H15OO<=>C7H14OOH                         1.514E+11   0.00     19000
 REV          / 1.000E+11   0.00  11000 /
C7H14OOH+O2<=>OOC7H14OOH                   3.162E+11   0.00     00.0
 REV          / 2.512E+13   0.00  27400 /
OOC7H14OOH=>OC7H13OOH+OH                   8.913E+10   0.00     17000
C7H16+OH=>C7H15+H2O                        1.000E+13   0.00     3000
C7H15+O2<=>C7H14+HO2                       3.162E+11   0.00     6000
 REV          / 3.162E+11   0.00  19500 /
C7H14+HO2+7O2=>7CO+7H2O+HO2                3.162E+13   0.00     10000
FORD /O2 0/
OC7H13OOH=>OC7H13O+OH                      3.981E+15   0.00     43000
OC7H13O+O2<=>OC7H12O+HO2                   3.162E+11   0.00     6000
 REV          / 3.162E+11   0.00  19500 /
HO2+OC7H12O+O2=>H2O2+OC7H10O+HO2           3.162E+13   0.00     10000
FORD /O2 0/
HO2+OC7H10O+5O2=>7CO+5H2O+HO2              3.162E+13   0.00     10000
FORD /O2 0/


!---------------OCTANE REACTIONS----------------------------------------------
C8H18+O2<=>C8H17+HO2                       1.000E+16   0.00     46000
 REV          / 1.000E+12   0.00   0.0 /
C8H17+O2<=>C8H17OO                         1.000E+12   0.00     00.0
 REV          / 2.512E+13   0.00  27400 /
C8H17OO<=>C8H16OOH                         1.135E+11   0.00     22400
 REV          / 1.000E+11   0.00  11000 /
C8H16OOH+O2<=>OOC8H16OOH                   3.162E+11   0.00     00.0
 REV          / 2.512E+13   0.00  27400 /
OOC8H16OOH=>OC8H15OOH+OH                   8.913E+10   0.00     17000
C8H18+OH=>C8H17+H2O                        1.000E+13   0.00     3000
C8H17+O2<=>C8H16+HO2                       3.162E+11   0.00     6000
 REV          / 3.162E+11   0.00  19500 /
C8H16+HO2+8O2=>8CO+8H2O+HO2                1.995E+13   0.00     10000
```

164

```
FORD /O2 0/
OC8H15OOH=>OC8H15O+OH                           3.981E+15    0.00     43000
OC8H15O+O2<=>OC8H14O+HO2                         3.162E+11    0.00      6000
 REV            / 3.162E+11  0.00   19500 /
HO2+OC8H14O+O2=>H2O2+OC8H12O+HO2                 1.585E+13    0.00     10000
FORD /O2 0/
HO2+OC8H12O+6O2=>8CO+6H2O+HO2                    1.585E+13    0.00     10000
FORD /O2 0/


!--------------Interaction of heptane and iso-octane----------------------
C8H18+C7H15<=>C7H16+C8H17                        5.012E12     0.00      0000

!----------------H2 & O2 Reaction from LLNL----------
OH+H2=H+H2O                                      2.14E+08     1.52    3449.0 !Marinov 1995a
O+OH=O2+H                                        2.02E+14    -0.4        0.0 !Marinov 1995a
O+H2=OH+H                                        5.06E+04     2.67    6290.0 !Marinov 1995a
H+O2(+M)=HO2(+M)                                 4.52E+13     0.0        0.0 !Marinov 1995a 4.52
  LOW / 1.05E+19 -1.257 0.0 /                                               !Marinov 1995a
  H2O/0.0/ H2/0.0/ N2/0.0/
H+O2(+N2)=HO2(+N2)                               4.52E+13     0.0        0.0 !Marinov 1995a 4.52
  LOW / 2.03E+20 -1.59 0.0 /                                                !Marinov 1995a
H+O2(+H2)=HO2(+H2)                               4.52E+13     0.0        0.0 !Marinov 1995a 4.52
  LOW / 1.52E+19 -1.133 0.0 /                                               !Marinov 1995a
H+O2(+H2O)=HO2(+H2O)                             4.52E+13     0.0        0.0 !Marinov 1995a 4.52
  LOW / 2.10E+23 -2.437 0.0 /                                               !Marinov 1995a
OH+HO2=H2O+O2                                    2.13E+28    -4.827   3500.0 !Hippler 1995
  DUPLICATE
OH+HO2=H2O+O2                                    9.10E+14     0.0    10964.0 !Hippler 1995
  DUPLICATE
H+HO2=OH+OH                                      1.50E+14     0.0     1000.0 !Marinov 1995a 1.50
H+HO2=H2+O2                                      8.45E+11     0.65    1241.0 !Marinov 1995a
H+HO2=O+H2O                                      3.01E+13     0.0     1721.0 !Marinov 1995a
O+HO2=O2+OH                                      3.25E+13     0.0        0.0 !Marinov 1995a
OH+OH=O+H2O                                      3.57E+04     2.4    -2112.0 !Marinov 1995a
H+H+M=H2+M                                       1.00E+18    -1.0        0.0 !Marinov 1995a
  H2O/0.0/ H2/0.0/
H+H+H2=H2+H2                                     9.20E+16    -0.6        0.0 !Marinov 1995a
H+H+H2O=H2+H2O                                   6.00E+19    -1.25       0.0 !Marinov 1995a
H+OH+M=H2O+M                                     2.21E+22    -2.0        0.0 !Marinov 1995a
  H2O/6.4/
H+O+M=OH+M                                       4.71E+18    -1.0        0.0 !Marinov 1995a
  H2O/6.4/
O+O+M=O2+M                                       1.89E+13     0.0    -1788.0 !Marinov 1995a
HO2+HO2=>H2O2+O2                                 1.995E+10    0.0     5000.0 !1.995E12 0
H2O2+M=>OH+OH+M                                  1.000E+16    0.0    48000.0 !1.259E17 46000
H2O2+H=HO2+H2                                    1.98E+06     2.0     2435.0 !Marinov 1995a
H2O2+H=OH+H2O                                    3.07E+13     0.0     4217.0 !Marinov 1995a
H2O2+O=OH+HO2                                    9.55E+06     2.0     3970.0 !Marinov 1995a
H2O2+OH=H2O+HO2                                  2.40E+00     4.042  -2162.0 !Marinov 1995a !

!----------------CO Oxidation---------------------
O+CO(+M)<=>CO2(+M)                               1.800E+10    .000    2385.00 !GRI Mech 3
  LOW/ 6.020E+14    .000    3000.00/
H2/2.00/ O2/6.00/ H2O/6.00/ CO/1.50/ CO2/3.50/ AR/ .50/
O2+CO<=>O+CO2                                    2.500E+12   0.000   47800.00 !GRI Mech
CO+OH<=>CO2+H                                    4.760E+07   1.228      70.00 !GRI Mech 3
HO2+CO<=>OH+CO2                                  4.760E+13   0.000   23600.00 !GRI Mech 1.5E14

END
```

## 4.7.2 CHEMKIN transport input file

```
! Transport coefficients for PRF model of Tanaka and Keck (2003)
! <pey 6-aug-04> original comments are in parens
AR              0    136.500    3.330    0.000    0.000    0.000 ! LLNL h2
H               0    145.000    2.050    0.000    0.000    0.000 ! LLNL h2
H2              1     38.000    2.920    0.000    0.790  280.000 ! LLNL h2
H2O             2    572.400    2.605    1.844    0.000    4.000 ! LLNL h2
```

```
H2O2            2   107.400   3.458   0.000   0.000   3.800 ! LLNL h2
HO2             2   107.400   3.458   0.000   0.000   1.000 ! LLNL h2 (*)
N2              1    97.530   3.621   0.000   1.760   4.000 ! LLNL h2
O               0    80.000   2.750   0.000   0.000   0.000 ! LLNL h2
O2              1   107.400   3.458   0.000   1.600   3.800 ! LLNL h2
OH              1    80.000   2.750   0.000   0.000   0.000 ! LLNL h2
CO              1    98.100   3.650   0.000   1.950   1.800 ! GRI
CO2             1   244.000   3.763   0.000   2.650   2.100 ! GRI
C7H16           2   459.6     6.253   0.0     0.0     1.0   ! LLNL c7, nc7h16
(TcPc)
C7H15           2   459.6     6.253   0.0     0.0     1.0   ! LLNL c7, c7h15-1
(wjp)
C7H14           2   457.8     6.173   0.3     0.0     1.0   ! LLNL c7, c7h14-1
(TcPc)
C7H15OO         2   561.0     6.317   1.7     0.0     1.0   ! LLNL c7,
c7h15o2-1 (wjp)
C7H14OOH        2   561.0     6.317   1.7     0.0     1.0   ! LLNL c7,
c7h14ooh1-2 (wjp)
OOC7H14OOH      2   600.6     7.229   1.8     0.0     1.0   ! LLNL c7,
c7h14ooh1-2o2 (nc10h22o wjp)
OC7H13OOH       2   581.3     6.506   2.0     0.0     1.0   ! LLNL c7,
nc7ket12 (1c8h17oh wjp)
OC7H13O         2   581.3     6.506   2.0     0.0     1.0   ! LLNL c7,
nc7ket12 (1c8h17oh wjp)
OC7H12O         2   581.3     6.506   2.0     0.0     1.0   ! LLNL c7,
nc7ket12 (1c8h17oh wjp)
OC7H10O         2   581.3     6.506   2.0     0.0     1.0   ! LLNL c7,
nc7ket12 (1c8h17oh wjp)
C8H18           2   458.5     6.414   0.0     0.0     1.0   ! LLNL c8, ic8h18
(wjp)
C8H17           2   458.5     6.414   0.0     0.0     1.0   ! LLNL c8, ac8h17
(wjp)
C8H16           2   485.6     6.440   0.3     0.0     1.0   ! LLNL c8, ic8h16
(wjp)
C8H17OO         2   581.3     6.506   2.0     0.0     1.0   ! LLNL c8,
ac8h17o2 (WJP, c8h17oh-1)
C8H16OOH        2   581.3     6.506   2.0     0.0     1.0   ! LLNL c8,
ac8h17o2h (WJP, c8h17oh-1)
OOC8H16OOH      2   581.3     6.506   2.0     0.0     1.0   ! LLNL c8,
ac8h16ooh-ao2 (WJP, c8h17oh-1)
OC8H15OOH       2   581.3     6.506   2.0     0.0     1.0   ! LLNL c8,
ic8ketaa (WJP, c8h17oh-1)
OC8H15O         2   581.3     6.506   2.0     0.0     1.0   ! LLNL c8,
ic8ketaa (WJP, c8h17oh-1)
OC8H14O         2   581.3     6.506   2.0     0.0     1.0   ! LLNL c8,
ic8ketaa (WJP, c8h17oh-1)
OC8H12O         2   581.3     6.506   2.0     0.0     1.0   ! LLNL c8,
ic8ketaa (WJP, c8h17oh-1)
```

# Chapter 5: A Detailed Study of *n*-Heptane Oxidation Using Automatic Model Generation

## 5.1 Introduction

The performance maps for HCCI engines constructed in Chapter 3 proved to be useful for identifying trends and relative effects of various engine parameters and operating conditions on engine performance. However, because of limitations in the chemistry model these simulations are more *postdictive* (i.e. can explain experimental measurements and show relative effects of engine parameters) than *predictive* (e.g. can tell an engine designer precisely what valve timing to use so that the correct amount of exhaust gas is recycled, giving ideal combustion timing).

In Chapter 3, it was shown that the intake air temperature had to be adjusted in the simulations by about 30 K in order to match the experimental pressure traces from the Ford HCCI test engine. This disagreement between model and experiment is likely due to errors in the physical model (both in model assumptions and parameters) and in the chemistry model. The previous chapter also demonstrated the sensitivity of our predictions to both sources of error. We decided to focus our attention on the chemistry model because we were better equipped to make improvements in that area.

This chapter describes work that was done to extend automatic reaction mechanism generation software to engine systems. Although no specific technical barriers have prohibited this accomplishment, it appears that this is the first time that automatically-generated models have been constructed specifically for engine applications. Our goal was to determine the feasibility of automatic chemistry model construction for engines, rather than the build the industry-standard model for HCCI combustion. This next step could certainly be done, but as other researchers have found,

requires a certain amount of tuning of model parameters to get good agreement with experiment.

This study focused on *n*-heptane oxidation because our previous design study showed that low-octane fuels like *n*-heptane are ideal for HCCI combustion because no auxiliary heating is necessary to achieve autoignition. The first part of this chapter describes extensions that were made to the automatic reaction mechanism generation software of Song et al. [1]. The second part of this chapter describes construction of *n*-heptane oxidation models for two test cases. The first test case is a jet-stirred reactor experiment performed by Dagaut et al. [2]. The second test case is a rapid-compression machine experiment performed by Minetti et al. [3, 4]. For both cases, the physical and chemistry models are discussed and the performance of the automatically-constructed mechanism is compared to the published mechanism of Curran et al. [5].

## 5.2 Automatic Chemistry Model Construction Background

Detailed elementary-step reaction mechanisms for oxidation of higher hydrocarbons are very complex; for example, a recently published model for the oxidation of iso-octane by Curran et al. [6] employs over 1000 chemical species and 4000 elementary reaction steps. Construction of a detailed chemistry model of this complexity requires not only a great deal of chemical intuition but also remarkable perseverance and attention to detail.

In order to avoid this tedious and error prone construction process, many groups have studied computer-aided chemistry model construction. Susnow et al. [7] describe a rate-based screening algorithm for automatic model construction and apply it to pyrolysis modeling. Ranzi et al. [8] use model generation and automated lumping of species to

study pyrolysis, partial oxidation, and combustion. Come et al. [9] also use combined automated generation and lumping to build models for *n*-heptane and iso-octane oxidation. Matheu et al. [10] studied methane pyrolysis using automatic mechanism generation integrated with pressure-dependent rate calculations to explain the autocatalytic effect observed experimentally. Finally, Song [1] used an enlightened object-oriented software design and an extensive database of thermochemical and kinetic parameters to model *n*-butane oxidation in the negative temperature coefficient regime.

The automatic kinetic model generation software used in this study is an extension of the Reaction Mechanism Generator (RMG) program described by Song [1]. RMG uses the rate-based screening algorithm and termination criteria of Susnow et al. [7] to iteratively enlarge the pool of chemical species included in the model. The algorithm, which is shown pictorially in Figure 5.1, starts with an initial pool of species including the reactants and a few key species known beforehand to be important to the chemistry. Using a database of reaction rate estimation rules and group-additivity thermochemical values, a chemistry model (defining thermochemical properties and reaction rates) is built for the current set of chemical species. Using that chemistry model, the reactor-model governing equations are integrated for some incremental timestep. At the end of that timestep, the reactive fluxes to potential species not included in the chemistry model are calculated. If the maximum flux to a non-included species is above a user-specified tolerance, that species is added to the chemistry model. The reaction set is updated and the integration is restarted at the initial time. This procedure continues to iteratively enlarge the reaction mechanism until the fluxes to all non-included species are below the tolerance for all times during the simulation.

170

**Figure 5.1:** Pictorial representation of the rate-based screening algorithm for iteratively enlarging a chemistry model. Letters A through G represent chemical species and arrows represent reactive fluxes. The box represents the boundary between included (or reacted) species and non-included (or unreacted) species. The model is complete when all the fluxes to non-included species ($R_j$) are less than some tolerance ($R_{min}$). Figure adapted from J. Song.
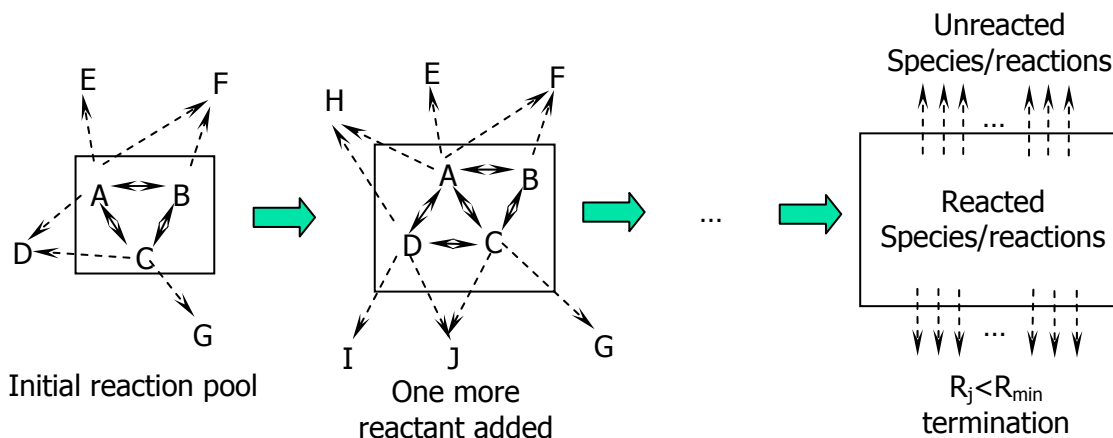


In RMG, Song implements a software design that breaks down the model construction algorithm into interrelated software objects, such as reactions, chemical species, and atom-connectivity graphs, that make the code understandable and easily-extensible. Song also employs a database-driven approach to storing the reaction rate estimates and group-additivity values, which eliminates complicated if-then structures that plagued early model-generation software and allows new chemical information to be easily added without modifying the program. RMG also includes the integrated pressure-dependence algorithm of Matheu et al. [10], which efficiently calculates rates for those reactions that depend of pressure as well as temperature. Finally, RMG uses a detailed library of reaction rate estimates for over 30 reaction families compiled by R. Sumathi and C. Wijaya [11]. Group-additivity thermochemical groups, radical corrections, and ring corrections were collected and organized by J. Yu [12]. These rate parameters and thermochemical groups were organized into a hierarchical tree structure which speeds searches and improves matching.

In this work, extensions were made to RMG to allow chemistry models to be constructed for engine conditions and high molecular-weight fuels important to engines. These extensions included: 1) addition of an engine-like reactor model, 2) extension of RMG to allow variable temperatures and pressures during model building, 3) calculation and parameterization of pressure-dependent rate constants for variable temperature and pressure, 4) extrapolation of thermochemical properties to high temperatures common to engines, 5) extension and reorganization of the ring correction database. Essential collaborative effort was provided by Jing Song to incorporate many of these changes. The following sections describe the implementation and testing of these changes for two experimental test cases.

## 5.3 Modifications to the Reaction Model Generation (RMG) Software for Engine Calculations

This section describes changes made to the Reaction Model Generation (RMG) software of Song [1] to allow chemistry models to be automatically constructed for engine systems.

### 5.3.1 Addition of External CHEMKIN-based Reactor Models

Previous automated model building research done with RMG and its predecessor XMG assumed a reactor model that is maintained at constant temperature and pressure. This reactor model is suited for batch reactors and flow reactors that use a very dilute mixture of reactants but is not suited for engine systems where the temperature and pressure can vary by more than 2000 K and 100 atm. Therefore the task of adding a engine reactor model to RMG was undertaken.

RMG is written in the Java programming language, which is very convenient for managing large object-oriented software projects. However, the numerical software

needed for solving the stiff ordinary differential equations governing chemical kinetics is written in the C and FORTRAN languages (e.g. CVODE [13], DASPK [14]). Song linked RMG to DASPK to using the Java Native Interface (JNI) and a C++ wrapper. Because this approach proved tedious, we abandoned it for an external CHEMKIN-based reactor model. Our external reactor model communicates with RMG through the read/write of a text file, and this approach is advantageous because it retains the platform-independence of RMG. Because Java was designed to run on any operating system or architecture for which a Java Virtual Machine (JVM) exists, pure Java programs are platform-independent; however, that feature is lost when Java is linked to other programming languages. A pure-Java version of RMG could be more easily implemented by other researchers using different types of computers.

Two external reactor models were implemented. The first is a constant-$T,P$ reactor equivalent to the one already linked to RMG. This reactor model solves the equation

$$\frac{dY_k}{dt} = v\dot{\omega}_k W_k \tag{5.1}$$

for each chemical species where $t, v, Y_k, \dot{\omega}_k$, and $W_k$ are respectively time, specific volume of the mixture, mass fraction, molar rate of production, and molecular weight of species $k$. The form of Eq. (5.1) is slightly different from that used in the previous implementation of the constant-$T,P$ reactor, which was

$$\frac{d[X_k]}{dt} = \dot{\omega}_k \tag{5.2}$$

where $[X_k]$ is the molar concentration of species $k$. Strictly speaking, Eq. (5.2) is only valid for a constant-volume system, whereas Eq. (5.1) is general.

173

The second reactor model that was implemented is the engine reactor model. This model solves the equations for a variable-volume, adiabatic, homogeneous, closed reactor. The species conservation equations are the same as Eq. (5.1), but the temperature varies in time according to the transient form of the energy equation,

$$C_v \frac{dT}{dt} + p \frac{dv}{dt} = -v \sum_{k=1}^{K} u_k \dot{\omega}_k W_k \qquad (5.3)$$

where $C_v$, $T$, $p$, and $u_k$ are the constant-volume heat capacity, temperature, pressure, and internal energy of species $k$, respectively. Additionally, the volume is specified as a function of time using the slider-crank formula [15] to describe piston motion in an engine, and the ideal gas law is used to calculate the pressure.

$$pv = \frac{RT}{\bar{W}}, \quad v = \frac{V(t)}{m} \qquad (5.4)$$

Here $V(t)$ is the engine cylinder volume as a function of time, $\bar{W}$ is the mean molecular weight of the reacting mixture and $m$ is the mass of the system. The engine speed can also be set to zero to model a constant-volume, adiabatic reactor. The reaction rates and thermochemical properties are calculated using the CHEMKIN [16] library of subroutines.

As mentioned, information is passed between RMG and the external reactor models via a text file. File input/output can lead to unexpected results on different platforms because operating systems use different hidden characters to signify a carriage return. The eXtensible Markup Language (XML) was invented as a platform-independent standard for transferring information stored in text files. XML, which uses tags similar to the HTML language used for webpages, has numerous other advantages such as being

self-documenting and easily parsed. In order to maintain the platform independence of Java, an XML interface for the external reactor models was written.

The two files are needed are an input file, which sends information from RMG to the reactor model, and an output file, which sends information from the reactor model to RMG. The input file, shown in Figure 5.2, tells the reactor model the reactor type (constant-$T,P$ or engine-model), integration time, error tolerances, and the initial temperature, pressure, and composition. A placeholder was also left to hold the chemistry information, such as reaction rates and thermodynamic properties, but our current implementation passes that information through a CHEMKIN-formatted text file. The output file shown in Figure 5.3 returns to RMG the temperature, pressure, and composition at the end of the integration. Also returned to RMG is a field called "returnmessage" that tells whether the integration was successful, and if not returns an message describing the error. This file format offers great flexibility to allow RMG users to employ any type of reactor model they choose. For example, one could imagine a computational fluid dynamicist using RMG to build a kinetic model for each finite volume in a simulation of a reactive flow.

**Figure 5.2:** An example of the XML-formatted input file that transfers information from RMG to an external reactor model. (Some species were omitted for brevity.)

```
<?xml version="1.0" standalone="no"?>
<!DOCTYPE reactorinput SYSTEM
"/home/paul/rmg/software/reactorModel/documentTypeDefinitions/reactorInput.dtd">
<reactorinput>
<header>
<title>Reactor Input File</title>
<description>RMG-generated file used to call an external reactor model</description>
</header>
<inputvalues>
<integrationparameters>
<reactortype>ic_engine</reactortype>
<starttime units="SEC">       0.015000</starttime>
<endtime units="SEC">       0.020000</endtime>
<rtol>1.0E-4</rtol>
<atol>1.0E-25</atol>
</integrationparameters>
<chemistry>
</chemistry>
<systemstate>
<temperature units="K">      923.651850</temperature>
<pressure units="Pa">   481608.000000</pressure>
<amount units="molPerCm3" speciesid="nC7H16(1)">5.937562E-7</amount>
<amount units="molPerCm3" speciesid="O2(2)">1.2501993E-5</amount>
<amount units="molPerCm3" speciesid="N2">3.6307827E-5</amount>
<amount units="molPerCm3" speciesid="Ar">0.0</amount>
</systemstate>
</inputvalues>
</reactorinput>
```

**Figure 5.3:** An example of the XML-formatted output file that transfers information from the external reactor model to RMG. (Some species were omitted for brevity.)

```
<?xml version="1.0" standalone="no"?>
<!DOCTYPE reactoroutput SYSTEM "./documentTypeDefinitions/reactorOutput.dtd">
<reactoroutput>
<header>
<title>Reactor Output File</title>
<description>External-solver-generated file that returns the mixture state to
RMG</description>
</header>
<returnmessage>SUCCESSFULLY COMPLETED RUN.</returnmessage>
<outputvalues>
<time units="sec">  0.20000000E-001 </time>
<systemstate>
<temperature units="K">  0.92964749E+003 </temperature>
<pressure units="Pa">  0.49228660E+006 </pressure>
<amount units="molPerCm3" speciesid="N2">  0.36307827E-004 </amount>
<amount units="molPerCm3" speciesid="Ar">  0.00000000E+000 </amount>
<amount units="molPerCm3" speciesid="nC7H16(1)">  0.23323510E-006 </amount>
<amount units="molPerCm3" speciesid="O2(2)">  0.12188782E-004 </amount>
<flux units="molPerCm3-Sec" speciesid="N2">  0.00000000E+000 </flux>
<flux units="molPerCm3-Sec" speciesid="Ar">  0.00000000E+000 </flux>
<flux units="molPerCm3-Sec" speciesid="nC7H16(1)"> -0.67698939E-004 </flux>
<flux units="molPerCm3-Sec" speciesid="O2(2)"> -0.71535380E-004 </flux>
</systemstate>
</outputvalues>
</reactoroutput>
```

Another advantage of the extensible markup language is that parsers for XML can check documents to make sure they are well-formed (i.e. have the correct tags and attributes). This checking is done with another file called a document type definition (DTD) that specifies the format for XML documents. Figure 5.3 and Figure 5.4 show the DTDs for the input and output XML documents, respectively. XML documents are hierarchical and each "ELEMENT" entry in the DTD specifies a tag, its attributes, and the number and type of its children. For example, in Figure 5.4 the element *systemstate* has the following children: 1) exactly one *temperature*, 2) exactly one *pressure*, and 3) one or more *amount* entries. Continuing we see that the entry *amount* has two attributes: 1) *unit* which can be *molPerCm3* or *moleFraction* and 2) *speciesid* which gives a unique name to the species. As shown with the *amount* tag, DTDs are also useful for checking that the physical units used for numerical quantities are understood by the receiving program.

**Figure 5.4:** The Document Type Definition (DTD) used to check the XML input file for well-formedness

```
<!-- *******
Reactor Input File Document Type Definition (DTD)
PEY (2/4/04)
note: reaction and thermo have not yet been fully defined
******* -->
<!ELEMENT reactorinput (header, inputvalues)>
<!ELEMENT header (title?, description?)>
<!ELEMENT title (#PCDATA)>
<!ELEMENT description (#PCDATA)>
<!ELEMENT inputvalues (integrationparameters, chemistry?, systemstate)>
<!ELEMENT integrationparameters (reactortype, starttime, endtime, rtol, atol)>
<!ELEMENT reactortype (#PCDATA)>
<!ELEMENT starttime (#PCDATA)>
   <!ATTLIST starttime units (sec) #REQUIRED>
<!ELEMENT endtime (#PCDATA)>
   <!ATTLIST endtime units (sec) #REQUIRED>
<!ELEMENT rtol (#PCDATA)>
<!ELEMENT atol (#PCDATA)>
<!-- *** Remove the ?'s from the next line when chemistry must be included in this
file *** -->
<!ELEMENT chemistry (elementlist?, specieslist?, thermolist?, reactionlist?)>
<!ELEMENT elementlist (element*)>
<!ELEMENT element (#PCDATA)>
<!ELEMENT specieslist (species*)>
<!ELEMENT species (#PCDATA)>
   <!ATTLIST species name CDATA "">
<!ELEMENT thermolist (thermo*)>
<!ELEMENT thermo ANY>
<!ELEMENT reactionlist (reaction*)>
<!ELEMENT reaction ANY>
<!ELEMENT systemstate (temperature, pressure, amount+)>
<!ELEMENT temperature (#PCDATA)>
   <!ATTLIST temperature units (K | C) #REQUIRED>
<!ELEMENT pressure (#PCDATA)>
   <!ATTLIST pressure units (Pa | atm | bar) #REQUIRED>
<!ELEMENT amount (#PCDATA)>
   <!ATTLIST amount units (molPerCm3 | moleFraction) #REQUIRED
                    speciesid CDATA #REQUIRED
   >
```

178

**Figure 5.5:** The Document Type Definition (DTD) used to check the XML output file for well-formedness

```
<!-- *******
Reactor Output File Document Type Definition (DTD)
PEY (15/6/04)
******* -->
<!ELEMENT reactoroutput (header, returnmessage, outputvalues?)>
<!ELEMENT header (title?, description?)>
<!ELEMENT title (#PCDATA)>
<!ELEMENT description (#PCDATA)>
<!ELEMENT returnmessage (#PCDATA)>
<!ELEMENT outputvalues (time, systemstate)>
<!ELEMENT time (#PCDATA)>
   <!ATTLIST time units (sec) #REQUIRED>
<!ELEMENT systemstate (temperature, pressure, amount+, flux+)>
<!ELEMENT temperature (#PCDATA)>
   <!ATTLIST temperature units (K | C) #REQUIRED>
<!ELEMENT pressure (#PCDATA)>
   <!ATTLIST pressure units (Pa | atm | bar) #REQUIRED>
<!ELEMENT amount (#PCDATA)>
   <!ATTLIST amount units (molPerCm3 | moleFraction) #REQUIRED
                    speciesid CDATA #REQUIRED
   >
<!ELEMENT flux (#PCDATA)>
   <!ATTLIST flux units (molPerCm3-Sec) #REQUIRED
                    speciesid CDATA #REQUIRED
   >
```

## 5.3.2 Pressure-Dependent Rates at Variable Temperature and Pressure

As described above, internal combustion engines (and many other systems of practical interest) traverse a wide range of temperature and pressure. For many reactions, the reaction rate constant is solely temperature-dependent and the modified Arrhenius expression adequately captures this dependence. However, it is well known that some reactions proceed through the formation of an energized adduct and hence their rate constants are functions of both temperature and pressure. In these cases, the model generation software should be able to calculate and parameterize expressions for the pressure dependent rate, $k(T,P)$. Matheu [17] describes an algorithm for automated model generation with integrated pressure dependence, which is implemented in RMG. This algorithm uses the rate-based screening process to iteratively explore networks of pressure dependent reactions at the same time that chemical species are added to the

179

chemistry model. Each time an isomer is added to a pressure-dependent network, the calculation of the pressure dependent rate for that system is improved. CHEMDIS [18], which uses the QRRK method to estimate $k(E)$ and the modified strong collision approximation for the collisional energy transfer rate, is used to estimate the pressure dependent rate constants.

The pyrolysis and combustion cases studied by Matheu [10, 17] and Song [1] were at constant temperature and pressure, so CHEMDIS need only return one number, the value of $k(T,P)$ at that particular $T$ and $P$. For the engine case, we need an expression for $k(T,P)$ valid at whatever conditions arise in the simulation. The approach taken was to calculate $k(T,P)$ with CHEMDIS for each new network over a range of temperatures and pressures and fit the rate constant to a Chebyshev polynomial, which has been used successfully by others for parameterizing $k(T,P)$ [19, 20].

The Chebyshev polynomial fit is a purely mathematical parameterization of pressure dependence proposed by Venkatesh et al. [19] and has no relation to the real physics like the fits of Lindemann, Troe, and Stewart (SRI). Those simpler fits are often quite accurate for single-well pressure-dependent networks but not for complicated multi-well networks often encountered in model generation. Chebyshev polynomials have the attractive property that their basis functions are orthogonal. As a result, the coefficients can be quickly calculated by evaluation of an analytical function given that $k(T,P)$ data are provided at the nodes of the basis functions (i.e. the Gauss-Chebyshev points). Additionally, the Chebyshev format is included as an option in CHEMKIN versions 3.6.2 and later so that rates in this format can be easily exchanged between researchers.

The *i*-th Chebyshev basis function, $\Phi_i(x)$, (which more precisely is the Chebyshev polynomial of degree *i*-1) is given by,

$$\Phi_i(x) = \cos\left[(i-1)\arccos(x)\right]. \tag{5.5}$$

The first five basis functions are plotted in Figure 5.6. An arbitrary function $g(x)$ defined on the interval [-1 1] can be approximated by a sum of these basis functions multiplied by constant coefficients,

$$g(x) \approx \sum_{i=1}^{N} c_i \Phi_i(x). \tag{5.6}$$

The $N$ coefficients, $c_i$, can be calculated analytically (i.e. without using a fitting procedure such as least-squares regression) via,

$$c_{i>1} = \frac{2}{N}\sum_{n=1}^{N} f(x_{0n})\Phi_i(x_{0n}), \tag{5.7}$$

$$c_1 = \frac{1}{N} f(x_{0n})\Phi_1(x_{0n}),$$

where $x_{0n}$ are the Gauss-Chebyshev points. Since $\Phi_i(x)$ is also always in the range [-1 1], the importance of a term in the polynomial can be determined by simply looking at the magnitude of the coefficient without regard for the size of the basis function. Computational experiments show that the magnitudes of the coefficients quickly decrease, and the series can be truncated while maintaining good accuracy.

**Figure 5.6:** Chebyshev basis functions, $\Phi_i(x)$, as calculated by Eq. (5.5). Strictly speaking, $\Phi_i(x)$ is the Chebyshev polynomial of degree $i$-1 (see e.g. [21]). Note that the basis functions are bounded by ±1, and that $\Phi_i(x)$ has $i$-1 roots, which are the Gauss-Chebyshev points.
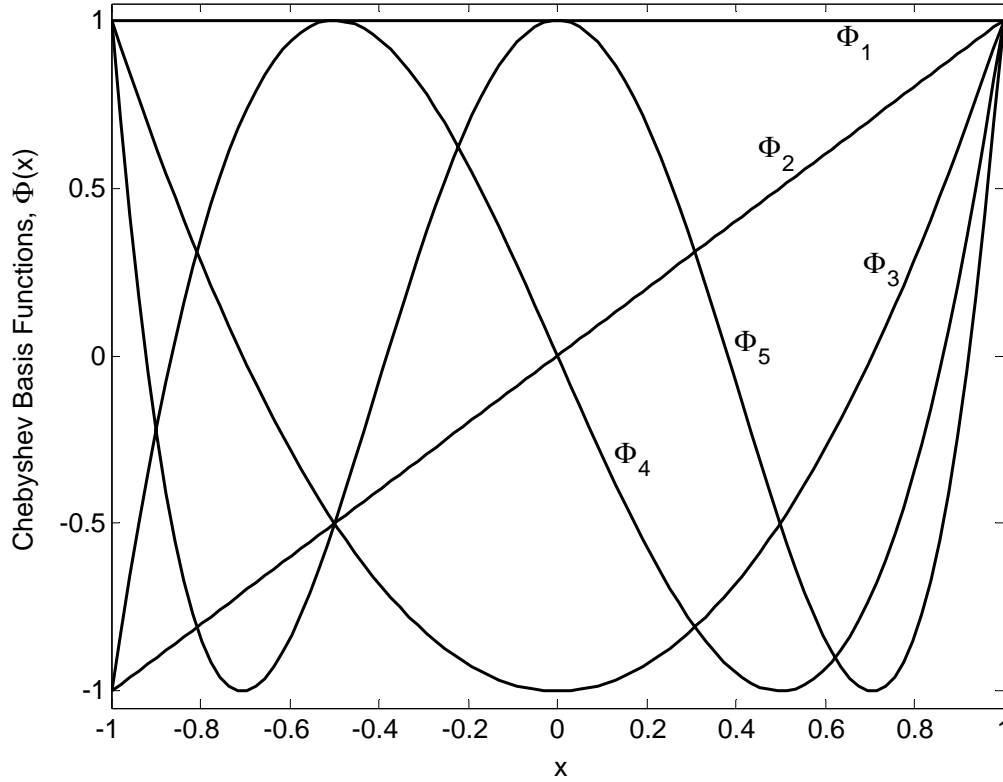


A function of two variables like $k(T,P)$ can be fit by direct extrapolation of Eq. (5.6) to two dimensions. First temperature and pressure are transformed and mapped to the interval [-1 1]. The fitting is done in terms of $\log(k)$ as a function $T^{-1}$ and $\log(P)$ to better capture the Arrhenius $T$-dependence and large ranges of pressure [19]. The transformed, scaled temperature ($\bar{T}$) and pressure ($\bar{P}$) are calculated from the expressions

$$\bar{T} = \frac{2T^{-1} - T_{min}^{-1} - T_{max}^{-1}}{T_{min}^{-1} - T_{max}^{-1}} \tag{5.8}$$

$$\bar{P} = \frac{2\log(P) - \log(P_{min}) - \log(P_{max})}{\log(P_{max}) - \log(P_{min})}, \tag{5.9}$$

where $T_{min}$, $T_{max}$ are the bounds of the temperature range, and $P_{min}$ and $P_{max}$ are the bounds of the pressure range.[4] Finally, the pressure-dependent rate constant is calculated from

$$\log\left[k\left(\overline{T},\overline{P}\right)\right] = \sum_{i=1}^{N_T}\sum_{j=1}^{N_P} c_{ij}\Phi_i\left(\overline{T}\right)\Phi_j\left(\overline{P}\right). \tag{5.10}$$

As mentioned, the coefficients, $c_{ij}$, can be calculated directly given that $k\left(\overline{T},\overline{P}\right)$ is provided at the Gauss-Chebyshev points $(\overline{T}_{0m},\overline{P}_{0n})$ by evaluating the following double sum.

$$c_{ij} = \frac{\alpha}{d_T d_P}\sum_{m=1}^{d_T}\sum_{n=1}^{d_P}\log\left[k\left(\overline{T}_{0m},\overline{P}_{0n}\right)\right]\Phi_i\left(\overline{T}_{0m}\right)\Phi_j\left(\overline{P}_{0n}\right)$$
$$\text{where}\quad \alpha = \begin{cases} 4 & i,j \neq 1 \\ 2 & i=1, j \neq 1 \wedge i \neq 1, j = 1 \\ 1 & i,j = 1 \end{cases} \tag{5.11}$$

Here $d_T$ and $d_P$ are the number of data points for $k(T,P)$ used to derive the Chebyshev coefficients, meaning that $d_T \times d_P$ CHEMDIS calculations must be performed for each network. $N_T$ and $N_P$ in Eq. (5.10) are the number of temperature and pressure coefficients used in the truncated fit. In our calculations $d_T = d_P = 10$, $N_T = 7$, and $N_P = 4$ as suggested by Naik, Carstensen, and Dean [20]. With this choice of the number of gridpoints and parameters, those researchers observed average absolute errors of less than 5% and maximum absolute errors of less than 25%. Considering that the QRRK estimates of $k(T,P)$ from CHEMDIS generally have uncertainties of at least a factor of two, we believe this level of fitting accuracy to be more than sufficient. Figure 5.7 shows the results for a

---

[4] After writing this chapter, I discovered that the expression for $\overline{T}$ used in commercial releases of Chemkin differs from Eq. (5.8) by a minus sign. Eq. (5.8) is what appears in the original paper by Venkatesh et al. [19] and even the Chemkin documentation from Reaction Design. Unfortunately, this means that our chemistry models do not work with commercial releases of Chemkin.

parameterization done at this level of approximation, which visually appear quite satisfactory. The maximum error observed in this particular case was about 10%.

**Figure 5.7:** Temperature-dependent and chemically-activated behavior of the rate constant, $k(T,P)$, for the reaction $C_2H_5 + O_2 (+M) \leftrightarrow C_2H_4 + HO_2 (+M)$. Shown are a) the raw data and b) the Chebyshev fit evaluated at some additional points. Pressure-dependent rate data from H-H. Carstensen (personal communication, 2004).
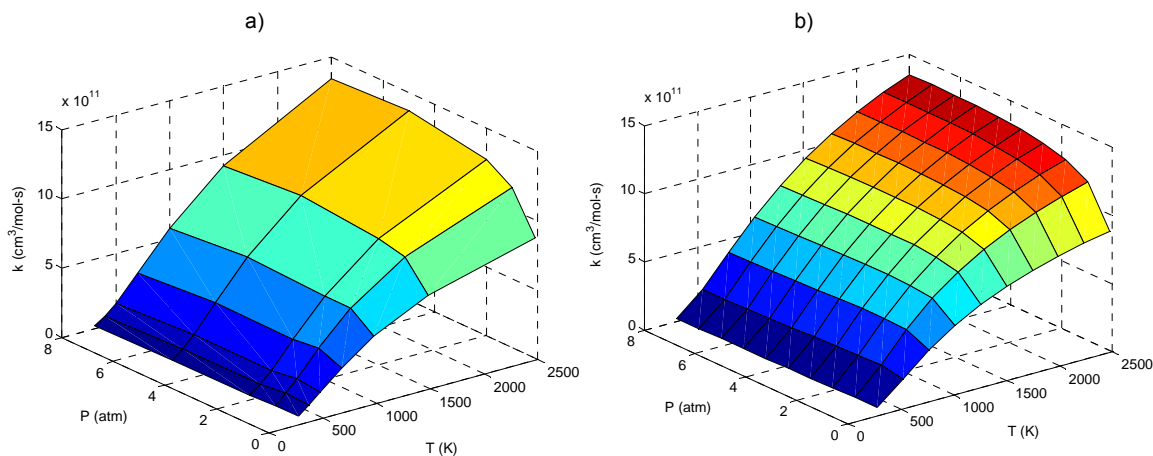


Modifications were made to CHEMDIS to implement Eq. (5.11) that returns the Chebyshev coefficients to RMG. Also modifications were made to the CHEMKIN II library of subroutines[5] to allow calculation of the rates from Eq. (5.10). J. Song added evaluation of Chebyshev rate expressions inside RMG and made the many changes associated with using variable temperature and pressure. Equally important were the Chebyshev fitting/evaluating programs provided by H-H. Carstensen, which guided my modifications to CHEMDIS and CHEMKIN.

### 5.3.3  Extrapolation of Heat Capacity Data to High Temperatures

The group-additivity methods of Benson [22] and Bozzelli [23] are powerful techniques to estimate the thermochemical properties of an unknown chemical species. These techniques exploit the observation that most forces between atoms are short range,

---

[5] CHEMKIN II is a legacy version of CHEMKIN written before the Chebyshev option was implemented by Reaction Design.

and therefore the contributions of each atom to a molecule's thermochemical properties are nearly additive. Group additivity has proven successful for aliphatic hydrocarbons and can be extended to radicals and ring species using various corrections.

The results of summing the group contributions for a molecule are the standard heat-of-formation, $\Delta h_f^0$ (298 K), the standard entropy, $s^0$(298 K), and the ideal-gas constant-pressure heat-capacity, $C_p^0$, at 300 K, 400 K, 500 K, 600 K, 800 K, 1000 K, and sometimes 1500 K. Unlike other the chapters, the superscript $0$ is used here to stress that these properties refer to the ideal-gas standard state at a pressure of one atmosphere. This temperature range for $C_p^0$ is sufficient for many reactor systems, and linear interpolation with a simple trapezoid-rule integration can be used calculate $C_p^0(T)$, $h^0(T)$, and $s^0(T)$ at the temperature of interest. This approach was used successfully by Song [1] to model butane oxidation at 715 K. However, the temperature in an engine can extend to 2500 K or higher. Since these temperatures are beyond the domain were group-additivity information is available, a technique to extrapolate heat-capacity data is needed. We decided to use the Wilhoit polynomial function [24] to perform this extrapolation.

The Wilhoit polynomial uses the statistical thermodynamic limits for $C_p$ at zero-Kelvin and infinite temperature to extrapolate the group additivity data. The Wilhoit polynomial is written,

$$C_p^0(T) = C_p^0(0) + \left[C_p^0(\infty) - C_p^0(0)\right] y^2 \left[1 + (y-1)\sum_{i=0}^{3} a_i y^i\right] \qquad (5.12)$$

where $C_p^0(0)$ and $C_p^0(\infty)$ are the heat-capacity at zero-Kelvin and infinite temperature. The quantity $y = T/(T+B)$ is a scaled temperature that varies from 0 to 1, and $a_i$ is the

*i*-th order polynomial coefficient. In our implementation, *B* is taken as a constant 500 K. The low-temperature limit, $C_p^0(0)$, is calculated as $3.5R$ (linear molecules), or $4R$ (nonlinear molecules). The high-temperature limit, $C_p^0(\infty)$, is calculated as $[3N_{atoms} - 1.5]R$ (linear molecules), or $[3N_{atoms} - (2 + 0.5N_{rotors})]R$ (nonlinear molecules), where $N_{atoms}$ and $N_{rotors}$ are the number of atoms and internal rotors in the molecule. The expression for nonlinear molecules assumes that all internal rotors have become free rotors at very high temperature. Therefore, the contribution to the heat-capacity from these rotors is the $0.5R$ associated with rotational degrees of freedom, rather than the $1.0R$ associated with internal vibrations. Monatomic gases are assigned a fixed heat-capacity of $2.5R$, and extrapolation is not necessary. After some rearrangement, the coefficients in Eq. (5.12) can be approximated by a linear least-squares regression.

Burcat [25] gives the analytical integral expressions for the enthalpy[6] and entropy,

$$h^0(T) = I + C_p^0(0)T - \left[C_p^0(\infty) - C_p^0(0)\right]T$$

$$\left\{\left(2 + \sum_{i=0}^{3} a_i\right) \times \left[\frac{y}{2} - 1 + \left(\frac{1}{y} - 1\right)\ln\frac{T}{y}\right] + y^2 \sum_{i=0}^{3} \frac{y^i}{(i+2)(i+3)}\left(\sum_{j=0}^{3} f_{ij}a_j\right)\right\} \qquad (5.13)$$

$$\text{where } f_{ij} = \begin{cases} 3+j & \text{for } i = j \\ 1 & \text{for } j > i \\ 0 & \text{for } i < j \end{cases}$$

$$s^0(T) = J + C_p^0(\infty)\ln T - \left[C_p^0(\infty) - C_p^0(0)\right] \times \left[\ln y + \left(1 + y\sum_{i=0}^{3} \frac{a_i y^i}{2+i}\right)y\right] \qquad (5.14)$$

---

[6] Note that the equation for enthalpy in Burcat [25] contains some typographical errors that have been corrected here. Perhaps these rather tedious expressions for the enthalpy and entropy are the reason that the Wilhoit polynomial, which has excellent goodness-of-fit and a small number of parameters, has failed to gain widespread acceptance in the scientific and engineering communities.

where *I* and *J* are integration constants that can be evaluated using $\Delta h_f^0$ (298 K) and $s^0$(298 K). Figure 5.8 shows an example of Wilhoit extrapolation of heat-capacity data for propane at the seven group-additivity temperatures (i.e. 300 K, 400 K, 500 K, 600 K, 800 K, 1000 K, 1500 K) over the range 0-5000 K. Notice that the fit smoothly approaches the statistical mechanical limits at both high and low temperatures. By contrast, extrapolation of the common NASA polynomial representation of $C_p^0$ would lead to totally unrealistic values outside of its range of validity.

A class was added to RMG that has the Wilhoit parameters as attributes and contains methods to calculate the statistical thermodynamic limits, determine the polynomial coefficients, and calculate $h^0$, $s^0$, and $C_p^0$. The linear least-square problem to calculate the polynomial coefficients is solved using a QR factorization routine from the NIST library of basic linear algebra routines for Java (JAMA).

**Figure 5.8:** Wilhoit extrapolation of the ideal-gas heat-capacity for propane over the range 0-5000 K using data available from the group-additivity methods of Benson [22] and others. The group-additivity methods tabulate group values for $C_p^0$ at 300 K, 400 K, 500 K, 600 K, 800 K, 1000 K and 1500 K.
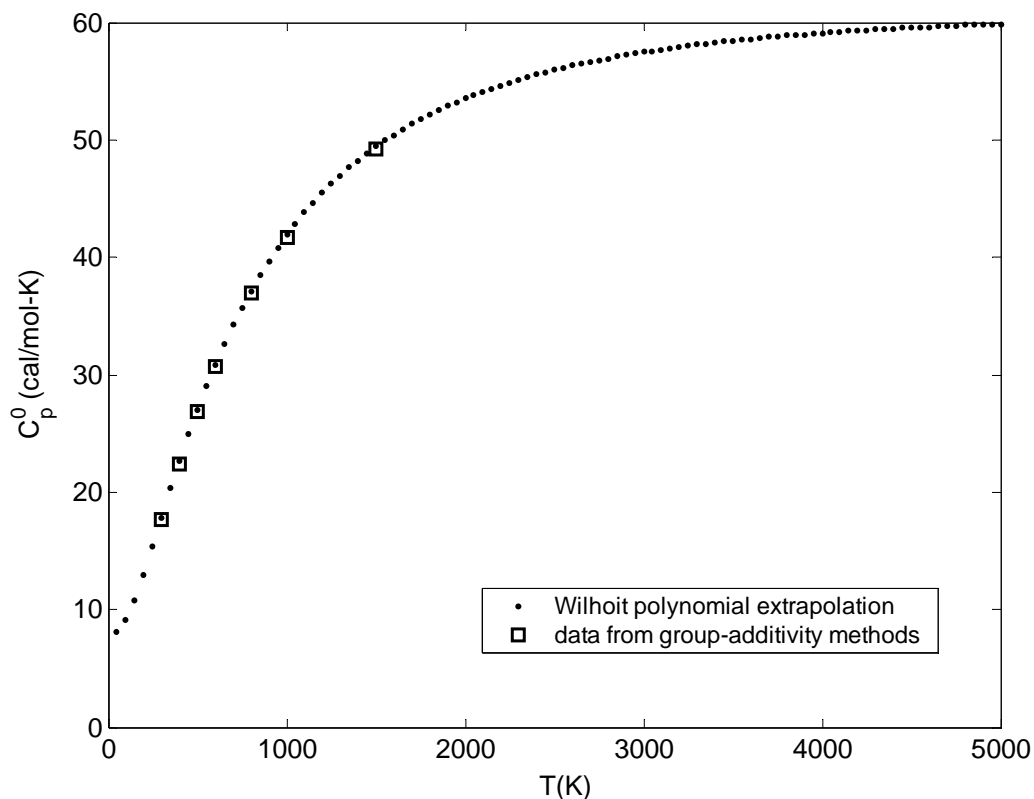


### 5.3.4 Construction of a Ring Correction Tree

Because rings are a non-local attribute of a molecule, corrections must be used to adjust the group-additivity estimates of the corresponding acyclic molecule. These ring corrections have been tabulated by Benson [22], Dorofeeva [26], Lay et al. [27] and others. Each ring correction corresponds to a specific ring group, such as a five-member ring of single-bonded carbon atoms. During automated model construction, however, ring species are formed that do not exactly match the corrections in our ring correction library. In order to at least roughly estimate the ring correction for species not in the database, the

ring corrections were organized into a hierarchical tree. RMG uses similar trees to organize other group-additivity values and rate estimation rules.
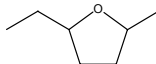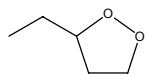
A subset of the group additivity tree is shown in Figure 5.9. The classification was done purely based on ring size. For example,  would be assigned the tetrahydrofuran correction, but  would be assigned the generic five-member ring correction because an exact match is not available. This classification scheme is expected to give reasonable estimates for the entropy correction, which is proportional to the number of internal rotors that are lost in the rigid ring structure. The correction to the enthalpy depends strongly on the atom- and bond-types in ring as well as ring size; therefore, corrections to the enthalpy are expected to be more uncertain than those for entropy. The ring corrections for the generic three- to nine-member rings are those for the corresponding cycloalkane with the same number of carbons. The ring-correction tree structure can be easily refined and restructured as more information becomes available.

**Figure 5.9:** A portion of the hierarchical tree used to estimate ring corrections for cyclic species
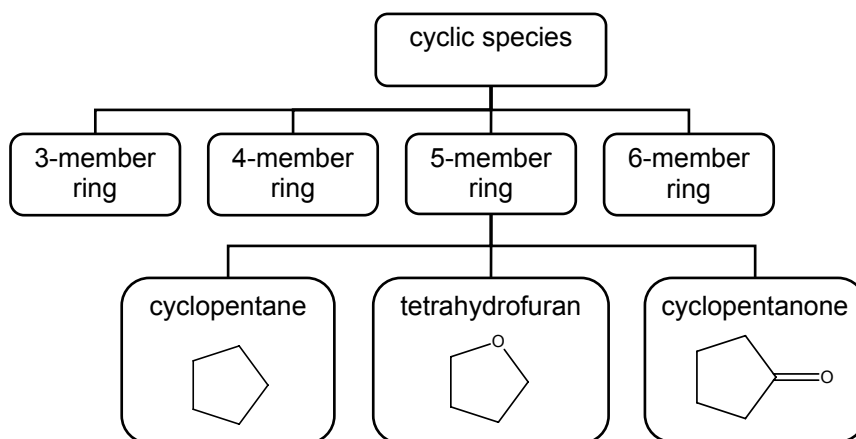
## 5.4  Results and Discussion

This section describes the results of application of automatic kinetic model generation to the study of *n*-heptane oxidation. The chemistry model predictions are compared to data from a jet-stirred reactor experiment by Dagaut et al. [2] and rapid-compression machine experiment by Minetti et al. [3].

### 5.4.1  Jet-Stirred Reactor Test Case

Before attempting to model a variable temperature and pressure experiment, a somewhat simpler, constant *T* and *P*, steady-state experiment in a jet-stirred reactor was simulated. This test case uses the external reactor model, Chebyshev polynomial representation of $k(T,P)$, Wilhoit parameterization of thermodynamic properties, and ring correction tree described in the previous section. However, these changes to the program were really necessitated by the variable temperature and pressure rapid-compression machine test case described later.

### 5.4.1.1 Description of Experiments

Dagaut et al. [2] studied oxidation of dilute stoichiometric mixtures of *n*-heptane and oxygen at 10 and 40 atm over the temperature range 550-1150 K in the jet-stirred reactor shown in Figure 5.10.  Vaporized fuel is mixed with a stream of oxygen and nitrogen in a convergent cone just before the reactor inlet. The inlet mixture is then expelled through four turbulent jets (ca. 1 mm diameter) to achieve a nearly homogeneous mixture in the reactor. Use of dilute fuel air mixtures (too dilute to support a flame) minimizes the effects of chemical heat release and allows the reactor to operate at steady-state. The reactor vessel (shown in Figure 5.11) was constructed of fused silica in order to prevent wall catalytic reactions [28]. The reactor has a movable gas sampling probe and thermocouple that can be used to test the spatial homogeneity of the reactor.

These tests showed that temperature gradients are typically 2-5 K (and always < 10 K) across the reactor, and no gradients in composition could be detected. The concentrations of 40 chemical species were measured in the reactor effluent using gas chromatography and combined gas chromatography/mass spectrometry (GS-MS). Carbon balances were reported to close to within 10% or better.

This model building exercise focused on a series of experiments conducted using a stoichiometric $n$-heptane mixture (0.1 mol % $n$-heptane, 1.1% oxygen, 98.8 % nitrogen) at a pressure of 10 atm, a mean residence time of 1 sec, and temperatures ranging from 550-1150 K. Predicted concentrations of $n$-heptane, CO, $CO_2$, and several important aldehydes and alkenes were compared with experimental measurements.

**Figure 5.10:** Diagram of the jet-stirred reactor used by Dagaut et al. [2]. A, oxygen + nitrogen inlet; B, hydrocarbon + nitrogen inlet; C, resistive preheater; D, resistive heater; E, spherical quartz reactor; F, pressure-resistant vessel; G, probe position adjuster; H, sonic sampling probe; I, thermocouple; J, exhaust line. Figure adapted from [28].
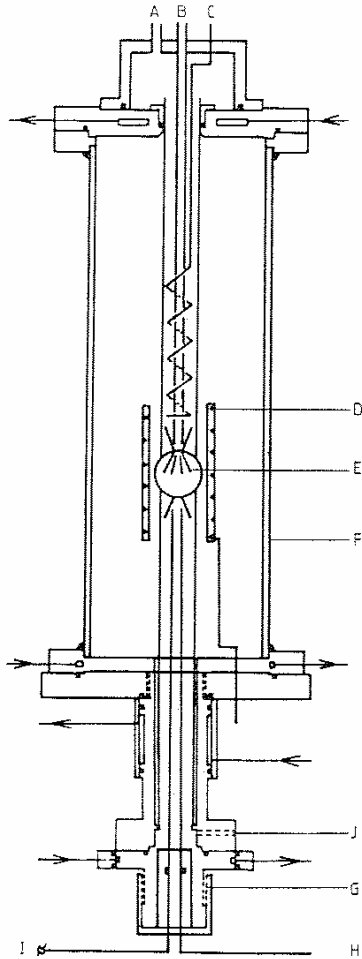
**Figure 5.11:** Detail of jet-stirred reactor used by Dagaut et al. [2]. A, external probe; B, convergent mixing cone; C, injectors; D, spherical quartz reactor vessel; E, divergent cone; F, movable sonic sampling probe and thermocouple; G, feed line surrounded by preheater. Figure adapted from [28].
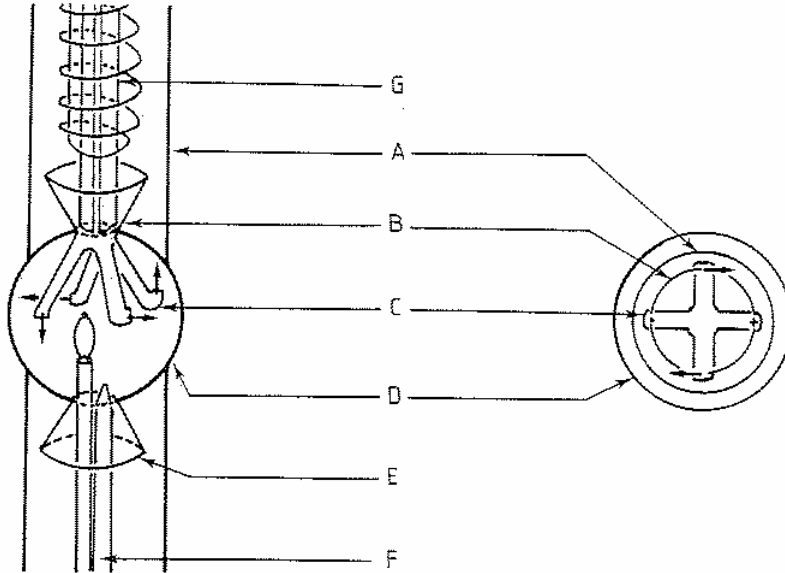


## 5.4.1.2 Reactor Model Assumptions

The jet-stirred reactor was modeled as a homogeneous, continuous, stirred-tank reactor (CSTR). Heterogeneous chemistry at the reactor wall was neglected, and the reactor was assumed to operate at a fixed temperature and pressure. The resulting set of governing equations is

$$Y_{k,out} - Y_{k,in} = \tau\left(v\dot{\omega}_k W_k\right) \tag{5.15}$$

where $\tau, v, Y_{k,in}, Y_{k,out}, \dot{\omega}_k$ and $W_k$ are the residence time, specific volume, inlet mass fraction, outlet mass fraction, molar rate of production, and molecular weight of species $k$, respectively. These model equations were solved by the CHEMKIN application AURORA, which uses a damped Newton's method combined with timestepping. When the initial guess for $Y_{k,out}$ was within the convergence domain of the Newton's method, AURORA quickly and efficiently found the solution. However, when the initial guess

was outside of the convergence domain, it was tedious and time-consuming to find a solution with AURORA.

Consequently, a new CSTR program was written that adds an unsteady term to the reactor equations and integrates to a steady-state solution. The modified equations are

$$\frac{dY_k}{dt} = \frac{Y_{k,in} - Y_{k,out}}{\tau} + v\dot{\omega}_k W_k .$$
(5.16)

After integrating for a long time (typically $10\tau$), the system approaches steady-state, and the unsteady term on the left-hand side of Eq. (5.16) goes to zero. At that point, the solution is essentially the same as the solution to Eq. (5.15). The time-integration was done using DASSL and the reaction rates were calculated using the CHEMKIN library of subroutines. Good agreement was observed between solutions from the new CSTR program and those calculated with AURORA. It was observed that the maximum timestep in DASSL needed to be manually limited in order to avoid oscillations in the species profiles. Typically a maximum timestep of 0.0001 sec was appropriate, but some low temperature cases needed an even smaller maximum timestep of 1E-6 sec. It was observed that the new CSTR program was more computationally expensive than AURORA but was also more robust. Consequently, the new CSTR program was used to find converged solutions for low temperature conditions where AURORA was failing.

### 5.4.1.3 RMG-Generated Chemistry Model

The RMG-generated chemistry model for the oxidation of dilute, stoichiometric *n*-heptane/oxygen mixtures at 10 bar and 900 K contained 72 chemical species and 569 elementary reactions. The initial reacted species pool contained C1 and C2 species from the methane oxidation mechanism developed at Leeds University [29, 30]. The reaction rates from the Leeds methane model were also included in the primary reaction library.

Those library reactions included solely temperature-dependent reactions, third-body reactions, and Troe-formatted pressure-dependent reactions. The larger intermediate species needed to describe the decomposition of $n$-heptane to C1 and C2 species were identified and added by RMG. Solely temperature-dependent reaction rates were estimated with the rate rule database. The reaction families included in this calculation were cyclic ether formation (reverse: cyclic ether decomposition to alkyl-hydroperoxyl radical), H abstraction, $HO_2$ elimination from peroxy radical, radical addition to a multiple bond (reverse: β-scission), bond dissociation (reverse: radical recombination), and CO addition to a radical (reverse: CO elimination from carbonyl radical). The pressure-dependent rates were estimated with CHEMDIS and parameterized using Chebyshev polynomials. The error tolerance used to determine $R_{min}$ was set to 0.05, and the goal conversion was 99.99%. The next section compares the predicted reactor effluent concentrations with the experimental measurements.

## 5.4.1.4 Comparison of Model Predictions with Experiment

The RMG chemistry model described in Section 5.4.1.3 and the physical reactor model described in Section 5.4.1.2 were used to predict the effluent composition of the jet-stirred reactor experiment of Dagaut et al. [2]. The comparison between model predictions and experiments are shown in Figures 5.12-15 for $n$-heptane, CO, $CO_2$, major aldehydes and major alkenes. Also shown are the predictions using the chemistry model of Curran et al. [5].

When comparing Curran's predictions to ours, it is important to remember than Curran's model is much larger (544 species and 2446 reactions versus 72 species and 569 reactions) and, more importantly, that Curran tuned key rate parameters so his results

match the experiments of Dagaut and others. In contrast the RMG results are *pure predictions*—no parameters have been adjusted to match the data. Additionally, no reaction rate families have been added or subtracted to try to improve agreement. This approach tests the *predictive* capability of chemical kinetics in its current stage of development. In other words, these are the predictions you would make if you built a kinetic model for these conditions with *no prior knowledge of the experimental results*.

With that said, many of the predictions are quite satisfactory. Figure 5.12 shows that above 750 K the predicted conversion of *n*-heptane is in reasonable agreement with experiment and is comparable to the prediction of Curran's model. Below 750 K, a solution could not be found to the CSTR equations with the RMG model—both AURORA and the new timestepping CSTR model failed. In general, it was very difficult to get converged solutions at conditions where the conversion is very low. It does not appear that the RMG model is capturing the cool-flame chemistry at lower temperatures (T < 750 K), which leads to low conversions and convergence problems.

Figure 5.13 shows that the predictions for $CO_2$ formation are quite accurate; however, the predictions for CO are low by about a factor of 4. The RMG model produces ethene and propene in larger quantities than seen experimentally. In the simulation, carbon remains in the form of these alkenes and does not further oxidize to form CO. Figure 5.14 shows the concentrations of various aldehydes. RMG is able to predict that formaldehyde is the favored product over acetaldehyde and propanal. In addition, above 750 K, the peak concentration of formaldehyde agrees with the experiment to within a factor of 2. Figure 5.15 shows the predictions for C7 alkenes. RMG predicts the relative importance of these species correctly (3-heptene > 2-heptene >

1-heptene). At higher temperatures, the concentrations of 3-heptene and 2-heptene agree with the experiment to within a factor of 2. Also, the prediction for the peak 3-heptene concentration (at about 800 K) is almost identical to the prediction of Curran's model.

**Figure 5.12:** Comparison of measured and predicted *n*-heptane concentrations from a jet-stirred reactor (inlet conditions, 0.01 mol % *n*-heptane, 1.1 % oxygen, 98.8 % nitrogen; 10 bar; 1 sec mean residence time). Filled symbols, experimental data of Dagaut et al. [2]; solid line, prediction using the chemistry model of Curran et al. [5]; dashed line, prediction using the RMG generated chemistry model.
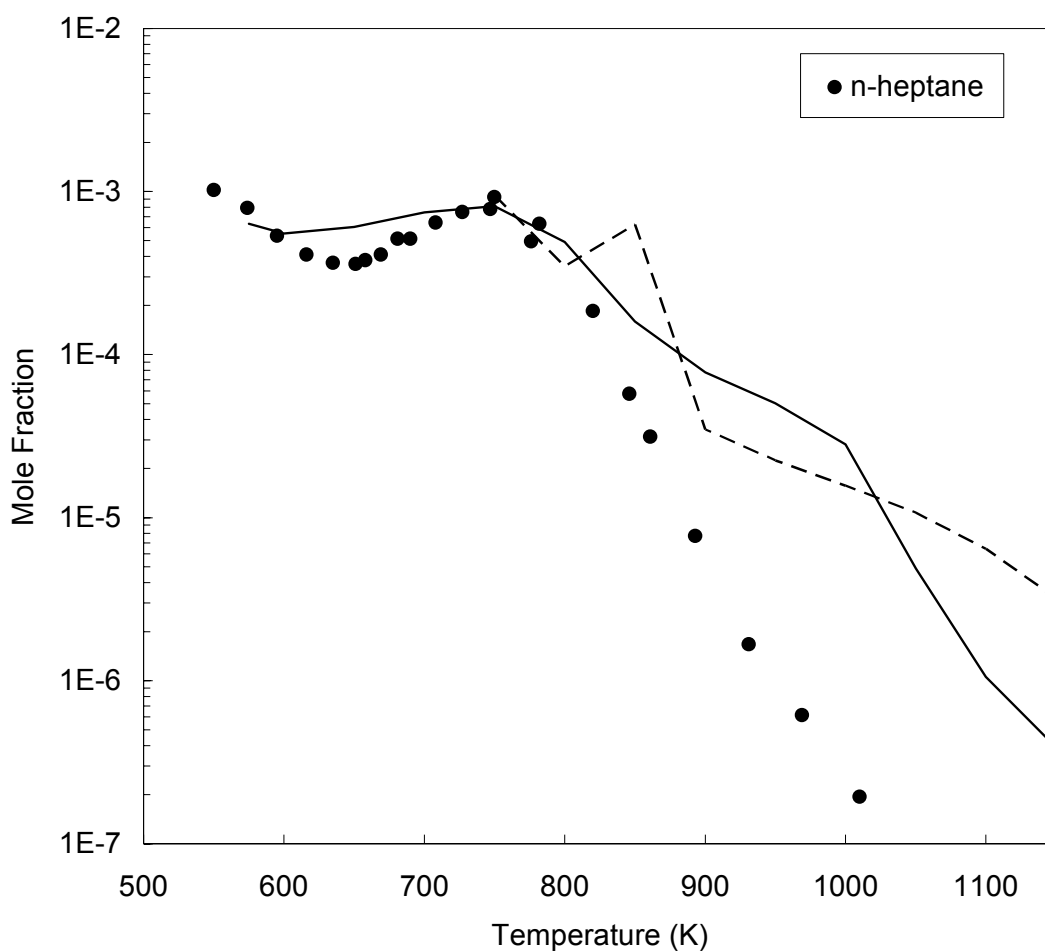
**Figure 5.13:** Comparison of measured and predicted CO and $CO_2$ concentrations from a jet-stirred reactor (inlet conditions, 0.01 mol % *n*-heptane, 1.1 % oxygen, 98.8 % nitrogen; 10 bar; 1 sec mean residence time). Filled symbols, experimental data of Dagaut et al. [2]; solid lines, predictions using the chemistry model of Curran et al. [5]; dashed lines, predictions using the RMG generated chemistry model.
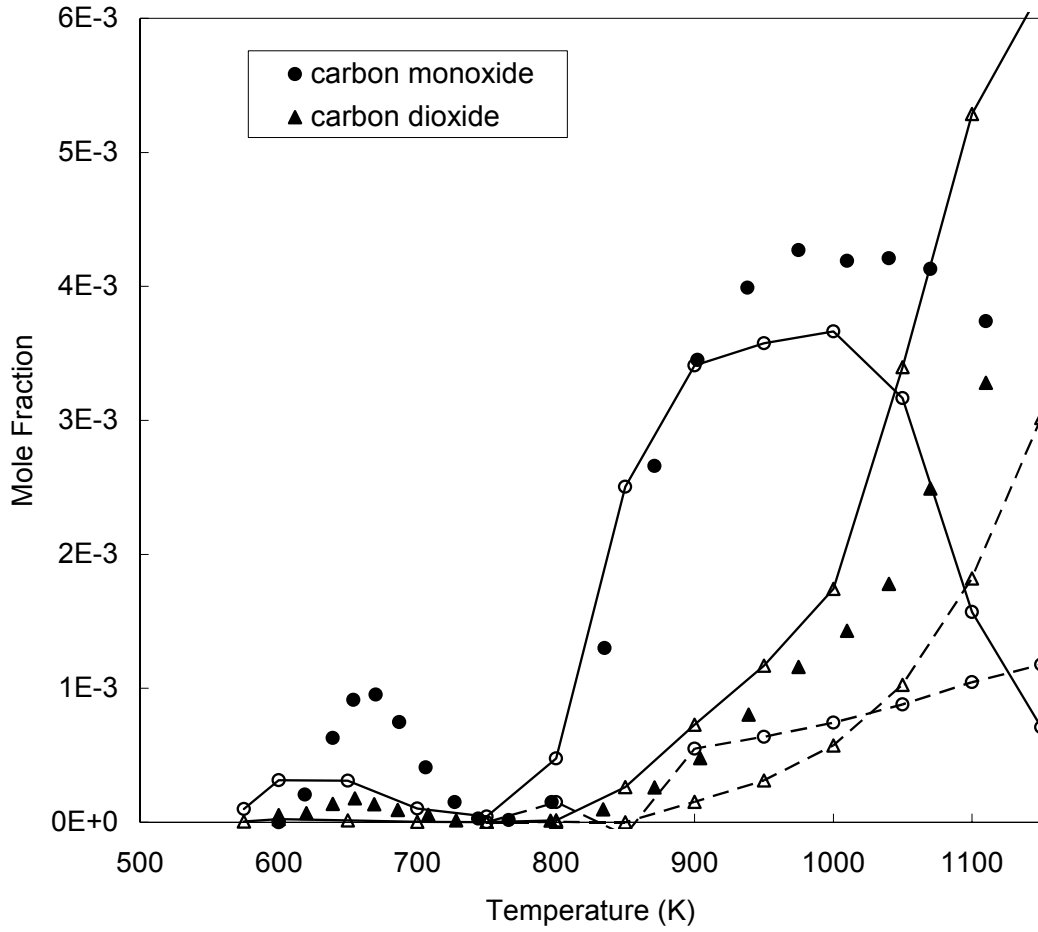
**Figure 5.14:** Comparison of measured and predicted aldehyde concentrations from a jet-stirred reactor (inlet conditions, 0.01 mol % *n*-heptane, 1.1 % oxygen, 98.8 % nitrogen; 10 bar; 1 sec mean residence time). Filled symbols, experimental data of Dagaut et al. [2]; solid lines, predictions using the chemistry model of Curran et al. [5]; dashed lines, predictions using the RMG generated chemistry model.
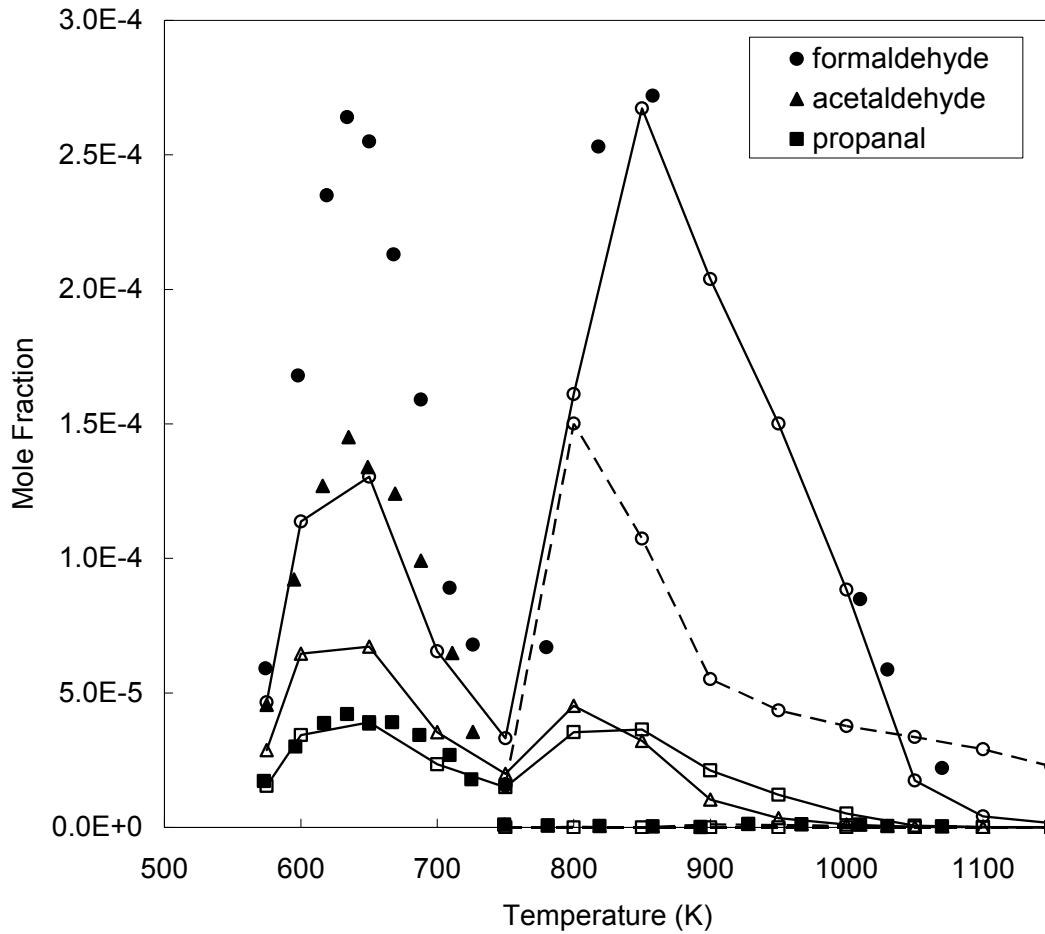
**Figure 5.15:** Comparison of measured and predicted alkene concentrations from a jet-stirred reactor (inlet conditions, 0.01 mol % *n*-heptane, 1.1 % oxygen, 98.8 % nitrogen; 10 bar; 1 sec mean residence time). Filled symbols, experimental data of Dagaut et al. [2]; solid lines, predictions using the chemistry model of Curran et al. [5]; dashed lines, predictions using the RMG generated chemistry model.
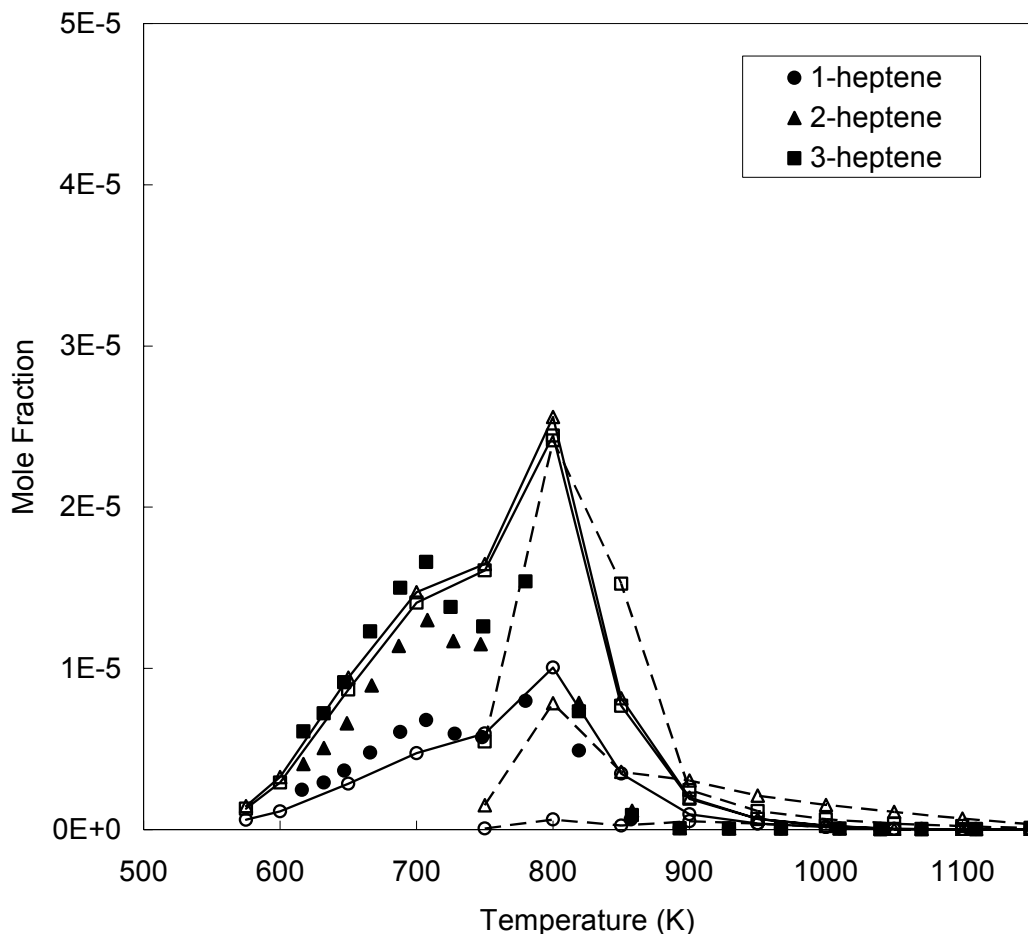


## 5.4.2 Rapid-Compression Machine Test Case

The jet-stirred reactor (JSR) test case described in the previous section is relevant to engines because low-temperature *n*-heptane oxidation chemistry in the JSR is similar to the early autoignition chemistry in an engine. However, the transient temperature- and pressure-time profiles in the engine differ from the dilute steady-state conditions of the JSR. Experiments conducted in rapid-compression machines (RCM) are more representative of practical engines. Consequently, a test case was performed using the

new variable temperature and pressure capability of RMG to simulate the RCM experiments of Minetti et al. [3].

### 5.4.2.1 Description of Experiments

The rapid-compression machine of Minetti et al. [3, 4, 31, 32] uses high-pressure air to drive a piston that compresses a homogeneous fuel/air/inerts mixture. The design of the RCM uses a unique right-angle design shown in Figure 5.16. The RCM fires by rapidly pressurizing the volume above the driving piston (3) which pulls the cam device (1) to the right. This motion causes the compression piston (4) to move up and compress the gases in the combustion chamber (2). The cam channel design (6) and the shock absorber (5) prevent the piston from rebounding. The compression time varies with the driving pressure in the high-pressure reservoir (7). Pressure and light emissions are measured from the combustion chamber. Additionally a gas sample can be collected at a given point in time during the experiment by means by puncturing an aluminum diaphragm (not shown) and rapidly expanding the gases into a large collection vessel that has been previously evacuated.

**Figure 5.16:** Diagram of the Lille rapid compression machine used by Minetti et al. [3]. 1, right-angle cam; 2, combustion chamber; 3, driving piston; 4, compressing piston; 5, shock absorber; 6, cam channel; 7, high-pressure gas reservoir; 8, cam release; 9 lateral windows; 10, axial window. Figure adapted from [32].
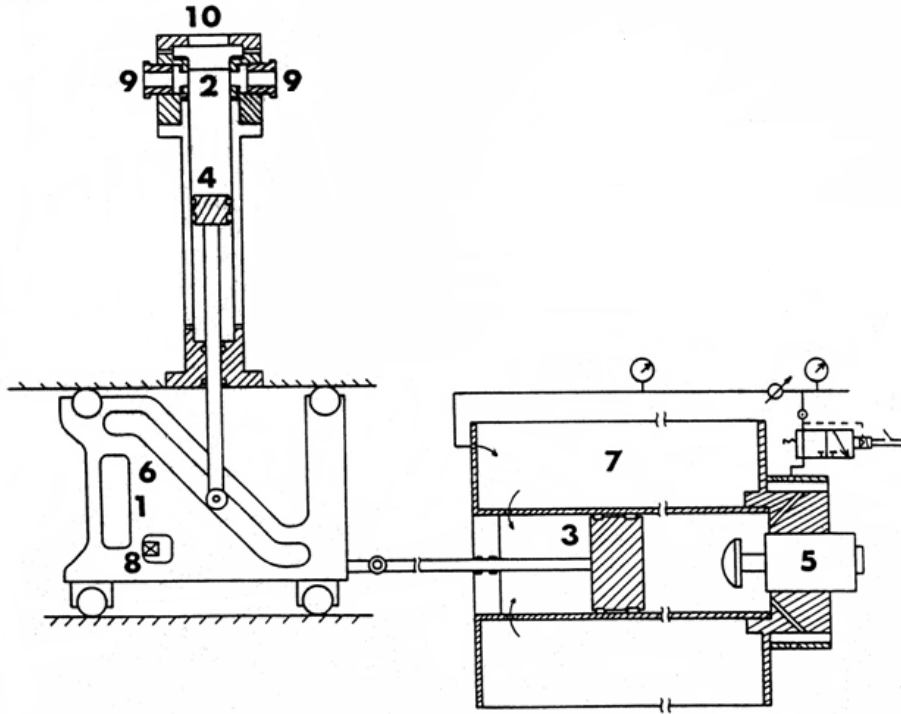


A detail of the RCM combustion chamber is shown in Figure 5.17. Rapid-compression machine experiments are more difficult to simulate than JSR experiments because of gradients of temperature in the combustion chamber caused by wall heat-losses, especially from the piston crevice. Previous simulations of similar rapid compression machines suggest, however, that a nearly adiabatic core gas region spans about 85% of the chamber diameter [3]. As discussed in the next section, our own computational-fluid dynamics simulations of this rapid-compression machine were performed to verify this claim.

The particular experimental conditions modeled in this work were for a stoichiometric *n*-heptane/'air' mixture. Air is in quotes because although the ratio of oxygen to inert gases was the same as air, some of the nitrogen was replaced by carbon-

dioxide to modulate the heat-capacity and hence control the compression temperature. The composition of the mixture in the experiment was 1.87 mol% *n*-heptane, 20.61% oxygen, 58.00% nitrogen, 17.52% carbon-dioxide, and 2.00% neon (included as an internal standard). Notice that this mixture is about a factor of 10 less dilute than that used in the JSR experiments. The initial temperature and pressure were 355K and 162 torr (0.216 bar) and the compression ratio was 9.8. The end-of-compression pressure was measured at 3.4 bar with a core-gas temperature estimated at 667 K.

**Figure 5.17:** Detail of the Lille combustion chamber of the rapid-compression machine used by Minetti et al. [3]. 1 and 2, piston rings; 3, rapid gas-sampling device; 4, axial window. Figure adapted from [32].
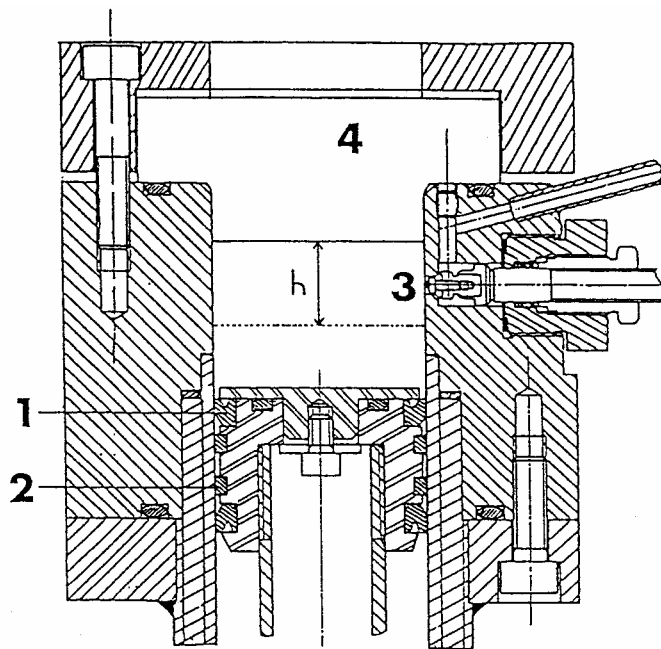


## 5.4.2.2 Reactor Model Assumptions

The rapid-compression machine was simulated at two levels of complexity. The simpler model ignored the compression process (60 ms in duration) and treated the combustion chamber as a homogeneous, adiabatic, constant-volume reactor. This model has been used by Minetti et al. [3] and Curran et al. [5] to simulate these experiments.

The temperature and pressure at the end-of-compression were calculated from the measured pressure trace and the assumption that the core gas was adiabatic. The equations used in this simulation are Eq. (5.1) for the species evolution and Eq (5.3) for the temperature evolution, where the compression work term is zero because of the constant-volume assumption. This simple model neglects spatial inhomogeneity, reactions during the compression phase, and heat losses to the walls.

Curran et al. [5] showed that heat-losses can be important, and speculated that temperature gradients might also affect model predictions. Therefore the more detailed multi-zone model described in Chapter 2 was applied to the Lille rapid-compression machine. The first step was to estimate the spatial temperature distribution during the compression phase using the KIVA computational fluid dynamics program [33]. The combustion chamber was assumed to be axis-symmetric and the geometry shown in Figure 5.17 was used in the simulations. The computational mesh used 10 connected blocks to describe the geometry. A fine mesh was used to resolve the wall boundary layer and the piston crevice, and coarser mesh was used in the core region. The mixture was assumed to be initially quiescent. Chemical reactions were not considered during compression, and wall heat losses were calculated using the turbulent law-of-the-wall [33].

Because KIVA was designed for internal-combustion engine simulations, the piston motion is governed by the slider-crank equation [15]; however, the piston motion in the RCM follows a different trajectory. Attempts to match the RCM piston profile using the slider-crank equation were not satisfactory. Therefore KIVA was modified so that the piston motion followed the correct RCM profile. This profile was obtained by

digitizing a figure from Ribacour et al. [32] which showed the Lille RCM piston motion in a similar experiment (see Figure 5.18).

**Figure 5.18:** Piston motion in the Lille rapid-compression machine used by Minetti et al. [3]. Shown are a) the measured piston position from Ribacour et al. [32] and b) the digitized position-time data and the corresponding calculated volume-time profile.
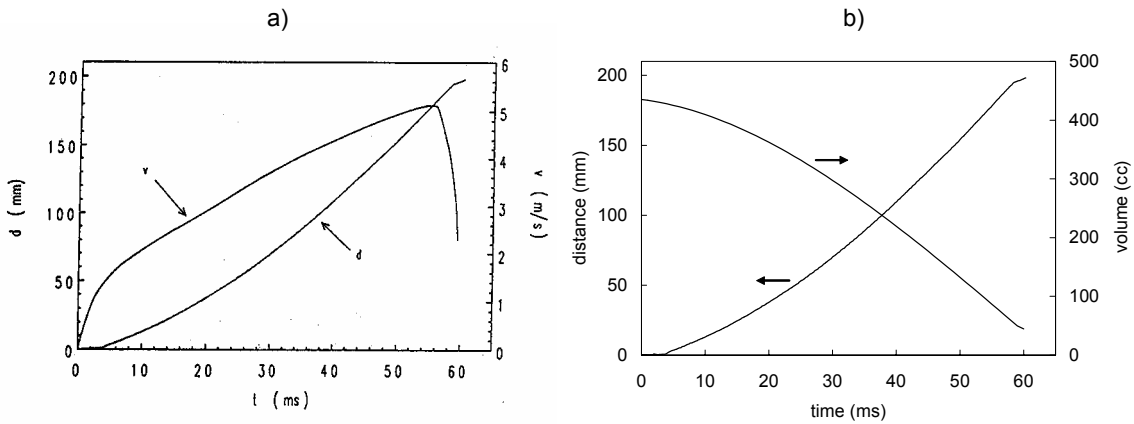


As mentioned, the initial pressure used in the experiment was 162 torr (216 mbar). When this initial pressure was used, the predicted end-of-compression pressure was slightly higher than the experimental pressure. This discrepancy is most likely caused by piston blow-by in the experiment that is not included in the KIVA calculations. To better match the experimental pressure, the initial pressure in the simulation was adjusted down by 20 mbar. The adjusted initial pressure (196 mbar) accurately reproduced the experimental end-of-compression pressure of 3.4 bar.

The KIVA simulation of compression in the Lille RCM predicted the interesting flow pattern shown in Figure 5.19. A obvious roll-up vortex has formed by at the end-of-compression (60 ms) which leads to a torodial region of hot gases (70-90 ms). Unexpectedly, the gas in the center of the chamber is cooler than the gas in this doughnut-shaped region. Experimental temperature field measurements obtained by

205

Clarkson et al. [34] using laser scattering techniques in an RCM also show the same result.

**Figure 5.19:** Prediction of the temperature field in the Lille rapid-compression machine used by Minetti et al. [3] during compression (stoichiometric *n*-heptane/'air' mixture; initial temperature, 355 K; initial pressure, 196 mbar; compression ratio, 9.8; compression duration, 60 ms).
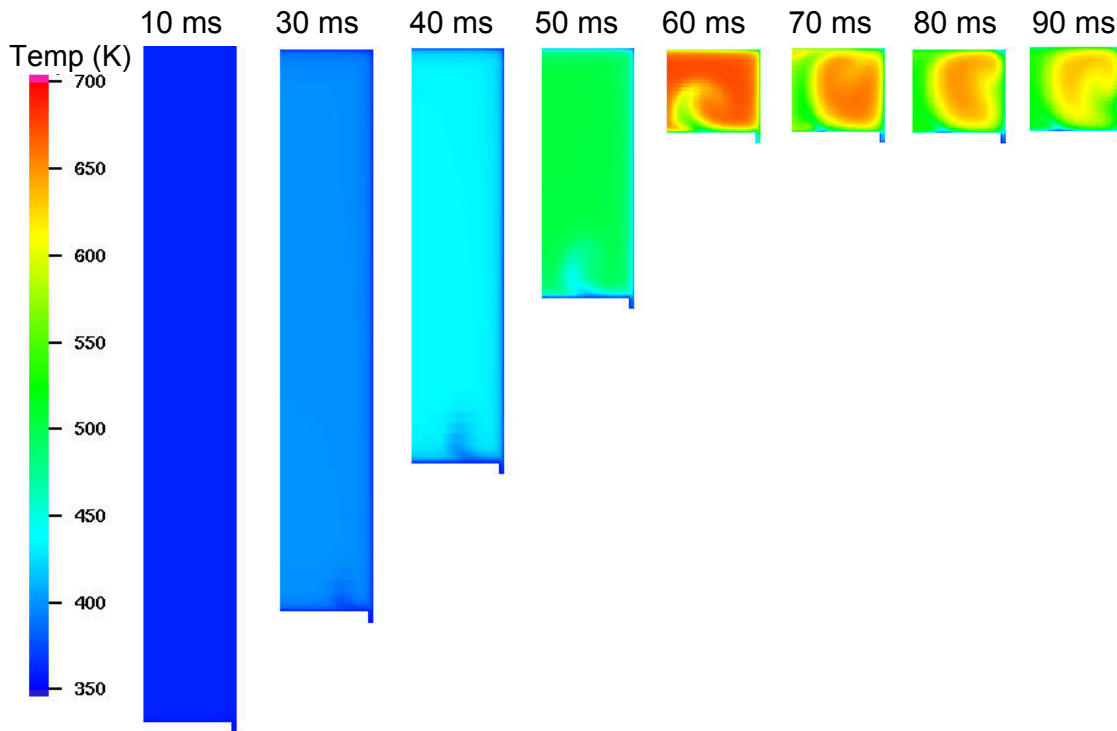


The temperature field data from KIVA, was then averaged to produced 10 zone temperature profiles based on a predetermined temperature-mass distribution. The particular temperature-mass distribution used was [2% 1% 1% 1% 2% 5% 10% 18% 25% 35%], which means zone 1 contains the coldest 2% of the mass, zone 2 contains the next coldest 1% of the mass, etc. The average zone temperature profiles and the cylinder pressure profile are shown in Figure 5.20. Using this information, the multi-zone calculations were performed for the RCM in exactly the same way as the HCCI multi-

zone calculations performed in Chapter 2 (see that chapter for details on the multi-zone governing equations). Results from these calculations are discussed in Section 5.4.2.4.

**Figure 5.20:** Cylinder pressure and average zone temperatures used in the multi-zone calculation of the Lille rapid-compression machine.
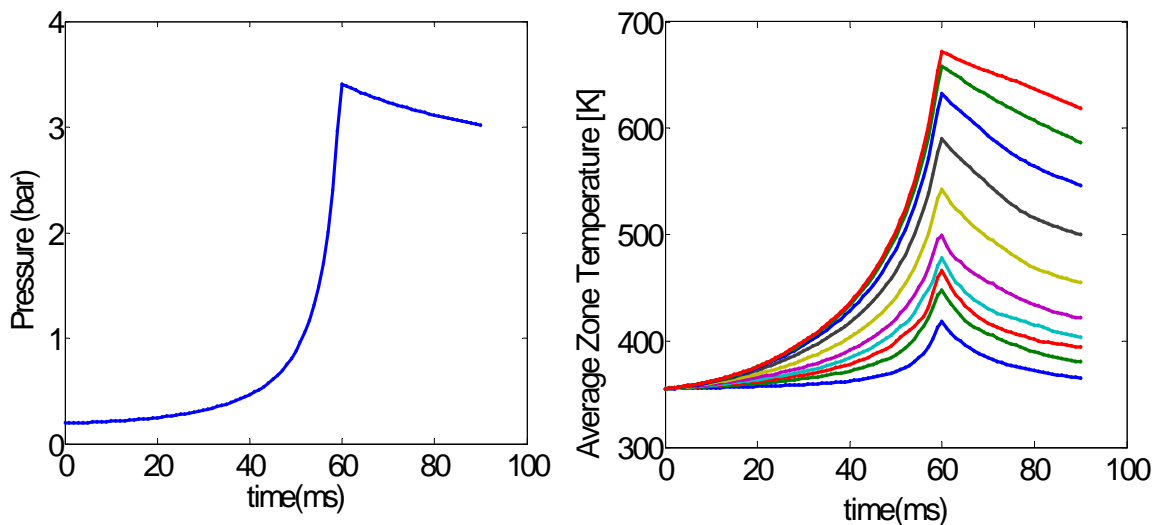


### 5.4.2.3 Generated Chemistry Model

Unfortunately attempts to generate chemistry models at the RCM operating conditions (667 K, 3.4 bar) did not lead to autoignition. It appears that some key initiation reactions or missing or that their rates are too low. Using our current rate-rule database, RMG finds that very little chemistry is happening at 667 K and does not add any species to the model. The observation that some important low-temperature ignition reactions are missing is corroborated by our calculations for the JSR, which showed no appreciable conversion at temperatures below 750 K.

Consequently a model was built for a 40% higher initial temperature and pressure (total density was held constant). At these conditions (934 K and 4.7 bar), ignition does occur in RMG. We believe this calculation is the first time that the energy equation has been solved during model construction to determine the conditions of temperature and

207

pressure in the reactor vessel. The model was constructed using the same reaction families used for the JSR test case (see Section 5.4.1.3). The error tolerance used to determine $R_{min}$ was set to 0.15. Two different finish-controllers were used leading to two different chemistry models. RMG Model A used a goal conversion of 99.9% as the finish-controller and resulted in a model with 61 species and 516 reactions. RMG Model B used a simulation time of 30 ms as the finish-controller and resulted in a model with 97 species and 875 reactions. Both models include solely temperature-dependent reactions, third-body reactions, Troe fall-off reactions, and Chebyhsev-formatted pressure dependent reactions. The predictions of these two models are compared with Curran's predictions in the next section.

## 5.4.2.4 Comparison of Model Predictions with Experiment

Since a successful RMG-generated chemistry model was not obtained at the conditions of the Minetti's experiment, a direct comparison with that data could not be made. However, several interesting conclusions can still be drawn from this work. First, I use Curran's chemistry model to show the importance of the physical model in simulating rapid compression machine experiments. Second, I compare the results of the RMG chemistry model and Curran's chemistry model at 934 K and 4.7 bar.

*Effect of the physical model in RCM simulations*

Minetti et al. [3] noticed that kinetic model simulations of their RCM data seriously overpredicted the fraction of fuel consumed in the first-stage ignition. They observe that about 20% of *n*-heptane was consumed in the first-stage, but detailed kinetic models predicted that about 80% is consumed. This overprediction of fuel conversion disrupts all the other predictions of stable intermediates. Our simulations show this

overprediction in *n*-heptane conversion in the first-stage ignition might be due to the fact that Minetti et al. [3] neglected temperature gradients in the chamber and assumed the RCM to be perfectly homogeneous. Figure 5.21 shows about 80% *n*-heptane conversion was observed with the homogeneous-reactor model calculation. By comparison, Figure 5.22 shows the results of using the multi-zone model described in Section 5.4.2.2 to simulate same conditions. In order to compare only the effect of spatial temperature inhomogeneity, this multi-zone calculation does not include heat losses after the end-of-compression. As shown, the combustion event was more gradual and the fraction of fuel consumed in the first stage of ignition was close to 50%. The stair-step appearance in the *n*-heptane profile is caused by time lag between the first-stage ignitions of the two fairly large high-temperature zones. These results show that RCM experiments should be simulated with at least this level of sophistication, and predictions would benefit from even more detailed models (e.g. more zones). This example shows the danger of tuning kinetic rate parameters to experimental data when the physical model has deficiencies. The result of these tuning exercises is a chemistry that no longer contains only information about true chemical processes—compensations for deficiencies in the physical model are also included.

**Figure 5.21:** Homogeneous-reactor model predictions of *n*-heptane conversion and CO formation in the rapid-compression machine experiment of Minetti et al. [3] using the chemistry model of Curran et al. [5]. (0 ms corresponds to the end-of-compression)
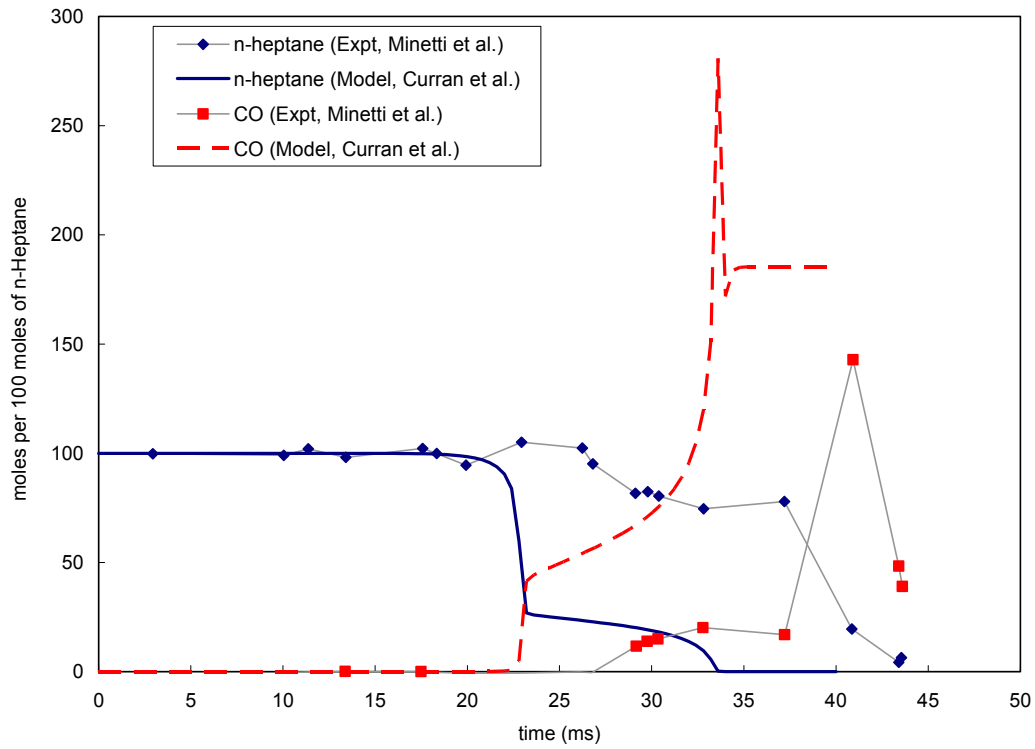
**Figure 5.22:** Multi-zone model predictions of *n*-heptane conversion and CO formation in the rapid-compression machine experiment of Minetti et al. [3] using the chemistry model of Curran et al. [5]. (0 ms corresponds to the end-of-compression)
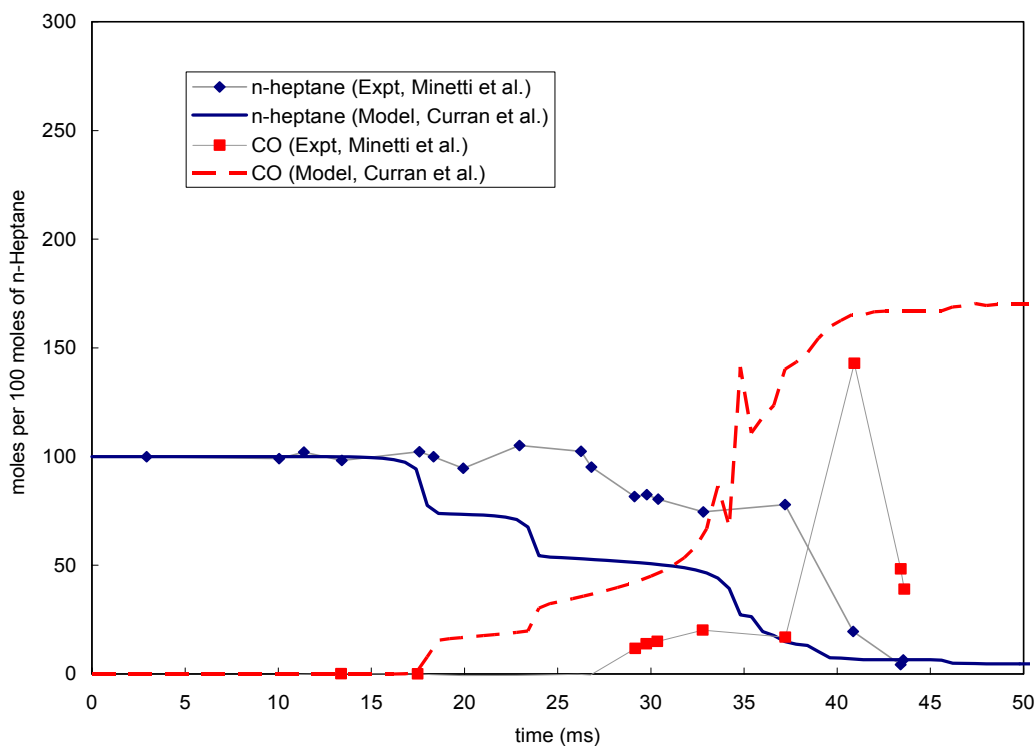


*Comparison of the RMG and Curran et al. chemistry models at 934K*

Figure 5.23 shows a comparison the RMG-generated chemistry models and the *n*-heptane model of Curran et al. [5] at 934K and 4.7 atm. The ignition delay predicted by Curran's model is in good agreement with the experimental ignition from Minetti [3] at this temperature (ca. 20 ms). Curran's chemistry model shows a one-stage ignition process at this temperature (934 K), unlike the two-stage ignition predicted for the lower temperature (667 K, Figure 5.21). Interestingly, the RMG-generated models show two-stage ignition with the ignition delay for the first-stage about the same as the total ignition delay predicted by Curran. Minetti et al. [3] do not report whether a two-stage ignition was observed at 934 K. RMG Model A predicts a total ignition delay of 67 ms, about a factor of 3 high for these conditions. RMG Model B predicts an ignition delay of

33 ms, which agrees quite well with the experiment and Curran. Also the equilibrium temperature predicted by Model B (2747 K) is in much better agreement with Curran's model (2748 K) than Model A (2641 K). Because there are so many parameters in the chemistry model and we are only comparing one observation, namely temperature, we cannot say whether Model B is more mechanistically correct than Model A; however, the results of the larger Model B are promising.

Again these RMG results are *pure predictions* with no tuning of rate parameters or other efforts to give good agreement with experiment. These results show the current efficacy of detailed chemical kinetics as a *predictive* tool for complex oxidation systems. Overall, I would say that the results are promising but tuning rate constants to match experiments (given that the physical model is accurate) is still necessary for application of detailed chemical kinetics to practical engineering simulations of combustion.

**Figure 5.23:** Comparison of two RMG-generated chemistry model with the Curran et al. [5] chemistry model at 934 K and 4.7 bar. RMG Model A has 61 species and 516 reactions. RMG Model B has 97 species and 875 reactions. The assumed end-of-compression temperature and pressure are 40% higher than those used in the experiment of Minetti et al. [3], but the total density is the same.
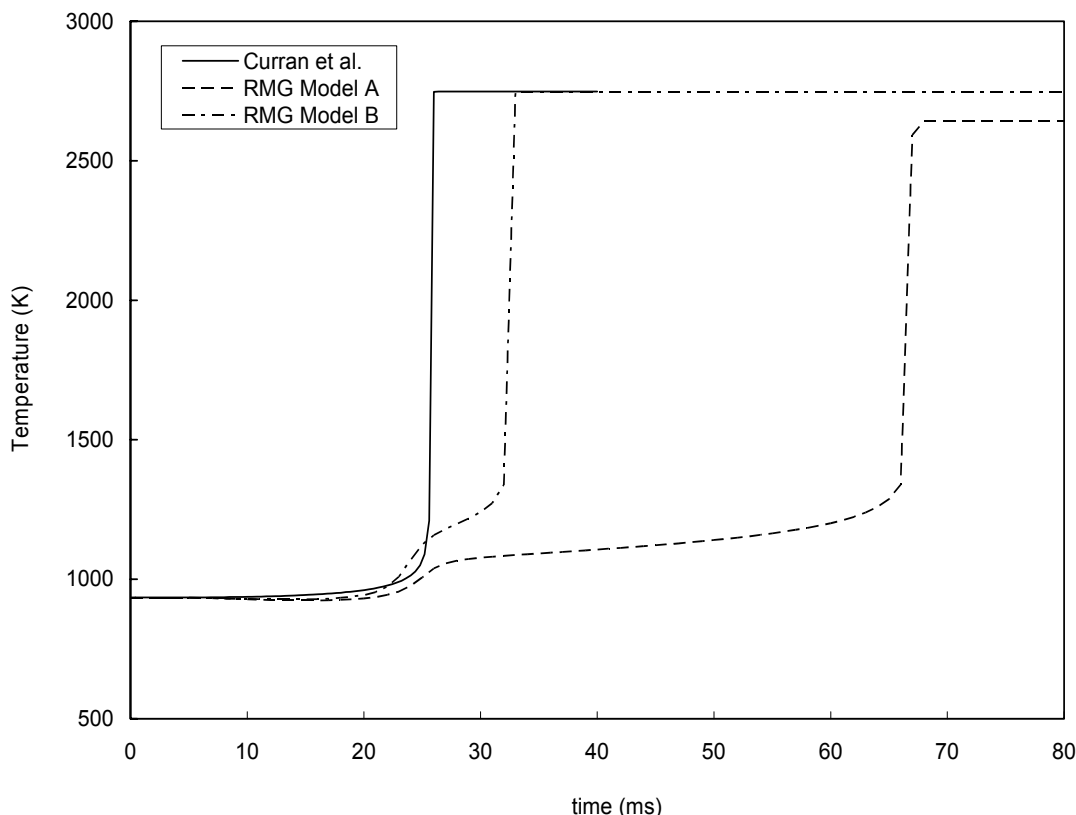


## 5.5  Conclusions

- Automatically generated chemistry models for oxidation of higher hydrocarbons in systems where temperature and pressure are time-varying have been performed using an extension of the RMG model-generation software developed by Song [1].

- Multi-zone calculations show that consideration of spatial temperature gradients is important when interpreting rapid-compression machine data. These gradients can partially explain the overprediction of *n*-heptane conversion during first-stage ignition predicted by homogeneous reactor models with detailed chemistry. Prior

studies that neglected temperature inhomogeneity in RCM experiments probably incorrectly adjusted reaction rate parameters to force a fit with this data.

- Purely predictive chemistry models for *n*-heptane oxidation in two test cases showed that reasonable agreement can be obtained with no tuning of kinetic parameters or addition/subtraction of reaction families. Nonetheless, some chemistry model tuning is necessary to construct models that are quantitatively useful for practical engineering simulations of combustion system, such as HCCI engines.

## 5.6  References

1.  Song, J., *Building Robust Chemical Reaction Mechanisms: Next Generation of Automatic Model Construction Software*, in *Department of Chemical Engineering*. 2004, Massachusetts Institute of Technology: Cambridge, MA.

2.  Dagaut, P., M. Reuillon, and M. Cathonnet, *Experimental Study of the Oxidation of n-Heptane in a Jet Stirred Reactor from Low to High Temperature and Pressures up to 40 Atm.* Combustion and Flame, 1995. **101**: p. 132-140.

3.  Minetti, R., et al., *A Rapid Compression Machine Investigation of Oxidation and Auto-Ignition on n-Heptane: Measurements and Modeling.* Combustion and Flame, 1995. **102**: p. 298-309.

4.  Minetti, R., et al., *Comparison of oxidation and autoignition of the two primary reference fuels by rapid compression.* Proceedings of the Combustion Institute, 1996. **26**: p. 747-753.

5.  Curran, H.J., et al., *A Comprehensive Modeling Study of n-Heptane Oxidation.* Combustion and Flame, 1998. **114**: p. 149-177.

6.  Curran, H.J., et al., *A Comprehensive Modeling Study of iso-Octane Oxidation.* Combustion and Flame, 2002. **129**: p. 253-280.

7.  Susnow, R.G., et al., *Rate-Based Construction of Kinetic Models for Complex Systems.* J. Phys. Chem. A., 1997. **101**: p. 3731-3740.

8.  Ranzi, E., et al., *Lumping procedures in detailed kinetic modeling of gasification, pyrolysis, partial oxidation and combustion of hydrocarbon mixtures.* Prog. Energy Combust. Sci., 2001. **27**: p. 99-139.

9.  Come, G.M., et al., *Computer aided design of gas-phase oxidation mechanism : Application to the modelling of normal-heptane and iso-octane oxidation.* Proceedings of the Combustion Institute, 1997. **26**: p. 755-762.

10. Matheu, D.M., et al., *Mechanism Generation with Integrated Pressure Dependence: A New Model for Methane Pyrolysis.* J. Phys. Chem. A., 2003. **107**(41): p. 8552-8565.

11. Widjaya, C., *Ph.D. Thesis*, in *Department of Chemical Engineering*. 2003, Massachusetts Institute of Technology: Cambridge, MA.

12. Yu, J., *Estimation Method for the Thermochemical Properties of Polycyclic Aromatic Molecules*, in *Department of Chemical Engineering*. 2004, Massachusetts Institute of Technology: Cambridge, MA.

13. Brown, P.N., G.D. Byrne, and A.C. Hindmarsh, *Vode - a Variable-Coefficient Ode Solver.* Siam Journal on Scientific and Statistical Computing, 1989. **10**(5): p. 1038-1051.

14. Brown, P.N., A.C. Hindmarsh, and L.R. Petzold, *Using Krylov Methods in the Solution of Large-Scale Differential-Algebraic Systems.* Siam Journal on Scientific Computing, 1994. **15**(6): p. 1467-1488.

15. Heywood, J.B., *Internal Combustion Engine Fundamentals*. 1988, New York: McGraw-Hill, Inc. pp. 100-107.

16. Kee, R.J., et al., *CHEMKIN III: A FORTRAN Chemical Kinetics Package for the analysis of gas-phase chemical and plasma kinetics*. 1996, Sandia National Laboratories: Livermore, CA.

17.     Matheu, D.M., *Integrated Pressure-Dependence in Automated Mechanism Generation: A New Tool for Building Gas-Phase Kinetic Models*, in *Department of Chemical Engineering*. 2002, Massachusetts Institute of Technology: Cambridge, MA.

18.     Chang, A.Y., J.W. Bozzelli, and A.M. Dean, *Kinetic analysis of complex chemical activation and unimolecular dissociation reactions using QRRK theory and the modified strong collision approximation*. Zeitschrift Fur Physikalische Chemie-International Journal of Research in Physical Chemistry & Chemical Physics, 2000. **214**: p. 1533-1568.

19.     Venkatesh, P.K., et al., *Parameterization of Pressure- and Temperature-Dependent Kinetics in Multiple Wells Reactions*. AIChE Journal, 1997. **43**(5): p. 1331-1340.

20.     Naik, C., H.-H. Carstensen, and A.M. Dean, *Reaction Rate Representation Using Chebyshev Polynomials*. 2002: Golden, CO.

21.     Press, W.H., et al., *Numerical Recipes in Fortran 77: The Art of Scientific Computing*. 2 ed. Vol. 1. 1992, Cambridge, England: Cambridge University Press.

22.     Benson, S.W., *Thermochemical Kinetics*. 1976, New York: Wiley.

23.     Ritter, E.R., *THERM:  A Computer Code for Estimating Thermodynamics Properties for Species Important to Combustion and Reaction Modeling*. J. Chem. Inf. Comput. Sci., 1991. **31**(3): p. 400-409.

24.     Wilhoit, R.C., Thermodynamics Research Center Current Data News, 1975. **3**(2).

25.     Burcat, A., *Thermodynamic Data for Combustion Calculations*, in *Combustion Chemistry*, W.C. Gardiner Jr., Editor. 1984, Springer-Verlag: New York.

26.     Dorofeeva, O.V., *Ideal gas thermodynamic properties of oxygen heterocyclic compounds.  Part 2.  Six-membered, seven-membered and eight-membered rings*. Thermochimica Acta, 1992. **200**: p. 121-150.

27.     Lay, T.H., et al., *Thermodynamic parameters and group additivity ring corrections for three- to six-membered oxygen heterocyclic hydrocarbons*. Journal of Physical Chemistry A, 1997. **101**(13): p. 2471-2477.

28.     Dagaut, P., et al., *A jet-stirred reactor for kinetic studies of homogeneous gas-phase reactions at pressures up to ten atmospthers (~1 MPa)*. J. Phys. E: Sci. Instrum., 1986. **19**.

29.     Hughes, K.J., et al., *Development and Testing of a Comprehensive Chemical Mechanism for the Oxidation of Methane*. Int. J. Chem. Kinet., 2001. **33**: p. 513-538.

30.     Baulch, D.L., et al., *Summary Table of Evaluated Kinetic Data for Combustion Modeling: Supplement 1*. Combustion and Flame, 1994. **98**: p. 59-79.

31.     Minetti, R., et al., *Experimental and Modeling Study of Oxidation and Autoignition of Butane at High Pressure*. Combustion and Flame, 1994. **96**: p. 201-211.

32.     Ribaucour, M., et al., *Autoinflammation a haute pression. Conception, realisation et test d'une machine a compression rapide*. J. Chim. Phys., 1992. **89**: p. 2127-2152.

33.     Amsden, A., *KIVA-3V: A Block-Structured KIVA Program for Engines with Vertical or Canted Valves*. 1997, Los Alamos National Laboratory: Los Alamos, NM.

34.     Clarkson, J., et al., *Temperature fields during the development of combustion in a rapid compression machine.* Combustion and Flame. **125**(3): p. 1162-1175.

## 5.7  Supplementary Material

## 5.7.1  KIVA3v2 input file for the Lille RCM (itape5)

```
K122298 Lille RCM run with crevice / 10 block  (PEY 22/06/04)
 irest      0
nohydro     0
 lwall      1
 lpr        0
 irez       2
 ncfilm 9999
 nctap8 9999
 nclast 9999
 ncmon     10
ncaspec    12
 -175.0, -150.0, -120.0, -90.0, -60.0, -30.0, -5.0, 0.0, 10.0,
  30.0, 60.0, 90.0
 gmv        1.0
 cafilm   9.99e+9
 cafin   95.0
 angmom    1.0
 pgssw     1.0
 dti   1.000e-5
 dtmxca    1.0
 dtmax    9.99e+9
 tlimd     1.0
 twfilm   9.99e+9
 twfin    9.99e+9
 fchsp    0.25
 bore      5.0
 stroke   19.9
 squish    1.23
 rpm      5.0e+2
 atdc    -180.0
 datdct    0.0
 revrep    2.0
 conrod   15.0
 swirl     0.0
 swipro    0.0
 thsect    0.5
 sector    1.0
 deact     0.0
 epsy      1.0e-3
 epsv      1.0e-3
 epsp      1.0e-4
 epst      1.0e-3
 epsk      1.0e-3
 epse      1.0e-3
 gx        0.0
 gy        0.0
 gz        0.0
 tcylwl  355.0
 thead   355.0
 tpistn  355.0
 pardon    0.0
 a0        0.0
 b0        1.0
 artvis    0.0
 ecnsrv    0.0
 adia      0.0
 anu0      0.0
 visrat-.66666667
 tcut    800.0
 tcute  1200.0
 epschm   0.02
 omgchm   1.0
 turbsw   1.0
 sgsl      0.0
trbchem    0.0
```

```
  capa       18.0
pmplict      0.0
lospeed      0.0
 airmu1   1.457e-5
 airmu2    110.0
 airla1    252.0
 airla2    200.0
 prl        0.74
 rpr        1.11
 rsc        1.11
 xignit     0.0
 t1ign     -1.0
 tdign     -1.0
 ca1ign    -27.0
 cadign     9.6
 xignl1     0.25
 xignr1     0.75
 yignf1     0.0
 yignd1     0.238
 zignb1    11.75
 zignt1    12.50
 xignl2     0.0
 xignr2     0.0
 yignf2     0.0
 yignd2     0.0
 zignb2     0.0
 zignt2     0.0
 kwikeq     0
 numnoz     0
 numinj     0
 numvel     0
injdist     1
 kolide     0
 tpi      350.0
 turb       1.0
breakup      0.0
 evapp      0.0
 nsp        4
   c7h16
     o2    mw2    32.000   htf2     0.0
     n2    mw3    28.016   htf3     0.0
    co2    mw4    44.011   htf4   -93.965
stoifuel    1.0
 stoio2     2.0
 nreg       1
'presi',   1.9600e+5
'tempi',    355.0
'tkei',      0.10
'scli',      0.0
'er',        0.00
'mfracfu',   0.0577
'mfraco2',   0.2035
'mfracn2',   0.5010
'mfracco2',  0.2378
 nrk        0
 nre        0
nvalves     0
 isoot      0
```

## 5.7.2  KIVA3v2 mesh generation file for the Lille RCM (iprep)

```
K3PREP/100198 10-block grid for Lille RCM with crevice (PEY 24/6/04)
  bore       5.0
  stroke    19.9
  squish     1.23
  thsect     0.5
 nblocks    10
   1 100  1  90   0   2   1   0
```

```
 2.0     2.0     0.0     0.0     2.0     2.0     0.0     0.0
 0.0     0.0     0.0     0.0     0.0     0.0     0.0     0.0
 0.79    0.79    0.79    0.79    0.79    0.79    0.79    0.79
 3.0     4.0     5.0     6.0     4.0     4.0
-1.0    -1.0    -1.0    -1.0    -1.0    -1.0
  2  30   1  90   0   2   1    0
 2.35    2.35    2.0     2.0     2.35    2.35    2.0     2.0
 0.0     0.0     0.0     0.0     0.0     0.0     0.0     0.0
 0.79    0.79    0.79    0.79    0.79    0.79    0.79    0.79
 4.0     4.0     5.0     6.0     4.0     4.0
-1.0    -1.0    -1.0    -1.0    -1.0    -1.0
  3 100   1  50   0   1   1    0
 2.0     2.0     0.0     0.0     2.0     2.0     0.0     0.0
 0.0     0.0     0.0     0.0     0.0     0.0     0.0     0.0
 0.29    0.29    0.29    0.29    0.79    0.79    0.79    0.79
 3.0     4.0     5.0     6.0     1.0     4.0
-1.0    -1.0    -1.0    -1.0    0.0     -1.0
  4  30   1  50   0   1   1    0
 2.35    2.35    2.0     2.0     2.35    2.35    2.0     2.0
 0.0     0.0     0.0     0.0     0.0     0.0     0.0     0.0
 0.29    0.29    0.29    0.29    0.79    0.79    0.79    0.79
 4.0     4.0     5.0     6.0     1.0     4.0
-1.0    -1.0    -1.0    -1.0    0.0     -1.0
  5 100   1  50   0   3   1    0
 2.0     2.0     0.0     0.0     2.0     2.0     0.0     0.0
 0.0     0.0     0.0     0.0     0.0     0.0     0.0     0.0
 0.0     0.0     0.0     0.0     0.5     0.5     0.5     0.5
 3.0     4.0     5.0     6.0     4.0     2.0
-1.0    -1.0    -1.0    -1.0    -1.0    -1.0
  6  30   1  50   0   3   1    0
 2.35    2.35    2.0     2.0     2.35    2.35    2.0     2.0
 0.0     0.0     0.0     0.0     0.0     0.0     0.0     0.0
 0.0     0.0     0.0     0.0     0.5     0.5     0.5     0.5
 4.0     4.0     5.0     6.0     4.0     2.0
-1.0    -1.0    -1.0    -1.0    -1.0    -1.0
  7  20   1  30   0   1   1    0
 2.5     2.5     2.35    2.35    2.5     2.5     2.35    2.35
 0.0     0.0     0.0     0.0     0.0     0.0     0.0     0.0
 0.0     0.0     0.0     0.0     0.29    0.29    0.29    0.29
 1.0     2.0     5.0     6.0     1.0     4.0
 0.0    -1.0    -1.0    -1.0    0.0     -1.0
  8  20   1  50   0   1   1    0
 2.5     2.5     2.35    2.35    2.5     2.5     2.35    2.35
 0.0     0.0     0.0     0.0     0.0     0.0     0.0     0.0
 0.29    0.29    0.29    0.29    0.79    0.79    0.79    0.79
 4.0     2.0     5.0     6.0     4.0     4.0
-1.0    -1.0    -1.0    -1.0    -1.0    -1.0
  9  20   1  90   0   2   1    0
 2.5     2.5     2.35    2.35    2.5     2.5     2.35    2.35
 0.0     0.0     0.0     0.0     0.0     0.0     0.0     0.0
 0.79    0.79    0.79    0.79    0.79    0.79    0.79    0.79
 4.0     2.0     5.0     6.0     4.0     4.0
-1.0    -1.0    -1.0    -1.0    -1.0    -1.0
 10  20   1  50   0   3   1    0
 2.5     2.5     2.35    2.35    2.5     2.5     2.35    2.35
 0.0     0.0     0.0     0.0     0.0     0.0     0.0     0.0
 0.0     0.0     0.0     0.0     0.5     0.5     0.5     0.5
 4.0     2.0     5.0     6.0     4.0     2.0
-1.0    -1.0    -1.0    -1.0    -1.0    -1.0
 ncopy     0
 tiltflag     0
 pentflag     0
wedgeflag     0
translate     0
  nlocxy     0
  reshape     0
npentxy     0
nvguide     0
nvalvport     0
nrunner     0
nsiamese     0
```

```
 nround       0
  npatch   13
  2    1   1   1   1    2
  1    5   3   1   1    1
  2    5   4   1   1    2
  4    1   3   1   1    4
  5    5   1   1   1    5
  6    5   2   1   1    6
  6    1   5   1   1    6
  8    5   7   1   1    8
  9    5   8   1   1    9
 10    5   9   1   1   10
  8    1   4   1   1    8
  9    1   2   1   1    9
 10    1   6   1   1   10
  nrelaxb      0
 nprovtop      0
 nprovfce      0
 nzcylwall     0
     tilt      0
ndish          0
nscallop       0
xoffset    0.0
yoffset    0.0
write17    1.0
plotmesh   1.0
 xband     0.0
 yband     0.0
 zband     0.0
 nxplots    0
 nyplots    1
  0.0
 nzplots    0
  nvhide    0
```

# Chapter 6:    Final Conclusions and Recommendations

## 6.1 Final Conclusions

### 6.1.1 Conclusions from Multi-zone Engine Modeling

- It has been shown that numerical simulations can be used to predict the viable operating range of HCCI combustion. The predicted operating range is shown to be in good agreement with literature experimental data.

- The multi-zone modeling technique has been extended to allow even extremely detailed fuel chemistry (more that 1000 species and 4000 reactions) to be quickly simulated on a standard PC by exploiting sparsity in the model equations.

- A fundamental criterion for determining the onset of knock was developed based on the idea that HCCI knock originates because of local overpressures due to very fast chemical heat-release. This knock criterion is shown to give accurate predictions of the knock limit and hence maximum torque available from an HCCI engine. This ability to predict the limits of viable HCCI operation should allow engine designs and control strategies to be rapidly screened before experiments are performed.

### 6.1.2 Conclusions from HCCI Design Study

- Cycle simulations and perfectly-stirred reactor models can be used to construct performance maps for HCCI engine designs and evaluate performance over the range of operating conditions seen in regulatory drive cycles.

- A dimensionless knock parameter and PSR model can be used to predict the onset of HCCI knock and hence the maximum attainable torque. The predictions of the knock parameter, $\beta$, from the perfectly-stirred reactor model are in good agreement with the multi-zone model, which has been shown previously to accurately predict knock in experimental engines.

- For detailed chemistry models, computational time can be reduced by a factor of 10 or more by exploiting sparsity in the model equations for a perfectly-stirred reactor.

- Numerical simulations of HCCI engines are quite sensitive to the heat-transfer model and chemistry model. Accurate heat-transfer measurements and good chemical kinetics are necessary to achieve quantitative accuracy from the simulations.

- Variable-valve timing is an effective control strategy for controlling combustion timing over the range of engine speed and engine load necessary for automotive applications.

- Due to its low ignition temperature, n-heptane is an attractive fuel for HCCI because supplemental intake air heating would not be necessary even for modest compression ratios. Use of lower compression ratios leads to dramatically lower peak pressures.

- Supercharging can be used to achieve higher torques from an HCCI engine because the $\phi$ and combustion temperature are lower than a naturally-aspirated engine at the same load. Lower combustion temperatures result in lower heat-release rates and hence a decrease in the tendency of the engine to "knock".

### 6.1.3 Conclusions from Knock/Detonation Simulations

- An analysis of high-speed photographic records and pressure traces from knocking cycles in spark-ignition engines suggest that high apparent combustion wave speeds during end-gas autoignition and large pressure oscillations can be explained by thermal explosion of the end-gas rather than formation of detonation waves.

- Numerical reacting flow simulations and theoretical calculations for a quasi-steady detonation wave show that only hot-spots larger than some critical size can initiate detonation waves. This critical size is estimated to 4 cm in diameter for a typical spark-ignited engine under knocking conditions.

- The fuel/air mixtures typically used in homogeneous-charge compression-ignition (HCCI) engines are too lean to support the formation of detonations regardless of hot-spot size. For our initial conditions, an equivalence ratio of $\phi > 0.9$ was necessary to initiate detonation waves.

## 6.1.4 Conclusions from Automatic Chemistry Model Building

- Automatically generated chemistry models for oxidation of higher hydrocarbons in systems where temperature and pressure are time-varying have been performed using an extension of the RMG model-generation software developed by Song [1].

- Multi-zone calculations show that consideration of spatial temperature gradients is important when interpreting rapid-compression machine data. These gradients can partially explain the overprediction of *n*-heptane conversion during first-stage ignition predicted by homogeneous reactor models with detailed chemistry. Prior studies that neglected temperature inhomogeneity in RCM experiments probably incorrectly adjusted reaction rate parameters to force a fit with this data.

- Purely predictive chemistry models for *n*-heptane oxidation in two test cases showed that reasonable agreement can be obtained with no tuning of kinetic parameters or addition/subtraction of reaction families. Nonetheless, some chemistry model tuning is necessary to construct models that are quantitatively

useful for practical engineering simulations of combustion system, such as HCCI engines.

## 6.2  Recommendations

### 6.2.1  Recommendations for further HCCI modeling

- Since the rate of chemical heat-release was identified as the key variable controlling HCCI knock, a study of the effect of fuel additives on heat-release rate would be useful. We observed that heat-release can be controlled by changing the density of inert gases, but this leads to the need for a supercharger to maintain good energy density. It would be interesting to study the effect of radical scavenging additives on heat-release rate to determine if this is a good strategy for operating range expansion.

- Heat-release rate (or excitation time) is a difficult quantity to measure experimentally. Usually one can only determine a lower bound on heat-release rate from rapid-compression machine experiments because of temperature gradients in the combustion chamber. An experimental investigation is recommended to study combustion heat-release rates using micro-reactors where the small reactor size would make the system near-homogeneous. This study could be complimented with a kinetic study of excitation time, an oft overlooked property of combustion.

- The effect of wall heat-transfer was shown to be equally important as chemistry in making accurate predictions of HCCI operating ranges. A detailed experimental or literature-review based study of HCCI heat transfer is recommended. In particular, better correlations for heat-losses from the intake/exhaust manifolds, encountered when using large valve-overlaps to re-induct hot exhaust gases, would be useful.

## 6.2.2 Recommendations for Automatic Kinetic Model Building

- The kinetic models built in Chapter 5 were pure predictions without any tuning or optimization. A detailed rate-of-production study and sensitivity analysis could be performed to explain the discrepancies between the RMG model, literature *n*-heptane models, and the two experimental test cases.

- Our modeling studies revealed that constructing large chemistry models (say larger than 100 species) requires a large amount of computational time. Consequently, a study to identify bottlenecks in RMG using commercial Java optimization tools would be beneficial for improving computational efficiency. Also, developing a parallel version RMG might be a worthwhile pursuit.

- Attempts to build chemistry models specifically for HCCI engine simulations should be revived once the two proceeding recommendations are addressed. RMG has the potential to be a powerful tool for building models that can be used to design these engines. Specifically, it would be interesting to study chemical pathways that become important under fuel-lean conditions used in these engines. Lean oxidation chemistry has not been well-studied experimentally or computationally because of the concentration on spark-ignited engines.

# Chapter 7:    Appendix

## 7.1 RMG-Generated Chemistry Model for the Jet-Stirred Reactor Experiments at 900 K

### 7.1.1 Species Adjacency Lists

```
Species 1      Name: nc7h16
ChemFormula: C7H16
1  C 0 {2,S}
2  C 0 {1,S} {3,S}
3  C 0 {4,S} {2,S}
4  C 0 {3,S} {5,S}
5  C 0 {4,S} {6,S}
6  C 0 {7,S} {5,S}
7  C 0 {6,S}

Species 2      Name: o2
ChemFormula: O2
1  O 0 {2,D}
2  O 0 {1,D}

Species 3      Name: H2
ChemFormula: H2

Species 4      Name: CH4
ChemFormula: CH4
1  C 0

Species 5      Name: C2H2
ChemFormula: C2H2
1  C 0 {2,T}
2  C 0 {1,T}

Species 6      Name: C2H4
ChemFormula: C2H4
1  C 0 {2,D}
2  C 0 {1,D}

Species 7      Name: C2H6
ChemFormula: C2H6
1  C 0 {2,S}
2  C 0 {1,S}

Species 8      Name: C3H4
ChemFormula: C3H4
1  C 0 {2,D}
2  C 0 {3,D} {1,D}
3  C 0 {2,D}

Species 9      Name: C3H6
ChemFormula: C3H6
1  C 0 {2,D}
2  C 0 {1,D} {3,S}
3  C 0 {2,S}

Species 10     Name: C4H2
ChemFormula: C4H2
1  C 0 {2,T}
2  C 0 {3,S} {1,T}
3  C 0 {2,S} {4,T}
4  C 0 {3,T}

Species 11     Name: H2O
ChemFormula: H2O
1  O 0
Species 12     Name: H2O2
ChemFormula: H2O2
1  O 0 {2,S}
2  O 0 {1,S}
```

```
Species 13     Name: CO
ChemFormula: COJ2
1  C 2T {2,D}
2  O 0 {1,D}

Species 14     Name: CO2
ChemFormula: CO2
1  C 0 {2,D} {3,D}
2  O 0 {1,D}
3  O 0 {1,D}

Species 15     Name: CH2O
ChemFormula: CH2O
1  C 0 {2,D}
2  O 0 {1,D}

Species 16     Name: CH2CO
ChemFormula: C2H2O
1  C 0 {2,D}
2  C 0 {3,D} {1,D}
3  O 0 {2,D}

Species 17     Name: H
ChemFormula: HJ

Species 18     Name: CH
ChemFormula: CHJ3
1  C 3

Species 19     Name: CH2
ChemFormula: CH2J2
1  C 2T

Species 20     Name: CH2(S)
ChemFormula: CH2J2
1  C 2S

Species 21     Name: CH3
ChemFormula: CH3J
1  C 1

Species 22     Name: C2H
ChemFormula: C2HJ
1  C 1 {2,T}
2  C 0 {1,T}

Species 23     Name: C2H3
ChemFormula: C2H3J
1  C 1 {2,D}
2  C 0 {1,D}

Species 24     Name: C2H5
ChemFormula: C2H5J
1  C 1 {2,S}
2  C 0 {1,S}

Species 25     Name: C3H2
ChemFormula: C3H2J2
1  C 1 {2,D}
2  C 0 {1,D} {3,D}
3  C 1 {2,D}
```

```
isomer2:                                          Species 35    Name: CH2HCO
ChemFormula: C3H2J2                                ChemFormula: C2H3OJ
1  C 2 {2,S}                                       1  C 1 {2,S}
2  C 0 {1,S} {3,T}                                 2  C 0 {1,S} {3,D}
3  C 0 {2,T}                                       3  O 0 {2,D}

Species 26    Name: H2CCCH                         isomer1:
ChemFormula: C3H3J                                 ChemFormula: C2H3OJ
1  C 1 {2,S}                                       1  C 0 {2,D}
2  C 0 {3,T} {1,S}                                 2  C 0 {3,S} {1,D}
3  C 0 {2,T}                                       3  O 1 {2,S}

isomer1:                                           Species 36    Name: ch3cho
ChemFormula: C3H3J                                 ChemFormula: C2H4O
1  C 0 {2,D}                                       1  C 0 {2,S}
2  C 0 {1,D} {3,D}                                 2  C 0 {3,D} {1,S}
3  C 1 {2,D}                                       3  O 0 {2,D}

Species 27    Name: H2CCCCH                        Species 37    Name: c2h5cho
ChemFormula: C4H3J                                 ChemFormula: C3H6O
1  C 0 {2,D}                                       1  C 0 {2,S}
2  C 0 {3,D} {1,D}                                 2  C 0 {3,S} {1,S}
3  C 0 {2,D} {4,D}                                 3  C 0 {4,D} {2,S}
4  C 1 {3,D}                                       4  O 0 {3,D}

isomer2:                                           Species 38    Name: c7h14-1
ChemFormula: C4H3J                                 ChemFormula: C7H14
1  C 0 {2,D}                                       1  C 0 {2,D}
2  C 1 {1,D} {3,S}                                 2  C 0 {3,S} {1,D}
3  C 0 {4,T} {2,S}                                 3  C 0 {4,S} {2,S}
4  C 0 {3,T}                                       4  C 0 {3,S} {5,S}
                                                   5  C 0 {4,S} {6,S}
Species 28    Name: O                              6  C 0 {7,S} {5,S}
ChemFormula: OJ2                                   7  C 0 {6,S}
1  O 2T
                                                   Species 39    Name: c7h14-2
Species 29    Name: OH                             ChemFormula: C7H14
ChemFormula: HOJ                                   1  C 0 {2,S}
1  O 1                                             2  C 0 {1,S} {3,D}
                                                   3  C 0 {2,D} {4,S}
Species 30    Name: HO2                            4  C 0 {3,S} {5,S}
ChemFormula: HO2J                                  5  C 0 {6,S} {4,S}
1  O 1 {2,S}                                       6  C 0 {7,S} {5,S}
2  O 0 {1,S}                                       7  C 0 {6,S}

Species 31    Name: HCO                            Species 40    Name: c7h14-3
ChemFormula: CHOJ                                  ChemFormula: C7H14
1  C 1 {2,D}                                       1  C 0 {2,S}
2  O 0 {1,D}                                       2  C 0 {1,S} {3,S}
                                                   3  C 0 {4,D} {2,S}
Species 32    Name: CH3O                           4  C 0 {5,S} {3,D}
ChemFormula: CH3OJ                                 5  C 0 {6,S} {4,S}
1  C 0 {2,S}                                       6  C 0 {5,S} {7,S}
2  O 1 {1,S}                                       7  C 0 {6,S}

Species 33    Name: CH2OH                          Species 41    Name: C7H15J
ChemFormula: CH3OJ                                 ChemFormula: C7H15J
1  C 1 {2,S}                                       2   C 0 {22,S} {9,S}
2  O 0 {1,S}                                       9   C 0 {2,S} {14,S}
                                                   10  C 0 {18,S}
Species 34    Name: HCCO                           14  C 0 {19,S} {9,S}
ChemFormula: C2HOJ                                 18  C 1 {22,S} {10,S}
1  C 1 {2,D}                                       19  C 0 {14,S}
2  C 0 {1,D} {3,D}                                 22  C 0 {2,S} {18,S}
3  O 0 {2,D}
                                                   Species 42    Name: C7H15J
isomer1:                                           ChemFormula: C7H15J
ChemFormula: C2HOJ                                 2   C 0 {9,S} {22,S}
1  C 0 {2,T}                                       9   C 0 {2,S} {14,S}
2  C 0 {3,S} {1,T}                                 10  C 0 {18,S}
3  O 1 {2,S}
```

231

```
14   C 0 {19,S} {9,S}
18   C 0 {22,S} {10,S}
19   C 0 {14,S}
22   C 1 {18,S} {2,S}


Species 43     Name: C6H13J
ChemFormula: C6H13J
2    C 0 {7,S} {19,S}
7    C 0 {2,S} {10,S}
10   C 0 {15,S} {7,S}
14   C 1 {19,S}
15   C 0 {10,S}
19   C 0 {2,S} {14,S}


Species 44     Name: C7H15J
ChemFormula: C7H15J
2    C 1 {8,S} {22,S}
8    C 0 {2,S} {13,S}
9    C 0 {17,S}
13   C 0 {8,S} {18,S}
17   C 0 {9,S} {22,S}
18   C 0 {13,S}
22   C 0 {17,S} {2,S}


Species 45     Name: C7H15J
ChemFormula: C7H15J
2    C 0 {22,S} {8,S}
8    C 0 {2,S} {13,S}
9    C 0 {17,S}
13   C 0 {8,S} {18,S}
17   C 0 {9,S} {22,S}
18   C 1 {13,S}
22   C 0 {2,S} {17,S}


Species 46     Name: C4H9J
ChemFormula: C4H9J
2    C 1 {7,S}
7    C 0 {10,S} {2,S}
10   C 0 {7,S} {12,S}
12   C 0 {10,S}


Species 47     Name: C3H7J
ChemFormula: C3H7J
3    C 0 {7,S}
7    C 0 {3,S} {10,S}
10   C 1 {7,S}


Species 48     Name: C5H11J
ChemFormula: C5H11J
1    C 0 {6,S} {16,S}
6    C 1 {1,S}
7    C 0 {13,S}
13   C 0 {7,S} {16,S}
16   C 0 {1,S} {13,S}


Species 285    Name: C3H5J
ChemFormula: C3H5J
5    C 0 {7,D}
6    C 1 {7,S}
7    C 0 {6,S} {5,D}


Species 294    Name: C7H13J
ChemFormula: C7H13J
4    C 1 {7,S}
7    C 0 {20,S} {4,S}
8    C 0 {16,S}
10   C 0 {20,S} {14,D}
14   C 0 {16,S} {10,D}
16   C 0 {8,S} {14,S}
20   C 0 {7,S} {10,S}
```

```
Species 297    Name: C7H13J
ChemFormula: C7H13J
4    C 0 {6,S}
6    C 0 {4,S} {20,S}
7    C 0 {16,S}
9    C 1 {13,S} {20,S}
13   C 0 {16,D} {9,S}
16   C 0 {13,D} {7,S}
20   C 0 {6,S} {9,S}


isomer2:
ChemFormula: C7H13J
4    C 0 {6,S}
6    C 0 {20,S} {4,S}
7    C 0 {16,S}
9    C 0 {13,D} {20,S}
13   C 0 {9,D} {16,S}
16   C 1 {13,S} {7,S}
20   C 0 {6,S} {9,S}


Species 299    Name: C7H13J
ChemFormula: C7H13J
4    C 0 {7,S}
7    C 0 {4,S} {20,S}
8    C 1 {16,S}
9    C 0 {13,D} {20,S}
13   C 0 {9,D} {16,S}
16   C 0 {8,S} {13,S}
20   C 0 {7,S} {9,S}


Species 366    Name: C5H7OJ
ChemFormula: C5H7OJ
2    C 0 {9,D}
4    C 1 {7,S}
7    C 0 {4,S} {12,S} {11,D}
9    C 0 {12,S} {2,D}
11   C 0 {7,D}
12   O 0 {9,S} {7,S}


Species 478    Name: C3H3O2J
ChemFormula: C3H3O2J
1    O 1 {5,S}
2    C 0 {8,D} {6,D}
5    O 0 {8,S} {1,S}
6    C 0 {2,D}
8    C 0 {5,S} {2,D}


Species 574    Name: C5H7J
ChemFormula: C5H7J
1    C 1 {7,S}
3    C 0 {7,S} {4,D}
4    C 0 {3,D} {9,D}
7    C 0 {1,S} {3,S}
9    C 0 {4,D}


Species 664    Name: C4H5OJ
ChemFormula: C4H5OJ
1    C 0 {8,S} {6,D}
5    C 0 {8,S} {10,D}
6    C 1 {1,D}
8    O 0 {5,S} {1,S}
10   C 0 {5,D}


Species 668    Name: C5H5J
ChemFormula: C5H5J
1    C 0 {8,S} {6,D}
5    C 0 {10,D} {8,D}
6    C 1 {1,D}
8    C 0 {1,S} {5,D}
10   C 0 {5,D}
```

```
Species 724    Name: C7H12
ChemFormula: C7H12
2   C 0 {8,S}
3   C 0 {5,D}
5   C 0 {12,S} {3,D}
8   C 0 {2,S} {16,S}
12  C 0 {5,S} {13,D}
13  C 0 {12,D} {16,S}
16  C 0 {13,S} {8,S}

Species 734    Name: C7H13O2J
ChemFormula: C7H13O2J
1   C 0 {7,S} {5,D}
4   C 0 {17,S} {11,S}
5   C 0 {11,S} {1,D}
7   C 0 {18,S} {1,S} {15,S}
11  C 0 {5,S} {4,S}
13  O 1 {18,S}
15  C 0 {7,S}
17  C 0 {4,S}
18  O 0 {7,S} {13,S}

Species 783    Name: C7H11J
ChemFormula: C7H11J
4   C 0 {6,S} {12,S}
6   C 0 {4,S} {13,D}
8   C 1 {18,S}
10  C 0 {18,D} {13,S}
12  C 0 {4,S}
13  C 0 {6,D} {10,S}
18  C 0 {10,D} {8,S}

isomer2:
ChemFormula: C7H11J
4   C 0 {6,S} {12,S}
6   C 0 {13,D} {4,S}
8   C 0 {18,D}
10  C 1 {18,S} {13,S}
12  C 0 {4,S}
13  C 0 {6,D} {10,S}
18  C 0 {8,D} {10,S}

isomer3:
ChemFormula: C7H11J
4   C 0 {6,S} {12,S}
6   C 1 {13,S} {4,S}
8   C 0 {18,D}
10  C 0 {18,S} {13,D}
12  C 0 {4,S}
13  C 0 {6,S} {10,D}
18  C 0 {8,D} {10,S}

Species 816    Name: C7H11O2J
ChemFormula: C7H11O2J
1   C 0 {4,D} {10,S}
4   C 0 {1,D} {15,S}
10  C 0 {16,S} {1,S} {17,S}
12  O 1 {16,S}
15  C 0 {18,S} {4,S}
16  O 0 {10,S} {12,S}
17  C 0 {19,D} {10,S}
18  C 0 {15,S}
19  C 0 {17,D}

Species 817    Name: C7H11O2J
ChemFormula: C7H11O2J
1   C 0 {10,D} {4,S}
4   C 0 {15,S} {16,S} {1,S}
10  C 0 {1,D} {17,S}
12  O 1 {16,S}
15  C 0 {18,S} {4,S}
```

```
16  O 0 {4,S} {12,S}
17  C 0 {10,S} {19,D}
18  C 0 {15,S}
19  C 0 {17,D}

Species 823    Name: C6H8
ChemFormula: C6H8
2   C 0 {10,D}
3   C 0 {5,D}
5   C 0 {13,S} {3,D}
8   C 0 {13,D} {10,S}
10  C 0 {8,S} {2,D}
13  C 0 {8,D} {5,S}

Species 961    Name: C6H9OJ
ChemFormula: C6H9OJ
1   O 0 {6,S}
3   C 0 {10,S} {15,D}
6   C 0 {1,S} {16,S}
9   C 1 {15,S}
10  C 0 {3,S} {16,D}
15  C 0 {9,S} {3,D}
16  C 0 {6,S} {10,D}

isomer2:
ChemFormula: C6H9OJ
1   O 0 {6,S}
3   C 1 {10,S} {15,S}
6   C 0 {1,S} {16,S}
9   C 0 {15,D}
10  C 0 {16,D} {3,S}
15  C 0 {9,D} {3,S}
16  C 0 {10,D} {6,S}

isomer3:
ChemFormula: C6H9OJ
1   O 0 {6,S}
3   C 0 {15,S} {10,D}
6   C 0 {1,S} {16,S}
9   C 0 {15,D}
10  C 0 {16,S} {3,D}
15  C 0 {3,S} {9,D}
16  C 1 {6,S} {10,S}

Species 962    Name: C6H9OJ
ChemFormula: C6H9OJ
1   O 0 {10,S}
3   C 0 {10,S} {15,D}
6   C 0 {16,D}
9   C 1 {15,S}
10  C 0 {3,S} {16,S} {1,S}
15  C 0 {3,D} {9,S}
16  C 0 {6,D} {10,S}

isomer2:
ChemFormula: C6H9OJ
1   O 0 {10,S}
3   C 1 {15,S} {10,S}
6   C 0 {16,D}
9   C 0 {15,S}
10  C 0 {1,S} {16,S} {3,S}
15  C 0 {3,S} {9,D}
16  C 0 {6,D} {10,S}

Species 1253    Name: C6H9O3J
ChemFormula: C6H9O3J
3   C 0 {6,D}
4   C 0 {10,D}
6   C 0 {3,D} {9,S}
7   O 0 {9,S}
9   C 0 {6,S} {18,S} {7,S}
```

233

```
10  C 0 {18,S} {4,D}
11  O 1 {15,S}
15  O 0 {11,S} {18,S}
18  C 0 {10,S} {9,S} {15,S}


Species 1316    Name: C6H10O3
ChemFormula: C6H10O3
2   O 0 {14,S}
3   C 0 {14,S} {13,D}
7   C 0 {15,S} {10,D}
10  C 0 {7,D}
12  O 0 {16,S}
13  C 0 {15,S} {3,D}
14  C 0 {3,S} {2,S}
15  C 0 {7,S} {16,S} {13,S}
16  O 0 {15,S} {12,S}


Species 1317    Name: C6H10O3
ChemFormula: C6H10O3
2   O 0 {14,S}
3   C 0 {14,S} {16,S} {13,S}
7   C 0 {10,D} {15,S}
10  C 0 {7,D}
12  O 0 {16,S}
13  C 0 {15,D} {3,S}
14  C 0 {3,S} {2,S}
15  C 0 {13,D} {7,S}
```

```
16   O 0 {3,S} {12,S}


Species 1328    Name: C6H9O3J
ChemFormula: C6H9O3J
3   C 0 {6,S} {7,S}
4   C 0 {10,D}
6   C 0 {3,S} {9,D}
7   O 0 {3,S}
9   C 0 {18,S} {6,D}
10  C 0 {18,S} {4,D}
11  O 1 {15,S}
15  O 0 {18,S} {11,S}
18  C 0 {15,S} {10,S} {9,S}


Species 1329    Name: C6H9O3J
ChemFormula: C6H9O3J
3   C 0 {7,S} {6,S}
4   C 0 {10,D}
6   C 0 {15,S} {3,S} {9,S}
7   O 0 {3,S}
9   C 0 {18,D} {6,S}
10  C 0 {18,S} {4,D}
11  O 1 {15,S}
15  O 0 {6,S} {11,S}
18  C 0 {10,S} {9,D}
```

## 7.1.2 CHEMKIN-formatted reaction model

```
CHEMKIN INTERPRETER OUTPUT: CHEMKIN-II Version 3.6 Apr. 1994
                      DOUBLE PRECISION
```

```
                    --------------------
                    ELEMENTS    ATOMIC
                    CONSIDERED  WEIGHT
                    --------------------
                    1.  H       1.00797
                    2.  C       12.0112
                    3.  O       15.9994
                    4.  N       14.0067
                    5.  Ne      20.1830
                    6.  Ar      39.9480
                    --------------------
```

```
-------------------------------------------------------------------------------
                    C
                P   H
                H   A
                A   R
SPECIES         S G MOLECULAR TEMPERATURE    ELEMENT COUNT
CONSIDERED      E E WEIGHT    LOW    HIGH     H   C   O   N  Ne Ar
-------------------------------------------------------------------------------
  1. N2           G 0  28.01340 300.0 5000.0  0   0   0   2   0   0
  2. Ar           G 0  39.94800 300.0 5000.0  0   0   0   0   0   1
  3. HCO(31)      G 0  29.01852 300.0 5000.0  1   1   1   0   0   0
  4. C7H15J(41)   G 0  99.19760 300.0 5000.0 15   7   0   0   0   0
  5. C6H9O3J(1253) G 0 129.13683 300.0 5000.0 9   6   3   0   0   0
  6. CH2HCO(35)   G 0  43.04561 300.0 5000.0  3   2   1   0   0   0
  7. C7H11O2J(817) G 0 127.16452 300.0 5000.0 11 7   2   0   0   0
  8. C3H2(25)     G 0  38.04939 300.0 5000.0  2   3   0   0   0   0
  9. OH(29)       G 0  17.00737 300.0 5000.0  1   0   1   0   0   0
 10. C7H13J(299)  G 0  97.18166 300.0 5000.0 13   7   0   0   0   0
 11. CH3(21)      G 0  15.03506 300.0 5000.0  3   1   0   0   0   0
 12. C3H3O2J(478) G 0  71.05616 300.0 5000.0  3   3   2   0   0   0
 13. O(28)        G 0  15.99940 300.0 5000.0  0   0   1   0   0   0
 14. C3H6(9)      G 0  42.08127 300.0 5000.0  6   3   0   0   0   0
 15. C3H4(8)      G 0  40.06533 300.0 5000.0  4   3   0   0   0   0
 16. C7H15J(42)   G 0  99.19760 300.0 5000.0 15   7   0   0   0   0
 17. HCCO(34)     G 0  41.02967 300.0 5000.0  1   2   1   0   0   0
 18. CH4(4)       G 0  16.04303 300.0 5000.0  4   1   0   0   0   0
 19. c7h14-1(38)  G 0  98.18963 300.0 5000.0 14   7   0   0   0   0
 20. C7H13J(297)  G 0  97.18166 300.0 5000.0 13   7   0   0   0   0
 21. C7H15J(45)   G 0  99.19760 300.0 5000.0 15   7   0   0   0   0
 22. c7h14-3(40)  G 0  98.18963 300.0 5000.0 14   7   0   0   0   0
 23. CH2CO(16)    G 0  42.03764 300.0 5000.0  2   2   1   0   0   0
 24. C2H5(24)     G 0  29.06215 300.0 5000.0  5   2   0   0   0   0
 25. CH(18)       G 0  13.01912 300.0 5000.0  1   1   0   0   0   0
 26. C3H5J(285)   G 0  41.07330 300.0 5000.0  5   3   0   0   0   0
 27. nc7h16(1)    G 0 100.20557 300.0 5000.0 16   7   0   0   0   0
 28. C6H8(823)    G 0  80.13066 300.0 5000.0  8   6   0   0   0   0
 29. C7H11J(783)  G 0  95.16572 300.0 5000.0 11   7   0   0   0   0
 30. C6H10O3(1317) G 0 130.14480 300.0 5000.0 10 6   3   0   0   0
 31. C6H9OJ(961)  G 0  97.13803 300.0 5000.0  9   6   1   0   0   0
 32. C6H13J(43)   G 0  85.17051 300.0 5000.0 13   6   0   0   0   0
 33. C4H9J(46)    G 0  57.11633 300.0 5000.0  9   4   0   0   0   0
 34. C5H7J(574)   G 0  67.11154 300.0 5000.0  7   5   0   0   0   0
 35. o2(2)        G 0  31.99880 300.0 5000.0  0   0   2   0   0   0
 36. CO(13)       G 0  28.01055 300.0 5000.0  0   1   1   0   0   0
 37. C7H15J(44)   G 0  99.19760 300.0 5000.0 15   7   0   0   0   0
 38. ch3cho(36)   G 0  44.05358 300.0 5000.0  4   2   1   0   0   0
 39. CH2(19)      G 0  14.02709 300.0 5000.0  2   1   0   0   0   0
 40. C7H13J(294)  G 0  97.18166 300.0 5000.0 13   7   0   0   0   0
 41. C6H9O3J(1328) G 0 129.13683 300.0 5000.0 9 6   3   0   0   0
 42. C5H11J(48)   G 0  71.14342 300.0 5000.0 11   5   0   0   0   0
 43. HO2(30)      G 0  33.00677 300.0 5000.0  1   0   2   0   0   0
 44. H2O2(12)     G 0  34.01474 300.0 5000.0  2   0   2   0   0   0
 45. C2H3(23)     G 0  27.04621 300.0 5000.0  3   2   0   0   0   0
```

```
46. H2CCCCH(27)      G 0   51.06851  300.0 5000.0  3  4  0  0  0  0
47. C7H11O2J(816)    G 0  127.16452  300.0 5000.0 11  7  2  0  0  0
48. H2(3)            G 0    2.01594  300.0 5000.0  2  0  0  0  0  0
49. C5H5J(668)       G 0   65.09560  300.0 5000.0  5  5  0  0  0  0
50. CH3O(32)         G 0   31.03446  300.0 5000.0  3  1  1  0  0  0
51. C6H9O3J(1329)    G 0  129.13683  300.0 5000.0  9  6  3  0  0  0
52. C2H6(7)          G 0   30.07012  300.0 5000.0  6  2  0  0  0  0
53. C7H12(724)       G 0   96.17369  300.0 5000.0 12  7  0  0  0  0
54. H2CCCH(26)       G 0   39.05736  300.0 5000.0  3  3  0  0  0  0
55. C6H10O3(1316)    G 0  130.14480  300.0 5000.0 10  6  3  0  0  0
56. H2O(11)          G 0   18.01534  300.0 5000.0  2  0  1  0  0  0
57. C2H(22)          G 0   25.03027  300.0 5000.0  1  2  0  0  0  0
58. CH2(S)(20)       G 0   14.02709  300.0 5000.0  2  1  0  0  0  0
59. C3H7J(47)        G 0   43.08924  300.0 5000.0  7  3  0  0  0  0
60. CO2(14)          G 0   44.00995  300.0 5000.0  0  1  2  0  0  0
61. C6H9OJ(962)      G 0   97.13803  300.0 5000.0  9  6  1  0  0  0
62. C7H13O2J(734)    G 0  129.18046  300.0 5000.0 13  7  2  0  0  0
63. H(17)            G 0    1.00797  300.0 5000.0  1  0  0  0  0  0
64. c2h5cho(37)      G 0   58.08067  300.0 5000.0  6  3  1  0  0  0
65. C5H7OJ(366)      G 0   83.11094  300.0 5000.0  7  5  1  0  0  0
66. C2H4(6)          G 0   28.05418  300.0 5000.0  4  2  0  0  0  0
67. C4H2(10)         G 0   50.06054  300.0 5000.0  2  4  0  0  0  0
68. c7h14-2(39)      G 0   98.18963  300.0 5000.0 14  7  0  0  0  0
69. C4H5OJ(664)      G 0   69.08385  300.0 5000.0  5  4  1  0  0  0
70. CH2OH(33)        G 0   31.03446  300.0 5000.0  3  1  1  0  0  0
71. CH2O(15)         G 0   30.02649  300.0 5000.0  2  1  1  0  0  0
72. C2H2(5)          G 0   26.03824  300.0 5000.0  2  2  0  0  0  0
```
-------------------------------------------------------------------------------

|     | | (k = A T**b exp(-E/RT)) | | |
| --- | --- | --- | --- | --- |
| REACTIONS CONSIDERED | | A | b | E |
| 1. CH2O(15)+OH(29)=HCO(31)+H2O(11) | | 3.43E+09 | 1.2 | -0.4 |
| 2. C2H4(6)+O(28)=>C2H3(23)+OH(29) | | 1.51E+07 | 1.9 | 8.9 |
| 3. o2(2)+CH2OH(33)=CH2O(15)+HO2(30) | | 1.57E+15 | -1.0 | 0.0 |
| 4. o2(2)+CH3O(32)=CH2O(15)+HO2(30) | | 2.17E+10 | 0.0 | 1.7 |
| 5. C7H15J(45)=C7H15J(42) | | 1.71E+12 | -1.1 | 11.8 |
| 6. C7H15J(45)=C7H15J(41) | | 2.39E+10 | 0.7 | 38.0 |
| 7. C7H15J(45)=C7H15J(44) | | 6.44E+09 | 0.1 | 20.7 |
| 8. C7H15J(42)=C7H15J(41) | | 1.35E+10 | 0.9 | 38.0 |
| 9. C7H15J(44)=C7H15J(41) | | 2.20E+09 | 1.0 | 36.4 |
| 10. C7H15J(44)=C7H15J(42) | | 1.35E+10 | 0.9 | 38.0 |
| 11. CH4(4)+HO2(30)=CH3(21)+H2O2(12) | | 9.03E+12 | 0.0 | 24.7 |
| 12. o2(2)+C2H(22)=CO2(14)+CH(18) | | 9.05E+12 | 0.0 | 0.0 |
| 13. C2H6(7)+OH(29)=C2H5(24)+H2O(11) | | 7.23E+06 | 2.0 | 0.9 |
| 14. C2H4(6)+C2H(22)=C2H3(23)+C2H2(5) | | 8.85E+09 | 0.7 | 10.0 |
| 15. CH4(4)+CH(18)=C2H4(6)+H(17) | | 3.01E+13 | 0.0 | -0.4 |
| 16. H2O2(12)+OH(29)=H2O(11)+HO2(30) | | 7.83E+12 | 0.0 | 1.3 |
| 17. HCO(31)+HCO(31)=CH2O(15)+CO(13) | | 3.01E+13 | 0.0 | 0.0 |
| 18. CH4(4)+OH(29)=CH3(21)+H2O(11) | | 1.57E+07 | 1.8 | 2.8 |
| 19. c7h14-3(40)+CH3(21)=C7H13J(294)+CH4(4) | | 8.34E+05 | 1.9 | 11.1 |
| 20. c7h14-3(40)+CH3(21)=C7H13J(299)+CH4(4) | | 8.34E+05 | 1.9 | 11.1 |
| 21. c7h14-3(40)+O(28)=>C7H13J(294)+OH(29) | | 2.56E+04 | 3.0 | 3.1 |
| 22. c7h14-3(40)+O(28)=>C7H13J(299)+OH(29) | | 2.56E+04 | 3.0 | 3.1 |
| 23. CH2CO(16)+H(17)=CH3(21)+CO(13) | | 1.81E+13 | 0.0 | 3.4 |
| 24. H2(3)+O(28)=OH(29)+H(17) | | 5.12E+04 | 2.7 | 6.3 |
| 25. c7h14-3(40)+CH2(19)=>C7H13J(294)+CH3(21) | | 5.00E+05 | 2.3 | 3.7 |
| 26. c7h14-3(40)+CH2(19)=>C7H13J(299)+CH3(21) | | 5.00E+05 | 2.3 | 3.7 |
| 27. C2H2(5)+O(28)=CH2(19)+CO(13) | | 2.17E+06 | 2.1 | 1.6 |
| 28. o2(2)+CH(18)=CO(13)+OH(29) | | 1.66E+13 | 0.0 | 0.0 |
| 29. CH2O(15)+CH2(19)=>HCO(31)+CH3(21) | | 6.04E+09 | 0.0 | 0.0 |
| 30. o2(2)+CH2(19)=CO2(14)+H(17)+H(17) | | 5.43E+12 | 0.0 | 1.5 |
| 31. C2H4(6)+CH3(21)=CH4(4)+C2H3(23) | | 4.16E+12 | 0.0 | 11.1 |
| 32. C6H10O3(1316)+C7H13J(294) =C6H9O3J(1328)+c7h14-3(40) | | 9.12E+14 | -0.7 | 7.2 |
| 33. C6H10O3(1316)+C7H13J(299) =C6H9O3J(1328)+c7h14-3(40) | | 9.12E+14 | -0.7 | 7.2 |
| 34. C6H10O3(1317)+C7H13J(294) =C6H9O3J(1329)+c7h14-3(40) | | 9.12E+14 | -0.7 | 7.2 |

```
35. C6H10O3(1317)+C7H13J(299)                          9.12E+14   -0.7      7.2
    =C6H9O3J(1329)+c7h14-3(40)
36. CH(18)+O(28)=CO(13)+H(17)                          3.97E+13    0.0      0.0
37. C2H2(5)+C2H(22)=C4H2(10)+H(17)                     9.03E+13    0.0      0.0
38. nc7h16(1)+C7H15J(42)=C7H15J(41)+nc7h16(1)          6.08E+01    3.2     10.3
39. nc7h16(1)+C7H15J(44)=C7H15J(41)+nc7h16(1)          6.08E+01    3.2     10.3
40. nc7h16(1)+C7H15J(44)=C7H15J(42)+nc7h16(1)          6.08E+01    3.2     10.3
41. nc7h16(1)+C7H15J(45)=C7H15J(44)+nc7h16(1)          3.08E+03    2.7     10.1
42. nc7h16(1)+C7H15J(45)=C7H15J(41)+nc7h16(1)          6.16E+03    2.7     10.1
43. nc7h16(1)+C7H15J(45)=C7H15J(42)+nc7h16(1)          6.16E+03    2.7     10.1
44. CH(18)+CH3(21)=C2H3(23)+H(17)                      3.00E+13    0.0      0.0
45. c7h14-3(40)+H(17)=C7H13J(294)+H2(3)                1.88E+08    1.8      7.5
46. c7h14-3(40)+H(17)=C7H13J(299)+H2(3)                1.88E+08    1.8      7.5
47. C2H4(6)+OH(29)=C2H3(23)+H2O(11)                    2.05E+13    0.0      5.9
48. C2H4(6)+H(17)=C2H3(23)+H2(3)                       5.42E+14    0.0     14.9
49. H2O2(12)+H(17)=OH(29)+H2O(11)                      1.02E+13    0.0      3.6
50. CH2O(15)+HO2(30)=H2O2(12)+HCO(31)                  3.01E+12    0.0     13.1
51. H2(3)+CH2(S)(20)=CH3(21)+H(17)                     7.23E+13    0.0      0.0
52. H2(3)+CH2(19)=>H(17)+CH3(21)                       1.85E+10    0.9     28.3
53. OH(29)+OH(29)=O(28)+H2O(11)                        1.51E+09    1.1      0.1
54. CH2O(15)+O(28)=HCO(31)+OH(29)                      4.16E+11    0.6      2.8
55. OH(29)+HCO(31)=H2O(11)+CO(13)                      1.02E+14    0.0      0.0
56. CH2(19)+C2H3(23)=C2H2(5)+CH3(21)                   1.81E+13    0.0      0.0
57. nc7h16(1)+C2H(22)=C7H15J(42)+C2H2(5)               2.42E+12    0.0      0.0
58. nc7h16(1)+C2H(22)=C7H15J(41)+C2H2(5)               2.42E+12    0.0      0.0
59. nc7h16(1)+C2H(22)=C7H15J(44)+C2H2(5)               1.21E+12    0.0      0.0
60. nc7h16(1)+C2H(22)=C7H15J(45)+C2H2(5)               3.61E+12    0.0      0.0
61. C6H10O3(1316)+C2H5(24)=C6H9O3J(1328)+C2H6(7)       9.12E+14   -0.7      7.2
62. C6H10O3(1317)+C2H5(24)=C6H9O3J(1329)+C2H6(7)       9.12E+14   -0.7      7.2
63. CH2(19)+OH(29)=CH2O(15)+H(17)                      1.81E+13    0.0      0.0
64. C2H6(7)+C2H(22)=C2H5(24)+C2H2(5)                   3.61E+12    0.0      0.0
65. HO2(30)+HO2(30)=H2O2(12)+o2(2)                     4.22E+14    0.0     12.0
66. H2O2(12)+H(17)=HO2(30)+H2(3)                       1.69E+12    0.0      3.8
67. o2(2)+HCO(31)=HO2(30)+CO(13)                       3.01E+12    0.0      0.0
68. CH(18)+CH2(19)=C2H2(5)+H(17)                       4.00E+13    0.0      0.0
69. O(28)+CH2OH(33)=CH2O(15)+OH(29)                    9.03E+13    0.0      0.0
70. O(28)+CH3O(32)=CH2O(15)+OH(29)                     1.81E+12    0.0      0.0
71. C3H6(9)+C7H13J(299)=c7h14-3(40)+C3H5J(285)         1.68E+12    0.0     12.4
72. C3H6(9)+C7H13J(294)=c7h14-3(40)+C3H5J(285)         1.68E+12    0.0     12.4
73. CH2CO(16)+O(28)=CH2O(15)+CO(13)                    4.58E+11    0.0      1.4
74. nc7h16(1)+CH3(21)=C7H15J(42)+CH4(4)                5.80E+06    1.8      8.5
75. nc7h16(1)+CH3(21)=C7H15J(45)+CH4(4)                1.67E+06    1.9     11.1
76. nc7h16(1)+CH3(21)=C7H15J(44)+CH4(4)                2.90E+06    1.8      8.5
77. nc7h16(1)+CH3(21)=C7H15J(41)+CH4(4)                5.80E+06    1.8      8.5
78. H(17)+CH3O(32)=CH2O(15)+H2(3)                      1.81E+13    0.0      0.0
79. H(17)+CH2OH(33)=CH2O(15)+H2(3)                     3.08E+13    0.0      0.0
80. C6H10O3(1316)+C6H9O3J(1329)                        1.73E+01    3.4     -1.1
    =>C6H9O3J(1328)+C6H10O3(1317)
81. C6H10O3(1317)+C6H9O3J(1328)                        1.73E+01    3.4     -1.1
    =>C6H9O3J(1329)+C6H10O3(1316)
82. c7h14-3(40)+OH(29)=C7H13J(294)+H2O(11)             7.89E+07    1.8      0.3
83. c7h14-3(40)+OH(29)=C7H13J(299)+H2O(11)             7.89E+07    1.8      0.3
84. H2O2(12)+C7H15J(41)=nc7h16(1)+HO2(30)              2.88E+12   -0.1      7.5
85. H2O2(12)+C7H15J(42)=nc7h16(1)+HO2(30)              2.88E+12   -0.1      7.5
86. H2O2(12)+C7H15J(45)=nc7h16(1)+HO2(30)              1.82E+15   -0.7      7.2
87. H2O2(12)+C7H15J(44)=nc7h16(1)+HO2(30)              2.88E+12   -0.1      7.5
88. CH2O(15)+C6H9O3J(1328)=C6H10O3(1316)+HCO(31)       4.12E+04    2.5     10.2
89. CH2O(15)+C6H9O3J(1329)=C6H10O3(1317)+HCO(31)       4.12E+04    2.5     10.2
90. CH2O(15)+H(17)=HCO(31)+H2(3)                       1.26E+08    1.6      2.2
91. C2H6(7)+O(28)=C2H5(24)+OH(29)                      1.00E+09    1.5      5.8
92. o2(2)+H(17)+H2O(11)=HO2(30)+H2O(11)                6.89E+15    0.0     -2.1
93. o2(2)+CH3(21)=CH2O(15)+OH(29)                      3.31E+11    0.0      8.9
94. C2H6(7)+H(17)=C2H5(24)+H2(3)                       1.45E+09    1.5      7.4
95. o2(2)+CH2(19)=CH2O(15)+O(28)                       4.20E+12    0.0      1.5
96. o2(2)+CH2(19)=CO(13)+H2O(11)                       1.48E+12    0.0      1.5
97. H(17)+HO2(30)=OH(29)+OH(29)                        1.69E+14    0.0      0.9
98. CH4(4)+CH2(19)=CH3(21)+CH3(21)                     4.30E+12    0.0     10.0
99. CH4(4)+CH2(S)(20)=CH3(21)+CH3(21)                  7.00E+13    0.0      0.0
100. o2(2)+CH2(S)(20)=CO(13)+OH(29)+H(17)              3.13E+13    0.0      0.0
101. o2(2)+CH2(19)=CO(13)+OH(29)+H(17)                 8.15E+12    0.0      1.5
102. C2H4(6)+CH(18)=C3H4(8)+H(17)                      1.32E+14    0.0     -0.3
```

237

```
103. H(17)+HO2(30)=H2O(11)+O(28)                      3.01E+13    0.0    1.7
104. C2H5(24)+O(28)=CH2O(15)+CH3(21)                  6.62E+13    0.0    0.0
105. O(28)+HCO(31)=CO(13)+OH(29)                      3.01E+13    0.0    0.0
106. CO(13)+OH(29)=CO2(14)+H(17)                      1.66E+07    1.3   -0.8
107. O(28)+HCO(31)=CO2(14)+H(17)                      3.01E+13    0.0    0.0
108. CH2O(15)+C3H5J(285)=HCO(31)+C3H6(9)              5.50E+03    2.8    5.9
109. CH2(19)+O(28)=CO(13)+H2(3)                       4.80E+13    0.0    0.0
110. OH(29)+CH3O(32)=CH2O(15)+H2O(11)                 1.81E+13    0.0    0.0
111. OH(29)+CH2OH(33)=CH2O(15)+H2O(11)                2.41E+13    0.0    0.0
112. nc7h16(1)+C2H3(23)=C7H15J(42)+C2H4(6)            2.04E+03    3.1    8.8
113. nc7h16(1)+C2H3(23)=C7H15J(41)+C2H4(6)            2.04E+03    3.1    8.8
114. nc7h16(1)+C2H3(23)=C7H15J(44)+C2H4(6)            1.02E+03    3.1    8.8
115. nc7h16(1)+C2H3(23)=C7H15J(45)+C2H4(6)            8.70E+03    2.9    8.8
116. C2H6(7)+C7H13J(294)=c7h14-3(40)+C2H5(24)         3.95E+03    2.7   12.9
117. C2H6(7)+C7H13J(299)=c7h14-3(40)+C2H5(24)         3.95E+03    2.7   12.9
118. CH(18)+C2H3(23)=CH2(19)+C2H2(5)                  5.00E+13    0.0    0.0
119. CH2(19)+CH3(21)=C2H4(6)+H(17)                    4.22E+13    0.0    0.0
120. CH2(19)+HCO(31)=CH3(21)+CO(13)                   1.81E+13    0.0    0.0
121. CH4(4)+o2(2)=CH3(21)+HO2(30)                     3.97E+13    0.0   56.9
122. o2(2)+CH2O(15)=HCO(31)+HO2(30)                   6.02E+13    0.0   40.6
123. H2O2(12)+O(28)=OH(29)+HO2(30)                    6.62E+11    0.0    4.0
124. C3H6(9)+CH2(19)=>C3H5J(285)+CH3(21)              5.00E+05    2.3    3.7
125. c7h14-3(40)+C2H(22)=C7H13J(294)+C2H2(5)          1.81E+12    0.0    0.0
126. c7h14-3(40)+C2H(22)=C7H13J(299)+C2H2(5)          1.81E+12    0.0    0.0
127. CH2O(15)+C7H15J(41)=nc7h16(1)+HCO(31)            1.08E+11    0.0    7.0
128. CH2O(15)+C7H15J(42)=nc7h16(1)+HCO(31)            1.08E+11    0.0    7.0
129. CH2O(15)+C7H15J(45)=nc7h16(1)+HCO(31)            5.50E+03    2.8    5.9
130. CH2O(15)+C7H15J(44)=nc7h16(1)+HCO(31)            1.08E+11    0.0    7.0
131. H2O2(12)+C7H13J(294)=c7h14-3(40)+HO2(30)         1.82E+15   -0.7    7.2
132. H2O2(12)+C7H13J(299)=c7h14-3(40)+HO2(30)         1.82E+15   -0.7    7.2
133. C2H6(7)+CH(18)=C2H4(6)+CH3(21)                   1.08E+14    0.0   -0.3
134. CH(18)+OH(29)=HCO(31)+H(17)                      3.00E+13    0.0    0.0
135. H2O(11)+H(17)=H2(3)+OH(29)                       4.52E+08    1.6   18.4
136. C2H6(7)+CH2(S)(20)=CH3(21)+C2H5(24)              2.40E+14    0.0    0.0
137. C2H6(7)+CH2(19)=>C2H5(24)+CH3(21)                1.00E+06    2.3    3.7
138. nc7h16(1)+OH(29)=C7H15J(42)+H2O(11)              3.60E+06    2.0   -1.1
139. nc7h16(1)+OH(29)=C7H15J(41)+H2O(11)              3.60E+06    2.0   -1.1
140. nc7h16(1)+OH(29)=C7H15J(44)+H2O(11)              1.80E+06    2.0   -1.1
141. nc7h16(1)+OH(29)=C7H15J(45)+H2O(11)              1.58E+08    1.8    0.3
142. CH2CO(16)+O(28)=HCO(31)+HCO(31)                  2.52E+11    0.0    1.4
143. C3H6(9)+C7H15J(44)=nc7h16(1)+C3H5J(285)          8.61E+11    0.0   12.3
144. C3H6(9)+C7H15J(45)=nc7h16(1)+C3H5J(285)          1.68E+12    0.0   12.4
145. C3H6(9)+C7H15J(42)=nc7h16(1)+C3H5J(285)          8.61E+11    0.0   12.3
146. C3H6(9)+C7H15J(41)=nc7h16(1)+C3H5J(285)          8.61E+11    0.0   12.3
147. C6H10O3(1316)+OH(29)=C6H9O3J(1328)+H2O(11)       1.73E+01    3.4   -1.1
148. C6H10O3(1317)+OH(29)=C6H9O3J(1329)+H2O(11)       1.73E+01    3.4   -1.1
149. C6H10O3(1316)+CH3(21)=C6H9O3J(1328)+CH4(4)       6.95E+13   -1.1    2.6
150. C6H10O3(1317)+CH3(21)=C6H9O3J(1329)+CH4(4)       6.95E+13   -1.1    2.6
151. o2(2)+CO(13)=CO2(14)+O(28)                       1.26E+13    0.0   47.0
152. H2O2(12)+C3H5J(285)=HO2(30)+C3H6(9)              2.97E+03    2.4    9.7
153. H2O2(12)+C2H3(23)=HO2(30)+C2H4(6)                2.88E+01    3.1    6.9
154. C6H10O3(1316)+C2H3(23)=C2H4(6)+C6H9O3J(1328)     1.44E+01    3.1    6.9
155. C6H10O3(1317)+C2H3(23)=C2H4(6)+C6H9O3J(1329)     1.44E+01    3.1    6.9
156. C2H3(23)+O(28)=CO(13)+CH3(21)                    3.00E+13    0.0    0.0
157. C2H(22)+C2H3(23)=C2H2(5)+C2H2(5)                 1.90E+13    0.0    0.0
158. CO2(14)+CH(18)=HCO(31)+CO(13)                    3.43E+12    0.0    0.7
159. nc7h16(1)+O(28)=>C7H15J(42)+OH(29)               1.91E+05    2.7    2.1
160. nc7h16(1)+O(28)=>C7H15J(41)+OH(29)               1.91E+05    2.7    2.1
161. nc7h16(1)+O(28)=>C7H15J(44)+OH(29)               9.54E+04    2.7    2.1
162. nc7h16(1)+O(28)=>C7H15J(45)+OH(29)               5.13E+04    3.0    3.1
163. CH2(19)+O(28)=CO(13)+H(17)+H(17)                 7.20E+13    0.0    0.0
164. CH3(21)+O(28)=CH2O(15)+H(17)                     8.43E+13    0.0    0.0
165. C6H10O3(1316)+C2H(22)=C6H9O3J(1328)+C2H2(5)      1.21E+12    0.0    0.0
166. C6H10O3(1317)+C2H(22)=C6H9O3J(1329)+C2H2(5)      1.21E+12    0.0    0.0
167. C3H6(9)+C2H3(23)=C2H4(6)+C3H5J(285)              2.32E+13    0.0    7.5
168. CH2O(15)+CH(18)=CH2(19)+HCO(31)                  9.64E+13    0.0   -0.5
169. H(17)+CH2OH(33)=CH3(21)+OH(29)                   1.02E+13    0.0    0.0
170. c7h14-3(40)+C7H13J(294)                          1.98E+03    2.7   12.9
     =>C7H13J(299)+c7h14-3(40)
171. c7h14-3(40)+C7H13J(299)                          1.98E+03    2.7   12.9
     =>C7H13J(294)+c7h14-3(40)
```

```
172. C7H13J(294)=>C7H13J(299)                              1.79E+10   0.7   38.0
173. C7H13J(299)=>C7H13J(294)                              1.79E+10   0.7   38.0
174. C3H6(9)+H(17)=C3H5J(285)+H2(3)                        1.30E+06   2.4    2.8
175. CH2(19)+CH2(19)=C2H2(5)+H2(3)                         1.20E+13   0.0    0.8
176. nc7h16(1)+C7H13J(294)=C7H15J(44)+c7h14-3(40)         3.08E+03   2.7   10.1
177. nc7h16(1)+C7H13J(294)=C7H15J(41)+c7h14-3(40)         6.16E+03   2.7   10.1
178. nc7h16(1)+C7H13J(294)=C7H15J(42)+c7h14-3(40)         6.16E+03   2.7   10.1
179. nc7h16(1)+C7H13J(294)=C7H15J(45)+c7h14-3(40)         3.95E+03   2.7   12.9
180. nc7h16(1)+C7H13J(299)=C7H15J(44)+c7h14-3(40)         3.08E+03   2.7   10.1
181. nc7h16(1)+C7H13J(299)=C7H15J(41)+c7h14-3(40)         6.16E+03   2.7   10.1
182. nc7h16(1)+C7H13J(299)=C7H15J(42)+c7h14-3(40)         6.16E+03   2.7   10.1
183. nc7h16(1)+C7H13J(299)=C7H15J(45)+c7h14-3(40)         3.95E+03   2.7   12.9
184. C2H2(5)+CH2(19)=>C2H22+CH3(21)                        1.85E+10   0.9   28.3
185. CH3(21)+HCO(31)=CH4(4)+CO(13)                         1.20E+14   0.0    0.0
186. H(17)+CH2(19)=CH(18)+H2(3)                            6.02E+12   0.0   -1.8
187. H(17)+H(17)+H2(3)=H2(3)+H2(3)                         9.79E+16  -0.6    0.0
188. CH2O(15)+C2H3(23)=HCO(31)+C2H4(6)                     5.42E+03   2.8    5.9
189. CH4(4)+O(28)=CH3(21)+OH(29)                           7.23E+08   1.6    8.5
190. OH(29)+HO2(30)=H2O(11)+o2(2)                          2.89E+13   0.0   -0.5
191. C3H6(9)+C2H5(24)=C2H6(7)+C3H5J(285)                   1.68E+12   0.0   12.4
192. CH2O(15)+C2H(22)=HCO(31)+C2H2(5)                      1.44E+08   1.3    5.1
193. O(28)+HO2(30)=o2(2)+OH(29)                            3.19E+13   0.0    0.0
194. CH2O(15)+C7H13J(294)=c7h14-3(40)+HCO(31)             5.50E+03   2.8    5.9
195. CH2O(15)+C7H13J(299)=c7h14-3(40)+HCO(31)             5.50E+03   2.8    5.9
196. c7h14-3(40)+C2H3(23)=C7H13J(294)+C2H4(6)             4.35E+03   2.9    8.8
197. c7h14-3(40)+C2H3(23)=C7H13J(299)+C2H4(6)             4.35E+03   2.9    8.8
198. CH2(19)+CH2(19)=C2H2(5)+H(17)+H(17)                   1.08E+14   0.0    0.8
199. o2(2)+CH2(19)=CO2(14)+H2(3)                           5.43E+12   0.0    1.5
200. C3H6(9)+CH3(21)=CH4(4)+C3H5J(285)                     2.41E+02   2.9    7.2
201. CH3(21)+CH3(21)=C2H5(24)+H(17)                        3.01E+13   0.0   13.5
202. CH4(4)+C2H(22)=CH3(21)+C2H2(5)                        1.81E+12   0.0    0.0
203. CH2CO(16)+O(28)=CH2(19)+CO2(14)                       1.33E+12   0.0    1.4
204. C2H6(7)+C2H3(23)=C2H5(24)+C2H4(6)                     8.70E+03   2.9    8.8
205. C6H10O3(1316)+H(17)=H2(3)+C6H9O3J(1328)              1.06E+10   1.1    8.9
206. C6H10O3(1317)+H(17)=H2(3)+C6H9O3J(1329)              1.06E+10   1.1    8.9
207. H(17)+C2H3(23)=C2H2(5)+H2(3)                          1.20E+13   0.0    0.0
208. CH3O(32)=CH2OH(33)                                    1.79E+10   0.7   38.0
209. C3H6(9)+C2H(22)=C3H5J(285)+C2H2(5)                    1.81E+12   0.0    0.0
210. C2H4(6)+CH2(19)=>C2H3(23)+CH3(21)                     1.91E+09   1.3    5.7
211. CH2CO(16)+OH(29)=CH3(21)+CO2(14)                      2.52E+12   0.0    0.0
212. C3H6(9)+O(28)=>C3H5J(285)+OH(29)                      2.56E+04   3.0    3.1
213. H(17)+HO2(30)=H2(3)+o2(2)                             4.28E+13   0.0    1.4
214. o2(2)+H(17)=OH(29)+O(28)                              9.76E+13   0.0   14.8
215. nc7h16(1)+C2H5(24)=C7H15J(42)+C2H6(7)                6.16E+03   2.7   10.1
216. nc7h16(1)+C2H5(24)=>C7H15J(45)+C2H6(7)               3.95E+03   2.7   12.9
217. nc7h16(1)+C2H5(24)=C7H15J(44)+C2H6(7)                3.08E+03   2.7   10.1
218. nc7h16(1)+C2H5(24)=C7H15J(41)+C2H6(7)                6.16E+03   2.7   10.1
219. C2H6(7)+C7H15J(45)=>nc7h16(1)+C2H5(24)               3.95E+03   2.7   12.9
220. C6H10O3(1316)+CH2(19)=>C6H9O3J(1328)+CH3(21)         1.44E+01   3.1    6.9
221. C6H10O3(1317)+CH2(19)=>C6H9O3J(1329)+CH3(21)         1.44E+01   3.1    6.9
222. CH2CO(16)+O(28)=HCO(31)+H(17)+CO(13)                  2.52E+11   0.0    1.4
223. H(17)+CH2(S)(20)=CH2(19)+H(17)                        2.00E+14   0.0    0.0
224. C2H3(23)+OH(29)=C2H2(5)+H2O(11)                       5.00E+12   0.0    0.0
225. H2O2(12)+CH2(19)=>HO2(30)+CH3(21)                     2.88E+01   3.1    6.9
226. C2H2(5)+O(28)=>C2H(22)+OH(29)                         3.40E+08   1.5   30.4
227. CO(13)+HO2(30)=CO2(14)+OH(29)                         1.51E+14   0.0   23.7
228. H2(3)+C2H(22)=C2H2(5)+H(17)                           1.08E+13   0.0    2.2
229. nc7h16(1)+H(17)=C7H15J(42)+H2(3)                      5.20E+08   1.7    4.8
230. nc7h16(1)+H(17)=C7H15J(41)+H2(3)                      5.20E+08   1.7    4.8
231. nc7h16(1)+H(17)=C7H15J(44)+H2(3)                      2.60E+08   1.7    4.8
232. nc7h16(1)+H(17)=C7H15J(45)+H2(3)                      3.77E+08   1.8    7.5
233. H2O2(12)+C2H(22)=HO2(30)+C2H2(5)                      2.42E+12   0.0    0.0
234. o2(2)+CH3(21)=CH3O(32)+O(28)                          4.40E+13   0.0   31.4
235. C2H6(7)+CH3(21)=C2H5(24)+CH4(4)                       1.51E-07   6.0    6.0
236. C2H(22)+O(28)=CH(18)+CO(13)                           1.00E+13   0.0    0.0
237. CH2CO(16)+OH(29)=CH2OH(33)+CO(13)                     4.68E+12   0.0    0.0
238. C2H2(5)+CH(18)=C2H(22)+CH2(19)                        2.11E+14   0.0   -0.1
239. C2H4(6)+O(28)=CH2CO(16)+H2(3)                         6.80E+05   1.9    0.2
240. C2H(22)+OH(29)=CH2(19)+CO(13)                         1.81E+13   0.0    0.0
241. C2H4(6)+O(28)=CH3(21)+HCO(31)                         8.13E+06   1.9    0.2
242. C2H2(5)+o2(2)=C2H(22)+HO2(30)                         1.20E+13   0.0   74.5
```

```
243. C6H10O3(1316)+C7H15J(44)                          1.44E+12   -0.1    7.5
     =C6H9O3J(1328)+nc7h16(1)
244. C6H10O3(1316)+C7H15J(42)                          1.44E+12   -0.1    7.5
     =C6H9O3J(1328)+nc7h16(1)
245. C6H10O3(1316)+C7H15J(41)                          1.44E+12   -0.1    7.5
     =C6H9O3J(1328)+nc7h16(1)
246. C6H10O3(1316)+C7H15J(45)                          9.12E+14   -0.7    7.2
     =C6H9O3J(1328)+nc7h16(1)
247. C6H10O3(1317)+C7H15J(44)                          1.44E+12   -0.1    7.5
     =C6H9O3J(1329)+nc7h16(1)
248. C6H10O3(1317)+C7H15J(42)                          1.44E+12   -0.1    7.5
     =C6H9O3J(1329)+nc7h16(1)
249. C6H10O3(1317)+C7H15J(41)                          1.44E+12   -0.1    7.5
     =C6H9O3J(1329)+nc7h16(1)
250. C6H10O3(1317)+C7H15J(45)                          9.12E+14   -0.7    7.2
     =C6H9O3J(1329)+nc7h16(1)
251. nc7h16(1)+CH2(19)=>C7H15J(42)+CH3(21)             3.02E+00    3.5    7.5
252. nc7h16(1)+CH2(19)=>C7H15J(41)+CH3(21)             3.02E+00    3.5    7.5
253. nc7h16(1)+CH2(19)=>C7H15J(44)+CH3(21)             1.51E+00    3.5    7.5
254. nc7h16(1)+CH2(19)=>C7H15J(45)+CH3(21)             1.00E+06    2.3    3.7
255. CH3(21)+OH(29)=CH2(S)(20)+H2O(11)                 7.23E+13    0.0    2.8
256. H2O(11)+CH2(19)=>OH(29)+CH3(21)                   1.45E+08    1.4    9.8
257. C2H2(5)+OH(29)=C2H(22)+H2O(11)                    6.00E+13    0.0   12.9
258. C6H10O3(1316)+C3H5J(285)                          1.49E+03    2.4    9.7
     =C6H9O3J(1328)+C3H6(9)
259. C6H10O3(1317)+C3H5J(285)                          1.49E+03    2.4    9.7
     =C6H9O3J(1329)+C3H6(9)
260. H2O2(12)+C6H9O3J(1328)=C6H10O3(1316)+HO2(30)      3.46E+01    3.4   -1.1
261. H2O2(12)+C6H9O3J(1329)=C6H10O3(1317)+HO2(30)      3.46E+01    3.4   -1.1
262. CH2O(15)+C2H5(24)=C2H6(7)+HCO(31)                 5.50E+03    2.8    5.9
263. C6H10O3(1316)+O(28)=>C6H9O3J(1328)+OH(29)         1.00E+13    0.0    4.7
264. C6H10O3(1317)+O(28)=>C6H9O3J(1329)+OH(29)         1.00E+13    0.0    4.7
265. C2H6(7)+HO2(30)=H2O2(12)+C2H5(24)                 1.32E+13    0.0   20.5
266. C2H4(6)+CH2(S)(20)=C3H6(9)                        9.64E+13    0.0    0.0
267. CH2O(15)+CH3(21)=CH4(4)+HCO(31)                   7.83E-08    6.1    2.0
268. C2H2(5)+CH2(19)=C3H4(8)                           1.20E+13    0.0    6.6
269. H(17)+HCO(31)=CO(13)+H2(3)                        9.03E+13    0.0    0.0
270. o2(2)+CH(18)=CO2(14)+H(17)                        1.66E+13    0.0    0.0
271. C3H6(9)+OH(29)=C3H5J(285)+H2O(11)                 7.46E+07    1.7    3.6
272. CO2(14)+CH2(19)=CH2O(15)+CO(13)                   2.35E+10    0.0    0.0
273. CH4(4)+H(17)=CH3(21)+H2(3)                        1.32E+04    3.0    8.0
274. o2(2)+C2H3(23)=C2H2(5)+HO2(30)                    5.42E+12    0.0    0.0
275. H(17)+O(28)+m=OH(29)+m                            1.18E+19   -1.0    0.0
         H2O(11)          Enhanced by    6.500E+00
         C2H6(7)          Enhanced by    3.000E+00
         N2               Enhanced by    4.000E-01
         CH4(4)           Enhanced by    3.000E+00
         CO(13)           Enhanced by    7.500E-01
         Ar               Enhanced by    3.500E-01
         CO2(14)          Enhanced by    1.500E+00
         o2(2)            Enhanced by    4.000E-01
276. H(17)+H(17)+m=H2(3)+m                             1.87E+18   -1.0    0.0
         H2O(11)          Enhanced by    6.500E+00
         C2H6(7)          Enhanced by    3.000E+00
         N2               Enhanced by    4.000E-01
         CH4(4)           Enhanced by    3.000E+00
         CO(13)           Enhanced by    7.500E-01
         Ar               Enhanced by    3.500E-01
         CO2(14)          Enhanced by    1.500E+00
         H2(3)            Enhanced by    0.000E+00
         o2(2)            Enhanced by    4.000E-01
277. CH2O(15)+m=HCO(31)+H(17)+m                        1.40E+36   -5.5   96.7
         H2O(11)          Enhanced by    6.500E+00
         C2H6(7)          Enhanced by    3.000E+00
         N2               Enhanced by    4.000E-01
         CH4(4)           Enhanced by    3.000E+00
         CO(13)           Enhanced by    7.500E-01
         Ar               Enhanced by    3.500E-01
         CO2(14)          Enhanced by    1.500E+00
         o2(2)            Enhanced by    4.000E-01
278. C2H2(5)+H(17)(+m)=C2H3(23)(+m)                    8.43E+12    0.0    2.6
```

```
        H2O(11)           Enhanced by   6.500E+00
        C2H6(7)           Enhanced by   3.000E+00
        N2                Enhanced by   4.000E-01
        CH4(4)            Enhanced by   3.000E+00
        CO(13)            Enhanced by   7.500E-01
        Ar                Enhanced by   3.500E-01
        CO2(14)           Enhanced by   1.500E+00
        o2(2)             Enhanced by   4.000E-01
     Low pressure limit:  0.34300E+19  0.00000E+00  0.14690E+01
     TROE centering:      0.10000E+01  0.10000E+01  0.10000E+01  0.12310E+04
279. H(17)+CH3(21)(+m)=CH4(4)(+m)                     1.69E+14    0.0       0.0
        H2O(11)           Enhanced by   6.500E+00
        C2H6(7)           Enhanced by   3.000E+00
        N2                Enhanced by   4.000E-01
        CH4(4)            Enhanced by   3.000E+00
        CO(13)            Enhanced by   7.500E-01
        Ar                Enhanced by   3.500E-01
        CO2(14)           Enhanced by   1.500E+00
        o2(2)             Enhanced by   4.000E-01
     Low pressure limit:  0.14080E+25 -0.18000E+01  0.00000E+00
     TROE centering:      0.37000E+00  0.33150E+04  0.61000E+02
280. C2H4(6)+m=C2H2(5)+H2(3)+m                        9.97E+16    0.0      71.5
        H2O(11)           Enhanced by   6.500E+00
        C2H6(7)           Enhanced by   3.000E+00
        N2                Enhanced by   4.000E-01
        CH4(4)            Enhanced by   3.000E+00
        CO(13)            Enhanced by   7.500E-01
        Ar                Enhanced by   3.500E-01
        CO2(14)           Enhanced by   1.500E+00
        o2(2)             Enhanced by   4.000E-01
281. CH2O(15)+m=H2(3)+CO(13)+m                        3.26E+36   -5.5      96.7
        H2O(11)           Enhanced by   6.500E+00
        C2H6(7)           Enhanced by   3.000E+00
        N2                Enhanced by   4.000E-01
        CH4(4)            Enhanced by   3.000E+00
        CO(13)            Enhanced by   7.500E-01
        Ar                Enhanced by   3.500E-01
        CO2(14)           Enhanced by   1.500E+00
        o2(2)             Enhanced by   4.000E-01
282. C2H4(6)+H(17)(+m)=C2H5(24)(+m)                   3.97E+09    1.3       1.3
        H2O(11)           Enhanced by   6.500E+00
        C2H6(7)           Enhanced by   3.000E+00
        N2                Enhanced by   4.000E-01
        CH4(4)            Enhanced by   3.000E+00
        CO(13)            Enhanced by   7.500E-01
        Ar                Enhanced by   3.500E-01
        CO2(14)           Enhanced by   1.500E+00
        o2(2)             Enhanced by   4.000E-01
     Low pressure limit:  0.13500E+20  0.00000E+00  0.75500E+00
     TROE centering:      0.76000E+00  0.40000E+02  0.10250E+04
283. CH2(S)(20)+m=CH2(19)+m                           1.51E+13    0.0       0.0
        C2H2(5)           Enhanced by   3.200E+00
        H2O(11)           Enhanced by   6.500E+00
        C2H6(7)           Enhanced by   1.440E+00
        N2                Enhanced by   4.000E-01
        CH4(4)            Enhanced by   4.800E-01
        CO(13)            Enhanced by   7.500E-01
        C2H4(6)           Enhanced by   1.600E+00
        Ar                Enhanced by   2.400E-01
        CO2(14)           Enhanced by   1.500E+00
        o2(2)             Enhanced by   4.000E-01
284. o2(2)+H(17)+m=HO2(30)+m                          2.10E+18   -0.8       0.0
        H2O(11)           Enhanced by   0.000E+00
        C2H6(7)           Enhanced by   3.000E+00
        N2                Enhanced by   6.700E-01
        CH4(4)            Enhanced by   3.000E+00
        CO(13)            Enhanced by   7.500E-01
        Ar                Enhanced by   2.900E-01
        CO2(14)           Enhanced by   1.500E+00
        o2(2)             Enhanced by   4.000E-01
285. CH2CO(16)+m=CH2(19)+CO(13)+m                     6.57E+15    0.0      57.6
```

```
          H2O(11)           Enhanced by    6.500E+00
          C2H6(7)           Enhanced by    3.000E+00
          N2                Enhanced by    4.000E-01
          CH4(4)            Enhanced by    3.000E+00
          CO(13)            Enhanced by    7.500E-01
          Ar                Enhanced by    3.500E-01
          CO2(14)           Enhanced by    1.500E+00
          o2(2)             Enhanced by    4.000E-01
286. H(17)+OH(29)+m=H2O(11)+m                          5.53E+22   -2.0        0.0
          H2O(11)           Enhanced by    2.550E+00
          C2H6(7)           Enhanced by    3.000E+00
          N2                Enhanced by    4.000E-01
          CH4(4)            Enhanced by    3.000E+00
          CO(13)            Enhanced by    7.500E-01
          Ar                Enhanced by    1.500E-01
          CO2(14)           Enhanced by    1.500E+00
          o2(2)             Enhanced by    4.000E-01
287. O(28)+O(28)+m=o2(2)+m                             5.40E+13    0.0       -1.8
          H2O(11)           Enhanced by    6.500E+00
          C2H6(7)           Enhanced by    3.000E+00
          N2                Enhanced by    4.000E-01
          CH4(4)            Enhanced by    3.000E+00
          CO(13)            Enhanced by    7.500E-01
          Ar                Enhanced by    3.500E-01
          CO2(14)           Enhanced by    1.500E+00
          o2(2)             Enhanced by    4.000E-01
288. CH3O(32)+m=CH2O(15)+H(17)+m                       1.55E+14    0.0       13.5
          H2O(11)           Enhanced by    6.500E+00
          C2H6(7)           Enhanced by    3.000E+00
          N2                Enhanced by    4.000E-01
          CH4(4)            Enhanced by    3.000E+00
          CO(13)            Enhanced by    7.500E-01
          Ar                Enhanced by    3.500E-01
          CO2(14)           Enhanced by    1.500E+00
          o2(2)             Enhanced by    4.000E-01
289. CH2OH(33)+m=CH2O(15)+H(17)+m                      1.26E+16    0.0       30.0
          H2O(11)           Enhanced by    6.500E+00
          C2H6(7)           Enhanced by    3.000E+00
          N2                Enhanced by    4.000E-01
          CH4(4)            Enhanced by    3.000E+00
          CO(13)            Enhanced by    7.500E-01
          Ar                Enhanced by    3.500E-01
          CO2(14)           Enhanced by    1.500E+00
          o2(2)             Enhanced by    4.000E-01
290. OH(29)+OH(29)(+m)=H2O2(12)(+m)                    7.23E+13   -0.4        0.0
          H2O(11)           Enhanced by    6.500E+00
          C2H6(7)           Enhanced by    3.000E+00
          N2                Enhanced by    4.000E-01
          CH4(4)            Enhanced by    3.000E+00
          CO(13)            Enhanced by    7.500E-01
          Ar                Enhanced by    3.500E-01
          CO2(14)           Enhanced by    1.500E+00
          o2(2)             Enhanced by    4.000E-01
     Low pressure limit:  0.55300E+20 -0.76000E+00  0.00000E+00
     TROE centering:      0.10000E+01  0.10000E+01  0.10000E+01  0.10400E+04
291. HCO(31)+m=H(17)+CO(13)+m                          4.49E+14    0.0       15.7
          H2O(11)           Enhanced by    6.500E+00
          C2H6(7)           Enhanced by    3.000E+00
          N2                Enhanced by    4.000E-01
          CH4(4)            Enhanced by    3.000E+00
          CO(13)            Enhanced by    7.500E-01
          Ar                Enhanced by    3.500E-01
          CO2(14)           Enhanced by    1.500E+00
          o2(2)             Enhanced by    4.000E-01
292. CH3(21)+CH3(21)(+m)=C2H6(7)(+m)                   3.61E+13    0.0        0.0
          H2O(11)           Enhanced by    6.500E+00
          C2H6(7)           Enhanced by    3.000E+00
          N2                Enhanced by    4.000E-01
          CH4(4)            Enhanced by    3.000E+00
          CO(13)            Enhanced by    7.500E-01
          Ar                Enhanced by    3.500E-01
```

242

```
                CO2(14)            Enhanced by    1.500E+00
                o2(2)              Enhanced by    4.000E-01
        Low pressure limit:  0.36300E+42 -0.70000E+01  0.27620E+01
        TROE centering:      0.62000E+00  0.73000E+02  0.11800E+04
293. CH3(21)+m=CH2(19)+H(17)+m                        2.91E+16    0.0     90.6
                H2O(11)            Enhanced by    6.500E+00
                C2H6(7)            Enhanced by    3.000E+00
                N2                 Enhanced by    4.000E-01
                CH4(4)             Enhanced by    3.000E+00
                CO(13)             Enhanced by    7.500E-01
                Ar                 Enhanced by    3.500E-01
                CO2(14)            Enhanced by    1.500E+00
                o2(2)              Enhanced by    4.000E-01
294. CO(13)+O(28)+m=CO2(14)+m                         1.54E+15    0.0      3.0
                H2O(11)            Enhanced by    6.500E+00
                C2H6(7)            Enhanced by    3.000E+00
                N2                 Enhanced by    4.000E-01
                CH4(4)             Enhanced by    3.000E+00
                CO(13)             Enhanced by    7.500E-01
                Ar                 Enhanced by    3.500E-01
                CO2(14)            Enhanced by    1.500E+00
                o2(2)              Enhanced by    4.000E-01
295. C2H2(5)+m=C2H(22)+H(17)+m                        1.14E+17    0.0    106.8
                H2O(11)            Enhanced by    6.500E+00
                C2H6(7)            Enhanced by    3.000E+00
                N2                 Enhanced by    4.000E-01
                CH4(4)             Enhanced by    3.000E+00
                CO(13)             Enhanced by    7.500E-01
                Ar                 Enhanced by    3.500E-01
                CO2(14)            Enhanced by    1.500E+00
                o2(2)              Enhanced by    4.000E-01
296. C2H4(6)+m=C2H3(23)+H(17)+m                       7.40E+17    0.0     96.5
                H2O(11)            Enhanced by    6.500E+00
                C2H6(7)            Enhanced by    3.000E+00
                N2                 Enhanced by    4.000E-01
                CH4(4)             Enhanced by    3.000E+00
                CO(13)             Enhanced by    7.500E-01
                Ar                 Enhanced by    3.500E-01
                CO2(14)            Enhanced by    1.500E+00
                o2(2)              Enhanced by    4.000E-01
297. nc7h16(1)(+m)=>C4H9J(46)+C3H7J(47)(+m)           1.00E+00    0.0      0.0
        Tmin, Tmax:    0.30000E+03  0.15000E+04
        Pmin, Pmax:    0.10000E+01  0.10000E+03
        CHEB Polynomials:    0.70000E+01  0.40000E+01
        CHEB Polynomials:   -0.19927E+02  0.23930E-01 -0.47800E-02  0.31000E-03
        CHEB Polynomials:   -0.24995E+02 -0.46370E-01  0.91400E-02 -0.57000E-03
        CHEB Polynomials:   -0.17753E+00  0.42170E-01 -0.79800E-02  0.42000E-03
        CHEB Polynomials:    0.73500E-01 -0.35920E-01  0.63000E-02 -0.20000E-03
        CHEB Polynomials:   -0.41370E-01  0.28580E-01 -0.44000E-02 -0.17140E-04
        CHEB Polynomials:    0.27290E-01 -0.21130E-01  0.26000E-02  0.20000E-03
        CHEB Polynomials:   -0.18760E-01  0.14420E-01 -0.11500E-02 -0.31000E-03
298. nc7h16(1)(+m)=>C7H15J(44)+H(17)(+m)              1.00E+00    0.0      0.0
        Tmin, Tmax:    0.30000E+03  0.15000E+04
        Pmin, Pmax:    0.10000E+01  0.10000E+03
        CHEB Polynomials:    0.70000E+01  0.40000E+01
        CHEB Polynomials:   -0.27314E+02  0.36680E-01 -0.69500E-02  0.38000E-03
        CHEB Polynomials:   -0.28384E+02 -0.70780E-01  0.13200E-01 -0.67000E-03
        CHEB Polynomials:   -0.12094E+00  0.63480E-01 -0.11220E-01  0.43000E-03
        CHEB Polynomials:    0.72850E-01 -0.52780E-01  0.83800E-02 -0.98985E-04
        CHEB Polynomials:   -0.50280E-01  0.40430E-01 -0.52600E-02 -0.23000E-03
        CHEB Polynomials:    0.35580E-01 -0.28270E-01  0.24200E-02  0.47000E-03
        CHEB Polynomials:   -0.24420E-01  0.17800E-01 -0.27000E-03 -0.59000E-03
299. nc7h16(1)(+m)=>C6H13J(43)+CH3(21)(+m)            1.00E+00    0.0      0.0
        Tmin, Tmax:    0.30000E+03  0.15000E+04
        Pmin, Pmax:    0.10000E+01  0.10000E+03
        CHEB Polynomials:    0.70000E+01  0.40000E+01
        CHEB Polynomials:   -0.20794E+02  0.25180E-01 -0.49900E-02  0.32000E-03
        CHEB Polynomials:   -0.25533E+02 -0.48770E-01  0.95500E-02 -0.58000E-03
        CHEB Polynomials:   -0.14001E+00  0.44280E-01 -0.83100E-02  0.42000E-03
        CHEB Polynomials:    0.65780E-01 -0.37620E-01  0.65200E-02 -0.20000E-03
        CHEB Polynomials:   -0.39880E-01  0.29810E-01 -0.45100E-02 -0.35524E-04
```

```
       CHEB Polynomials:      0.27450E-01  -0.21910E-01   0.26000E-02   0.23000E-03
       CHEB Polynomials:     -0.19220E-01   0.14830E-01  -0.10800E-02  -0.34000E-03
300.  nc7h16(1)(+m)=>C7H15J(42)+H(17)(+m)              1.00E+00     0.0         0.0
       Tmin, Tmax:     0.30000E+03  0.15000E+04
       Pmin, Pmax:     0.10000E+01  0.10000E+03
       CHEB Polynomials:      0.70000E+01   0.40000E+01
       CHEB Polynomials:     -0.27013E+02   0.36680E-01  -0.69500E-02   0.38000E-03
       CHEB Polynomials:     -0.28384E+02  -0.70780E-01   0.13200E-01  -0.67000E-03
       CHEB Polynomials:     -0.12094E+00   0.63480E-01  -0.11220E-01   0.43000E-03
       CHEB Polynomials:      0.72850E-01  -0.52780E-01   0.83800E-02  -0.98985E-04
       CHEB Polynomials:     -0.50280E-01   0.40430E-01  -0.52600E-02  -0.23000E-03
       CHEB Polynomials:      0.35580E-01  -0.28270E-01   0.24200E-02   0.47000E-03
       CHEB Polynomials:     -0.24420E-01   0.17800E-01  -0.27000E-03  -0.59000E-03
301.  nc7h16(1)(+m)=>C7H15J(41)+H(17)(+m)              1.00E+00     0.0         0.0
       Tmin, Tmax:     0.30000E+03  0.15000E+04
       Pmin, Pmax:     0.10000E+01  0.10000E+03
       CHEB Polynomials:      0.70000E+01   0.40000E+01
       CHEB Polynomials:     -0.26944E+02   0.36520E-01  -0.69300E-02   0.38000E-03
       CHEB Polynomials:     -0.28412E+02  -0.70470E-01   0.13140E-01  -0.67000E-03
       CHEB Polynomials:     -0.10877E+00   0.63220E-01  -0.11170E-01   0.43000E-03
       CHEB Polynomials:      0.69620E-01  -0.52570E-01   0.83600E-02  -0.10000E-03
       CHEB Polynomials:     -0.49130E-01   0.40290E-01  -0.52500E-02  -0.22000E-03
       CHEB Polynomials:      0.35260E-01  -0.28190E-01   0.24200E-02   0.47000E-03
       CHEB Polynomials:     -0.24280E-01   0.17760E-01  -0.28000E-03  -0.59000E-03
302.  nc7h16(1)(+m)=>C2H5(24)+C5H11J(48)(+m)           1.00E+00     0.0         0.0
       Tmin, Tmax:     0.30000E+03  0.15000E+04
       Pmin, Pmax:     0.10000E+01  0.10000E+03
       CHEB Polynomials:      0.70000E+01   0.40000E+01
       CHEB Polynomials:     -0.19917E+02   0.23870E-01  -0.47700E-02   0.31000E-03
       CHEB Polynomials:     -0.25005E+02  -0.46270E-01   0.91200E-02  -0.57000E-03
       CHEB Polynomials:     -0.17161E+00   0.42080E-01  -0.79700E-02   0.42000E-03
       CHEB Polynomials:      0.71930E-01  -0.35860E-01   0.62900E-02  -0.21000E-03
       CHEB Polynomials:     -0.41360E-01   0.28530E-01  -0.44000E-02  -0.15834E-04
       CHEB Polynomials:      0.27310E-01  -0.21100E-01   0.26000E-02   0.20000E-03
       CHEB Polynomials:     -0.18500E-01   0.14410E-01  -0.11500E-02  -0.31000E-03
303.  nc7h16(1)(+m)=>C7H15J(45)+H(17)(+m)              1.00E+00     0.0         0.0
       Tmin, Tmax:     0.30000E+03  0.15000E+04
       Pmin, Pmax:     0.10000E+01  0.10000E+03
       CHEB Polynomials:      0.70000E+01   0.40000E+01
       CHEB Polynomials:     -0.27719E+02   0.39810E-01  -0.74800E-02   0.39000E-03
       CHEB Polynomials:     -0.29280E+02  -0.76750E-01   0.14170E-01  -0.68000E-03
       CHEB Polynomials:     -0.73690E-01   0.68650E-01  -0.11970E-01   0.42000E-03
       CHEB Polynomials:      0.63600E-01  -0.56790E-01   0.88400E-02  -0.64411E-04
       CHEB Polynomials:     -0.51000E-01   0.43170E-01  -0.54100E-02  -0.28000E-03
       CHEB Polynomials:      0.36560E-01  -0.29820E-01   0.23100E-02   0.54000E-03
       CHEB Polynomials:     -0.25150E-01   0.18420E-01   0.23241E-05  -0.66000E-03
304.  C7H15J(42)+o2(2)(+m)                             1.00E+00     0.0         0.0
       =>c7h14-3(40)+HO2(30)(+m)
       Tmin, Tmax:     0.30000E+03  0.15000E+04
       Pmin, Pmax:     0.10000E+01  0.10000E+03
       CHEB Polynomials:      0.70000E+01   0.40000E+01
       CHEB Polynomials:      0.76336E+01  -0.71794E+00  -0.23250E-01  -0.77000E-03
       CHEB Polynomials:     -0.31837E+01  -0.45118E+00   0.28900E-01   0.25900E-02
       CHEB Polynomials:      0.11618E+00   0.21131E+00   0.22600E-02  -0.31300E-02
       CHEB Polynomials:      0.22778E+00  -0.20970E-01  -0.15400E-01   0.10700E-02
       CHEB Polynomials:     -0.78770E-01  -0.42830E-01   0.82500E-02   0.11400E-02
       CHEB Polynomials:     -0.24560E-01   0.24760E-01   0.13300E-02  -0.11100E-02
       CHEB Polynomials:      0.35950E-01   0.31300E-02  -0.30800E-02  -0.74257E-04
305.  C7H15J(42)+o2(2)(+m)                             1.00E+00     0.0         0.0
       =>c7h14-2(39)+HO2(30)(+m)
       Tmin, Tmax:     0.30000E+03  0.15000E+04
       Pmin, Pmax:     0.10000E+01  0.10000E+03
       CHEB Polynomials:      0.70000E+01   0.40000E+01
       CHEB Polynomials:      0.76336E+01  -0.71794E+00  -0.23250E-01  -0.77000E-03
       CHEB Polynomials:     -0.31837E+01  -0.45118E+00   0.28900E-01   0.25900E-02
       CHEB Polynomials:      0.11618E+00   0.21131E+00   0.22600E-02  -0.31300E-02
       CHEB Polynomials:      0.22778E+00  -0.20970E-01  -0.15400E-01   0.10700E-02
       CHEB Polynomials:     -0.78770E-01  -0.42830E-01   0.82500E-02   0.11400E-02
       CHEB Polynomials:     -0.24560E-01   0.24760E-01   0.13300E-02  -0.11100E-02
       CHEB Polynomials:      0.35950E-01   0.31300E-02  -0.30800E-02  -0.74257E-04
306.  C7H15J(44)+o2(2)(+m)                             1.00E+00     0.0         0.0
```

```
                  =>c7h14-3(40)+HO2(30)(+m)
            Tmin, Tmax:    0.30000E+03  0.15000E+04
            Pmin, Pmax:    0.10000E+01  0.10000E+03
            CHEB Polynomials:    0.70000E+01  0.40000E+01
            CHEB Polynomials:    0.80151E+01 -0.74197E+00 -0.24070E-01 -0.78000E-03
            CHEB Polynomials:   -0.33156E+01 -0.42080E+00  0.32410E-01  0.25100E-02
            CHEB Polynomials:    0.18108E+00  0.21271E+00 -0.28000E-02 -0.32400E-02
            CHEB Polynomials:    0.22216E+00 -0.36320E-01 -0.13020E-01  0.16500E-02
            CHEB Polynomials:   -0.96380E-01 -0.34810E-01  0.96000E-02  0.58000E-03
            CHEB Polynomials:   -0.13480E-01  0.27260E-01 -0.58000E-03 -0.11200E-02
            CHEB Polynomials:    0.36950E-01 -0.13300E-02 -0.29200E-02  0.28000E-03
307.  C7H15J(45)+o2(2)(+m)                             1.00E+00     0.0        0.0
            =>c7h14-1(38)+HO2(30)(+m)
            Tmin, Tmax:    0.30000E+03  0.15000E+04
            Pmin, Pmax:    0.10000E+01  0.10000E+03
            CHEB Polynomials:    0.70000E+01  0.40000E+01
            CHEB Polynomials:    0.70721E+01 -0.76024E+00 -0.24800E-01 -0.84000E-03
            CHEB Polynomials:   -0.36637E+01 -0.40025E+00  0.35390E-01  0.25400E-02
            CHEB Polynomials:    0.21151E+00  0.22021E+00 -0.65900E-02 -0.34400E-02
            CHEB Polynomials:    0.23009E+00 -0.54520E-01 -0.12330E-01  0.22900E-02
            CHEB Polynomials:   -0.10695E+00 -0.25480E-01  0.12320E-01  0.74553E-04
            CHEB Polynomials:   -0.95800E-02  0.29020E-01 -0.31100E-02 -0.13200E-02
            CHEB Polynomials:    0.37520E-01 -0.56500E-02 -0.28100E-02  0.82000E-03
308.  c2h5cho(37)(+m)=>C2H5(24)+HCO(31)(+m)            1.00E+00     0.0        0.0
            Tmin, Tmax:    0.30000E+03  0.15000E+04
            Pmin, Pmax:    0.10000E+01  0.10000E+03
            CHEB Polynomials:    0.70000E+01  0.40000E+01
            CHEB Polynomials:   -0.19118E+02  0.67020E-01 -0.10550E-01  0.64000E-03
            CHEB Polynomials:   -0.23832E+02 -0.12146E+00  0.17870E-01 -0.78000E-03
            CHEB Polynomials:   -0.23087E+00  0.91520E-01 -0.10930E-01 -0.91199E-04
            CHEB Polynomials:    0.11217E+00 -0.57460E-01  0.42000E-02  0.63000E-03
            CHEB Polynomials:   -0.60540E-01  0.29670E-01 -0.34936E-04 -0.63000E-03
            CHEB Polynomials:    0.31840E-01 -0.12000E-01 -0.14300E-02  0.34000E-03
            CHEB Polynomials:   -0.15380E-01  0.31700E-02  0.12900E-02 -0.48377E-04
309.  C7H15J(45)(+m)=>c7h14-1(38)+H(17)(+m)            1.00E+00     0.0        0.0
            Tmin, Tmax:    0.30000E+03  0.15000E+04
            Pmin, Pmax:    0.10000E+01  0.10000E+03
            CHEB Polynomials:    0.70000E+01  0.40000E+01
            CHEB Polynomials:   -0.30713E+01  0.19864E+00 -0.21070E-01 -0.16000E-03
            CHEB Polynomials:   -0.10173E+02 -0.33610E+00  0.30750E-01  0.12700E-02
            CHEB Polynomials:   -0.33024E+00  0.19858E+00 -0.84100E-02 -0.23200E-02
            CHEB Polynomials:    0.16379E+00 -0.70360E-01 -0.64600E-02  0.17200E-02
            CHEB Polynomials:   -0.54350E-01  0.24000E-02  0.78000E-02 -0.18000E-03
            CHEB Polynomials:    0.94100E-02  0.11470E-01 -0.26200E-02 -0.64000E-03
            CHEB Polynomials:   -0.18000E-02 -0.36500E-02 -0.91000E-03  0.38000E-03
310.  C7H15J(45)(+m)=>C2H4(6)+C5H11J(48)(+m)           1.00E+00     0.0        0.0
            Tmin, Tmax:    0.30000E+03  0.15000E+04
            Pmin, Pmax:    0.10000E+01  0.10000E+03
            CHEB Polynomials:    0.70000E+01  0.40000E+01
            CHEB Polynomials:    0.11456E+01  0.18496E+00 -0.19690E-01 -0.17000E-03
            CHEB Polynomials:   -0.89637E+01 -0.31673E+00  0.29650E-01  0.11100E-02
            CHEB Polynomials:   -0.44140E+00  0.19482E+00 -0.98900E-02 -0.20300E-02
            CHEB Polynomials:    0.19631E+00 -0.76610E-01 -0.43900E-02  0.16500E-02
            CHEB Polynomials:   -0.69090E-01  0.89500E-02  0.70200E-02 -0.36000E-03
            CHEB Polynomials:    0.15970E-01  0.91900E-02 -0.30200E-02 -0.49000E-03
            CHEB Polynomials:   -0.32100E-02 -0.43500E-02 -0.41000E-03  0.42000E-03
311.  C7H15J(42)(+m)=>c7h14-2(39)+H(17)(+m)            1.00E+00     0.0        0.0
            Tmin, Tmax:    0.30000E+03  0.15000E+04
            Pmin, Pmax:    0.10000E+01  0.10000E+03
            CHEB Polynomials:    0.70000E+01  0.40000E+01
            CHEB Polynomials:   -0.30879E+01  0.20298E+00 -0.18910E-01 -0.34000E-03
            CHEB Polynomials:   -0.98735E+01 -0.34738E+00  0.28100E-01  0.13100E-02
            CHEB Polynomials:   -0.33523E+00  0.21141E+00 -0.80200E-02 -0.20600E-02
            CHEB Polynomials:    0.18326E+00 -0.78530E-01 -0.62600E-02  0.15300E-02
            CHEB Polynomials:   -0.62700E-01  0.24700E-02  0.82100E-02 -0.15000E-03
            CHEB Polynomials:    0.73300E-02  0.16390E-01 -0.32600E-02 -0.67000E-03
            CHEB Polynomials:    0.30400E-02 -0.79500E-02 -0.75000E-03  0.49000E-03
312.  C7H15J(42)(+m)=>c7h14-3(40)+H(17)(+m)            1.00E+00     0.0        0.0
            Tmin, Tmax:    0.30000E+03  0.15000E+04
            Pmin, Pmax:    0.10000E+01  0.10000E+03
            CHEB Polynomials:    0.70000E+01  0.40000E+01
```

```
      CHEB Polynomials:     -0.30828E+01  0.20378E+00 -0.19000E-01 -0.34000E-03
      CHEB Polynomials:     -0.99195E+01 -0.34851E+00  0.28170E-01  0.13200E-02
      CHEB Polynomials:     -0.33384E+00  0.21161E+00 -0.79400E-02 -0.20700E-02
      CHEB Polynomials:      0.18163E+00 -0.78100E-01 -0.63900E-02  0.15300E-02
      CHEB Polynomials:     -0.61790E-01  0.20000E-02  0.82700E-02 -0.15000E-03
      CHEB Polynomials:      0.71500E-02  0.16590E-01 -0.32500E-02 -0.67000E-03
      CHEB Polynomials:      0.29600E-02 -0.79100E-02 -0.79000E-03  0.48000E-03
313.  CH3(21)+HO2(30)(+m)=>CH3O(32)+OH(29)(+m)       1.00E+00    0.0        0.0
      Tmin, Tmax:     0.30000E+03  0.15000E+04
      Pmin, Pmax:     0.10000E+01  0.10000E+03
      CHEB Polynomials:      0.70000E+01  0.40000E+01
      CHEB Polynomials:      0.13081E+02 -0.15400E-02 -0.74000E-03 -0.26000E-03
      CHEB Polynomials:     -0.39000E-03 -0.12300E-02 -0.59000E-03 -0.20000E-03
      CHEB Polynomials:     -0.12000E-03  0.30000E-03  0.15000E-03  0.50367E-04
      CHEB Polynomials:      0.23000E-03  0.25565E-04  0.12105E-04  0.41002E-05
      CHEB Polynomials:     -0.16000E-03 -0.46930E-04 -0.22426E-04 -0.77386E-05
      CHEB Polynomials:      0.82972E-04  0.19794E-04  0.94815E-05  0.32875E-05
      CHEB Polynomials:     -0.38349E-04 -0.41735E-05 -0.20081E-05 -0.70246E-06
314.  C3H7J(47)(+m)=>CH3(21)+C2H4(6)(+m)             1.00E+00    0.0        0.0
      Tmin, Tmax:     0.30000E+03  0.15000E+04
      Pmin, Pmax:     0.10000E+01  0.10000E+03
      CHEB Polynomials:      0.70000E+01  0.40000E+01
      CHEB Polynomials:     -0.31247E+00  0.19673E+00 -0.23500E-01  0.12900E-02
      CHEB Polynomials:     -0.91481E+01 -0.30971E+00  0.25320E-01  0.12500E-02
      CHEB Polynomials:     -0.41778E+00  0.17224E+00 -0.14300E-02 -0.26000E-02
      CHEB Polynomials:      0.20728E+00 -0.66180E-01 -0.75700E-02  0.11500E-02
      CHEB Polynomials:     -0.91770E-01  0.12870E-01  0.58000E-02  0.31000E-03
      CHEB Polynomials:      0.33140E-01  0.40300E-02 -0.19200E-02 -0.59000E-03
      CHEB Polynomials:     -0.77500E-02 -0.52900E-02 -0.16000E-03  0.26000E-03
315.  C3H7J(47)(+m)=>C3H6(9)+H(17)(+m)               1.00E+00    0.0        0.0
      Tmin, Tmax:     0.30000E+03  0.15000E+04
      Pmin, Pmax:     0.10000E+01  0.10000E+03
      CHEB Polynomials:      0.70000E+01  0.40000E+01
      CHEB Polynomials:     -0.31681E+01  0.22977E+00 -0.29840E-01  0.22700E-02
      CHEB Polynomials:     -0.10122E+02 -0.33891E+00  0.25430E-01  0.21900E-02
      CHEB Polynomials:     -0.37434E+00  0.17467E+00  0.24900E-02 -0.32900E-02
      CHEB Polynomials:      0.19335E+00 -0.60050E-01 -0.97700E-02  0.97000E-03
      CHEB Polynomials:     -0.84110E-01  0.77700E-02  0.60100E-02  0.61000E-03
      CHEB Polynomials:      0.28920E-01  0.61700E-02 -0.15100E-02 -0.65000E-03
      CHEB Polynomials:     -0.54100E-02 -0.56700E-02 -0.39000E-03  0.17000E-03
316.  C6H10O3(1316)(+m)=>C6H9O3J(1328)+H(17)(+m)     1.00E+00    0.0        0.0
      Tmin, Tmax:     0.30000E+03  0.15000E+04
      Pmin, Pmax:     0.10000E+01  0.10000E+03
      CHEB Polynomials:      0.70000E+01  0.40000E+01
      CHEB Polynomials:     -0.25217E+02  0.47448E+00 -0.58540E-01  0.48300E-02
      CHEB Polynomials:     -0.24499E+02 -0.46148E+00 -0.15600E-01  0.11240E-01
      CHEB Polynomials:     -0.56912E+00  0.11617E+00  0.34220E-01 -0.12400E-02
      CHEB Polynomials:      0.17589E+00  0.25750E-01 -0.12290E-01 -0.42000E-02
      CHEB Polynomials:      0.22300E-02 -0.39740E-01 -0.49000E-02  0.24800E-02
      CHEB Polynomials:     -0.48750E-01  0.17430E-01  0.73400E-02  0.30000E-03
      CHEB Polynomials:      0.38550E-01 -0.21000E-03 -0.31900E-02 -0.11400E-02
317.  C3H5J(285)+o2(2)(+m)=>HO2(30)+C3H4(8)(+m)      1.00E+00    0.0        0.0
      Tmin, Tmax:     0.30000E+03  0.15000E+04
      Pmin, Pmax:     0.10000E+01  0.10000E+03
      CHEB Polynomials:      0.70000E+01  0.40000E+01
      CHEB Polynomials:      0.55054E+01 -0.12599E+00 -0.46000E-01 -0.87100E-02
      CHEB Polynomials:     -0.40882E+01 -0.14716E+00 -0.50580E-01 -0.77600E-02
      CHEB Polynomials:      0.71870E-01 -0.10000E-01  0.24000E-03  0.21500E-02
      CHEB Polynomials:     -0.14810E-01  0.14010E-01  0.55200E-02  0.11200E-02
      CHEB Polynomials:      0.56200E-02 -0.23000E-02 -0.15500E-02 -0.71000E-03
      CHEB Polynomials:     -0.30800E-02 -0.14600E-02 -0.43000E-03  0.15485E-04
      CHEB Polynomials:      0.13900E-02  0.10000E-02  0.48000E-03  0.15000E-03
318.  C2H6(7)(+m)=>C2H5(24)+H(17)(+m)                1.00E+00    0.0        0.0
      Tmin, Tmax:     0.30000E+03  0.15000E+04
      Pmin, Pmax:     0.10000E+01  0.10000E+03
      CHEB Polynomials:      0.70000E+01  0.40000E+01
      CHEB Polynomials:     -0.28212E+02  0.45446E+00 -0.92270E-01  0.52200E-02
      CHEB Polynomials:     -0.29101E+02 -0.17138E+00 -0.17740E-01  0.69000E-02
      CHEB Polynomials:     -0.22328E+00  0.91900E-01  0.93000E-02 -0.21900E-02
      CHEB Polynomials:      0.11292E+00 -0.29730E-01 -0.54900E-02 -0.48616E-04
      CHEB Polynomials:     -0.48990E-01  0.74500E-02  0.22300E-02  0.25000E-03
```

```
         CHEB Polynomials:     0.20750E-01 -0.46000E-03 -0.55000E-03 -0.16000E-03
         CHEB Polynomials:    -0.74300E-02 -0.19000E-03  0.93688E-04  0.29055E-04
319.  ch3cho(36)(+m)=>HCO(31)+CH3(21)(+m)          1.00E+00     0.0         0.0
      Tmin, Tmax:    0.30000E+03  0.15000E+04
      Pmin, Pmax:    0.10000E+01  0.10000E+03
         CHEB Polynomials:     0.70000E+01  0.40000E+01
         CHEB Polynomials:    -0.20292E+02  0.12837E+00 -0.20590E-01  0.19000E-02
         CHEB Polynomials:    -0.24132E+02 -0.19604E+00  0.22510E-01  0.13000E-03
         CHEB Polynomials:    -0.24805E+00  0.11134E+00 -0.49800E-02 -0.16000E-02
         CHEB Polynomials:     0.12237E+00 -0.48120E-01 -0.24700E-02  0.97000E-03
         CHEB Polynomials:    -0.57650E-01  0.15060E-01  0.29100E-02 -0.95461E-04
         CHEB Polynomials:     0.24910E-01 -0.24800E-02 -0.13600E-02 -0.21000E-03
         CHEB Polynomials:    -0.98000E-02 -0.60000E-03  0.26000E-03  0.15000E-03
320.  CH3(21)+C2H4(6)(+m)=>C3H7J(47)(+m)           1.00E+00     0.0         0.0
      Tmin, Tmax:    0.30000E+03  0.15000E+04
      Pmin, Pmax:    0.10000E+01  0.10000E+03
         CHEB Polynomials:     0.70000E+01  0.40000E+01
         CHEB Polynomials:     0.82027E+01  0.19762E+00 -0.23390E-01  0.12900E-02
         CHEB Polynomials:    -0.25310E+01 -0.31028E+00  0.25090E-01  0.12200E-02
         CHEB Polynomials:    -0.33740E+00  0.17154E+00 -0.14200E-02 -0.25500E-02
         CHEB Polynomials:     0.18665E+00 -0.65640E-01 -0.73800E-02  0.11500E-02
         CHEB Polynomials:    -0.85420E-01  0.12970E-01  0.56700E-02  0.25000E-03
         CHEB Polynomials:     0.31050E-01  0.38100E-02 -0.19500E-02 -0.56000E-03
         CHEB Polynomials:    -0.71400E-02 -0.52700E-02 -0.91166E-04  0.28000E-03
321.  CH3(21)+C2H4(6)(+m)=>C3H6(9)+H(17)(+m)       1.00E+00     0.0         0.0
      Tmin, Tmax:    0.30000E+03  0.15000E+04
      Pmin, Pmax:    0.10000E+01  0.10000E+03
         CHEB Polynomials:     0.70000E+01  0.40000E+01
         CHEB Polynomials:     0.45755E+01 -0.63381E+00 -0.37820E-01  0.21200E-02
         CHEB Polynomials:    -0.51151E+01 -0.47199E+00  0.12030E-01  0.57100E-02
         CHEB Polynomials:     0.18513E+00  0.16215E+00  0.22720E-01 -0.29100E-02
         CHEB Polynomials:     0.38950E-01 -0.83500E-02 -0.16490E-01 -0.16000E-02
         CHEB Polynomials:    -0.32880E-01 -0.22990E-01  0.30200E-02  0.18500E-02
         CHEB Polynomials:     0.10470E-01  0.15040E-01  0.20600E-02 -0.51000E-03
         CHEB Polynomials:    -0.60000E-03 -0.52700E-02 -0.19600E-02 -0.13000E-03
322.  C2H5(24)+o2(2)(+m)=>C2H4(6)+HO2(30)(+m)      1.00E+00     0.0         0.0
      Tmin, Tmax:    0.30000E+03  0.15000E+04
      Pmin, Pmax:    0.10000E+01  0.10000E+03
         CHEB Polynomials:     0.70000E+01  0.40000E+01
         CHEB Polynomials:     0.94271E+01 -0.54491E+00 -0.40150E-01  0.14000E-02
         CHEB Polynomials:    -0.15526E+01 -0.47248E+00 -0.71000E-02  0.54600E-02
         CHEB Polynomials:     0.14202E+00  0.10286E+00  0.23620E-01  0.37000E-03
         CHEB Polynomials:     0.29590E-01  0.17220E-01 -0.73600E-02 -0.19100E-02
         CHEB Polynomials:    -0.15200E-01 -0.22380E-01 -0.13900E-02  0.57000E-03
         CHEB Polynomials:     0.31000E-03  0.91400E-02  0.20000E-02  0.97632E-04
         CHEB Polynomials:     0.29800E-02 -0.18500E-02 -0.94000E-03 -0.12000E-03
323.  C7H13J(299)(+m)=>C7H12(724)+H(17)(+m)        1.00E+00     0.0         0.0
      Tmin, Tmax:    0.30000E+03  0.15000E+04
      Pmin, Pmax:    0.10000E+01  0.10000E+03
         CHEB Polynomials:     0.70000E+01  0.40000E+01
         CHEB Polynomials:    -0.17325E+01  0.66280E-01 -0.15840E-01  0.11600E-02
         CHEB Polynomials:    -0.96787E+01 -0.12349E+00  0.28930E-01 -0.19000E-02
         CHEB Polynomials:    -0.55230E+00  0.99350E-01 -0.21760E-01  0.88000E-03
         CHEB Polynomials:     0.54810E-01 -0.67790E-01  0.12790E-01  0.24000E-03
         CHEB Polynomials:    -0.35880E-01  0.37490E-01 -0.48700E-02 -0.97000E-03
         CHEB Polynomials:     0.17540E-01 -0.14680E-01 -0.22000E-03  0.10900E-02
         CHEB Polynomials:    -0.55800E-02  0.14300E-02  0.22400E-02 -0.74000E-03
324.  c7h14-1(38)(+m)=>C5H11J(48)+C2H3(23)(+m)     1.00E+00     0.0         0.0
      Tmin, Tmax:    0.30000E+03  0.15000E+04
      Pmin, Pmax:    0.10000E+01  0.10000E+03
         CHEB Polynomials:     0.70000E+01  0.40000E+01
         CHEB Polynomials:    -0.26448E+02  0.64500E-01 -0.11090E-01  0.57000E-03
         CHEB Polynomials:    -0.28509E+02 -0.12237E+00  0.20510E-01 -0.92000E-03
         CHEB Polynomials:    -0.28730E+00  0.10425E+00 -0.16070E-01  0.38000E-03
         CHEB Polynomials:     0.13926E+00 -0.79180E-01  0.10270E-01  0.23000E-03
         CHEB Polynomials:    -0.81700E-01  0.52680E-01 -0.46900E-02 -0.63000E-03
         CHEB Polynomials:     0.49470E-01 -0.29480E-01  0.48000E-03  0.72000E-03
         CHEB Polynomials:    -0.27930E-01  0.12410E-01  0.19000E-03 -0.56000E-03
325.  c7h14-1(38)(+m)=>C4H9J(46)+C3H5J(285)(+m)    1.00E+00     0.0         0.0
      Tmin, Tmax:    0.30000E+03  0.15000E+04
      Pmin, Pmax:    0.10000E+01  0.10000E+03
```

```
          CHEB Polynomials:     0.70000E+01  0.40000E+01
          CHEB Polynomials:    -0.15669E+02  0.20410E-01 -0.43900E-02  0.38000E-03
          CHEB Polynomials:    -0.21274E+02 -0.39480E-01  0.84100E-02 -0.70000E-03
          CHEB Polynomials:    -0.12951E+00  0.35700E-01 -0.73700E-02  0.55000E-03
          CHEB Polynomials:     0.54990E-01 -0.30120E-01  0.58600E-02 -0.35000E-03
          CHEB Polynomials:    -0.32120E-01  0.23630E-01 -0.41700E-02  0.13000E-03
          CHEB Polynomials:     0.21310E-01 -0.17150E-01  0.25700E-02  0.52468E-04
          CHEB Polynomials:    -0.14300E-01  0.11420E-01 -0.12800E-02 -0.17000E-03
 326. C3H5J(285)(+m)=>H(17)+C3H4(8)(+m)               1.00E+00     0.0          0.0
          Tmin, Tmax:     0.30000E+03  0.15000E+04
          Pmin, Pmax:     0.10000E+01  0.10000E+03
          CHEB Polynomials:     0.70000E+01  0.40000E+01
          CHEB Polynomials:    -0.13059E+02  0.37340E-01 -0.83200E-02  0.62000E-03
          CHEB Polynomials:    -0.17848E+02 -0.70380E-01  0.15300E-01 -0.10100E-02
          CHEB Polynomials:    -0.18620E-01  0.58940E-01 -0.11840E-01  0.46000E-03
          CHEB Polynomials:     0.35340E-01 -0.43800E-01  0.75100E-02  0.12000E-03
          CHEB Polynomials:    -0.29790E-01  0.28720E-01 -0.35800E-02 -0.50000E-03
          CHEB Polynomials:     0.19960E-01 -0.16380E-01  0.83000E-03  0.59000E-03
          CHEB Polynomials:    -0.11190E-01  0.78500E-02  0.60000E-03 -0.46000E-03
 327. C7H13O2J(734)(+m)=>C7H12(724)+HO2(30)(+m)       1.00E+00     0.0          0.0
          Tmin, Tmax:     0.30000E+03  0.15000E+04
          Pmin, Pmax:     0.10000E+01  0.10000E+03
          CHEB Polynomials:     0.70000E+01  0.40000E+01
          CHEB Polynomials:    -0.82178E+00  0.37408E+00 -0.36180E-01  0.49000E-03
          CHEB Polynomials:    -0.83131E+01 -0.49948E+00  0.19680E-01  0.61200E-02
          CHEB Polynomials:    -0.27921E+00  0.14171E+00  0.20980E-01 -0.40800E-02
          CHEB Polynomials:     0.19270E-01  0.38150E-01 -0.15520E-01 -0.15300E-02
          CHEB Polynomials:     0.68530E-01 -0.49840E-01 -0.12500E-02  0.23600E-02
          CHEB Polynomials:    -0.43310E-01  0.10630E-01  0.58500E-02 -0.29000E-03
          CHEB Polynomials:     0.44000E-03  0.11110E-01 -0.19300E-02 -0.77000E-03
 328. c7h14-3(40)(+m)=>C7H13J(294)+H(17)(+m)          1.00E+00     0.0          0.0
          Tmin, Tmax:     0.30000E+03  0.15000E+04
          Pmin, Pmax:     0.10000E+01  0.10000E+03
          CHEB Polynomials:     0.70000E+01  0.40000E+01
          CHEB Polynomials:    -0.28030E+02  0.61560E-01 -0.11560E-01  0.63000E-03
          CHEB Polynomials:    -0.29248E+02 -0.11698E+00  0.21460E-01 -0.10300E-02
          CHEB Polynomials:    -0.10844E+00  0.10020E+00 -0.17040E-01  0.46000E-03
          CHEB Polynomials:     0.87570E-01 -0.76870E-01  0.11190E-01  0.18000E-03
          CHEB Polynomials:    -0.63690E-01  0.52050E-01 -0.54600E-02 -0.65000E-03
          CHEB Polynomials:     0.42230E-01 -0.30080E-01  0.10000E-02  0.81000E-03
          CHEB Polynomials:    -0.24790E-01  0.13620E-01  0.16800E-02 -0.70000E-03
 329. c7h14-3(40)(+m)=>C7H13J(299)+H(17)(+m)          1.00E+00     0.0          0.0
          Tmin, Tmax:     0.30000E+03  0.15000E+04
          Pmin, Pmax:     0.10000E+01  0.10000E+03
          CHEB Polynomials:     0.70000E+01  0.40000E+01
          CHEB Polynomials:    -0.28030E+02  0.61560E-01 -0.11560E-01  0.63000E-03
          CHEB Polynomials:    -0.29248E+02 -0.11698E+00  0.21460E-01 -0.10300E-02
          CHEB Polynomials:    -0.10844E+00  0.10020E+00 -0.17040E-01  0.46000E-03
          CHEB Polynomials:     0.87570E-01 -0.76870E-01  0.11190E-01  0.18000E-03
          CHEB Polynomials:    -0.63690E-01  0.52050E-01 -0.54600E-02 -0.65000E-03
          CHEB Polynomials:     0.42230E-01 -0.30080E-01  0.10000E-02  0.81000E-03
          CHEB Polynomials:    -0.24790E-01  0.13620E-01  0.16800E-02 -0.70000E-03
 330. C5H11J(48)(+m)=>C3H7J(47)+C2H4(6)(+m)           1.00E+00     0.0          0.0
          Tmin, Tmax:     0.30000E+03  0.15000E+04
          Pmin, Pmax:     0.10000E+01  0.10000E+03
          CHEB Polynomials:     0.70000E+01  0.40000E+01
          CHEB Polynomials:     0.10073E+01  0.22973E+00 -0.18720E-01  0.64640E-04
          CHEB Polynomials:    -0.87402E+01 -0.37428E+00  0.23020E-01  0.13000E-02
          CHEB Polynomials:    -0.56719E+00  0.19921E+00 -0.39000E-03 -0.20600E-02
          CHEB Polynomials:     0.23528E+00 -0.55240E-01 -0.87600E-02  0.71000E-03
          CHEB Polynomials:    -0.62900E-01 -0.95500E-02  0.53000E-02  0.59000E-03
          CHEB Polynomials:    -0.51200E-02  0.17620E-01 -0.60071E-04 -0.58000E-03
          CHEB Polynomials:     0.16380E-01 -0.72300E-02 -0.15600E-02  0.29691E-04
 331. C4H2(10)(+m)=>C2H(22)+C2H(22)(+m)               1.00E+00     0.0          0.0
          Tmin, Tmax:     0.30000E+03  0.15000E+04
          Pmin, Pmax:     0.10000E+01  0.10000E+03
          CHEB Polynomials:     0.70000E+01  0.40000E+01
          CHEB Polynomials:    -0.54793E+02  0.58905E+00 -0.86300E-01  0.48585E-04
          CHEB Polynomials:    -0.46509E+02 -0.33067E+00 -0.37700E-01  0.12540E-01
          CHEB Polynomials:    -0.47253E+00  0.54840E-01  0.28310E-01  0.31500E-02
          CHEB Polynomials:     0.15849E+00  0.39800E-02 -0.58700E-02 -0.37000E-02
```

```
       CHEB Polynomials:     -0.53480E-01 -0.74400E-02 -0.12800E-02  0.99000E-03
       CHEB Polynomials:      0.17320E-01  0.31400E-02  0.14600E-02  0.17000E-03
       CHEB Polynomials:     -0.51700E-02 -0.64000E-03 -0.59000E-03 -0.25000E-03
332. C6H10O3(1317)(+m)=>C6H9O3J(1329)+H(17)(+m)      1.00E+00     0.0         0.0
       Tmin, Tmax:    0.30000E+03  0.15000E+04
       Pmin, Pmax:    0.10000E+01  0.10000E+03
       CHEB Polynomials:      0.70000E+01  0.40000E+01
       CHEB Polynomials:     -0.25201E+02  0.46225E+00 -0.55880E-01  0.46800E-02
       CHEB Polynomials:     -0.24503E+02 -0.46858E+00 -0.11930E-01  0.10780E-01
       CHEB Polynomials:     -0.56783E+00  0.12171E+00  0.33440E-01 -0.16900E-03
       CHEB Polynomials:      0.17163E+00  0.26260E-01 -0.13190E-01 -0.39600E-02
       CHEB Polynomials:      0.58700E-02 -0.41390E-01 -0.45000E-02  0.26000E-02
       CHEB Polynomials:     -0.50540E-01  0.18090E-01  0.74400E-02  0.17000E-03
       CHEB Polynomials:      0.38280E-01 -0.52595E-04 -0.33300E-02 -0.11100E-02
333. C6H13J(43)(+m)=>C4H9J(46)+C2H4(6)(+m)           1.00E+00     0.0         0.0
       Tmin, Tmax:    0.30000E+03  0.15000E+04
       Pmin, Pmax:    0.10000E+01  0.10000E+03
       CHEB Polynomials:      0.70000E+01  0.40000E+01
       CHEB Polynomials:      0.11093E+01  0.19887E+00 -0.19920E-01 -0.54147E-04
       CHEB Polynomials:     -0.89127E+01 -0.33264E+00  0.27980E-01  0.11900E-02
       CHEB Polynomials:     -0.46199E+00  0.19078E+00 -0.63000E-02 -0.21400E-02
       CHEB Polynomials:      0.19438E+00 -0.63940E-01 -0.64500E-02  0.13300E-02
       CHEB Polynomials:     -0.60590E-01  0.43000E-03  0.63400E-02  0.12000E-03
       CHEB Polynomials:      0.92800E-02  0.10900E-01 -0.14800E-02 -0.62000E-03
       CHEB Polynomials:     -0.20000E-03 -0.31500E-02 -0.10700E-02  0.20000E-03
334. C7H15J(41)(+m)=>c7h14-2(39)+H(17)(+m)           1.00E+00     0.0         0.0
       Tmin, Tmax:    0.30000E+03  0.15000E+04
       Pmin, Pmax:    0.10000E+01  0.10000E+03
       CHEB Polynomials:      0.70000E+01  0.40000E+01
       CHEB Polynomials:     -0.32084E+01  0.21411E+00 -0.16660E-01 -0.30000E-03
       CHEB Polynomials:     -0.97416E+01 -0.37047E+00  0.24590E-01  0.11900E-02
       CHEB Polynomials:     -0.43463E+00  0.23340E+00 -0.63700E-02 -0.19400E-02
       CHEB Polynomials:      0.24176E+00 -0.92260E-01 -0.69700E-02  0.15000E-02
       CHEB Polynomials:     -0.83250E-01  0.24900E-02  0.90500E-02 -0.17000E-03
       CHEB Polynomials:     -0.25300E-02  0.27360E-01 -0.40900E-02 -0.75000E-03
       CHEB Polynomials:      0.27920E-01 -0.20930E-01 -0.75000E-03  0.67000E-03
335. C7H15J(41)(+m)=>c7h14-1(38)+H(17)(+m)           1.00E+00     0.0         0.0
       Tmin, Tmax:    0.30000E+03  0.15000E+04
       Pmin, Pmax:    0.10000E+01  0.10000E+03
       CHEB Polynomials:      0.70000E+01  0.40000E+01
       CHEB Polynomials:     -0.36618E+01  0.22757E+00 -0.17730E-01 -0.25000E-03
       CHEB Polynomials:     -0.10360E+02 -0.38957E+00  0.25210E-01  0.12900E-02
       CHEB Polynomials:     -0.43693E+00  0.23691E+00 -0.46300E-02 -0.22100E-02
       CHEB Polynomials:      0.23921E+00 -0.85090E-01 -0.91500E-02  0.15800E-02
       CHEB Polynomials:     -0.74600E-01 -0.58700E-02  0.98600E-02  0.13520E-04
       CHEB Polynomials:     -0.10580E-01  0.31450E-01 -0.35700E-02 -0.95000E-03
       CHEB Polynomials:      0.31710E-01 -0.20960E-01 -0.14900E-02  0.69000E-03
336. C7H15J(41)(+m)=>C3H6(9)+C4H9J(46)(+m)           1.00E+00     0.0         0.0
       Tmin, Tmax:    0.30000E+03  0.15000E+04
       Pmin, Pmax:    0.10000E+01  0.10000E+03
       CHEB Polynomials:      0.70000E+01  0.40000E+01
       CHEB Polynomials:      0.97880E+00  0.20676E+00 -0.16090E-01 -0.32000E-03
       CHEB Polynomials:     -0.87823E+01 -0.35969E+00  0.24190E-01  0.11500E-02
       CHEB Polynomials:     -0.54647E+00  0.23075E+00 -0.71900E-02 -0.18100E-02
       CHEB Polynomials:      0.27256E+00 -0.95580E-01 -0.58100E-02  0.14400E-02
       CHEB Polynomials:     -0.96540E-01  0.69100E-02  0.85200E-02 -0.24000E-03
       CHEB Polynomials:      0.42500E-02  0.24940E-01 -0.42800E-02 -0.66000E-03
       CHEB Polynomials:      0.24950E-01 -0.20690E-01 -0.36000E-03  0.65000E-03
337. C7H13J(299)+o2(2)(+m)                           1.00E+00     0.0         0.0
       =>C7H12(724)+HO2(30)(+m)
       Tmin, Tmax:    0.30000E+03  0.15000E+04
       Pmin, Pmax:    0.10000E+01  0.10000E+03
       CHEB Polynomials:      0.70000E+01  0.40000E+01
       CHEB Polynomials:      0.78493E+01 -0.74034E+00 -0.23300E-01 -0.77000E-03
       CHEB Polynomials:     -0.32881E+01 -0.42845E+00  0.31470E-01  0.25200E-02
       CHEB Polynomials:      0.17472E+00  0.22596E+00 -0.23600E-02 -0.33600E-02
       CHEB Polynomials:      0.22567E+00 -0.46010E-01 -0.14200E-01  0.18700E-02
       CHEB Polynomials:     -0.11533E+00 -0.35580E-01  0.11360E-01  0.56000E-03
       CHEB Polynomials:      0.41200E-02  0.35150E-01 -0.14200E-02 -0.14600E-02
       CHEB Polynomials:      0.30720E-01 -0.81000E-02 -0.35300E-02  0.66000E-03
338. H2O2(12)(+m)=>HO2(30)+H(17)(+m)                 1.00E+00     0.0         0.0
```

```
            Tmin, Tmax:    0.30000E+03  0.15000E+04
            Pmin, Pmax:    0.10000E+01  0.10000E+03
            CHEB Polynomials:    0.70000E+01  0.40000E+01
            CHEB Polynomials:   -0.27353E+02  0.99972E+00 -0.13000E-03 -0.46969E-04
            CHEB Polynomials:   -0.24288E+02 -0.23000E-03 -0.11000E-03 -0.37735E-04
            CHEB Polynomials:   -0.16262E+00  0.88775E-05  0.42695E-05  0.14906E-05
            CHEB Polynomials:    0.55190E-01  0.12265E-05  0.58582E-06  0.20305E-06
            CHEB Polynomials:   -0.18150E-01 -0.11094E-05 -0.53078E-06 -0.18450E-06
            CHEB Polynomials:    0.63600E-02  0.45583E-06  0.21742E-06  0.75620E-07
            CHEB Polynomials:   -0.24100E-02 -0.15079E-06 -0.71059E-07 -0.24725E-07
339. C7H15J(44)(+m)=>c7h14-3(40)+H(17)(+m)          1.00E+00     0.0          0.0
            Tmin, Tmax:    0.30000E+03  0.15000E+04
            Pmin, Pmax:    0.10000E+01  0.10000E+03
            CHEB Polynomials:    0.70000E+01  0.40000E+01
            CHEB Polynomials:   -0.28985E+01  0.23761E+00 -0.16760E-01 -0.36000E-03
            CHEB Polynomials:   -0.97145E+01 -0.40135E+00  0.23120E-01  0.13400E-02
            CHEB Polynomials:   -0.46446E+00  0.23215E+00 -0.27300E-02 -0.19300E-02
            CHEB Polynomials:    0.23402E+00 -0.71520E-01 -0.96200E-02  0.11000E-02
            CHEB Polynomials:   -0.61660E-01 -0.14560E-01  0.85200E-02  0.34000E-03
            CHEB Polynomials:   -0.13530E-01  0.29440E-01 -0.17700E-02 -0.86000E-03
            CHEB Polynomials:    0.22430E-01 -0.12910E-01 -0.21300E-02  0.36000E-03
340. C3H6(9)(+m)=>C3H5J(285)+H(17)(+m)              1.00E+00     0.0          0.0
            Tmin, Tmax:    0.30000E+03  0.15000E+04
            Pmin, Pmax:    0.10000E+01  0.10000E+03
            CHEB Polynomials:    0.70000E+01  0.40000E+01
            CHEB Polynomials:   -0.23716E+02  0.14560E-01 -0.27200E-02  0.22000E-03
            CHEB Polynomials:   -0.25663E+02 -0.27810E-01  0.51200E-02 -0.40000E-03
            CHEB Polynomials:    0.19020E-01  0.24190E-01 -0.42400E-02  0.28000E-03
            CHEB Polynomials:    0.10720E-01 -0.19130E-01  0.30600E-02 -0.14000E-03
            CHEB Polynomials:   -0.13670E-01  0.13710E-01 -0.18700E-02  0.20924E-04
            CHEB Polynomials:    0.10850E-01 -0.88400E-02  0.91000E-03  0.52786E-04
            CHEB Polynomials:   -0.72900E-02  0.50500E-02 -0.27000E-03 -0.77146E-04
341. C3H6(9)(+m)=>C2H3(23)+CH3(21)(+m)              1.00E+00     0.0          0.0
            Tmin, Tmax:    0.30000E+03  0.15000E+04
            Pmin, Pmax:    0.10000E+01  0.10000E+03
            CHEB Polynomials:    0.70000E+01  0.40000E+01
            CHEB Polynomials:   -0.26766E+02  0.62210E-01 -0.10370E-01  0.69000E-03
            CHEB Polynomials:   -0.29392E+02 -0.11307E+00  0.17750E-01 -0.91000E-03
            CHEB Polynomials:   -0.18830E+00  0.85640E-01 -0.11090E-01  0.54451E-04
            CHEB Polynomials:    0.96520E-01 -0.54220E-01  0.45300E-02  0.51000E-03
            CHEB Polynomials:   -0.52600E-01  0.28330E-01 -0.35000E-03 -0.55000E-03
            CHEB Polynomials:    0.28050E-01 -0.11660E-01 -0.12200E-02  0.30000E-03
            CHEB Polynomials:   -0.13650E-01  0.32000E-02  0.11800E-02 -0.28336E-04
342. C4H9J(46)(+m)=>C2H4(6)+C2H5(24)(+m)            1.00E+00     0.0          0.0
            Tmin, Tmax:    0.30000E+03  0.15000E+04
            Pmin, Pmax:    0.10000E+01  0.10000E+03
            CHEB Polynomials:    0.70000E+01  0.40000E+01
            CHEB Polynomials:    0.90976E+00  0.26462E+00 -0.21980E-01  0.92000E-03
            CHEB Polynomials:   -0.85821E+01 -0.39696E+00  0.17170E-01  0.19400E-02
            CHEB Polynomials:   -0.65574E+00  0.18609E+00  0.72900E-02 -0.19900E-02
            CHEB Polynomials:    0.29173E+00 -0.45950E-01 -0.99100E-02 -0.83163E-04
            CHEB Polynomials:   -0.10140E+00 -0.60100E-02  0.34900E-02  0.78000E-03
            CHEB Polynomials:    0.18090E-01  0.12040E-01  0.53000E-03 -0.30000E-03
            CHEB Polynomials:    0.82600E-02 -0.64400E-02 -0.10200E-02 -0.80793E-04
343. C3H7J(47)+o2(2)(+m)=>C3H6(9)+HO2(30)(+m)       1.00E+00     0.0          0.0
            Tmin, Tmax:    0.30000E+03  0.15000E+04
            Pmin, Pmax:    0.10000E+01  0.10000E+03
            CHEB Polynomials:    0.70000E+01  0.40000E+01
            CHEB Polynomials:    0.86388E+01 -0.64639E+00 -0.27260E-01  0.61000E-03
            CHEB Polynomials:   -0.20633E+01 -0.49576E+00  0.15050E-01  0.33200E-03
            CHEB Polynomials:    0.16148E+00  0.17119E+00  0.18770E-01 -0.24200E-02
            CHEB Polynomials:    0.88880E-01  0.36700E-02 -0.14780E-01 -0.11100E-02
            CHEB Polynomials:   -0.44380E-01 -0.36210E-01  0.15100E-02  0.15100E-02
            CHEB Polynomials:    0.39300E-02  0.19020E-01  0.32300E-02 -0.28000E-03
            CHEB Polynomials:    0.73300E-02 -0.32000E-02 -0.20700E-02 -0.28000E-03
344. C2H4(6)+C2H5(24)(+m)=>C4H9J(46)(+m)            1.00E+00     0.0          0.0
            Tmin, Tmax:    0.30000E+03  0.15000E+04
            Pmin, Pmax:    0.10000E+01  0.10000E+03
            CHEB Polynomials:    0.70000E+01  0.40000E+01
            CHEB Polynomials:    0.80842E+01  0.26533E+00 -0.21890E-01  0.91000E-03
            CHEB Polynomials:   -0.24953E+01 -0.39701E+00  0.17040E-01  0.19100E-02
```

```
       CHEB Polynomials:     -0.53959E+00  0.18531E+00  0.71500E-02 -0.19700E-02
       CHEB Polynomials:      0.26132E+00 -0.45930E-01 -0.97700E-02 -0.37186E-04
       CHEB Polynomials:     -0.92220E-01 -0.56800E-02  0.35500E-02  0.75000E-03
       CHEB Polynomials:      0.15260E-01  0.11990E-01  0.43000E-03 -0.34000E-03
       CHEB Polynomials:      0.92200E-02 -0.65000E-02 -0.10400E-02 -0.62102E-04
 345. C3H3O2J(478)(+m)=>H2CCCH(26)+o2(2)(+m)          1.00E+00     0.0          0.0
       Tmin, Tmax:    0.30000E+03  0.15000E+04
       Pmin, Pmax:    0.10000E+01  0.10000E+03
       CHEB Polynomials:      0.70000E+01  0.40000E+01
       CHEB Polynomials:      0.54439E+01  0.56564E+00 -0.47490E-01  0.76000E-03
       CHEB Polynomials:     -0.41732E+01 -0.33389E+00 -0.26210E-01  0.35800E-02
       CHEB Polynomials:     -0.55438E+00  0.63280E-01  0.10090E-01  0.10900E-02
       CHEB Polynomials:      0.14902E+00  0.42000E-02 -0.16100E-02 -0.39000E-03
       CHEB Polynomials:     -0.16290E-01 -0.85500E-02 -0.58000E-03  0.24024E-04
       CHEB Polynomials:     -0.12400E-01  0.36700E-02  0.52000E-03  0.33725E-04
       CHEB Polynomials:      0.10250E-01 -0.59000E-03 -0.19000E-03 -0.21641E-04
 346. C3H4(8)+HCO(31)=H2CCCH(26)+CH2O(15)             2.08E+04     2.8         28.6
 347. H2CCCH(26)+o2(2)(+m)=>C3H3O2J(478)(+m)          1.00E+00     0.0          0.0
       Tmin, Tmax:    0.30000E+03  0.15000E+04
       Pmin, Pmax:    0.10000E+01  0.10000E+03
       CHEB Polynomials:      0.70000E+01  0.40000E+01
       CHEB Polynomials:      0.10590E+02  0.56564E+00 -0.47490E-01  0.76000E-03
       CHEB Polynomials:      0.17956E+00 -0.33389E+00 -0.26210E-01  0.35800E-02
       CHEB Polynomials:     -0.45624E+00  0.63280E-01  0.10090E-01  0.10900E-02
       CHEB Polynomials:      0.12393E+00  0.42000E-02 -0.16100E-02 -0.39000E-03
       CHEB Polynomials:     -0.90500E-02 -0.85500E-02 -0.58000E-03  0.24051E-04
       CHEB Polynomials:     -0.14650E-01  0.36700E-02  0.52000E-03  0.33713E-04
       CHEB Polynomials:      0.10980E-01 -0.59000E-03 -0.19000E-03 -0.21636E-04
 348. C3H4(8)+HCCO(34)=H2CCCH(26)+CH2CO(16)           5.88E+13     0.0         20.2
 349. C7H12(724)+C2H(22)=C7H11J(783)+C2H2(5)          1.21E+12     0.0          0.0
 350. CH2HCO(35)+o2(2)(+m)=>CH2CO(16)+HO2(30)(+m)     1.00E+00     0.0          0.0
       Tmin, Tmax:    0.30000E+03  0.15000E+04
       Pmin, Pmax:    0.10000E+01  0.10000E+03
       CHEB Polynomials:      0.70000E+01  0.40000E+01
       CHEB Polynomials:      0.50685E+01 -0.25010E-01 -0.11410E-01 -0.35900E-02
       CHEB Polynomials:     -0.43425E+01 -0.27410E-01 -0.12360E-01 -0.37900E-02
       CHEB Polynomials:      0.10103E+00 -0.98000E-03 -0.30000E-03 -0.28092E-05
       CHEB Polynomials:     -0.24000E-01  0.24400E-02  0.11100E-02  0.35000E-03
       CHEB Polynomials:      0.68300E-02 -0.53000E-03 -0.27000E-03 -0.10000E-03
       CHEB Polynomials:     -0.22200E-02 -0.17000E-03 -0.72653E-04 -0.17874E-04
       CHEB Polynomials:      0.77000E-03  0.16000E-03  0.76038E-04  0.25619E-04
 351. OH(29)+HCCO(34)=CH2O(15)+CO(13)                 1.00E+13     0.0          0.0
 352. C4H2(10)+OH(29)=C3H2(25)+HCO(31)                6.68E+12     0.0         -0.4
 353. o2(2)+HCCO(34)=CO(13)+CO(13)+OH(29)             1.63E+12     0.0          0.9
 354. ch3cho(36)+C3H2(25)=>CH2HCO(35)+H2CCCH(26)      3.02E+13     0.0          9.2
 355. ch3cho(36)(+m)=>CH2HCO(35)+H(17)(+m)            1.00E+00     0.0          0.0
       Tmin, Tmax:    0.30000E+03  0.15000E+04
       Pmin, Pmax:    0.10000E+01  0.10000E+03
       CHEB Polynomials:      0.70000E+01  0.40000E+01
       CHEB Polynomials:     -0.23955E+02  0.15373E+00 -0.26140E-01  0.28400E-02
       CHEB Polynomials:     -0.25437E+02 -0.22046E+00  0.24160E-01  0.52000E-03
       CHEB Polynomials:     -0.17201E+00  0.11821E+00 -0.34200E-02 -0.20100E-02
       CHEB Polynomials:      0.10613E+00 -0.47660E-01 -0.37100E-02  0.92000E-03
       CHEB Polynomials:     -0.52340E-01  0.13340E-01  0.32000E-02  0.73418E-04
       CHEB Polynomials:      0.22810E-01 -0.15200E-02 -0.11900E-02 -0.28000E-03
       CHEB Polynomials:     -0.87200E-02 -0.81000E-03  0.55192E-04  0.13000E-03
 356. C3H4(8)+CH3(21)=H2CCCH(26)+CH4(4)               1.30E+04     2.6         14.0
 357. C6H9OJ(961)+HO2(30)(+m)                         1.00E+00     0.0          0.0
       =>C6H9O3J(1328)+H(17)(+m)
       Tmin, Tmax:    0.30000E+03  0.15000E+04
       Pmin, Pmax:    0.10000E+01  0.10000E+03
       CHEB Polynomials:      0.70000E+01  0.40000E+01
       CHEB Polynomials:     -0.88851E+01 -0.47922E+00 -0.57450E-01  0.43800E-02
       CHEB Polynomials:     -0.13292E+02 -0.47279E+00 -0.26700E-01  0.10670E-01
       CHEB Polynomials:      0.72570E-01  0.80590E-01  0.35930E-01  0.14000E-02
       CHEB Polynomials:      0.51800E-01  0.47430E-01 -0.57600E-02 -0.49300E-02
       CHEB Polynomials:     -0.23080E-01 -0.38000E-01 -0.95000E-02  0.11600E-02
       CHEB Polynomials:     -0.89000E-03  0.82700E-02  0.70900E-02  0.14800E-02
       CHEB Polynomials:      0.60200E-02  0.51000E-02 -0.10600E-02 -0.12600E-02
 358. C6H9OJ(961)+HO2(30)(+m)                         1.00E+00     0.0          0.0
       =>C6H9O3J(1329)+H(17)(+m)
```

251

```
        Tmin, Tmax:   0.30000E+03  0.15000E+04
        Pmin, Pmax:   0.10000E+01  0.10000E+03
        CHEB Polynomials:   0.70000E+01  0.40000E+01
        CHEB Polynomials:  -0.76895E+01 -0.48087E+00 -0.55340E-01  0.42100E-02
        CHEB Polynomials:  -0.12181E+02 -0.48071E+00 -0.25380E-01  0.10290E-01
        CHEB Polynomials:   0.13174E+00  0.77090E-01  0.35890E-01  0.14000E-02
        CHEB Polynomials:   0.39550E-01  0.51670E-01 -0.52500E-02 -0.48900E-02
        CHEB Polynomials:  -0.18270E-01 -0.38140E-01 -0.99900E-02  0.10400E-02
        CHEB Polynomials:  -0.29600E-02  0.66800E-02  0.70000E-02  0.15700E-02
        CHEB Polynomials:   0.65000E-02  0.60700E-02 -0.73000E-03 -0.12400E-02
359. C2H4(6)+C3H2(25)=>C2H3(23)+H2CCCH(26)          1.18E+14    0.0      20.2
360. C3H4(8)(+m)=>H2CCCH(26)+H(17)(+m)              1.00E+00    0.0       0.0
        Tmin, Tmax:   0.30000E+03  0.15000E+04
        Pmin, Pmax:   0.10000E+01  0.10000E+03
        CHEB Polynomials:   0.70000E+01  0.40000E+01
        CHEB Polynomials:  -0.22242E+02  0.47980E-01 -0.98000E-02  0.69000E-03
        CHEB Polynomials:  -0.25182E+02 -0.88640E-01  0.17370E-01 -0.10100E-02
        CHEB Polynomials:  -0.63570E-01  0.70200E-01 -0.12060E-01  0.20000E-03
        CHEB Polynomials:   0.51090E-01 -0.47620E-01  0.61300E-02  0.49000E-03
        CHEB Polynomials:  -0.34870E-01  0.27320E-01 -0.15900E-02 -0.75000E-03
        CHEB Polynomials:   0.21140E-01 -0.12780E-01 -0.82000E-03  0.60000E-03
        CHEB Polynomials:  -0.10780E-01  0.44200E-02  0.14300E-02 -0.26000E-03
361. ch3cho(36)+CH2(19)=>CH2HCO(35)+CH3(21)         5.00E+05    2.3       3.7
362. C7H12(724)+C7H13J(297)                         3.04E+06    1.9       9.4
     =C7H11J(783)+c7h14-3(40)
363. C7H12(724)+C7H13J(297)                         3.04E+06    1.9       9.4
     =C7H11J(783)+c7h14-2(39)
364. C7H12(724)+C7H13J(299)                         3.04E+06    1.9       9.4
     =C7H11J(783)+c7h14-3(40)
365. C7H12(724)+C7H13J(294)                         3.04E+06    1.9       9.4
     =C7H11J(783)+c7h14-3(40)
366. C4H5OJ(664)(+m)=>C2H2(5)+CH2HCO(35)(+m)        1.00E+00    0.0       0.0
        Tmin, Tmax:   0.30000E+03  0.15000E+04
        Pmin, Pmax:   0.10000E+01  0.10000E+03
        CHEB Polynomials:   0.70000E+01  0.40000E+01
        CHEB Polynomials:   0.81510E+01  0.76729E+00 -0.48080E-01 -0.28000E-02
        CHEB Polynomials:  -0.16331E+01 -0.22425E+00 -0.42320E-01 -0.53000E-03
        CHEB Polynomials:  -0.42459E+00  0.19490E-01  0.50200E-02  0.11200E-02
        CHEB Polynomials:   0.13740E-01  0.17260E-01  0.22100E-02 -0.17000E-03
        CHEB Polynomials:   0.45090E-01 -0.65400E-02 -0.14400E-02 -0.14000E-03
        CHEB Polynomials:  -0.21730E-01 -0.94447E-04  0.23000E-03  0.38764E-04
        CHEB Polynomials:   0.22600E-02  0.87000E-03  0.14000E-03  0.14578E-04
367. C2H2(5)+CH2HCO(35)(+m)=>C4H5OJ(664)(+m)        1.00E+00    0.0       0.0
        Tmin, Tmax:   0.30000E+03  0.15000E+04
        Pmin, Pmax:   0.10000E+01  0.10000E+03
        CHEB Polynomials:   0.70000E+01  0.40000E+01
        CHEB Polynomials:   0.95934E+01  0.76729E+00 -0.48080E-01 -0.28000E-02
        CHEB Polynomials:   0.10341E+00 -0.22425E+00 -0.42320E-01 -0.53000E-03
        CHEB Polynomials:  -0.28688E+00  0.19490E-01  0.50200E-02  0.11200E-02
        CHEB Polynomials:  -0.21350E-01  0.17260E-01  0.22100E-02 -0.17000E-03
        CHEB Polynomials:   0.55150E-01 -0.65400E-02 -0.14400E-02 -0.14000E-03
        CHEB Polynomials:  -0.24810E-01 -0.94437E-04  0.23000E-03  0.38765E-04
        CHEB Polynomials:   0.32500E-02  0.87000E-03  0.14000E-03  0.14577E-04
368. H2O(11)+C3H2(25)=>OH(29)+H2CCCH(26)            9.68E+02    2.9      28.2
369. C3H4(8)+O(28)=>H2CCCH(26)+OH(29)               1.51E+07    1.9       8.9
370. CH2CO(16)+OH(29)=HCCO(34)+H2O(11)              1.03E+13    0.0       5.9
371. H2O2(12)+H2CCCH(26)=HO2(30)+C3H4(8)            2.88E+01    3.1       6.9
372. CH2CO(16)+m=HCCO(34)+H(17)+m                   1.14E+09    0.0       0.0
        H2O(11)         Enhanced by   6.500E+00
        C2H6(7)         Enhanced by   3.000E+00
        N2              Enhanced by   4.000E-01
        CH4(4)          Enhanced by   3.000E+00
        CO(13)          Enhanced by   7.500E-01
        Ar              Enhanced by   3.500E-01
        CO2(14)         Enhanced by   1.500E+00
        o2(2)           Enhanced by   4.000E-01
373. o2(2)+H2CCCH(26)=CH2CO(16)+HCO(31)             3.01E+10    0.0       2.9
374. C3H4(8)+CH2HCO(35)=ch3cho(36)+H2CCCH(26)       8.81E+13    0.0      25.7
375. C7H13J(297)+HO2(30)(+m)                        1.00E+00    0.0       0.0
     =>C7H13O2J(734)+H(17)(+m)
        Tmin, Tmax:   0.30000E+03  0.15000E+04
```

```
      Pmin, Pmax:    0.10000E+01  0.10000E+03
      CHEB Polynomials:    0.70000E+01  0.40000E+01
      CHEB Polynomials:   -0.63728E+01 -0.58753E+00 -0.36260E-01  0.26100E-02
      CHEB Polynomials:   -0.10941E+02 -0.53204E+00  0.53300E-02  0.59900E-02
      CHEB Polynomials:    0.29822E+00  0.14787E+00  0.33310E-01 -0.32800E-02
      CHEB Polynomials:    0.55000E-01  0.44030E-01 -0.18260E-01 -0.33600E-02
      CHEB Polynomials:   -0.37510E-01 -0.60840E-01 -0.53800E-02  0.34500E-02
      CHEB Polynomials:   -0.11000E-02  0.21090E-01  0.11000E-01  0.50825E-04
      CHEB Polynomials:    0.11360E-01  0.60200E-02 -0.45900E-02 -0.17100E-02
376. CH2O(15)+HCCO(34)=HCO(31)+CH2CO(16)            5.42E+03   2.8       5.9
377. C7H12(724)+C2H3(23)=C7H11J(783)+C2H4(6)        8.36E+12  -0.2       6.2
378. C2H2(5)+O(28)=HCCO(34)+H(17)                    5.06E+06   2.1       1.6
379. H2(3)+C3H2(25)=>H(17)+H2CCCH(26)                1.80E+13   0.0      10.3
380. C3H4(8)+C2H3(23)=H2CCCH(26)+C2H4(6)             5.88E+13   0.0      20.2
381. C3H4(8)+C7H15J(41)=nc7h16(1)+H2CCCH(26)         1.30E+13   0.0      20.2
382. C3H4(8)+C7H15J(42)=nc7h16(1)+H2CCCH(26)         1.30E+13   0.0      20.2
383. C3H4(8)+C7H15J(45)=nc7h16(1)+H2CCCH(26)         3.13E+13   0.0      19.7
384. C3H4(8)+C7H15J(44)=nc7h16(1)+H2CCCH(26)         1.30E+13   0.0      20.2
385. c7h14-3(40)+C3H5J(285)=C7H13J(297)+C3H6(9)      1.54E+13  -0.5      16.2
386. c7h14-2(39)+C3H5J(285)=C7H13J(297)+C3H6(9)      1.54E+13  -0.5      16.2
387. o2(2)+C3H2(25)=HCO(31)+HCCO(34)                 1.00E+13   0.0       0.0
388. H2(3)+HCCO(34)=H(17)+CH2CO(16)                  8.98E+12   0.0      10.3
389. C3H6(9)+HCCO(34)=CH2CO(16)+C3H5J(285)           2.32E+13   0.0       7.5
390. C3H6(9)+C3H2(25)=>H2CCCH(26)+C3H5J(285)         4.64E+13   0.0       7.5
391. C7H12(724)+CH2HCO(35)=C7H11J(783)+ch3cho(36)    3.04E+06   1.9       9.4
392. ch3cho(36)+H(17)=CH2HCO(35)+H2(3)               2.71E+07   2.0       5.4
393. C2H6(7)+C3H2(25)=>C2H5(24)+H2CCCH(26)           1.74E+04   2.9       8.8
394. CH2(19)+HCCO(34)=C2H(22)+CH2O(15)               1.00E+13   0.0       2.0
395. C7H11O2J(816)(+m)=>C7H11J(783)+o2(2)(+m)        1.00E+00   0.0       0.0
      Tmin, Tmax:    0.30000E+03  0.15000E+04
      Pmin, Pmax:    0.10000E+01  0.10000E+03
      CHEB Polynomials:    0.70000E+01  0.40000E+01
      CHEB Polynomials:    0.91438E+01  0.65367E+00 -0.39510E-01 -0.11100E-02
      CHEB Polynomials:   -0.85134E+00 -0.42660E+00 -0.33640E-01  0.26500E-02
      CHEB Polynomials:   -0.27774E+00 -0.45330E-01  0.12630E-01  0.33700E-02
      CHEB Polynomials:   -0.93260E-01  0.51570E-01  0.78000E-02 -0.31000E-03
      CHEB Polynomials:    0.52000E-01  0.15600E-02 -0.33000E-02 -0.80000E-03
      CHEB Polynomials:    0.13800E-01 -0.98100E-02 -0.11000E-02  0.13000E-03
      CHEB Polynomials:   -0.22370E-01  0.22300E-02  0.98000E-03  0.14000E-03
396. C7H11O2J(817)(+m)=>C7H11J(783)+o2(2)(+m)        1.00E+00   0.0       0.0
      Tmin, Tmax:    0.30000E+03  0.15000E+04
      Pmin, Pmax:    0.10000E+01  0.10000E+03
      CHEB Polynomials:    0.70000E+01  0.40000E+01
      CHEB Polynomials:    0.85750E+01  0.61020E+00 -0.33740E-01 -0.52000E-03
      CHEB Polynomials:   -0.14614E+01 -0.45856E+00 -0.25720E-01  0.24400E-02
      CHEB Polynomials:   -0.42732E+00 -0.17320E-01  0.13890E-01  0.24000E-02
      CHEB Polynomials:   -0.80610E-01  0.58860E-01  0.49300E-02 -0.53000E-03
      CHEB Polynomials:    0.79990E-01 -0.83400E-02 -0.36800E-02 -0.48000E-03
      CHEB Polynomials:    0.87000E-03 -0.91400E-02 -0.15000E-03  0.15000E-03
      CHEB Polynomials:   -0.26750E-01  0.47500E-02  0.80000E-03  0.49939E-04
397. C7H11J(783)+o2(2)(+m)=>C7H11O2J(816)(+m)        1.00E+00   0.0       0.0
      Tmin, Tmax:    0.30000E+03  0.15000E+04
      Pmin, Pmax:    0.10000E+01  0.10000E+03
      CHEB Polynomials:    0.70000E+01  0.40000E+01
      CHEB Polynomials:    0.11619E+02  0.65367E+00 -0.39510E-01 -0.11100E-02
      CHEB Polynomials:    0.13195E+01 -0.42660E+00 -0.33640E-01  0.26500E-02
      CHEB Polynomials:   -0.20404E+00 -0.45330E-01  0.12630E-01  0.33700E-02
      CHEB Polynomials:   -0.11231E+00  0.51570E-01  0.78000E-02 -0.31000E-03
      CHEB Polynomials:    0.57640E-01  0.15600E-02 -0.33000E-02 -0.80000E-03
      CHEB Polynomials:    0.11960E-01 -0.98100E-02 -0.11000E-02  0.13000E-03
      CHEB Polynomials:   -0.21720E-01  0.22300E-02  0.98000E-03  0.14000E-03
398. C7H11J(783)+o2(2)(+m)=>C7H11O2J(817)(+m)        1.00E+00   0.0       0.0
      Tmin, Tmax:    0.30000E+03  0.15000E+04
      Pmin, Pmax:    0.10000E+01  0.10000E+03
      CHEB Polynomials:    0.70000E+01  0.40000E+01
      CHEB Polynomials:    0.11578E+02  0.61020E+00 -0.33740E-01 -0.52000E-03
      CHEB Polynomials:    0.14840E+01 -0.45856E+00 -0.25720E-01  0.24400E-02
      CHEB Polynomials:   -0.30559E+00 -0.17320E-01  0.13890E-01  0.24000E-02
      CHEB Polynomials:   -0.11222E+00  0.58860E-01  0.49300E-02 -0.53000E-03
      CHEB Polynomials:    0.89360E-01 -0.83400E-02 -0.36800E-02 -0.48000E-03
      CHEB Polynomials:   -0.21500E-02 -0.91400E-02 -0.15000E-03  0.15000E-03
```

253

```
     CHEB Polynomials:   -0.25730E-01  0.47500E-02  0.80000E-03  0.49954E-04
399. ch3cho(36)+O(28)=>CH2HCO(35)+OH(29)              2.56E+04   3.0       3.1
400. CO(13)+CH(18)=HCCO(34)                           2.77E+11   0.0      -1.7
401. C2H2(5)+C2H2(5)=H2CCCCH(27)+H(17)                2.00E+09   0.0      57.8
402. c7h14-2(39)+OH(29)=C7H13J(297)+H2O(11)           1.68E+09   1.0       5.1
403. c7h14-3(40)+OH(29)=C7H13J(297)+H2O(11)           1.68E+09   1.0       5.1
404. C2H2(5)+C3H2(25)=>C2H(22)+H2CCCH(26)             3.72E+09   1.5      41.7
405. C6H10O3(1316)+HCCO(34)                           1.44E+01   3.1       6.9
     =C6H9O3J(1328)+CH2CO(16)
406. C6H10O3(1317)+HCCO(34)                           1.44E+01   3.1       6.9
     =C6H9O3J(1329)+CH2CO(16)
407. nc7h16(1)+HCCO(34)=CH2CO(16)+C7H15J(45)          8.70E+03   2.9       8.8
408. nc7h16(1)+HCCO(34)=C7H15J(44)+CH2CO(16)          1.02E+03   3.1       8.8
409. nc7h16(1)+HCCO(34)=C7H15J(41)+CH2CO(16)          2.04E+03   3.1       8.8
410. nc7h16(1)+HCCO(34)=C7H15J(42)+CH2CO(16)          2.04E+03   3.1       8.8
411. C3H4(8)+C6H9O3J(1329)                            2.05E+13   0.0       5.9
     =C6H10O3(1317)+H2CCCH(26)
412. C3H4(8)+C6H9O3J(1328)                            2.05E+13   0.0       5.9
     =C6H10O3(1316)+H2CCCH(26)
413. CH2CO(16)+C3H2(25)=>HCCO(34)+H2CCCH(26)          5.88E+13   0.0      20.2
414. C6H10O3(1317)+C3H2(25)                           2.88E+01   3.1       6.9
     =>C6H9O3J(1329)+H2CCCH(26)
415. C6H10O3(1316)+C3H2(25)                           2.88E+01   3.1       6.9
     =>C6H9O3J(1328)+H2CCCH(26)
416. CH2O(15)+C3H2(25)=>HCO(31)+H2CCCH(26)            1.08E+04   2.8       5.9
417. C3H4(8)+C7H13J(297)=c7h14-2(39)+H2CCCH(26)       6.04E+13   0.0      31.7
418. C3H4(8)+C7H13J(297)=c7h14-3(40)+H2CCCH(26)       6.04E+13   0.0      31.7
419. C3H4(8)+C7H13J(299)=c7h14-3(40)+H2CCCH(26)       3.13E+13   0.0      19.7
420. C3H4(8)+C7H13J(294)=c7h14-3(40)+H2CCCH(26)       3.13E+13   0.0      19.7
421. C7H12(724)+C3H5J(285)=C7H11J(783)+C3H6(9)        1.54E+13  -0.5      16.2
422. C7H12(724)+H(17)=C7H11J(783)+H2(3)               1.40E+06   2.4       1.1
423. C7H12(724)+HCCO(34)=C7H11J(783)+CH2CO(16)        8.36E+12  -0.2       6.2
424. C5H5J(668)(+m)=>C2H2(5)+H2CCCH(26)(+m)           1.00E+00   0.0       0.0
     Tmin, Tmax:    0.30000E+03  0.15000E+04
     Pmin, Pmax:    0.10000E+01  0.10000E+03
     CHEB Polynomials:    0.70000E+01  0.40000E+01
     CHEB Polynomials:    0.63498E+01  0.57875E+00 -0.43680E-01 -0.35000E-03
     CHEB Polynomials:   -0.35504E+01 -0.37771E+00 -0.27130E-01  0.26900E-02
     CHEB Polynomials:   -0.63033E+00  0.51220E-01  0.12810E-01  0.16400E-02
     CHEB Polynomials:    0.13136E+00  0.17000E-01 -0.23348E-04 -0.51000E-03
     CHEB Polynomials:    0.15490E-01 -0.12620E-01 -0.17300E-02 -0.98127E-04
     CHEB Polynomials:   -0.29890E-01  0.32000E-02  0.68000E-03  0.10000E-03
     CHEB Polynomials:    0.14350E-01  0.48000E-03 -0.33785E-04 -0.20647E-04
425. C2H2(5)+H2CCCH(26)(+m)=>C5H5J(668)(+m)           1.00E+00   0.0       0.0
     Tmin, Tmax:    0.30000E+03  0.15000E+04
     Pmin, Pmax:    0.10000E+01  0.10000E+03
     CHEB Polynomials:    0.70000E+01  0.40000E+01
     CHEB Polynomials:    0.10481E+02  0.57875E+00 -0.43680E-01 -0.35000E-03
     CHEB Polynomials:    0.38892E+00 -0.37771E+00 -0.27130E-01  0.26900E-02
     CHEB Polynomials:   -0.51404E+00  0.51220E-01  0.12810E-01  0.16400E-02
     CHEB Polynomials:    0.10171E+00  0.17000E-01 -0.23421E-04 -0.51000E-03
     CHEB Polynomials:    0.24010E-01 -0.12620E-01 -0.17300E-02 -0.98116E-04
     CHEB Polynomials:   -0.32520E-01  0.32000E-02  0.68000E-03  0.10000E-03
     CHEB Polynomials:    0.15200E-01  0.48000E-03 -0.33762E-04 -0.20642E-04
426. OH(29)+HCCO(34)=HCO(31)+HCO(31)                  1.00E+13   0.0       0.0
427. c7h14-3(40)+CH3(21)=C7H13J(297)+CH4(4)           5.46E+13   0.0      10.4
428. c7h14-2(39)+CH3(21)=C7H13J(297)+CH4(4)           5.46E+13   0.0      10.4
429. c7h14-2(39)+O(28)=>C7H13J(297)+OH(29)            9.54E+04   2.7       2.1
430. c7h14-3(40)+O(28)=>C7H13J(297)+OH(29)            9.54E+04   2.7       2.1
431. H2CCCH(26)+O(28)=C2H2(5)+CO(13)+H(17)            1.39E+14   0.0       0.0
432. C6H10O3(1317)(+m)=>C6H9OJ(961)+HO2(30)(+m)       1.00E+00   0.0       0.0
     Tmin, Tmax:    0.30000E+03  0.15000E+04
     Pmin, Pmax:    0.10000E+01  0.10000E+03
     CHEB Polynomials:    0.70000E+01  0.40000E+01
     CHEB Polynomials:   -0.59061E+01  0.14375E+00 -0.15520E-01  0.32593E-04
     CHEB Polynomials:   -0.13483E+02 -0.25847E+00  0.25920E-01  0.33000E-03
     CHEB Polynomials:   -0.48060E+00  0.18530E+00 -0.13890E-01 -0.10600E-02
     CHEB Polynomials:    0.23181E+00 -0.10000E+00  0.19400E-02  0.13600E-02
     CHEB Polynomials:   -0.10224E+00  0.32350E-01  0.46400E-02 -0.92000E-03
     CHEB Polynomials:    0.30010E-01  0.44100E-02 -0.51900E-02  0.16000E-03
     CHEB Polynomials:    0.33000E-02 -0.14380E-01  0.24900E-02  0.34000E-03
```

```
433. C6H9OJ(961)+HO2(30)(+m)=>C6H10O3(1316)(+m)    1.00E+00    0.0         0.0
     Tmin, Tmax:    0.30000E+03  0.15000E+04
     Pmin, Pmax:    0.10000E+01  0.10000E+03
     CHEB Polynomials:    0.70000E+01  0.40000E+01
     CHEB Polynomials:    0.12462E+02  0.12231E+00 -0.13480E-01  0.17387E-04
     CHEB Polynomials:    0.28486E+00 -0.22264E+00  0.23130E-01  0.24000E-03
     CHEB Polynomials:   -0.26290E+00  0.16616E+00 -0.13810E-01 -0.78000E-03
     CHEB Polynomials:    0.17076E+00 -0.97560E-01  0.38700E-02  0.10700E-02
     CHEB Polynomials:   -0.90250E-01  0.39350E-01  0.25300E-02 -0.86000E-03
     CHEB Polynomials:    0.33140E-01 -0.36700E-02 -0.42000E-02  0.31000E-03
     CHEB Polynomials:   -0.20000E-02 -0.99500E-02  0.26500E-02  0.16000E-03
434. C6H9OJ(961)+HO2(30)(+m)=>C6H10O3(1317)(+m)    1.00E+00    0.0         0.0
     Tmin, Tmax:    0.30000E+03  0.15000E+04
     Pmin, Pmax:    0.10000E+01  0.10000E+03
     CHEB Polynomials:    0.70000E+01  0.40000E+01
     CHEB Polynomials:    0.12428E+02  0.14377E+00 -0.15520E-01  0.31065E-04
     CHEB Polynomials:    0.34363E+00 -0.25850E+00  0.25930E-01  0.33000E-03
     CHEB Polynomials:   -0.30132E+00  0.18532E+00 -0.13890E-01 -0.10700E-02
     CHEB Polynomials:    0.18661E+00 -0.99990E-01  0.19400E-02  0.13500E-02
     CHEB Polynomials:   -0.89930E-01  0.32340E-01  0.46400E-02 -0.92000E-03
     CHEB Polynomials:    0.26000E-01  0.44300E-02 -0.52000E-02  0.16000E-03
     CHEB Polynomials:    0.48000E-02 -0.14390E-01  0.24900E-02  0.34000E-03
435. C6H10O3(1316)(+m)=>C6H9OJ(961)+HO2(30)(+m)    1.00E+00    0.0         0.0
     Tmin, Tmax:    0.30000E+03  0.15000E+04
     Pmin, Pmax:    0.10000E+01  0.10000E+03
     CHEB Polynomials:    0.70000E+01  0.40000E+01
     CHEB Polynomials:   -0.47578E+01  0.12230E+00 -0.13470E-01  0.14791E-04
     CHEB Polynomials:   -0.12419E+02 -0.22264E+00  0.23120E-01  0.24000E-03
     CHEB Polynomials:   -0.39388E+00  0.16616E+00 -0.13810E-01 -0.78000E-03
     CHEB Polynomials:    0.20396E+00 -0.97570E-01  0.38700E-02  0.10700E-02
     CHEB Polynomials:   -0.99060E-01  0.39370E-01  0.25200E-02 -0.85000E-03
     CHEB Polynomials:    0.36010E-01 -0.36900E-02 -0.41800E-02  0.31000E-03
     CHEB Polynomials:   -0.31500E-02 -0.99500E-02  0.26400E-02  0.17000E-03
436. ch3cho(36)+HCCO(34)=CH2CO(16)+CH2HCO(35)         1.51E+13    0.0         9.2
437. C3H4(8)+C2H5(24)=H2CCCH(26)+C2H6(7)              3.13E+13    0.0        19.7
438. H(17)+HCCO(34)=CH2(19)+CO(13)                    1.51E+14    0.0         0.0
439. ch3cho(36)+C2H3(23)=CH2HCO(35)+C2H4(6)           1.51E+13    0.0         9.2
440. ch3cho(36)+C2H5(24)=CH2HCO(35)+C2H6(7)           9.41E+06    1.8        12.5
441. ch3cho(36)+CH3(21)=CH2HCO(35)+CH4(4)             9.41E+06    1.8        12.5
442. H2O2(12)+HCCO(34)=HO2(30)+CH2CO(16)              2.88E+01    3.1         6.9
443. C7H12(724)+C7H15J(42)=C7H11J(783)+nc7h16(1)      3.04E+06    1.9         9.4
444. C7H12(724)+C7H15J(41)=C7H11J(783)+nc7h16(1)      3.04E+06    1.9         9.4
445. C7H12(724)+C7H15J(45)=C7H11J(783)+nc7h16(1)      3.04E+06    1.9         9.4
446. C7H12(724)+C7H15J(44)=C7H11J(783)+nc7h16(1)      3.04E+06    1.9         9.4
447. c7h14-2(39)+C7H13J(299)                          3.04E+06    1.9         9.4
     =C7H13J(297)+c7h14-3(40)
448. c7h14-3(40)+C7H13J(299)                          3.04E+06    1.9         9.4
     =C7H13J(297)+c7h14-3(40)
449. c7h14-2(39)+C7H13J(294)                          3.04E+06    1.9         9.4
     =C7H13J(297)+c7h14-3(40)
450. c7h14-3(40)+C7H13J(294)                          3.04E+06    1.9         9.4
     =C7H13J(297)+c7h14-3(40)
451. c7h14-3(40)+C7H13J(297)                          3.04E+06    1.9         9.4
     =C7H13J(297)+c7h14-2(39)
452. C7H13J(299)=C7H13J(297)                          2.82E+08    1.3        27.9
453. C7H13J(294)=C7H13J(297)                          1.19E+10    0.7        38.0
454. C7H12(724)+CH3(21)=C7H11J(783)+CH4(4)            5.46E+13    0.0        10.4
455. CH2CO(16)+O(28)=>HCCO(34)+OH(29)                 7.56E+06    1.9         8.9
456. c7h14-3(40)+HCCO(34)=C7H13J(297)+CH2CO(16)       8.36E+12   -0.2         6.2
457. c7h14-2(39)+HCCO(34)=C7H13J(297)+CH2CO(16)       8.36E+12   -0.2         6.2
458. c7h14-3(40)+HCCO(34)=C7H13J(299)+CH2CO(16)       4.35E+03    2.9         8.8
459. c7h14-3(40)+HCCO(34)=C7H13J(294)+CH2CO(16)       4.35E+03    2.9         8.8
460. C3H4(8)+H(17)=H2(3)+H2CCCH(26)                   1.01E+08    2.0        11.8
461. c7h14-3(40)+CH2(19)=>C7H13J(297)+CH3(21)         1.51E+00    3.5         7.5
462. c7h14-2(39)+CH2(19)=>C7H13J(297)+CH3(21)         1.51E+00    3.5         7.5
463. ch3cho(36)+C7H15J(41)=nc7h16(1)+CH2HCO(35)       9.41E+06    1.8        12.5
464. ch3cho(36)+C7H15J(42)=nc7h16(1)+CH2HCO(35)       9.41E+06    1.8        12.5
465. ch3cho(36)+C7H15J(45)=nc7h16(1)+CH2HCO(35)       9.41E+06    1.8        12.5
466. ch3cho(36)+C7H15J(44)=nc7h16(1)+CH2HCO(35)       9.41E+06    1.8        12.5
467. H2O2(12)+C3H2(25)=>HO2(30)+H2CCCH(26)            5.76E+01    3.1         6.9
468. C2H2(5)+CH2(S)(20)=H2CCCH(26)+H(17)              1.75E+14    0.0         0.0
```

255

```
469. C4H2(10)+O(28)=C3H2(25)+CO(13)                          7.89E+12    0.0      1.3
470. C2H(22)+OH(29)=HCCO(34)+H(17)                           2.00E+13    0.0      0.0
471. ch3cho(36)+C2H(22)=CH2HCO(35)+C2H2(5)                   1.81E+12    0.0      0.0
472. C3H4(8)+C3H5J(285)=C3H6(9)+H2CCCH(26)                   2.14E+14    0.0     30.7
473. C7H13J(297)(+m)=>C7H12(724)+H(17)(+m)                   1.00E+00    0.0      0.0
     Tmin, Tmax:    0.30000E+03  0.15000E+04
     Pmin, Pmax:    0.10000E+01  0.10000E+03
     CHEB Polynomials:    0.70000E+01  0.40000E+01
     CHEB Polynomials:   -0.56617E+01  0.20151E+01 -0.14200E-01 -0.15000E-03
     CHEB Polynomials:   -0.12723E+02 -0.34997E+00  0.21080E-01  0.77000E-03
     CHEB Polynomials:   -0.45262E+00  0.22366E+00 -0.58000E-02 -0.13900E-02
     CHEB Polynomials:    0.26765E+00 -0.92800E-01 -0.54500E-02  0.11000E-02
     CHEB Polynomials:   -0.10559E+00  0.84100E-02  0.73200E-02 -0.12000E-03
     CHEB Polynomials:    0.12230E-01  0.21300E-01 -0.33400E-02 -0.56000E-03
     CHEB Polynomials:    0.20180E-01 -0.17560E-01 -0.57000E-03  0.49000E-03
474. c7h14-2(39)+C7H15J(44)=C7H13J(297)+nc7h16(1)            3.04E+06    1.9      9.4
475. c7h14-2(39)+C7H15J(45)=C7H13J(297)+nc7h16(1)            3.04E+06    1.9      9.4
476. c7h14-2(39)+C7H15J(42)=C7H13J(297)+nc7h16(1)            3.04E+06    1.9      9.4
477. c7h14-2(39)+C7H15J(41)=C7H13J(297)+nc7h16(1)            3.04E+06    1.9      9.4
478. c7h14-3(40)+C7H15J(44)=C7H13J(297)+nc7h16(1)            3.04E+06    1.9      9.4
479. c7h14-3(40)+C7H15J(45)=C7H13J(297)+nc7h16(1)            3.04E+06    1.9      9.4
480. c7h14-3(40)+C7H15J(42)=C7H13J(297)+nc7h16(1)            3.04E+06    1.9      9.4
481. c7h14-3(40)+C7H15J(41)=C7H13J(297)+nc7h16(1)            3.04E+06    1.9      9.4
482. C7H11J(783)+HO2(30)(+m)                                 1.00E+00    0.0      0.0
     =>C7H11O2J(816)+H(17)(+m)
     Tmin, Tmax:    0.30000E+03  0.15000E+04
     Pmin, Pmax:    0.10000E+01  0.10000E+03
     CHEB Polynomials:    0.70000E+01  0.40000E+01
     CHEB Polynomials:   -0.90951E+01 -0.55397E+00 -0.45630E-01  0.39800E-02
     CHEB Polynomials:   -0.13501E+02 -0.51002E+00 -0.56600E-02  0.85000E-02
     CHEB Polynomials:    0.96500E-01  0.12745E+00  0.36020E-01 -0.20800E-02
     CHEB Polynomials:    0.73770E-01  0.41720E-01 -0.14570E-01 -0.43500E-02
     CHEB Polynomials:   -0.38680E-01 -0.52070E-01 -0.68400E-02  0.29400E-02
     CHEB Polynomials:    0.12200E-02  0.17160E-01  0.97300E-02  0.64000E-03
     CHEB Polynomials:    0.88700E-02  0.47100E-02 -0.34300E-02 -0.16500E-02
483. C7H11J(783)+HO2(30)(+m)                                 1.00E+00    0.0      0.0
     =>C7H11O2J(817)+H(17)(+m)
     Tmin, Tmax:    0.30000E+03  0.15000E+04
     Pmin, Pmax:    0.10000E+01  0.10000E+03
     CHEB Polynomials:    0.70000E+01  0.40000E+01
     CHEB Polynomials:   -0.82368E+01 -0.54367E+00 -0.45490E-01  0.37900E-02
     CHEB Polynomials:   -0.12681E+02 -0.51133E+00 -0.77000E-02  0.84500E-02
     CHEB Polynomials:    0.13936E+00  0.11675E+00  0.35750E-01 -0.14800E-02
     CHEB Polynomials:    0.63240E-01  0.46930E-01 -0.12710E-01 -0.43400E-02
     CHEB Polynomials:   -0.31020E-01 -0.49890E-01 -0.77600E-02  0.24900E-02
     CHEB Polynomials:   -0.10200E-02  0.14620E-01  0.92200E-02  0.81000E-03
     CHEB Polynomials:    0.84500E-02  0.55400E-02 -0.27500E-02 -0.15300E-02
484. ch3cho(36)+OH(29)=CH2HCO(35)+H2O(11)                    1.55E+06    2.2      1.0
485. H2O2(12)+CH2HCO(35)=HO2(30)+ch3cho(36)                  2.97E+03    2.4      9.7
486. c7h14-3(40)+C6H9O3J(1328)                               1.68E+09    1.0      5.1
     =C7H13J(297)+C6H10O3(1316)
487. c7h14-2(39)+C6H9O3J(1328)                               1.68E+09    1.0      5.1
     =C7H13J(297)+C6H10O3(1316)
488. c7h14-3(40)+C6H9O3J(1329)                               1.68E+09    1.0      5.1
     =C7H13J(297)+C6H10O3(1317)
489. c7h14-2(39)+C6H9O3J(1329)                               1.68E+09    1.0      5.1
     =C7H13J(297)+C6H10O3(1317)
490. C7H13J(297)+o2(2)(+m)=>C7H13O2J(734)(+m)               1.00E+00    0.0      0.0
     Tmin, Tmax:    0.30000E+03  0.15000E+04
     Pmin, Pmax:    0.10000E+01  0.10000E+03
     CHEB Polynomials:    0.70000E+01  0.40000E+01
     CHEB Polynomials:    0.12475E+02  0.27827E+00 -0.24300E-01 -0.95000E-03
     CHEB Polynomials:    0.67120E+00 -0.44206E+00  0.29950E-01  0.31200E-02
     CHEB Polynomials:   -0.37540E+00  0.20586E+00  0.11200E-02 -0.34300E-02
     CHEB Polynomials:    0.11111E+00 -0.23280E-01 -0.13380E-01  0.11000E-02
     CHEB Polynomials:    0.19660E-01 -0.39050E-01  0.71100E-02  0.10000E-02
     CHEB Polynomials:   -0.37880E-01  0.25740E-01  0.98000E-03 -0.97000E-03
     CHEB Polynomials:    0.12190E-01 -0.72000E-03 -0.25900E-02  0.47448E-05
491. C7H13O2J(734)(+m)=>C7H13J(297)+o2(2)(+m)               1.00E+00    0.0      0.0
     Tmin, Tmax:    0.30000E+03  0.15000E+04
     Pmin, Pmax:    0.10000E+01  0.10000E+03
```

```
      CHEB Polynomials:      0.70000E+01  0.40000E+01
      CHEB Polynomials:      0.52640E+01  0.27823E+00 -0.24320E-01 -0.95000E-03
      CHEB Polynomials:     -0.47423E+01 -0.44198E+00  0.29980E-01  0.31200E-02
      CHEB Polynomials:     -0.49728E+00  0.20580E+00  0.10900E-02 -0.34400E-02
      CHEB Polynomials:      0.14296E+00 -0.23240E-01 -0.13360E-01  0.11000E-02
      CHEB Polynomials:      0.10110E-01 -0.39070E-01  0.71000E-02  0.10000E-02
      CHEB Polynomials:     -0.34750E-01  0.25760E-01  0.98000E-03 -0.96000E-03
      CHEB Polynomials:      0.11090E-01 -0.73000E-03 -0.25900E-02  0.39815E-05
492. c2h5cho(37)(+m)=>CH2HCO(35)+CH3(21)(+m)          1.00E+00     0.0         0.0
      Tmin, Tmax:     0.30000E+03  0.15000E+04
      Pmin, Pmax:     0.10000E+01  0.10000E+03
      CHEB Polynomials:      0.70000E+01  0.40000E+01
      CHEB Polynomials:     -0.17510E+02  0.36510E-01 -0.58000E-02  0.29000E-03
      CHEB Polynomials:     -0.21674E+02 -0.68300E-01  0.10490E-01 -0.44000E-03
      CHEB Polynomials:     -0.18255E+00  0.55900E-01 -0.76900E-02  0.12000E-03
      CHEB Polynomials:      0.82320E-01 -0.39920E-01  0.43700E-02  0.18000E-03
      CHEB Polynomials:     -0.45170E-01  0.24670E-01 -0.16300E-02 -0.32000E-03
      CHEB Polynomials:      0.25440E-01 -0.12900E-01 -0.17704E-04  0.29000E-03
      CHEB Polynomials:     -0.13610E-01  0.54100E-02  0.65000E-03 -0.17000E-03
493. C3H4(8)+C3H2(25)=>H2CCCH(26)+H2CCCH(26)          1.18E+14     0.0        20.2
494. C7H12(724)+O(28)=>C7H11J(783)+OH(29)             9.54E+04     2.7         2.1
495. C7H12(724)+HCO(31)=C7H11J(783)+CH2O(15)          7.57E+06     1.9        16.6
496. c7h14-3(40)+C2H5(24)=C7H13J(297)+C2H6(7)         3.04E+06     1.9         9.4
497. c7h14-2(39)+C2H5(24)=C7H13J(297)+C2H6(7)         3.04E+06     1.9         9.4
498. H2CCCCH(27)+m=C4H2(10)+H(17)+m                   1.12E+16     0.0        46.5
        H2O(11)           Enhanced by     6.500E+00
        C2H6(7)           Enhanced by     3.000E+00
        N2                Enhanced by     4.000E-01
        CH4(4)            Enhanced by     3.000E+00
        CO(13)            Enhanced by     7.500E-01
        Ar                Enhanced by     3.500E-01
        CO2(14)           Enhanced by     1.500E+00
        o2(2)             Enhanced by     4.000E-01
499. C7H12(724)+OH(29)=C7H11J(783)+H2O(11)            1.68E+09     1.0         5.1
500. CH2O(15)+CH2HCO(35)=HCO(31)+ch3cho(36)           5.50E+03     2.8         5.9
501. HCCO(34)+HCCO(34)=C2H2(5)+CO(13)+CO(13)          1.00E+13     0.0         0.0
502. C3H4(8)+C2H(22)=H2CCCH(26)+C2H2(5)               8.85E+09     0.7        10.0
503. c7h14-3(40)+H(17)=C7H13J(297)+H2(3)              1.40E+06     2.4         1.1
504. c7h14-2(39)+H(17)=C7H13J(297)+H2(3)              1.40E+06     2.4         1.1
505. C7H12(724)+H2CCCH(26)=C7H11J(783)+C3H4(8)        8.36E+12    -0.2         6.2
506. CH(18)+HCCO(34)=C2H2(5)+CO(13)                   5.00E+13     0.0         0.0
507. O(28)+HCCO(34)=H(17)+CO(13)+CO(13)               9.64E+13     0.0         0.0
508. o2(2)+C6H9OJ(962)(+m)=>C6H9O3J(1253)(+m)         1.00E+00     0.0         0.0
      Tmin, Tmax:     0.30000E+03  0.15000E+04
      Pmin, Pmax:     0.10000E+01  0.10000E+03
      CHEB Polynomials:      0.70000E+01  0.40000E+01
      CHEB Polynomials:      0.12261E+02  0.34867E+00 -0.23450E-01 -0.27000E-03
      CHEB Polynomials:      0.97751E+00 -0.50173E+00  0.16700E-01  0.31500E-02
      CHEB Polynomials:     -0.47750E+00  0.17026E+00  0.14310E-01 -0.21800E-02
      CHEB Polynomials:      0.10002E+00  0.17100E-01 -0.12540E-01 -0.92000E-03
      CHEB Polynomials:      0.44340E-01 -0.43530E-01  0.54000E-03  0.12700E-02
      CHEB Polynomials:     -0.43790E-01  0.14120E-01  0.31300E-02 -0.60182E-04
      CHEB Polynomials:      0.82000E-02  0.48400E-02 -0.92000E-03 -0.36000E-03
509. o2(2)+C6H9OJ(961)(+m)=>C6H9O3J(1328)(+m)         1.00E+00     0.0         0.0
      Tmin, Tmax:     0.30000E+03  0.15000E+04
      Pmin, Pmax:     0.10000E+01  0.10000E+03
      CHEB Polynomials:      0.70000E+01  0.40000E+01
      CHEB Polynomials:      0.11592E+02  0.65949E+00 -0.38370E-01 -0.12100E-02
      CHEB Polynomials:      0.12938E+01 -0.40732E+00 -0.31410E-01  0.23600E-02
      CHEB Polynomials:     -0.19262E+00 -0.35560E-01  0.10740E-01  0.26400E-02
      CHEB Polynomials:     -0.10260E+00  0.44730E-01  0.53100E-02 -0.37000E-03
      CHEB Polynomials:      0.52430E-01 -0.12000E-02 -0.25200E-02 -0.41000E-03
      CHEB Polynomials:      0.95700E-02 -0.72200E-02 -0.38000E-03  0.11000E-03
      CHEB Polynomials:     -0.18810E-01  0.23000E-02  0.59000E-03  0.25070E-04
510. o2(2)+C6H9OJ(961)(+m)=>C6H9O3J(1329)(+m)         1.00E+00     0.0         0.0
      Tmin, Tmax:     0.30000E+03  0.15000E+04
      Pmin, Pmax:     0.10000E+01  0.10000E+03
      CHEB Polynomials:      0.70000E+01  0.40000E+01
      CHEB Polynomials:      0.11753E+02  0.55256E+00 -0.32880E-01 -0.12000E-03
      CHEB Polynomials:      0.13825E+01 -0.48803E+00 -0.17840E-01  0.33900E-02
      CHEB Polynomials:     -0.35581E+00  0.17260E-01  0.17410E-01  0.18500E-02
```

```
     CHEB Polynomials:    -0.69360E-01  0.59140E-01  0.20900E-02 -0.10200E-02
     CHEB Polynomials:     0.86610E-01 -0.16770E-01 -0.38400E-02 -0.28000E-03
     CHEB Polynomials:    -0.13560E-01 -0.61100E-02  0.41000E-03  0.17000E-03
     CHEB Polynomials:    -0.19580E-01  0.55000E-02  0.63000E-03  0.45185E-04
511. C6H9O3J(1329)(+m)=>o2(2)+C6H9OJ(961)(+m)          1.00E+00     0.0          0.0
     Tmin, Tmax:    0.30000E+03  0.15000E+04
     Pmin, Pmax:    0.10000E+01  0.10000E+03
     CHEB Polynomials:     0.70000E+01  0.40000E+01
     CHEB Polynomials:     0.81628E+01  0.55256E+00 -0.32880E-01 -0.12000E-03
     CHEB Polynomials:    -0.19116E+01 -0.48803E+00 -0.17840E-01  0.33900E-02
     CHEB Polynomials:    -0.47707E+00  0.17260E-01  0.17410E-01  0.18500E-02
     CHEB Polynomials:    -0.38440E-01  0.59140E-01  0.20900E-02 -0.10200E-02
     CHEB Polynomials:     0.77720E-01 -0.16770E-01 -0.38400E-02 -0.28000E-03
     CHEB Polynomials:    -0.10830E-01 -0.61100E-02  0.41000E-03  0.17000E-03
     CHEB Polynomials:    -0.20460E-01  0.55000E-02  0.63000E-03  0.45175E-04
512. C6H9O3J(1253)(+m)=>o2(2)+C6H9OJ(962)(+m)          1.00E+00     0.0          0.0
     Tmin, Tmax:    0.30000E+03  0.15000E+04
     Pmin, Pmax:    0.10000E+01  0.10000E+03
     CHEB Polynomials:     0.70000E+01  0.40000E+01
     CHEB Polynomials:     0.59344E+01  0.34872E+00 -0.23430E-01 -0.26000E-03
     CHEB Polynomials:    -0.41806E+01 -0.50180E+00  0.16670E-01  0.31400E-02
     CHEB Polynomials:    -0.58564E+00  0.17029E+00  0.14320E-01 -0.21700E-02
     CHEB Polynomials:     0.12854E+00  0.17090E-01 -0.12540E-01 -0.92000E-03
     CHEB Polynomials:     0.35770E-01 -0.43510E-01  0.55000E-03  0.12700E-02
     CHEB Polynomials:    -0.41060E-01  0.14100E-01  0.31200E-02 -0.61907E-04
     CHEB Polynomials:     0.74000E-02  0.48300E-02 -0.93000E-03 -0.36000E-03
513. C6H9O3J(1328)(+m)=>o2(2)+C6H9OJ(961)(+m)          1.00E+00     0.0          0.0
     Tmin, Tmax:    0.30000E+03  0.15000E+04
     Pmin, Pmax:    0.10000E+01  0.10000E+03
     CHEB Polynomials:     0.70000E+01  0.40000E+01
     CHEB Polynomials:     0.91165E+01  0.65949E+00 -0.38370E-01 -0.12100E-02
     CHEB Polynomials:    -0.87728E+00 -0.40733E+00 -0.31410E-01  0.23600E-02
     CHEB Polynomials:    -0.26608E+00 -0.35560E-01  0.10740E-01  0.26400E-02
     CHEB Polynomials:    -0.83740E-01  0.44730E-01  0.53100E-02 -0.37000E-03
     CHEB Polynomials:     0.46930E-01 -0.12000E-02 -0.25200E-02 -0.41000E-03
     CHEB Polynomials:     0.11310E-01 -0.72200E-02 -0.38000E-03  0.11000E-03
     CHEB Polynomials:    -0.19390E-01  0.23000E-02  0.59000E-03  0.25091E-04
514. C6H9OJ(961)(+m)=>C6H8(823)+OH(29)(+m)             1.00E+00     0.0          0.0
     Tmin, Tmax:    0.30000E+03  0.15000E+04
     Pmin, Pmax:    0.10000E+01  0.10000E+03
     CHEB Polynomials:     0.70000E+01  0.40000E+01
     CHEB Polynomials:    -0.54031E+01  0.51120E-01 -0.10470E-01  0.63000E-03
     CHEB Polynomials:    -0.12984E+02 -0.96360E-01  0.19370E-01 -0.10600E-02
     CHEB Polynomials:    -0.94680E-01  0.80440E-01 -0.15190E-01  0.53000E-03
     CHEB Polynomials:     0.65350E-01 -0.58810E-01  0.97500E-02  0.58176E-04
     CHEB Polynomials:    -0.42530E-01  0.36670E-01 -0.46100E-02 -0.48000E-03
     CHEB Polynomials:     0.23870E-01 -0.18230E-01  0.85000E-03  0.61000E-03
     CHEB Polynomials:    -0.10690E-01  0.56500E-02  0.11600E-02 -0.48000E-03
515. C6H8(823)+OH(29)(+m)=>C6H9OJ(962)(+m)             1.00E+00     0.0          0.0
     Tmin, Tmax:    0.30000E+03  0.15000E+04
     Pmin, Pmax:    0.10000E+01  0.10000E+03
     CHEB Polynomials:     0.70000E+01  0.40000E+01
     CHEB Polynomials:     0.12640E+02  0.86540E-01 -0.14220E-01  0.36000E-03
     CHEB Polynomials:     0.17632E+00 -0.15987E+00  0.25330E-01 -0.39000E-03
     CHEB Polynomials:    -0.14320E+00  0.12523E+00 -0.17510E-01 -0.34000E-03
     CHEB Polynomials:     0.99920E-01 -0.81320E-01  0.84000E-02  0.96000E-03
     CHEB Polynomials:    -0.58120E-01  0.41090E-01 -0.12900E-02 -0.11100E-02
     CHEB Polynomials:     0.25950E-01 -0.12710E-01 -0.22900E-02  0.77000E-03
     CHEB Polynomials:    -0.61800E-02 -0.21600E-02  0.27500E-02 -0.23000E-03
516. C6H8(823)+OH(29)(+m)=>C6H9OJ(961)(+m)             1.00E+00     0.0          0.0
     Tmin, Tmax:    0.30000E+03  0.15000E+04
     Pmin, Pmax:    0.10000E+01  0.10000E+03
     CHEB Polynomials:     0.70000E+01  0.40000E+01
     CHEB Polynomials:     0.12683E+02  0.51140E-01 -0.10470E-01  0.63000E-03
     CHEB Polynomials:     0.95850E-01 -0.96400E-01  0.19360E-01 -0.10600E-02
     CHEB Polynomials:    -0.81720E-01  0.80470E-01 -0.15170E-01  0.54000E-03
     CHEB Polynomials:     0.62180E-01 -0.58830E-01  0.97400E-02  0.53879E-04
     CHEB Polynomials:    -0.41620E-01  0.36670E-01 -0.46000E-02 -0.48000E-03
     CHEB Polynomials:     0.23750E-01 -0.18230E-01  0.85000E-03  0.61000E-03
     CHEB Polynomials:    -0.10690E-01  0.56500E-02  0.11600E-02 -0.48000E-03
517. C6H9OJ(962)(+m)=>C6H8(823)+OH(29)(+m)             1.00E+00     0.0          0.0
```

```
        Tmin, Tmax:     0.30000E+03  0.15000E+04
        Pmin, Pmax:     0.10000E+01  0.10000E+03
        CHEB Polynomials:    0.70000E+01  0.40000E+01
        CHEB Polynomials:   -0.16447E+01  0.86940E-01 -0.14150E-01  0.36000E-03
        CHEB Polynomials:   -0.10048E+02 -0.16048E+00  0.25210E-01 -0.40000E-03
        CHEB Polynomials:   -0.17478E+00  0.12543E+00 -0.17400E-01 -0.32000E-03
        CHEB Polynomials:    0.10890E+00 -0.81150E-01  0.83400E-02  0.94000E-03
        CHEB Polynomials:   -0.60990E-01  0.40780E-01 -0.12900E-02 -0.10800E-02
        CHEB Polynomials:    0.26880E-01 -0.12510E-01 -0.22400E-02  0.76000E-03
        CHEB Polynomials:   -0.65400E-02 -0.21500E-02  0.27000E-02 -0.23000E-03
518. CH2HCO(35)(+m)=>CH2CO(16)+H(17)(+m)              1.00E+00     0.0        0.0
        Tmin, Tmax:     0.30000E+03  0.15000E+04
        Pmin, Pmax:     0.10000E+01  0.10000E+03
        CHEB Polynomials:    0.70000E+01  0.40000E+01
        CHEB Polynomials:   -0.67705E+01  0.13596E+00 -0.26570E-01  0.23500E-02
        CHEB Polynomials:   -0.13015E+02 -0.22681E+00  0.38220E-01 -0.14400E-02
        CHEB Polynomials:   -0.19144E+00  0.14489E+00 -0.15780E-01 -0.18400E-02
        CHEB Polynomials:    0.11267E+00 -0.72280E-01  0.78000E-03  0.25000E-02
        CHEB Polynomials:   -0.56190E-01  0.26930E-01  0.44100E-02 -0.14300E-02
        CHEB Polynomials:    0.25060E-01 -0.58100E-02 -0.38700E-02  0.26000E-03
        CHEB Polynomials:   -0.95600E-02 -0.10600E-02  0.18800E-02  0.27000E-03
519. c7h14-2(39)+CH2HCO(35)                           3.04E+06     1.9        9.4
        =C7H13J(297)+ch3cho(36)
520. c7h14-3(40)+CH2HCO(35)                           3.04E+06     1.9        9.4
        =C7H13J(297)+ch3cho(36)
521. ch3cho(36)+C7H13J(299)                           9.41E+06     1.8       12.5
        =c7h14-3(40)+CH2HCO(35)
522. ch3cho(36)+C7H13J(294)                           9.41E+06     1.8       12.5
        =c7h14-3(40)+CH2HCO(35)
523. o2(2)+C2H(22)=HCCO(34)+O(28)                     9.05E+12     0.0        0.0
524. c7h14-2(39)+HCO(31)=C7H13J(297)+CH2O(15)         7.57E+06     1.9       16.6
525. c7h14-3(40)+HCO(31)=C7H13J(297)+CH2O(15)         7.57E+06     1.9       16.6
526. C7H12(724)+HO2(30)=C7H11J(783)+H2O2(12)          1.68E+09     1.0        5.1
527. ch3cho(36)+C3H5J(285)=>C3H6(9)+CH2HCO(35)        9.41E+06     1.8       12.5
528. C3H6(9)+CH2HCO(35)=>ch3cho(36)+C3H5J(285)        8.72E+12     0.0       17.3
529. C7H12(724)+C2H5(24)=C7H11J(783)+C2H6(7)          3.04E+06     1.9        9.4
530. c7h14-2(39)+C2H3(23)=C7H13J(297)+C2H4(6)         8.36E+12    -0.2        6.2
531. c7h14-3(40)+C2H3(23)=C7H13J(297)+C2H4(6)         8.36E+12    -0.2        6.2
532. C7H11J(783)(+m)=>C6H8(823)+CH3(21)(+m)           1.00E+00     0.0        0.0
        Tmin, Tmax:     0.30000E+03  0.15000E+04
        Pmin, Pmax:     0.10000E+01  0.10000E+03
        CHEB Polynomials:    0.70000E+01  0.40000E+01
        CHEB Polynomials:   -0.57127E+01  0.74690E-01 -0.11580E-01  0.33000E-03
        CHEB Polynomials:   -0.13831E+02 -0.13927E+00  0.20940E-01 -0.44000E-03
        CHEB Polynomials:   -0.19140E+00  0.11230E+00 -0.15190E-01 -0.82045E-04
        CHEB Polynomials:    0.11187E+00 -0.76890E-01  0.81600E-02  0.59000E-03
        CHEB Polynomials:   -0.66080E-01  0.42610E-01 -0.22000E-02 -0.80000E-03
        CHEB Polynomials:    0.32710E-01 -0.16450E-01 -0.13100E-02  0.65000E-03
        CHEB Polynomials:   -0.11260E-01  0.93000E-03  0.23400E-02 -0.28000E-03
533. C3H4(8)+OH(29)=H2CCCH(26)+H2O(11)                2.05E+13     0.0        5.9
534. CH2CO(16)+CH2(19)=>HCCO(34)+CH3(21)              9.54E+08     1.3        5.7
535. C3H4(8)+CH2(19)=>H2CCCH(26)+CH3(21)              1.91E+09     1.3        5.7
536. C2H4(6)+O(28)=H(17)+CH2HCO(35)                   4.74E+06     1.9        0.2
537. C2H4(6)+HCCO(34)=C2H3(23)+CH2CO(16)              5.88E+13     0.0       20.2
538. C7H12(724)+C6H9O3J(1328)                         1.68E+09     1.0        5.1
        =C7H11J(783)+C6H10O3(1316)
539. C7H12(724)+C6H9O3J(1329)                         1.68E+09     1.0        5.1
        =C7H11J(783)+C6H10O3(1317)
540. c7h14-2(39)+C2H(22)=C7H13J(297)+C2H2(5)          1.21E+12     0.0        0.0
541. c7h14-3(40)+C2H(22)=C7H13J(297)+C2H2(5)          1.21E+12     0.0        0.0
542. CH2CO(16)+C2H(22)=HCCO(34)+C2H2(5)               4.43E+09     0.7       10.0
543. CH2(19)+HCCO(34)=C2H3(23)+CO(13)                 3.00E+13     0.0        0.0
544. CH4(4)+C3H2(25)=>CH3(21)+H2CCCH(26)              1.27E+15     0.0       13.7
545. C7H13J(297)+o2(2)(+m)                            1.00E+00     0.0        0.0
        =>C7H12(724)+HO2(30)(+m)
        Tmin, Tmax:     0.30000E+03  0.15000E+04
        Pmin, Pmax:     0.10000E+01  0.10000E+03
        CHEB Polynomials:    0.70000E+01  0.40000E+01
        CHEB Polynomials:    0.60400E+01 -0.54736E+00 -0.40330E-01  0.10400E-02
        CHEB Polynomials:   -0.47847E+01 -0.52869E+00  0.31300E-02  0.76400E-02
        CHEB Polynomials:    0.11063E+00  0.79680E-01  0.32210E-01 -0.17900E-02
```

259

```
      CHEB Polynomials:    0.68960E-01  0.73350E-01 -0.79400E-02 -0.39700E-02
      CHEB Polynomials:   -0.57000E-03 -0.42610E-01 -0.97400E-02  0.15900E-02
      CHEB Polynomials:   -0.22490E-01 -0.40800E-02  0.62000E-02  0.12400E-02
      CHEB Polynomials:    0.13010E-01  0.14920E-01  0.11700E-02 -0.10100E-02
546. C7H12(724)+CH2(19)=>C7H11J(783)+CH3(21)        1.51E+00     3.5        7.5
547. CH4(4)+HCCO(34)=CH3(21)+CH2CO(16)              6.36E+14     0.0       13.7
548. c7h14-3(40)(+m)=>C7H13J(297)+H(17)(+m)         1.00E+00     0.0        0.0
      Tmin, Tmax:   0.30000E+03  0.15000E+04
      Pmin, Pmax:   0.10000E+01  0.10000E+03
      CHEB Polynomials:    0.70000E+01  0.40000E+01
      CHEB Polynomials:   -0.23116E+02  0.32210E-01 -0.67400E-02  0.50000E-03
      CHEB Polynomials:   -0.24738E+02 -0.61960E-01  0.12790E-01 -0.90000E-03
      CHEB Polynomials:   -0.48030E-01  0.55070E-01 -0.10890E-01  0.64000E-03
      CHEB Polynomials:    0.45450E-01 -0.45080E-01  0.82200E-02 -0.31000E-03
      CHEB Polynomials:   -0.36290E-01  0.33770E-01 -0.53300E-02 -0.22512E-04
      CHEB Polynomials:    0.26550E-01 -0.22920E-01  0.27400E-02  0.26000E-03
      CHEB Polynomials:   -0.17950E-01  0.13840E-01 -0.81000E-03 -0.38000E-03
549. c7h14-2(39)(+m)=>C7H13J(297)+H(17)(+m)         1.00E+00     0.0        0.0
      Tmin, Tmax:   0.30000E+03  0.15000E+04
      Pmin, Pmax:   0.10000E+01  0.10000E+03
      CHEB Polynomials:    0.70000E+01  0.40000E+01
      CHEB Polynomials:   -0.23109E+02  0.32300E-01 -0.65600E-02  0.48000E-03
      CHEB Polynomials:   -0.24782E+02 -0.62120E-01  0.12450E-01 -0.86000E-03
      CHEB Polynomials:   -0.45390E-01  0.55170E-01 -0.10580E-01  0.62000E-03
      CHEB Polynomials:    0.45920E-01 -0.45090E-01  0.79600E-02 -0.29000E-03
      CHEB Polynomials:   -0.36560E-01  0.33690E-01 -0.51200E-02 -0.20891E-04
      CHEB Polynomials:    0.27040E-01 -0.22760E-01  0.25900E-02  0.25000E-03
      CHEB Polynomials:   -0.18540E-01  0.13640E-01 -0.71000E-03 -0.36000E-03
550. H2O2(12)+C7H13J(297)=c7h14-2(39)+HO2(30)       2.97E+03     2.4        9.7
551. H2O2(12)+C7H13J(297)=c7h14-3(40)+HO2(30)       2.97E+03     2.4        9.7
552. C7H12(724)(+m)=>C7H11J(783)+H(17)(+m)          1.00E+00     0.0        0.0
      Tmin, Tmax:   0.30000E+03  0.15000E+04
      Pmin, Pmax:   0.10000E+01  0.10000E+03
      CHEB Polynomials:    0.70000E+01  0.40000E+01
      CHEB Polynomials:   -0.18954E+02  0.68420E-01 -0.10570E-01  0.40000E-03
      CHEB Polynomials:   -0.22174E+02 -0.12906E+00  0.19370E-01 -0.60000E-03
      CHEB Polynomials:   -0.12452E+00  0.10799E+00 -0.14720E-01  0.12000E-03
      CHEB Polynomials:    0.10092E+00 -0.79430E-01  0.88200E-02  0.40000E-03
      CHEB Polynomials:   -0.72370E-01  0.50240E-01 -0.34400E-02 -0.69000E-03
      CHEB Polynomials:    0.45390E-01 -0.25870E-01 -0.25000E-03  0.67000E-03
      CHEB Polynomials:   -0.24160E-01  0.90600E-02  0.20100E-02 -0.43000E-03
553. C6H10O3(1316)+CH2HCO(35)                       1.49E+03     2.4        9.7
      =C6H9O3J(1328)+ch3cho(36)
554. C6H10O3(1317)+CH2HCO(35)                       1.49E+03     2.4        9.7
      =C6H9O3J(1329)+ch3cho(36)
555. C3H4(8)+CH2HCO(35)(+m)=>C5H7OJ(366)(+m)        1.00E+00     0.0        0.0
      Tmin, Tmax:   0.30000E+03  0.15000E+04
      Pmin, Pmax:   0.10000E+01  0.10000E+03
      CHEB Polynomials:    0.70000E+01  0.40000E+01
      CHEB Polynomials:    0.11320E+02  0.21526E+00 -0.18210E-01 -0.66815E-04
      CHEB Polynomials:   -0.36361E+00 -0.34928E+00  0.22220E-01  0.14200E-02
      CHEB Polynomials:   -0.40177E+00  0.18883E+00 -0.12700E-01 -0.17900E-02
      CHEB Polynomials:    0.19995E+00 -0.60350E-01 -0.70600E-02  0.52000E-03
      CHEB Polynomials:   -0.67130E-01  0.29300E-03  0.47400E-02  0.48000E-03
      CHEB Polynomials:    0.54400E-02  0.12650E-01 -0.72000E-03 -0.49000E-03
      CHEB Polynomials:    0.12280E-01 -0.81600E-02 -0.92000E-03  0.10000E-03
556. C5H7OJ(366)(+m)=>C3H4(8)+CH2HCO(35)(+m)        1.00E+00     0.0        0.0
      Tmin, Tmax:   0.30000E+03  0.15000E+04
      Pmin, Pmax:   0.10000E+01  0.10000E+03
      CHEB Polynomials:    0.70000E+01  0.40000E+01
      CHEB Polynomials:    0.69788E+00  0.21526E+00 -0.18210E-01 -0.66931E-04
      CHEB Polynomials:   -0.86891E+01 -0.34928E+00  0.22220E-01  0.14200E-02
      CHEB Polynomials:   -0.55022E+00  0.18883E+00 -0.12800E-02 -0.17900E-02
      CHEB Polynomials:    0.23778E+00 -0.60340E-01 -0.70600E-02  0.52000E-03
      CHEB Polynomials:   -0.77990E-01  0.29000E-03  0.47400E-02  0.48000E-03
      CHEB Polynomials:    0.87700E-02  0.12650E-01 -0.72000E-03 -0.49000E-03
      CHEB Polynomials:    0.11220E-01 -0.81700E-02 -0.92000E-03  0.10000E-03
557. C2H4(6)+H2CCCH(26)(+m)=>C5H7J(574)(+m)         1.00E+00     0.0        0.0
      Tmin, Tmax:   0.30000E+03  0.15000E+04
      Pmin, Pmax:   0.10000E+01  0.10000E+03
      CHEB Polynomials:    0.70000E+01  0.40000E+01
```

```
        CHEB Polynomials:    0.10413E+02  0.63272E+00 -0.43570E-01 -0.45000E-03
        CHEB Polynomials:    0.27736E+00 -0.34062E+00 -0.31020E-01  0.23700E-02
        CHEB Polynomials:   -0.39703E+00  0.44530E-01  0.87500E-02  0.11800E-02
        CHEB Polynomials:    0.39590E-01  0.17750E-01 -0.49000E-03 -0.35000E-03
        CHEB Polynomials:    0.41350E-01 -0.13400E-01 -0.10400E-02  0.11000E-03
        CHEB Polynomials:   -0.30830E-01  0.35400E-02  0.75000E-03 -0.36082E-05
        CHEB Polynomials:    0.11590E-01  0.52000E-03 -0.23000E-03 -0.36849E-04
558. C5H7J(574)(+m)=>C2H4(6)+H2CCCH(26)(+m)         1.00E+00    0.0        0.0
        Tmin, Tmax:    0.30000E+03  0.15000E+04
        Pmin, Pmax:    0.10000E+01  0.10000E+03
        CHEB Polynomials:    0.70000E+01  0.40000E+01
        CHEB Polynomials:    0.75854E+01  0.63302E+00 -0.43480E-01 -0.43000E-03
        CHEB Polynomials:   -0.22631E+01 -0.34107E+00 -0.31150E-01  0.23400E-02
        CHEB Polynomials:   -0.51733E+00  0.44650E-01  0.87900E-02  0.11900E-02
        CHEB Polynomials:    0.66420E-01  0.17920E-01 -0.46000E-03 -0.34000E-03
        CHEB Polynomials:    0.40300E-01 -0.13650E-01 -0.11000E-02  0.96189E-04
        CHEB Polynomials:   -0.33780E-01  0.36900E-02  0.78000E-03  0.13708E-05
        CHEB Polynomials:    0.11550E-01  0.53000E-03 -0.23000E-03 -0.35409E-04
559. nc7h16(1)+C3H2(25)=>C7H15J(45)+H2CCCH(26)      1.74E+04    2.9        8.8
560. nc7h16(1)+C3H2(25)=>C7H15J(44)+H2CCCH(26)      2.04E+03    3.1        8.8
561. nc7h16(1)+C3H2(25)=>C7H15J(41)+H2CCCH(26)      4.08E+03    3.1        8.8
562. nc7h16(1)+C3H2(25)=>C7H15J(42)+H2CCCH(26)      4.08E+03    3.1        8.8
563. C7H12(724)+C3H2(25)=>C7H11J(783)+H2CCCH(26)    1.67E+13   -0.2        6.2
564. C2H6(7)+HCCO(34)=C2H5(24)+CH2CO(16)            8.70E+03    2.9        8.8
565. c7h14-3(40)+C3H2(25)=>C7H13J(294)+H2CCCH(26)   8.70E+03    2.9        8.8
566. c7h14-3(40)+C3H2(25)=>C7H13J(299)+H2CCCH(26)   8.70E+03    2.9        8.8
567. c7h14-3(40)+C3H2(25)=>C7H13J(297)+H2CCCH(26)   1.67E+13   -0.2        6.2
568. c7h14-2(39)+C3H2(25)=>C7H13J(297)+H2CCCH(26)   1.67E+13   -0.2        6.2
569. C3H2(25)+H(17)=>H2CCCH(26)                     2.42E+14    0.0        0.0

   NOTE: E units Kcal/mol, A units mole-cm-sec-K
```